Wave Generation and Absorption using Force-feedback Control

Johannes Spinneken

Imperial College London

Department of Civil and Environmental Engineering

Thesis submitted for the degree of Doctor of Philosophy of the University of London and for the Diploma of Imperial College

Abstract

This thesis concerns absorbing wave machines where the absorption strategy is based on a force-feedback approach. A theoretical model, describing their behaviour correct up to second order, is developed. At first order, this model seeks to provide a theoretical transfer function, linking the demand signal to the amplitude of the desired progressive wave. In the context of force-controlled wave machines, this transfer function may be regarded as the equivalent to the well known Biésel coefficients; the latter linking the demand signal and the progressive wave mode for position-controlled machines.

Furthermore, it is shown that the absorption mechanism affects the first-order transfer function. As part of a comparative study, a consistent framework for optimum absorption controllers is presented. An approach utilizing a numerical optimisation procedure is formulated and compared to other available techniques. This work is also relevant to related disciples, including the successful operation of wave energy devices.

Whilst the comparison of optimum absorption strategies is limited to first order, a detailed investigation of the effects arising at second order is also presented. In so doing, the influence of the nonlinear hydrodynamic feedback, induced by the force-driven approach, is discussed. In the case of flap-type wave machines the dry-backed paddles have a significant benefit over position-controlled machines in that they seem to introduce very little spurious harmonic content. In contrast, force-driven piston-type wave machines seem to introduce a significant amount of spurious wave content, in some cases more than that associated with equivalent position-controlled machines. In considering these effects, the operation of both machine types is carefully examined.

At present, the development of the second-order theory is limited to uni-directional waves. However, a separate study concerning the generation of oblique waves is included and a first-order force transfer function for the operation of wave basins is presented. Throughout the thesis, the theoretical work is supported by extensive experimental evidence. The generation and absorption of uni-directional regular and irregular waves is investigated. In addition, the practical generation capabilities of a multi-directional wave basin are also assessed.

Acknowledgements

I would first like to thank my supervisor Professor Chris Swan. It has been a privilege to work with him. Without his support and encouragement over the past three years, this thesis would not exist.

Lasting over a period even longer than this, I have received constant support from Mr Douglas Rogers, effectively my second or industrial supervisor. This has been on both a personal and professional level and Douglas has become a friend.

I would also like to thank Edinburgh Designs Ltd. for providing technical and financial support for this project.

During my PhD time at Imperial College London I have had the pleasure to meet many gifted and inspiring individuals, most notably Marios, Eirini, Jools and Milena. In particular, I would like to thank Milena for always showing a genuine interest in my project and providing the most helpful feedback.

I must thank my parents. Their support, patience and guidance is ever lasting. Finally, I cannot forget to thank my girlfriend Ryoko for putting up with me through the writing up period.

Contents

Abstract i

Acknowledgements ii

1 Introduction 1

1.1 Project Motivation 1

1.2 Major Achievements 3

1.3 Thesis Overview 5

2 Wave Maker Theory 8

2.1 Introduction 8

2.2 Governing Equations 9

2.3 Generated Wave Field 15

2.3.1 First-order Solution 15

2.3.2 Second-order Solution 21

2.4 Evanescent Modes 23

2.5 Range of Applicability 28

3 Wave Absorption Strategies 31

3.1 Chapter Overview 31

3.2 Introduction to Wave Absorption 32

3.3 Physical Model 37

3.3.1 Wave Field Solution 37

3.3.2 Added Mass and Hydrodynamic Damping 40

3.4 Control of Absorbing Wave Makers 43

3.4.1 Absorption Based on a Filtered Force Signal 46
3.4.2 Absorption Based on a Filtered Velocity Signal 50
3.4.3 Absorption Based on Infinite Impulse Response Function Filters 53
3.4.4 Comparing the Approaches 58
3.5 Conclusions 62

4 Nonlinear Control of Absorbing Flap-type Wave Machines 63
4.1 Chapter Overview 63
PART I: A NEW THEORY FOR REGULAR WAVE GENERATION 64
4.2 Introduction 65
4.3 Physical Model 68
4.4 Hydrodynamic Feedback 69
4.4.1 Generated Wave Field 69
4.4.2 Wave Field at Second-harmonic in First-order Position Control 71
4.4.3 Hydrodynamic Torques on Flap-type Wave Machines 72
4.5 Wave Board Dynamics 74
4.6 Absorption Filter Design 75
4.7 Frequency Domain Model 77
4.8 Wave Generation at Second Harmonic and Second-order Correction 78
4.9 Simulation Models 80
4.10 Second-order Content for Flap-type Machines 81
4.11 Conclusions 85
PART II: AN EXPERIMENTAL VERIFICATION OF REGULAR WAVE GENERATION 86
4.12 Introduction to Experimental Investigation 86
4.13 Experimental Conditions 87
4.14 First-order Control and Wave Absorption 90
4.15 Errors Arising from a First-order Command Signal 94
4.16 Second-order Control 100
4.17 Conclusions 105

5 Nonlinear Control of Absorbing Piston-type Wave Machines 106

5.1 Chapter Overview 106

PART I: A NEW THEORY FOR IRREGULAR WAVE GENERATION 107

5.2 Introduction 108

5.3 Wave-wave Interaction 109

5.4 Application of Position-control Theory 111

5.4.1 Regular Waves 111

5.4.2 Irregular Waves 112

5.5 Application of Force-control Theory 114

5.5.1 Forces at First and Second Order 114

5.5.2 Nonlinear Feedback and Second-order Correction 116

5.5.3 Second-order Effects for Regular Waves 117

5.5.4 Second-order Effects for Irregular Waves 118

5.6 Comparison of First-order Position and First-order Force Control . 120

5.6.1 Regular Waves 120

5.6.2 Irregular waves 124

PART II: AN EXPERIMENTAL VERIFICATION OF IRREGULAR WAVE GENERATION 129

5.7 Introduction 129

5.8 Effects Arising at First Order 132

5.8.1 First-order Transfer Function 132

5.8.2 Validation of the First-order Transfer Function 134

5.8.3 Absorption Coefficient 138

5.8.4 Focused Wave Event 139

5.8.5 Irregular Waves 140

5.9 Effects Arising at Second Order 148

5.9.1 Regular Waves 148

5.9.2 Bi-chromatic Waves 152

5.9.3 Irregular Waves 157

5.10 Conclusions 167

6 Multi-directional Wave Generation using Force Control 168

6.1 Chapter Overview 168

6.2 Introduction 169

6.3 Directional Wave Generation 171

6.3.1 Directional Wave Maker of Finite Length 171

6.3.2 Segmented-type Wave Generators 175

6.3.3 Infinitely Long Wave Maker 180

6.3.4 Hydrodynamic Coefficients 183

6.4 Absorption Characteristic of a Wave Basin 185

6.5 Theoretical Transfer Function of a Wave Basin 188

6.6 Experimental Investigation 190

6.6.1 Amplitude Spectrum 191

6.6.2 Focused Wave Event 195

6.6.3 Energy Spectrum 205

6.7 Conclusions 208

7 Conclusions and Recommendations for further Work 209

7.1 Absorption Characteristic 210

7.2 First-order Behaviour 211

7.3 Second-order Behaviour 212

7.4 Multi-directional Waves 213

7.5 Closing Remarks 214

Appendix A - Position-control: Further Development of the Wave Field Coefficients 215

Appendix B - The Second-order Torques 218

Appendix C - The Second-order Forces 221

Appendix D - A Note on Closed Loop Control Systems 224

Appendix E - Directional Wave Maker of Finite Width 226

Appendix F - Evaluation of An Empirical Calibration Approach **228**

Appendix G - The Experimental Environment **233**

List of Figures

2.1 Wave maker geometry and definition of notation 10
2.2 Special cases of wave maker geometries 11
2.3 Dimensionless first-order wave field coefficients 18
2.4 Relevance of first-order wave field coefficients 19
2.5 Horizontal fluid velocity on piston-type machine (i) 25
2.6 Horizontal fluid velocity on piston-type machine (ii) 25
2.7 Horizontal fluid velocity on flap-type machine (ii) 26
2.8 Horizontal fluid velocity on flap-type machine (ii) 26
2.9 Evanescent mode decay characteristic 27
2.10 Range of applicability: evaluation of surface profiles 29
2.11 Range of applicability: maximum steepness 29

3.1 Transfer and impulse response function 34
3.2 Wave maker geometry and definition of notation 38
3.3 Hydrodynamic coefficients for a piston-type wave machine 42
3.4 Hydrodynamic coefficients for a flap-type wave machine 43
3.5 Schematic of controller model for absorbing wave maker; (a) Force based absorption filter and (b) Velocity based absorption filter . . . 44
3.6 Impulse response function - controller with filtered force signal . . . 47
3.7 Transfer function for controller with filtered force signal 49
3.8 Power absorption coefficient for a variety of tuning frequencies (i) . 49
3.9 Power absorption coefficient for a variety of tuning frequencies (ii) . 53
3.10 Bode plot for two IIR filters 55

3.11 Impulse response function for two IIR filters 55
3.12 Power absorption coefficient for a variety of tuning frequencies (iii) . 59
3.13 Power absorption coefficient optimised for low frequency range . . . 59
3.14 Power absorption coefficient optimised for intermediate frequency range 60
3.15 Power absorption coefficient for a variety of optimum frequencies . . 61

4.1 First-order position control: dimensionless spurious wave amplitude 72
4.2 Impedance matching for a bottom hinged wave maker 77
4.3 Schematic for general system model 78
4.4 First-order force control: dimensionless spurious wave amplitude (i) 82
4.5 First-order force control: dimensionless spurious wave amplitude (ii) 82
4.6 Dimensionless second-order correction torque 84
4.7 Definition sketch for the double ended flume at Imperial College . . 88
4.8 First-order force-control demand signal 91
4.9 Absorption coefficient for flap-type wave machine 92
4.10 Surface elevation for a standing wave in a double ended tank 93
4.11 Dimensionless spurious wave content amplitude for a bottom-hinged wave maker 95
4.12 Surface elevation for wave case $f = 32/64Hz$, $Hk/2 = 0.10$; first-order position control vs. first-order force control 98
4.13 Close-up of the water surface elevation for above case 98
4.14 Surface elevation for wave case $f = 56/64Hz$, $Hk/2 = 0.23$; first-order position control vs. first-order force control 99
4.15 Close-up of the water surface elevation for above case 99
4.16 Second-order force-control: dimensionless spurious wave amplitude . 101
4.17 Surface elevation for wave case $f = 34/64Hz$, $Hk/2 = 0.11$; first-order force control vs. second-order force control 103
4.18 Close-up of the water surface elevation for above case 103

4.19 Surface elevation for wave case $f = 48/64Hz$, $Hk/2 = 0.16$; first-order force control vs. second-order force control 104
4.20 Close-up of the water surface elevation for wave above case 104

5.1 Amplitude of the super-harmonic wave-wave interaction term 110
5.2 Amplitude of the sub-harmonic wave-wave interaction term 110
5.3 First-order position-control: dimensionless spurious wave amplitude for regular waves 112
5.4 First-order posi8ion control: spurious super-harmonic wave amplitude113
5.5 First-order posi8ion control: dimensionless spurious sub-harmonic wave amplitude 114
5.6 First-order force control: dimensionless spurious wave amplitude . . 117
5.7 First-order force control: super-harmonic spurious wave amplitude . 119
5.8 First-order force control: sub-harmonic spurious wave amplitude . . 119
5.9 Interference pattern arising from the bound and free travelling harmonics at second order 121
5.10 Surface profile evaluated for $h = 0.6m$, $f = 23/64Hz$ $(h/L_0 = 0.05)$ and $Hk/2 = 0.055$ $(S = 1)$ 122
5.11 Surface profile evaluated for $h = 0.6m$, $f = 40/64Hz$ $(h/L_0 = 0.15)$ and $Hk/2 = 0.2$ $(S = 0.85)$ 123
5.12 Surface profile evaluated for $h = 0.6m$, $f = 73/64Hz$ $(h/L_0 = 0.5)$ and $Hk/2 = 0.2$ $(S = 0.4)$ 123
5.13 First-order JONSWAP amplitude spectrum 125
5.14 Second-order JONSWAP spectrum (i) 126
5.15 Second-order JONSWAP spectrum (ii) 127
5.16 Two implementations of a sector-carrier piston-type wave machine: University College London (left) and Imperial College London (right)131
5.17 First-order force control: Surface elevation for a wave steepness of $Hk/2 = 0.05$ 136
5.18 Complex first-order force transfer function c_f 137

5.19 Power absorption coefficient for piston-type wave machine 138
5.20 Surface profile for focused wave event 141
5.21 Experimental setup for irregular wave generation 142
5.22 Irregular wave generation and absorption 143
5.23 Surface elevation for the JONSWAP target spectrum, randomised phase set 1 145
5.24 Surface elevation for the JONSWAP target spectrum, randomised phase set 2 146
5.25 First-order force control: Surface profile for the wave case $f = 26/64Hz$, $Hk/2 = 0.1$ 149
5.26 First-order force control: Surface profile for the wave case $f = 32/64Hz$, $Hk/2 = 0.1$ 149
5.27 Second-order force control: Surface profile for the wave case $f = 26/64Hz$, $Hk/2 = 0.1$ 151
5.28 Second-order force control: Surface profile for the wave case $f = 32/64Hz$, $Hk/2 = 0.1$ 151
5.29 Force control: dimensionless spurious wave amplitude; theory and experiment 152
5.30 Theoretical second-order surface profile for a bi-chromatic wave train 153
5.31 First-order force control: surface profile for a bi-chromatic wave (i) . 155
5.32 Second-order force control: surface profile for a bi-chromatic wave (i) 155
5.33 First-order force control: surface profile for a bi-chromatic wave (ii) 156
5.34 Second-order force control: surface profile for a bi-chromatic wave (ii) 157
5.35 Case 1: Surface elevation at $x = 2.15m$ based on first-order force control 159
5.36 Case 1: Surface elevation at $x = 2.15m$ based on second-order force control 160
5.37 Close-up of the surface elevation shown in figure 5.35 161
5.38 Close-up of the surface elevation shown in figure 5.36 161

5.39 Case 2: Surface elevation at $x = 2.15m$ based on first-order force control 163
5.40 Case 2: Surface elevation at $x = 2.15m$ based on second-order force control 164
5.41 Close-up of the surface elevation shown in figure 5.39 165
5.42 Close-up of the surface elevation shown in figure 5.40 165

6.1 Layout of a 3D wave basin 172
6.2 Surface elevation contours for finite length wave maker 173
6.3 Surface elevation contours for finite length wave maker and oblique waves 174
6.4 Motion approximated by a piecewise constant function as adopted in a realistic segmented-type wave maker 175
6.5 Spurious modes for the generation of oblique waves (i) 178
6.6 Spurious modes for the generation of oblique waves (ii) 178
6.7 Empirical transfer function for a 3D wave basin, after Masterton & Swan (2008) 179
6.8 Dimensionless first-order coefficients for a piston-type wave maker . 182
6.9 Dimensionless first-order coefficients for a flap-type wave maker with $d/h = 0.5$ 182
6.10 3D added mass coefficient for a piston-type wave maker 184
6.11 3D added mass coefficient for a flap-type wave maker 185
6.12 Absorption coefficient for oblique waves, flap-type wave maker . . . 187
6.13 Contour plot representing the power absorption coefficient γ for the wave machine discussed in figure 6.12 187
6.14 Magnitude and phase of first-order force transfer function c_f 188
6.15 Contour plot representing the magnitude of the theoretical first-order force transfer function 189
6.16 Contour plot representing the phase of the theoretical first-order force transfer function 189

6.17 Amplitude content for a random phase uni-directional JONSWAP spectrum propagating at $\alpha = 0°$ 193
6.18 Amplitude content for a random phase uni-directional JONSWAP spectrum propagating at $\alpha = 15°$ 194
6.19 Amplitude content for a random phase uni-directional JONSWAP spectrum propagating at $\alpha = 30°$ 194
6.20 Amplitude content for a random phase uni-directional JONSWAP spectrum propagating at $\alpha = 45°$ 195
6.21 Surface profile for a uni-directional JONSWAP *NewWave* spectrum with $\alpha = 0°$ 197
6.22 Surface profile for a uni-directional JONSWAP *NewWave* spectrum with $\alpha = 15°$ 198
6.23 Surface profile for a uni-directional JONSWAP *NewWave* spectrum with $\alpha = 30°$ 198
6.24 Surface profile for a multi-directional JONSWAP *NewWave* spectrum with $\sigma_\alpha = 30°$ 200
6.25 Spatial amplitude variation in the traverse direction for a multi-directional JONSWAP *NewWave* spectrum 200
6.26 Surface profile for multi-directional JONSWAP *NewWave* spectrum with $\sigma_\alpha = 30°$; $y = +1.2m$ 201
6.27 Surface profile for multi-directional JONSWAP *NewWave* spectrum with $\sigma_\alpha = 30°$; $y = -1.2m$ 201
6.28 Surface profile for a large multi-directional JONSWAP *NewWave* spectrum with $\sigma_\alpha = 30°$ 202
6.29 Surface profile for a uni-directional JONSWAP spectrum with $\alpha = 0°$ 204
6.30 Amplitude content for a random phase uni-directional JONSWAP spectrum with $\alpha = 0°$ 205
6.31 Energy content for a uni-directional JONSWAP spectrum with $\alpha = 0°$ 206
6.32 Energy content for a uni-directional JONSWAP spectrum with $\alpha = 20°$ 207

6.33 Energy content for a uni-directional JONSWAP spectrum with $\alpha = 40°$ 207

D-1 Generic controller model 224

F-1 Frequency dependent gain for a 3D wave basin 229

F-2 Effect of a finite window length on the FFT results, tophat spectrum 230

F-3 Effect of a finite window length on the FFT results, JONSWAP spectrum 231

F-4 JONSWAP spectrum computation 232

G-1 *Double Ended Wave Flume* definition sketch 233

G-2 *Coastal Wave Flume* definition sketch 234

G-3 Beach reflection coefficient of *Coastal Wave Flume* 235

G-4 Cross sectional area of directional wave basin 236

G-5 Wave gauge noise characteristic 237

G-6 Typical conductive wave probe calibration curve 238

G-7 Repeatability of surface elevation measurement 239

List of Tables

4.1 Laboratory test cases 89

5.1 Spectral properties for JONSWAP amplitude spectrum 128

5.2 RMS deviation of maximum and minimum surface elevation with the data being based on a zero up-crossing analysis 166

1

Introduction

1.1 Project Motivation

One of the first papers on wave making theory was titled *'Forced surface-wave on water'* (Havelock 1929). In a literal sense this precisely describes the objective of any wave generation system: to force the water particles on the paddle front in a prescribed motion and, in so doing, create a progressive wave that transmits the energy input into the wave flume or wave basin. Ideally, the combination of many progressive waves represents a prescribed sea state exactly and model testing can be performed with a high level of confidence regarding the input wave conditions.

Unfortunately, there is always an inherent mismatch between the velocity profile a wave board can prescribe and the velocity profile naturally occurring under a progressive wave train; this mismatch giving rise to additional unwanted wave components. Some of the additional components are standing waves and decay with increasing distance from the wave board. However, additional progressive waves are also introduced and contaminate the testing area. As a result, these latter modes are often referred to as spurious waves. The purpose of applying a nonlinear demand signal is to suppress these spurious wave modes.

Moreover, reflections from models and the tank's boundaries add to the contamination of the testing area. It has thus become common practice (or at least

best practice) to ensure that the wave generator is also an active wave absorber. As a result, the ideal wave making system is capable of generating waves of high quality (using a nonlinear input signal) and simultaneously provides active absorption of reflected waves.

To achieve this latter objective, active wave absorption, the wave generation system requires some additional information about the fluid's state, ideally in close proximity to the wave board. The acquisition and processing of such measured quantities, in order to determine the system's future actions, is called feedback or closed loop control. Measuring and controlling the position of the wave board only, as is traditionally the case, does not provide the required dependency for active wave absorption; the fluid motion is dependent on the wave board motion, but not vice versa. As a result, an additional measurement such as the surface elevation at the paddle face needs to be made; this measurement can only be taken at discrete points and hence gives incomplete information about the fluids current state.

Directly controlling the force acting on the paddle overcomes those two shortcomings: (i) the force is an integral quantity incorporating the average fluid motion and (ii) Newton's third law of action and reaction is employed; the wave machine and the fluid are linked directly as a coupled dynamic system. Furthermore, the combination of the physical quantities of force and velocity provides a direct measure for the system's power input/output; power being the actual quantity under consideration when discussing active wave absorption.

Adopting similar arguments, Salter et al. (1976) engineered a highly efficient wave energy converter based on force-feedback. Using the techniques developed for the wave energy extraction device, Salter (1982) designed an absorbing wave making facility. The success of his early designs was such that in excess of 500 wave paddles employing force-feedback control are in operation today. However, even though many laboratory facilities are equipped with these devices, there is a complete absence of published literature concerning the underlying theory or the wave quality that can be achieved in practice. This lack of both theoretical inves-

tigations and supporting laboratory observations, combined with many practical arguments that favour force control, was the motivation for the present thesis; the aim being to show that force-controlled wave machines can achieve comparable or improved wave quality when compared to position-controlled systems and to explain the reasons for this. To distinguish between the two approaches adopted throughout the thesis, the term *'position-controlled'* refers to machines where the wave board position is the only control parameter. In contrast, *'force-controlled'* refers to machines where the force acting on the wave board is one of the controlled quantities; the others being position, velocity and acceleration.

The lack of publications and documentation, particularly in the early days of force-driven wave making technology, has had another direct effect: despite their commercial and practical success, researchers have been reluctant to take on the challenge to improve the operation of such devices. This is in marked contrast to position-controlled machines where a large number of publications over the past three decades have initiated an active and ongoing debate regarding the wave quality achieved in practice. The present thesis may be seen as a first attempt at initiating a similar debate related to force-driven devices. The work presented herein includes both extensive theoretical work and an experimental verification over a wide range of wave conditions; the major achievements being summarised in the following section.

1.2 Major Achievements

In a recent publication, Masterton & Swan (2008) reported on an efficient method for the calibration of a multi-directional absorbing wave basin. Even though such an empirical calibration may remain the preferred approach to operate both wave flumes and basins, the present thesis provides the theoretical framework required to understand the wave machine's transfer function. In fact, the calibration approach has been applied to absorbing wave making equipment for nearly forty years. However, whilst the engineers who initially designed this technology had

a firm understanding of the mechanisms involved, this knowledge has not been successfully transferred. The explanation for this lies mainly due to the aforementioned lack of documentation and publications in the early days of wave power. In this light, the present thesis may be regarded as the combination of the following major achievements:

1. The existing knowledge concerning force-controlled absorbing wave makers has, for the first time, been documented thoroughly. This is particularly true for the wave making equipment and absorption strategy first described by Salter (1982).

2. Building upon this existing knowledge, the absorption strategy has been compared to other techniques and was shown to be superior. Such a comparison has not been reported prior to this work.

3. The direct comparison in a common notation establishes a framework that may be used to enhance the absorption efficiency of force-driven wave makers world wide - including but not limited to those supplied by Edinburgh Designs Ltd.

4. The theoretical aspects of wave generation and absorption have been combined into a novel theory allowing the theoretical prediction of the wave machine's first-order transfer function. The calibration mentioned earlier (Masterton & Swan 2008) may now be put into a theoretical context.

5. The developed theory has been extended correct to the second-order of wave steepness, enabling the generation of high quality waves with simultaneous absorption; a method thus far unreported.

6. A long suspected advantage of force-driven flap-type wave makers operating in deep and intermediate water depths has been proven theoretically: the wave quality when operating such devices with a first-order command signal is very good and superior to comparable position-controlled machines. In such cases second-order correction may not be required.

7. A first-order theory for multi-directional wave generation using force-feedback control has been developed.

8. Extensive experimental work, covering all aspects of the new theory, has been undertaken and substantiates the validity of the theoretical model.

Much of this work has already been published, see Spinneken & Swan (2009*a*), Spinneken & Swan (2009*b*) and Spinneken & Swan (2009c), with further publications in preparation. Moreover, a cooperation with Prof. Naito at Osaka University is envisaged in order to apply the modelling procedures to a different wave board geometry in a circular test basin.

1.3 Thesis Overview

The PhD thesis is divided into five major chapters. Each chapter, containing one or two parts, commences with an overview where the focus of the particular chapter is brought into the wider context of the thesis. Within Chapter 2 a firm background on wave making theory is presented and the commonly adopted notation introduced. Moreover, background material is introduced throughout the thesis, with the new work building upon it. The order of the chapters that follow is such that they involve an increasingly complex permutation of the following three pairs: (i) first order and second order, (ii) regular and irregular seas and (iii) uni-directional and multi-directional waves.

Chapter 3 deals with the concept of actively absorbing wave makers based on force control. The absorption strategy employed throughout the work is introduced and compared to other methods. This chapter is broadly based on the conference paper Spinneken & Swan (2009c), but has been revised and extended. Only first-order aspects are considered and any experimental evidence has been omitted; the latter being presented in detail as part of Chapters 4 and 5.

In Chapter 4, the absorption strategy established in Chapter 3 is applied to flap-type wave machines and the theory is extended to second order. This work

is presented as two parts; the first focusing on the theoretical aspects and the second providing an experimental justification for the new theory. Both studies are limited to the generation and absorption of regular waves only. The two parts are based on the work presented in Spinneken & Swan (2009*a*) and Spinneken & Swan (2009*b*). Apart from some minor editing, these two papers remain in their originally published form and provide evidence that the current work can withstand a thorough peer-review process.

One of the conclusions drawn from Chapter 4 is that second-order correction may often not be required. This conclusion is partly supported by the fact that most experiments within this study were undertaken in intermediate to deep water; the region where flap-type wave makers are most commonly employed. In an attempt to broaden these studies, a separate study was undertaken concerning the operation of force-controlled piston-type wave makers in shallow water; a region where second-order effects are known to be more pronounced. The level of complexity in this third step is further increased by including the second-order generation of irregular waves. As before, the work is divided into two parts, one with a focus on the theoretical aspects and the other the accompanying experimental work. Both aspects of this work are presented within Chapter 5.

In a fourth and final step, the theory is extended to include multi-directional force-driven wave generation. Even though this last step of the investigation is limited to first order, there are at least two relevant applications of the new theory. First, the calibration of a multi-directional wave making facility is a very time consuming procedure, as reported by Masterton & Swan (2008). A theoretical transfer function has the potential to significantly shorten this procedure for any future basin commissioning and also provide enhanced insight in the underlying physics. Second, a recent but as yet unpublished study (Newman 2008) showed that to correctly absorb waves in a numerical circular wave basin, some advanced absorption strategies need to be employed. Similar arguments apply to the absorption of oblique waves in rectangular basins. The present work provides the theoretical framework required to implement these advanced techniques. Both

the theoretical work and experimental evidence concerning the wave generation (or first-order transfer function) are presented in Chapter 6.

The thesis concludes with Chapter 7. This summarises the findings of each of the earlier chapters and provides some suggestions for further work.

2

Wave Maker Theory

2.1 Introduction

This chapter introduces the common wave making background that underpins much of the work presented in the later chapters. Even though the present work primarily concerns force-controlled wave machines, much of the existing theory for position-controlled systems may be employed: the wave field generated by a given sinusoidal paddle motion is identical for both position- and force-controlled machines. However, a single harmonic force-control signal does not inevitably lead to a paddle motion at this harmonic alone. Indeed, all the nonlinear processes in the generated wave field will contribute to the applied force and hence feed back into the generation process. This will be discussed in detail at a later stage.

Havelock (1929) presented a first general wave generation theory and his work is commonly regarded as the foundation for subsequent theories. In deriving this theory, Havelock introduced a first-order approximation of the boundary conditions and, adopting the Fourier integral theorem, obtained a depth dependent function that includes both the progressive wave mode and a local oscillation. In addition, Havelock derived an explicit expression for the wave field and surface elevation appropriate to a piston-type wave machine. Later on Biésel & Suquet derived explicit expressions for both flap and piston-type geometries and provide

extensive information as to their practical implementation. This work was originally published in the French Journal *La Houille Blanche.* However, given the practical significance of their work, these articles were translated into English and published as Biésel & Suquet (1954).

Assuming the first-order motion of the paddle is known, the generated wave field up to second order can be derived. This has been discussed extensively in the existing literature (Flick & Guza (1980), Sulisz & Hudspeth (1993), van Leeuwen & Klopman (1996), Schäffer (1996) and Zaman & Mak (2007)) and will not be repeated herein. Indeed, throughout this thesis a notation and solution similar to that presented by Schäffer (1996) is adopted; the present chapter summarising the notation and detailed mathematics on which the solution is based. This includes deriving all the boundary conditions appropriate to the problem from first principles and presenting the solution for the generated wave field. The lengthy algebra required to derive this solution is, however, omitted. Nevertheless, at any stage the reader may readily substitute the solution into the given boundary conditions to verify that the results presented are indeed correct.

2.2 Governing Equations

The present chapter investigates uni-directional, irregular waves based on the non-linear superposition of N wave components ranging from $n = 1..N$. A boundary-value problem based on a classical perturbation approach combined with Taylor expansions of the boundary conditions at the free surface is presented. Within this the following notation is adopted: the velocity potential $\Phi = \Phi(x, z, t)$ in Cartesian coordinates (x, z) is defined such that the velocity components are given by $(u, w) = (\partial\Phi/\partial x, \partial\Phi/\partial z)$, where x is defined as positive in the direction of wave propagation and z is measured vertically upwards from the still water level (SWL). The water surface elevation is given by $\eta = \eta(x, t)$ and the wave board position by $X = X(z, t)$; the wave board position at still water level ($z = 0$) being denoted by $X_0(t)$. Furthermore, θ, ω, g, h and t denote angular wave board displacement,

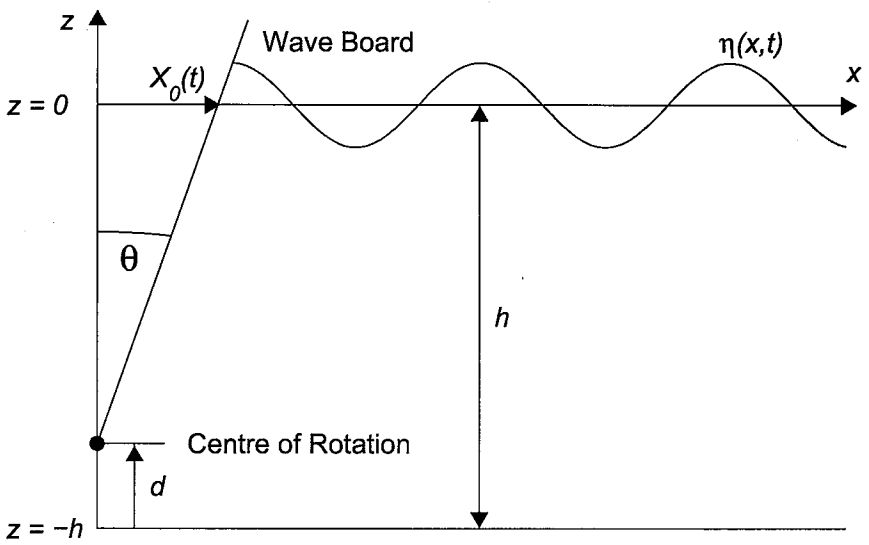


Figure 2.1: Wave maker geometry and definition of notation

angular wave frequency, acceleration of gravity, still water depth, and time, respectively. The displacement l is defined so that $z = -(h + l)$ gives the centre of rotation of the wave board and $d \geq 0$ is the elevation of the hinge above the bed. If the centre of rotation is below or at the bed then d is set to zero. For the special case of a piston-type wave maker, if follows that $l = \infty$ and $d = 0$. Figure 2.1 defines both the general wave maker geometry and the notation employed. The values for d and l for commonly employed wave maker geometries are further clarified in figure 2.2.

The boundary conditions appropriate to the problem defined on figure 2.1 are as follows:

a. With the bed assumed to be horizontal and impermeable, $w = 0$ on $z = -h$.

b. The water surface profile is a streamline defining the Kinematic Free Surface Boundary Condition (KFSBC).

c. The pressure acting on the water surface is constant (atmospheric) defining

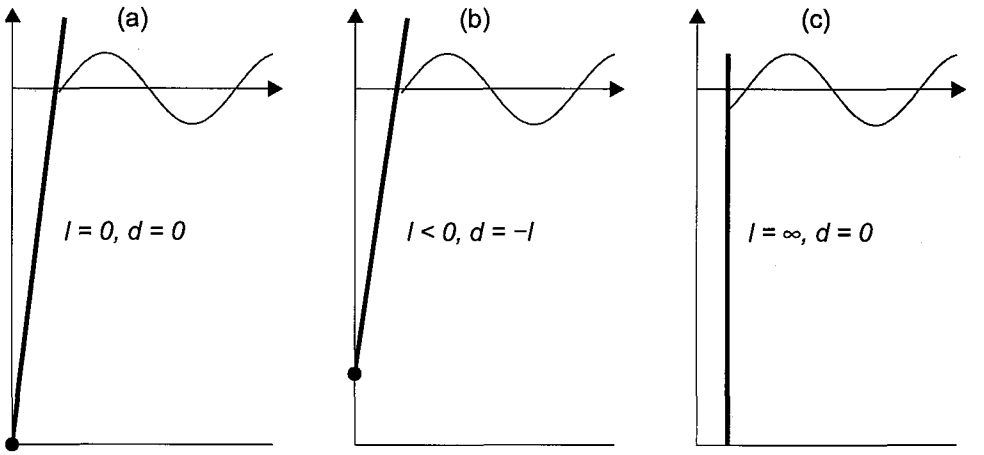


Figure 2.2: Wave maker geometries: (a) bottom hinged flap, (b) flap where the hinge is place above the bed, (c) full depth piston

the Dynamic Free Surface Boundary Condition (DFSBC)

d. On the wave board, the fluid velocity perpendicular to the wave board must be equal to the velocity of the wave board

The boundary conditions described above must be expressed as a set of equations. First, with the fluid assumed to be incompressible, conservation of mass ensures that the Laplace equation must apply throughout the fluid domain

$$\nabla^2\Phi = \frac{\partial^2\Phi}{\partial x^2} + \frac{\partial^2\Phi}{\partial z^2} = 0. \tag{2.1}$$

The bottom boundary condition, (a) above, readily yields

$$w = \frac{\partial\Phi}{\partial z} = 0, \tag{2.2}$$

on $z = -h$. Conditions (b) and (c), the KFSBC & DFSBC, may be defined as

$$\frac{\partial\eta}{\partial t} = w - u\frac{\partial\eta}{\partial x} = \frac{\partial\Phi}{\partial z} - \frac{\partial\Phi}{\partial x}\frac{\partial\eta}{\partial x} \tag{2.3}$$

and

$$\frac{\partial\Phi}{\partial t} = -g\eta - \frac{1}{2}\left(u^2 + w^2\right) = -g\eta - \frac{1}{2}\left[\left(\frac{\partial\Phi}{\partial x}\right)^2 + \left(\frac{\partial\Phi}{\partial z}\right)^2\right] \tag{2.4}$$

both being valid on $z = \eta$. Expanding (2.3) about the mean water level using a Taylor series expansion, and retaining terms up to a second-order of wave steepness, $O((ak)^2) = O(\epsilon^2)$, gives

$$\frac{\partial \eta^{(1)}}{\partial t} = \frac{\partial \Phi^{(1)}}{\partial z}, \tag{2.5}$$

at first order and

$$\frac{\partial \eta^{(2)}}{\partial t} = \frac{\partial \Phi^{(2)}}{\partial z} - \frac{\partial \Phi^{(1)}}{\partial t}\frac{\partial \eta^{(1)}}{\partial x} + \eta^{(1)}\frac{\partial^2 \Phi^{(1)}}{\partial z^2} \tag{2.6}$$

at second order, where the super-script denotes the order of the term involved. Similarly, expanding the DFSBC (equation 2.4) about the mean water level and retaining terms up to a second-order of wave steepness yields

$$\frac{\partial \Phi^{(1)}}{\partial t} = -g\eta^{(1)}, \tag{2.7}$$

at first order and

$$\frac{\partial \Phi^{(2)}}{\partial t} = -g\eta^{(2)} - \frac{1}{2}\left[\left(\frac{\partial \Phi^{(1)}}{\partial x}\right)^2 + \left(\frac{\partial \Phi^{(1)}}{\partial z}\right)^2\right] - \eta^{(1)}\frac{\partial^2 \Phi^{(1)}}{\partial z \partial t} \tag{2.8}$$

at second order. With the wave board assumed to be flat, solid and impermeable, the fluid velocity normal to the wave board has to be identical to the wave board's normal velocity:

$$v_n = r\frac{d\theta}{dt}, \tag{2.9}$$

where the radius r may be expressed in terms of wave board motion and depth as

$$r = \sqrt{(X(z,t))^2 + (l+h+z)^2} = (l+h+z)\sqrt{1+\tan^2\theta}. \tag{2.10}$$

The normal fluid velocity, defined in terms of the horizontal and vertical velocity

components (u, w), is given by

$$v_n = u\cos\theta - w\sin\theta, \tag{2.11}$$

and combining the two expressions for v_n yields

$$(l + h + z)\sqrt{1 + \tan^2\theta}\frac{d\theta}{dt} = u\cos\theta - w\sin\theta. \tag{2.12}$$

An assumption which is commonly adopted (Flick & Guza 1980, Barthel et al. 1983, Hughes 1993) is that the paddle stoke is small compared to its length, $X_0/(h + l) = \tan\theta = \delta << 1$. At this stage it is important to stress that the small quantity δ solely relates to the displacement of the wave board. As such, δ is entirely distinct from ϵ; the latter representing the wave steepness (ak) used as the expansion parameter for the perturbation analysis within which the second-order boundary-value problem will be solved. Observing the right hand side of equation (2.12)

$$u\cos\theta - w\sin\theta = \cos\theta(u - w\tan\theta) = \cos\theta(u - \delta w), \tag{2.13}$$

it is clear that the vertical velocity contribution may be neglected since $\delta w << u$. Adopting the small angle approximation throughout, the following approximations may be made:

$$\begin{aligned}
&\cos\theta(u - \delta w) \approx u = \frac{\partial\Phi}{\partial x} \\
&\tan^2\theta << 1 \\
&\theta \approx \tan\theta = \frac{X(z,t)}{l + h + z} = \frac{X_0(t)}{h + l}.
\end{aligned}$$

For further information concerning these approximations the reader is directed to Hughes (1993). Substituting the above, the wave maker boundary condition at

$x = X(z,t)$ reduces to

$$\frac{\partial \Phi}{\partial x} = \frac{\partial X(z,t)}{\partial t} = \left(1 + \frac{z}{h+l}\right) \frac{\partial X_0(t)}{\partial t}. \tag{2.14}$$

This expression is not easily solved; the boundary condition applies on $x = X(z,t)$ and is thus a function of depth and time. This can be overcome by expanding the boundary condition about the still wave board position ($x = 0$) in a similar fashion as expanding the KFSBC and DFSFB about the free surface ($z = 0$). However, this is more easily achieved in cylindrical coordinates

$$\Phi(\theta, z, t, \epsilon) = \epsilon \Phi^{(1)} + \epsilon^2 \left(\Phi^{(2)} + \theta^{(1)} \frac{\partial \Phi^{(1)}}{\partial \theta}\right), \tag{2.15}$$

and transforming into Cartesian coordinates yields

$$\Phi(\theta, z, t, \epsilon) = \epsilon \Phi^{(1)} + \epsilon^2 \left[\Phi^{(2)} + \theta^{(1)} \left((l + h + z)\frac{\partial \Phi^{(1)}}{\partial x} - x \frac{\partial \Phi^{(1)}}{\partial z}\right)\right]. \tag{2.16}$$

Combining the boundary condition on the wave board with the expanded velocity potential gives

$$\frac{\partial \Phi^{(1)}}{\partial x} = f(z) \frac{dX_0^{(1)}}{dt}, \tag{2.17}$$

at first order; the small angle $\theta^{(1)}$ having been replaced by its approximation given above. At second order the boundary condition reduces to

$$\frac{\partial \Phi^{(2)}}{\partial x} = \begin{cases} f(z)\frac{dX_0^{(2)}}{dt} - X_0^{(1)}\left[f(z)\frac{\partial^2 \Phi^{(1)}}{\partial x^2} - \frac{1}{l+h}\frac{\partial \Phi^{(1)}}{\partial z}\right] & \text{for } -(h-d) \leq z \leq 0 \\ 0 & \text{for } -h \leq z < -(h-d), \end{cases} \tag{2.18}$$

where again the super-script () denotes the order of term involved. Both equation (2.17) and (2.18) are valid for $x = 0$, where $X_0^{(1)}$ and $X_0^{(2)}$ are the first- and second-order control signals in position control.

2.3 Generated Wave Field

The potential solution for the wave field generated by a first-order position-control signal is conveniently separated into three components:

(i) *The first-order velocity potential* - $\Phi^{(1)}$

This describes the progressive wave to be generated as well as the associated evanescent modes arising at, or near, the wave paddle. It must satisfy the boundary condition on the wave maker, requiring the fluid velocity normal to the wave board to be equal to the wave board velocity.

(ii) *The wave-wave interaction potential* - $\Phi^{(21)}$

In the general case of an irregular sea state, the various first-order waves and their evanescent modes described by $\Phi^{(1)}$ will interact with each other; $\Phi^{(21)}$ describes these cross interaction terms as well as the self interaction or Stokes terms.

(iii) *The spurious free wave potential* - $\Phi^{(22)}$

Although $\Phi^{(1)}$ and $\Phi^{(21)}$ together satisfy the second-order free surface boundary conditions, they do not fully satisfy the second-order boundary condition at the wave maker. This leads to the generation of an unwanted free wave which is expressed as $\Phi^{(22)}$.

In order to correctly reproduce a demanded sea state, a compensation signal cancelling the additional spurious wave potential $\Phi^{(22)}$ has to be added to the control signal. This process will be discussed in detail within later sections of the thesis.

2.3.1 First-order Solution

Evaluating the boundary conditions for an inviscid and incompressible fluid, yields the first-order wave potential given by

$$\Phi^{(1)} = \sum_{n=1}^{N} \frac{1}{2} \left\{ \frac{igX_n}{\omega_n} \sum_{j=0}^{\infty} c_{jn} \frac{\cosh k_{jn}(z+h)}{\cosh k_{jn}h} e^{i(\omega_n t - k_{jn}x)} + c.c. \right\}, \qquad (2.19)$$

where X_n is the complex, first-order, paddle displacement amplitude for wave component n at the still water level and *c.c.* the complex conjugate of the preceding term. Using this result, the first-order paddle motion, $X_0^{(1)}$, may be defined as

$$X_0^{(1)} = \sum_{n=1}^{N} \frac{1}{2} \left\{ -iX_n e^{i\omega_n t} + c.c. \right\}. \tag{2.20}$$

Furthermore, the wave numbers, k_{jn}, are given by the solutions to the dispersion equation

$$\omega_n^2 = g k_{jn} \tanh k_{jn} h, \tag{2.21}$$

generalized to complex wave numbers (Dean & Dalrymple 1991). Within this solution, the real solution for $j = 0$ refers to the progressive part of the wave field whilst the purely imaginary solutions for $j = 1...\infty$ refer to the infinite series of evanescent modes; the latter accounting for the mismatch between the wave board velocity and the water particle velocity under the progressive wave. This involves satisfying the boundary condition on the wave board (condition (*d*) above) and yields the geometry dependent first-order coefficients c_{jn} given by

$$c_{jn} = \sinh(k_{jn} h) \frac{\Lambda_1(k_{jn})}{\Lambda_2(k_{jn})}, \tag{2.22}$$

where

$$\Lambda_1(k_{jn}) = \sinh(k_{jn} h) - \frac{d+l}{h+l} \sinh(k_{jn} d) + \frac{1}{h+l} \frac{\cosh(k_{jn} d) - \cosh(k_{jn} h)}{k_{jn}} \tag{2.23}$$

and

$$\Lambda_2(k_{jn}) = \frac{1}{2} \left[k_{jn} h + \sinh(k_{jn} h) \cosh(k_{jn} h) \right]. \tag{2.24}$$

The first-order surface elevation, $\eta^{(1)}$, may be expressed as

$$\eta^{(1)} = \sum_{n=1}^{N} \frac{1}{2} \left\{ X_n \sum_{j=0}^{\infty} c_{jn} e^{i(\omega_n t - k_{jn} x)} + c.c. \right\}, \tag{2.25}$$

which simply follows by substituting equation (2.19) into (2.7). Observing equation (2.25) for $\eta^{(1)}$ it is worthwhile noting that the progressive first-order amplitude of wave component n, denoted by A_{0n}, is given by

$$A_{0n} = c_{0n} X_n, \tag{2.26}$$

where c_{0n} is a real coefficient for all frequencies. Considering the equations for $X_0^{(1)}$ and $\eta^{(1)}$, (2.20) and (2.25) respectively, a notable result is seen: the generated progressive wave is phase shifted by a factor of i or 90 degree when compared to the wave board motion. Likewise, the generated progressive wave is in phase with the wave board's velocity, a result that is important when considering the system's dynamic behaviour in subsequent chapters.

The present thesis addresses three types of board geometries in particular: (i) bottom hinged wave makers (figure 2.2 (a), $l = 0$, $d = 0$); (ii) wave makers where the hinge is placed above the bed (figure 2.2 (b), $l = -d < 0$) and (iii) full depth piston-type wave machines (figure 2.2 (c), $l = \infty$, $d = 0$). Figure 2.3 shows the first-order coefficients c_{jn} for these three arrangements, where $L_0 = 2\pi g/\omega^2$ is the deep water wave length.

Herein, the solid line in each sub-figure (a) to (c) represents the real coefficient, c_{0n}, which directly relates the wave board motion to the amplitude of the progressive wave mode. For all three machine geometries shown, the coefficient c_{0n} approaches a limiting value of 2 for high frequencies. Again, this is a notable result: in very deep water the amplitude of the progressive wave mode will never exceed twice the wave machine's amplitude. It should also be noted that very low values of h/L_0 are only of interest to piston-type wave machines; the practical range of application of flap-type wave machines being discussed in Chapter 4. In considering figure 2.3, and many figures that follow, it is important to note that it was chosen to non-dimensionalise the water depth, h, with the deep water wave length, L_0. In the present example this range corresponds to $10^{-2} \leq h/L_0 \leq 10$, while in terms of a local non-dimensional water depth kh this expands from $kh = 0.25$ to

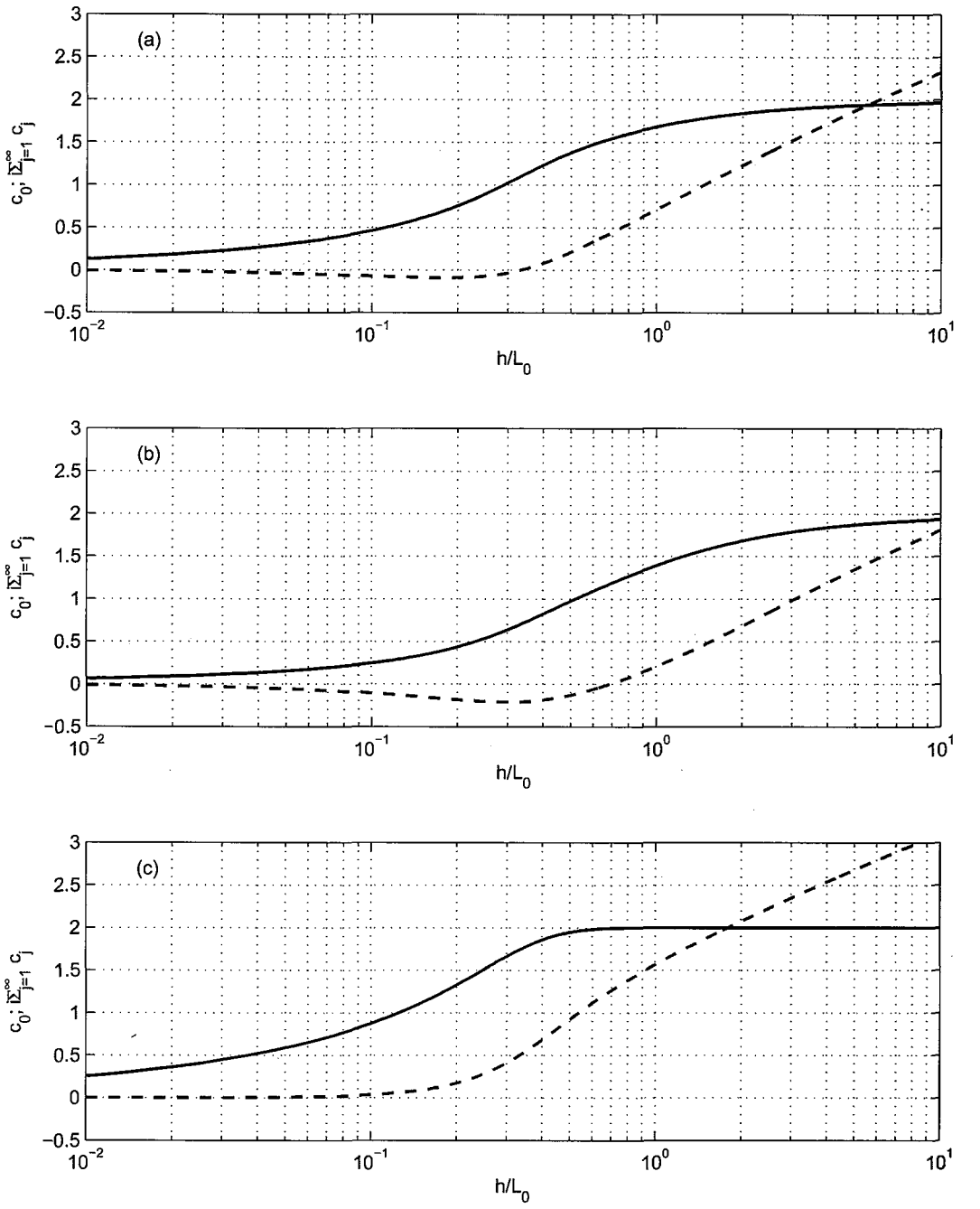


Figure 2.3: Dimensionless first-order coefficients; (a) wave maker hinged at $d/h = 0$, (b) wave maker hinged at $d/h = 0.5$, (c) piston-type wave maker; —— c_{0n}, characterising the propagating wave mode and – – $i\Sigma_{j=1}^{\infty} c_{jn}$, representing the sum of the evanescent modes

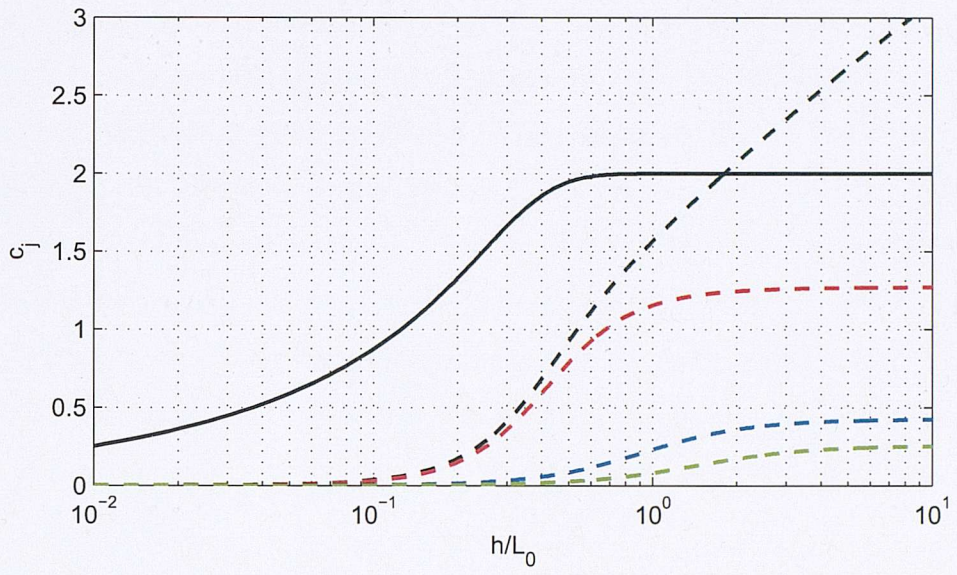


Figure 2.4: Relevance of various first-order coefficients for piston-type wave maker; —— c_{0n}, - - ic_{1n}, - - ic_{2n}, - - ic_{3n}, - - $i\Sigma_{j=1}^{\infty} c_{jn}$

very deep water.

The total magnitude of the evanescent modes expressed as $i\Sigma_{j=1}^{\infty} c_{jn}$. With the coefficients c_{jn} being purely imaginary for $j \geq 1$ this latter sum is real and hence plotted in the same plane as the coefficients c_{0n}. For increasing frequencies, or increasingly deep water, this sum steadily increases and does not approach a limiting value.

This observation becomes important once the wave machine's dynamic properties are considered. In dynamic terms, the real or progressive wave mode may be regarded as hydrodynamic damping; this follows directly from the discussion earlier where the progressive wave was found to be in phase with the oscillator's velocity and hence represents a damping term. Likewise, the imaginary- or evanescent-modes may be regarded as added mass since they are in phase with the oscillator's acceleration. This is discussed further when the absorption characteristic of wave machines is considered.

Figure 2.3 only considered the sum of all the evanescent wave modes, $i\Sigma_{j=1}^{\infty} c_{jn}$. In addition to the information given on figure 2.3, figure 2.4 also describes the first three evanescent modes for a piston-type wave machine. The first evanescent

mode, c_{1n}, clearly dominates, particularly for shallow water. However, the second and third mode are also of appreciable size and cannot be ignored. Indeed, it is clear that, particularly in deeper water, an increasing number of evanescent modes needs to be considered to accurately model the infinite sum. Similar arguments apply for the other two geometries discussed in figure 2.3 where the importance of higher modes, even in relatively shallow water, is seen to be even more important. The relevance of evanescent modes for a range of wave board geometries and various water depths is further discussed in Section 2.4.

2.3.2 Second-order Solution

As outlined earlier, the second-order velocity potential arising from a first-order wave board motion may be separated into two parts: a wave-wave interaction potential, $\Phi^{(21)}$, and a spurious free wave potential, $\Phi^{(22)}$. Closely following the solution presented by Schäffer (1996), the second-order wave-wave interaction potential may be expressed as

$$\Phi^{(21)} = 2\sum_{n=1}^{N}\sum_{m=n}^{N}\left(\Phi_{nm}^{(21)-} + \Phi_{nm}^{(21)+}\right), \tag{2.27}$$

with

$$\Phi_{nm}^{(21)\pm} = \frac{1}{2}\left\{\delta_{nm} i X_n X_m^{-*} \sum_{j=0}^{\infty}\sum_{l=0}^{\infty} c_{jn} c_{lm}^{-*} \frac{H_{jnlm}^{\pm}}{D_{jnlm}^{\pm}} \right.$$
$$\left. \frac{\cosh(k_{jn} \pm k_{lm}^{-*})(z+h)}{\cosh(k_{jn} \pm k_{lm}^{-*})h} e^{i(\omega_n t - k_{jn} x \pm (\omega_m t - k_{lm}^{-*} x))} + c.c. \right\}, \tag{2.28}$$

where δ_{nm} is defined as

$$\delta_{nm} = \begin{cases} 1 & \text{for } n \neq m \\ 0.5 & \text{for } n = m \end{cases} \tag{2.29}$$

and the superscript $-*$ is introduced for brevity and expresses the complex conjugate in the case of sub-harmonics. Likewise, the second-order spurious free wave potential, $\Phi^{(22)}$, may be expressed as

$$\Phi^{(22)} = 2\sum_{n=1}^{N}\sum_{m=n}^{N}\left(\Phi_{nm}^{(22)-} + \Phi_{nm}^{(22)+}\right), \tag{2.30}$$

where

$$\Phi_{nm}^{(22)\pm} = \frac{1}{2}\left\{\frac{i g c_{0n} X_n c_{0m}^{-*} X_m^{-*}}{h(\omega_n \pm \omega_m)} \sum_{p=0}^{\infty} c_p^{(22)\pm} \frac{\cosh K_p^{\pm}(z+h)}{\cosh K_p^{\pm} h} e^{i((\omega_n \pm \omega_m)t - K_p^{\pm} x)} + c.c. \right\} \tag{2.31}$$

and $K_p^{\pm}$ is the solution to

$$(\omega_n \pm \omega_m)^2 = gK_p^{\pm} \tanh K_p^{\pm} h. \tag{2.32}$$

As before, this is the dispersion equation generalized to complex wave numbers; the reader being referred to equation (2.21) and the associated discussion. Furthermore, the second-order wave-wave interaction surface elevation, $\eta^{(21)}$, may be expressed by

$$\eta^{(21)} = 2\sum_{n=1}^{N}\sum_{m=n}^{N}\left(\eta_{nm}^{(21)-} + \eta_{nm}^{(21)+}\right), \tag{2.33}$$

with

$$\eta_{nm}^{(21)\pm} = \frac{1}{2}\left\{X_n X_m^{-*}\sum_{j=0}^{\infty}\sum_{l=0}^{\infty} c_{jn}c_{lm}^{-*}G_{jnlm}^{\pm}e^{i(\omega_n t - k_{jn}x \pm (\omega_m t - k_{lm}^{-*}x))} + c.c.\right\}. \tag{2.34}$$

Similarly, the spurious free wave surface profile, $\eta^{(22)}$, is defined by

$$\eta^{(22)} = 2\sum_{n=1}^{N}\sum_{m=n}^{N}\left(\eta_{nm}^{(22)-} + \eta_{nm}^{(22)+}\right), \tag{2.35}$$

with

$$\eta^{(22)\pm} = \frac{1}{2}\left\{\frac{c_{0n}X_n c_{0m}X_m^{-*}}{h}\sum_{p=0}^{\infty} c_p^{(22)\pm}e^{i(\omega_n \pm \omega_m)t - K_p^{\pm}x} + c.c.\right\}. \tag{2.36}$$

The expressions for $H_{jnlm}^{\pm}$, $D_{jnlm}^{\pm}$, $G_{jnlm}^{\pm}$ and $c_p^{(22)\pm}$ in equations (2.28), (2.31), (2.34) and (2.36) are given in Appendix A. Further discussion of these second-order results is delayed until Chapters 4 and 5; the former dealing with the application of this second-order theory to regular waves, whilst the latter concerns the general case of irregular waves. In contrast, the following section gives some more explanation as to the importance of the evanescent modes arising in the vicinity of the wave board since this is not presented elsewhere.

2.4 Evanescent Modes

Considering the first-order potential solution, equation (2.19), the wave field is expressed as one progressive wave mode and an infinite series of evanescent modes. This section outlines the importance of these modes and gives some explanation as to their physical meaning. The first part of the solution, $j = 0$, expresses a real wave component that progresses without change in amplitude. This is in contrast to the modes expressed by $j = 1..\infty$; the latter being imaginary wave components that decay exponentially with increasing distance x from the wave board.

Mathematically, these modes are required to satisfy the boundary condition on the wave board: the fluid velocity perpendicular to the wave board must be equal to the velocity of the wave board. This condition is easily visualized by evaluating the depth dependent velocity of both wave board and fluid for various upper limits of j. Observing the wave board defined on figure 2.1, the depth dependent shape function, $f(z)$, may be expressed as

$$f(z) = \begin{cases} 1 + \frac{z}{h+l} & \text{for} \quad -(h-d) \leq z \leq 0 \\ 0 & \text{for} \quad -h \leq z < -(h-d). \end{cases} \tag{2.37}$$

With X_a being the amplitude of the first-order wave board displacement at still water level, the magnitude of the depth dependent wave board velocity, $U_a(z)$, is given by

$$U_a(z) = \omega X_a f(z). \tag{2.38}$$

Furthermore, the first-order amplitude of the horizontal fluid velocity, $u_a(z) = \partial\Phi^{(1)}/\partial x$, for the special case of a regular wave, is readily derived as

$$u_a(z) = \frac{gX_a}{\omega} \sum_{j=0}^{\infty} c_j k_j \frac{\cosh k_j(z+h)}{\cosh k_j h}, \tag{2.39}$$

where the derivative has been evaluated on the wave board with $x = 0$. Figures 2.5 to 2.8 show both the wave board's velocity and the fluid's horizontal velocity

over depth. Each of those figures contains three sub-plots: the fluid's horizontal velocity having been evaluated for an upper limit of $j = J$, with $J = 0$, $J = 10$ and $J = 100$ in sub-plots (a), (b) and (c) respectively. Consequently, the solution for $J = 0$ refers to the progressive wave mode only. The graphs are given for a dimensionless depth coordinate with $z' = z/h$ shown on the ordinate. Furthermore, the components of velocity shown on the abscissa are normalized over wave board stroke and wave frequency, $u'(z') = u/(\omega X_a)$. Also note that, wherever appropriate, the axis scale has been adopted to present the maximum level of detail.

The velocities within the first two figures, 2.5 and 2.6, are evaluated for a full depth piston-type machine; the former being computed for an intermediate water depth with $h/L_0 = 0.1$ and the latter being computed for deep water with $h/L_0 = 1.0$. It is clear from figure 2.5, the intermediate water case, that the wave board's velocity provides a good fit to the fluid's velocity and a small number of evanescent modes (figure 2.5 b) is sufficient to describe a near perfect match. In the deep water case, figure 2.6, a large number of evanescent modes has to be included in order to achieve a reasonable match (figure 2.6 c).

The velocities within the subsequent two figures, 2.7 and 2.8, are evaluated for a flap-type wave machine where the hinge is placed at $d = h/2$; again the former being computed for an intermediate water depth ($h/L_0 = 0.1$) and the latter being computed for deep water ($h/L_0 = 1.0$). In both cases a relatively small number of evanescent modes is sufficient to describe a reasonable match between the wave board's velocity and the fluid's horizontal velocity. As a result, this type of wave board geometry is suitable for a relatively wide range of water depths.

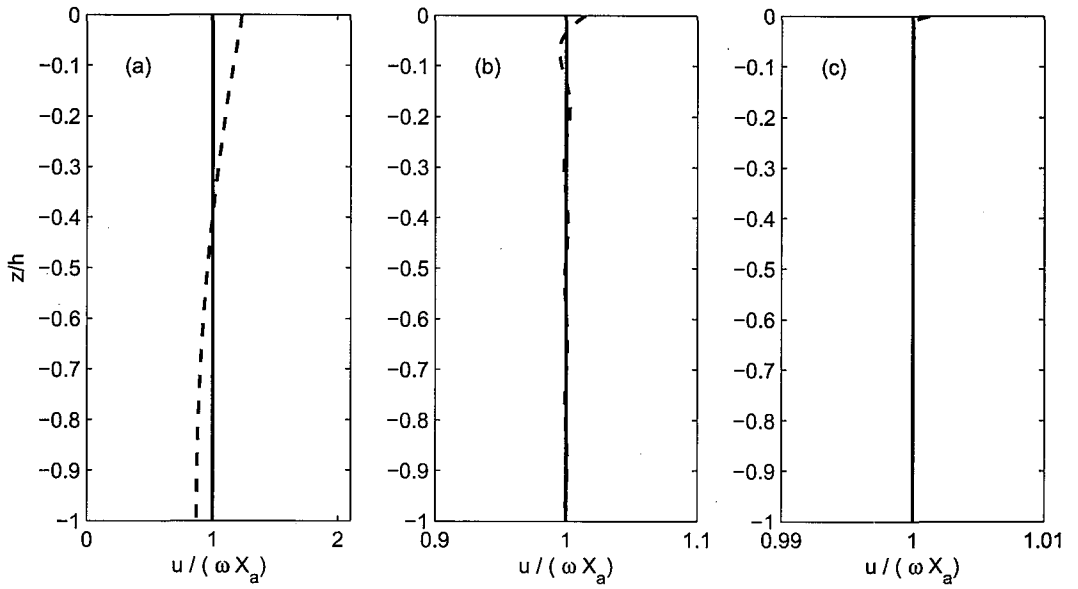


Figure 2.5: Horizontal fluid velocity on a full depth piston-type machine, intermediate water case with $h/L_0 = 0.1$; —— wave board velocity, – – fluid's horizontal velocity; (a) $J = 0$, (b) $J = 10$, (c) $J = 100$

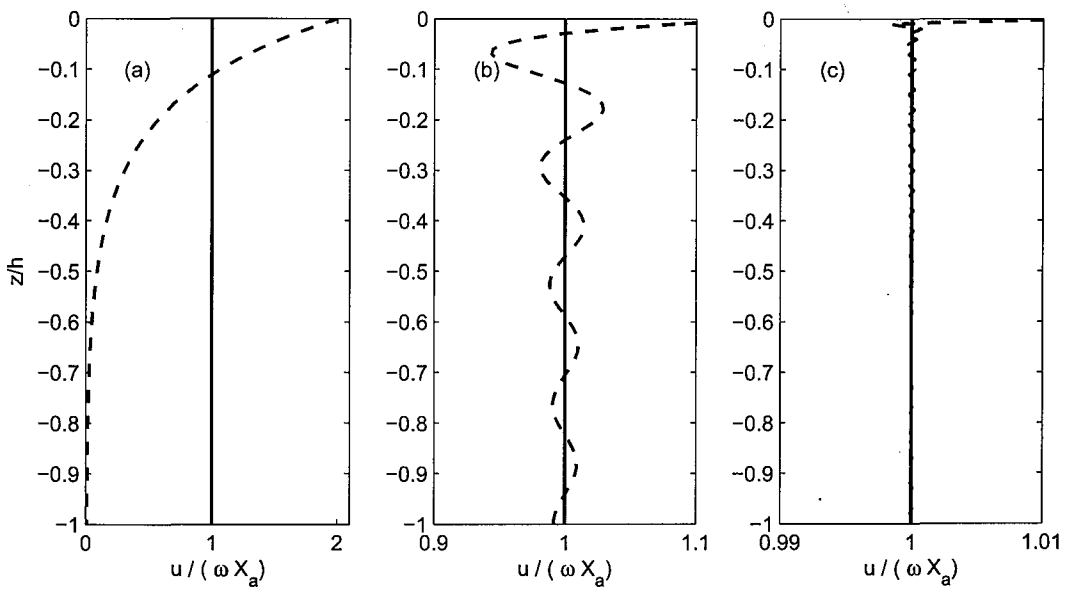


Figure 2.6: Horizontal fluid velocity on a full depth piston-type machine, deep water case with $h/L_0 = 1.0$; —— wave board velocity, – – fluid's horizontal velocity; (a) $J = 0$, (b) $J = 10$, (c) $J = 100$

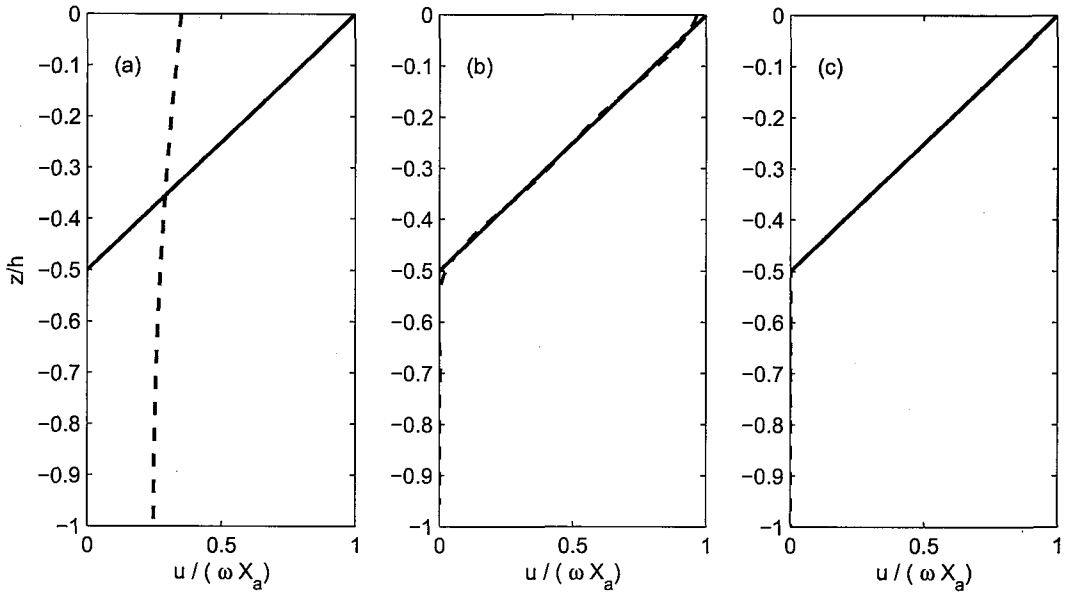


Figure 2.7: Horizontal fluid velocity on a flap-type machine with $d/h = 0.5$, intermediate water case with $h/L_0 = 0.1$; —— wave board velocity, – – fluid's horizontal velocity; (a) $J = 0$, (b) $J = 10$, (c) $J = 100$

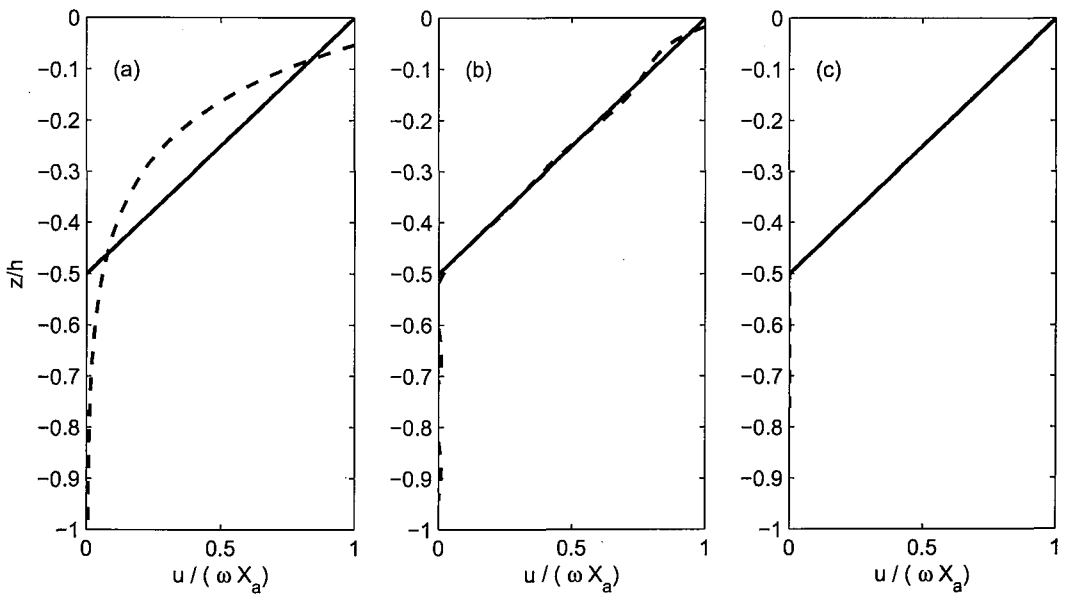


Figure 2.8: Horizontal fluid velocity on a flap-type machine with $d/h = 0.5$, deep water case with $h/L_0 = 1.0$; —— wave board velocity; – – fluid's horizontal velocity; (a) $J = 0$, (b) $J = 10$, (c) $J = 100$

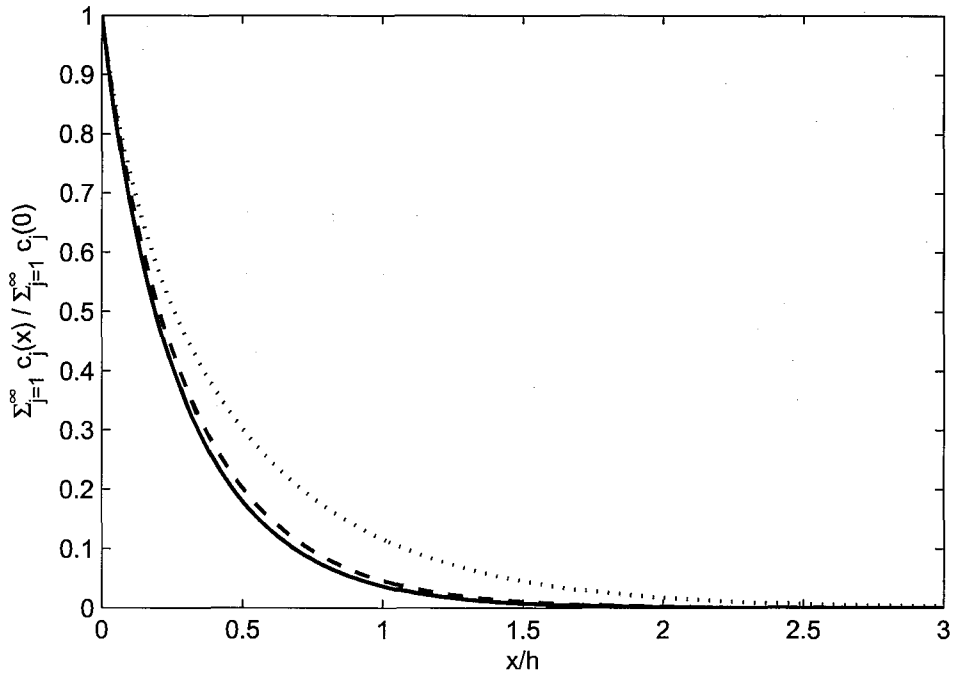


Figure 2.9: Evanescent mode decay characteristic for three wave cases; —— shallow water with $h/L_0 = 0.01$, – – intermediate water with $h/L_0 = 0.1$ and · · · · deep water with $h/L_0 = 1.0$

Model testing must be undertaken in an area sufficiently far from the wave board in order to neglect the influence of the evanescent modes. Given the exponential decay of these modes in space, their occurrence is confined to a relatively small region. Figure 2.9 illustrates this characteristic rapid decay for a shallow water case ($h/L_0 = 0.01$), an intermediate water case ($h/L_0 = 0.1$) and a deep water case ($h/L_0 = 1.0$). The curves are based on a piston-type wave board geometry and show the infinite sum of evanescent modes, $\sum_{j=1}^{\infty} c_j \exp(-|k_j|x)$, normalised with respect to their total magnitude at the wave board, $\sum_{j=1}^{\infty} c_j$. On the abscissa, the spatial location x is normalised with respect to the water depth h.

In the deep water case, where the exponential decay is slowest, the evanescent mode sum is reduced to 0.3% of the maximum value at a distance of three water depths. In both the shallow and the intermediate water depth cases, the ratio is reduced to less than 0.2% for $x = 2h$. Overall, in a testing area $x \geq 3h$ downstream of the wave generator the influence of the evanecent modes may be neglected.

2.5 Range of Applicability

It is well known that Stokes theory over predicts the magnitude of the second-order components in shallow water conditions. Schäffer (1996) introduced a non-linearity parameter S; a value of $S = 1$ corresponding to the 'limiting' case where second-order Stokes theory predicts secondary peaks in the trough of the primary wave. As a result, for $S > 1$ the theory fails to predict the correct second-order content. With the force-feedback model presented herein utilizing the wave field solution derived by Schäffer (1996), the same measure is applied. This non-linearity factor S is given by

$$S = 2H \left| G^{\pm}_{0n0m} \right|, \tag{2.40}$$

where the general solution of $G^{\pm}_{jnlm}$ is defined as equation (A-5) in Appendix A. For the special case of regular waves, H denotes wave height. For wave groups and irregular waves the characteristic wave height of the sea state may be considered to estimate the non-linearity factor S. However, this will only provide an indication of how well the theory performs for the given wave conditions.

Figure 2.10 shows the second-order surface profile computed utilizing the second-order theory outlined earlier. The wave has a period of $T = 2.0s$ and is evaluated for a water depth of $h = 0.5m$. The three cases shown relate to a non-linearity factor of $S = 0.5$, $S = 1.0$ and $S = 1.5$ which may also be expressed in terms of dimensionless steepness as $Hk/2 \approx 0.053$, $Hk/2 \approx 0.11$ and $Hk/2 \approx 0.16$ respectively. The centre case with $S = 1$ or $Hk/2 \approx 0.11$ relates to the limiting case. For steeper waves the theory fails to predict the correct second-order content; evidence of which is provided by the surface profile for the case with $S = 1.5$. For this latter case, the second-order Stokes content forms a secondary peak in the trough of the primary wave which is clearly unrealistic. If steeper waves or shallow water waves are to be considered, a stream function or a cnoidal wave maker theory would be more appropriate. Both approaches are outside the scope of the present study; the reader being referred to Zhang & Schäffer (2007).

Figure 2.11 shows the maximum wave steepness for regular waves with the non-

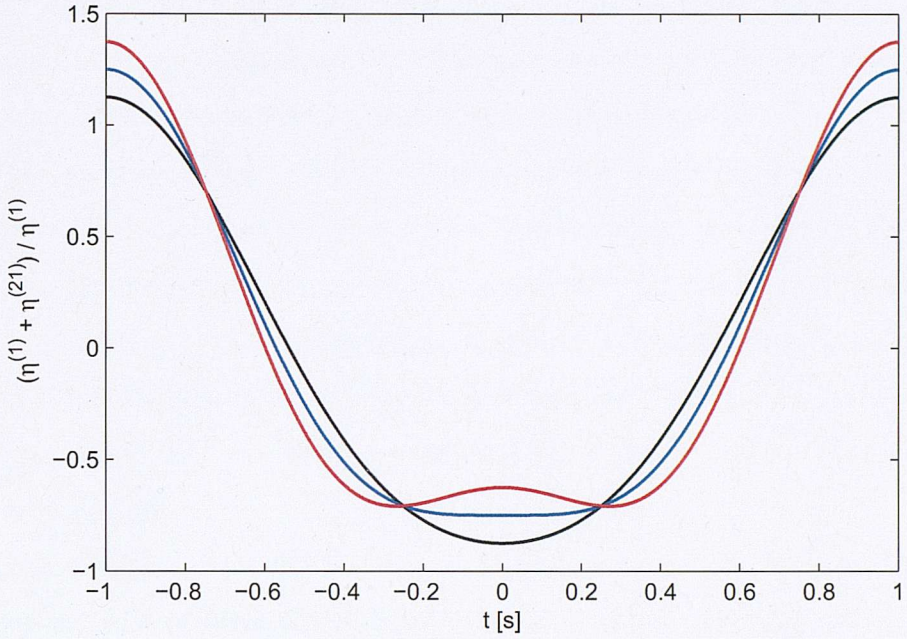


Figure 2.10: Second-order surface elevation for a wave with period $T = 2.0s$ in water of depth $h = 0.5m$, presented normalized as $\eta = (\eta^{(1)} + \eta^{(21)})/\eta^{(1)}$; — $S = 0.5$, — $S = 1.0$, — $S = 1.5$

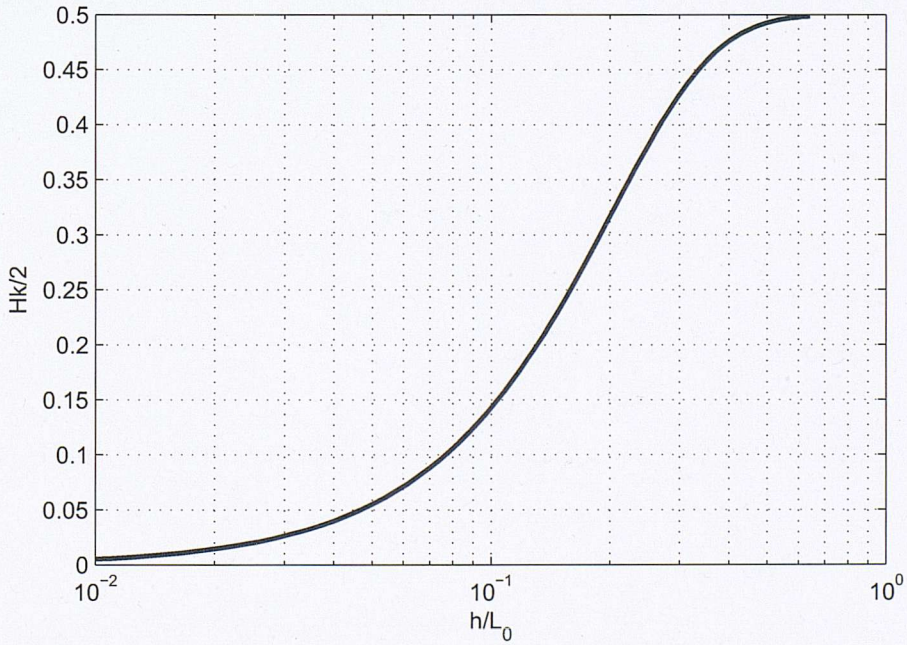


Figure 2.11: Maximum wave steepness for regular waves with the non-linearity factor set to $S = 1$. Note: the range of h/L_0 on the abscissa corresponds to $0.25 < kh < 6.28$.

linearity factor S set to unity. In considering this figure it is important to note that no account has been taken of the practical limit due to wave breaking. The regular wave case above corresponds to a dimensionless water depth of $h/L_0 \approx 0.08$ which limits the wave steepness to $Hk/2 \approx 0.11$ as already discussed. For longer waves, or shallower water, the maximum steepness is even further reduced and the theory is thus inappropriate in this regime. For values of $h/L_0 > 0.2$ the steepness may be as large as $Hk/2 = 0.3$ which is appropriate to most laboratory test cases. To put this dimensionless ratio into perspective, a value of $h/L_0 = 0.2$ is equivalent to a wave period of $T \approx 1.8s$ in a water depth $h = 1.0m$ or $T \approx 1.3s$ in a water depth of $h = 0.5m$.

In considering the present results, and those which follow, it is important to mention the role of wave instabilities. All experimental data presented within this thesis was obtained in relatively close proximity to the wave board, $x \leq 6L$. Further downstream, an effect commonly referred to as the Benjamin-Feir instability may occur. This is a separate topic which will not be considered further; the reader being referred to Benjamin & Feir (1967) and Benjamin (1967).

3

Wave Absorption Strategies

3.1 Chapter Overview

Within this chapter the concept of an absorbing force-feedback controlled wave machine is introduced. Chronologically, some of the work presented here was undertaken subsequent to the work on the second-order content presented in Chapter 4. Indeed, the motivation for the investigation of various force-feedback control strategies arose directly from the reviewers comments relating to the first draft of Spinneken & Swan (2009*a*).

In the initial stages of this study, the absorption strategy as outlined by Salter (1982) and further developed by Edinburgh Designs Ltd. was taken for granted. However, following the review process, the original strategy was compared to others available in the literature; the results of this direct comparison being published in Spinneken & Swan (2009c) and forming the basis of this chapter. The outcome of these comparisons is that the originally applied absorption strategy was, for the first time, shown to be superior to other available methods and, as a result, it has been applied throughout the thesis.

3.2 Introduction to Wave Absorption

Over the last three decades much effort has been made to formulate the problem of optimum control, or maximum power absorption, for wave energy devices. The techniques developed in this field are also adopted to describe the ideal controller for absorbing wave makers in laboratory flumes. Early work on this subject includes Jefferys (1984), Naito & Nakamura (1985), Falnes (1995) and Chatry et al. (1998). More recently, the review by Naito (2006) and the book by Falnes (2002) have contributed to this discussion.

Fundamentally, the following system identification problem arises: a simple mass-spring-damper arrangement can be regarded as a second-order low pass system. The optimum control of such a system is well understood and is easily modelled. The assumption made herein is that the coefficients for mass, spring and damping are constant over frequency. For many mechanical systems this assumptions is both reasonable and realistic. However, in the case of a hydrodynamic problem, this assumption cannot be made; the coefficients for added mass and hydrodynamic damping being strongly frequency dependent. This has severe implications on the system modelling, especially with regard to the integral transformations between the time domain and the frequency domain. As an example, the inverse Fourier transform, denoted by $\overset{\mathscr{F}^{-1}}{\rightarrow}$, of the inertia force $F(\omega)$ for a system with constant mass m is given by

$$F(\omega) = -\omega^2 m X(\omega) \overset{\mathscr{F}^{-1}}{\rightarrow} f(t) = m\ddot{x}(t), \tag{3.1}$$

where $f(t)$ is the inertia force in the time domain. This is in marked contrast to a hydrodynamic system with frequency dependent added mass $m(\omega)$ where the inverse Fourier transform evaluates to

$$F(\omega) = -\omega^2 m(\omega) X(\omega) \overset{\mathscr{F}^{-1}}{\rightarrow} f(t) = \int_{-\infty}^{\infty} \mathscr{F}^{-1}\{m(\omega)\}(\tau)\ddot{x}(t-\tau)d\tau, \tag{3.2}$$

with $f(t)$ being expressed as a convolution integral. Given the complex character-

istic for the added mass in most hydrodynamic systems, neither the inverse Fourier transform, $\mathscr{F}^{-1}\{m(\omega)\}$, nor the convolution integral can be solved analytically.

For an absorbing wave making system or, more generally speaking, a wave energy converter the equation of motion is given by

$$f(t) = m_c\ddot{x} + m(\omega) * \ddot{x} + d_{pto}\dot{x} + d(\omega) * \dot{x} + kx, \tag{3.3}$$

where $f(t)$ is the wave excitation force, m_c is the converter's mass, $m(\omega)$ is the added mass due to the radiation problem, d_{pto} is the power take off damping, $d(\omega)$ is the radiation damping and k is a spring constant. The $*$ symbol denotes convolution and is required since $m(\omega)$ and $d(\omega)$ are frequency dependent coefficients. The origins of this frequency dependency will be discussed in §3.3.2. If both coefficients are assumed to be constant, or a single frequency of oscillation is considered, the equation of motion simplifies to

$$f(t) = (m_c + m)\ddot{x} + (d_{pto} + d)\dot{x} + kx. \tag{3.4}$$

This is a commonly adopted approach that is applied throughout the thesis.

The second fundamental problem arises from the characteristic of the impulse response function for the optimum controller. By way of an introduction, a simple mechanical mass-spring-damper system is considered in the following. The impulse response function, most commonly denoted by $h(t)$, is the time domain representation of the system's dynamic behaviour; the corresponding representation in the frequency domain being the transfer function $H(\omega)$. Either of these two representations is sufficient to fully specify the system's dynamics. The impulse response function and the transfer function are directly related by the Fourier transform with $h(t)$ given by

$$h(t) = \frac{1}{2\pi}\int_{-\infty}^{\infty} H(\omega)e^{i\omega t}d\omega, \tag{3.5}$$

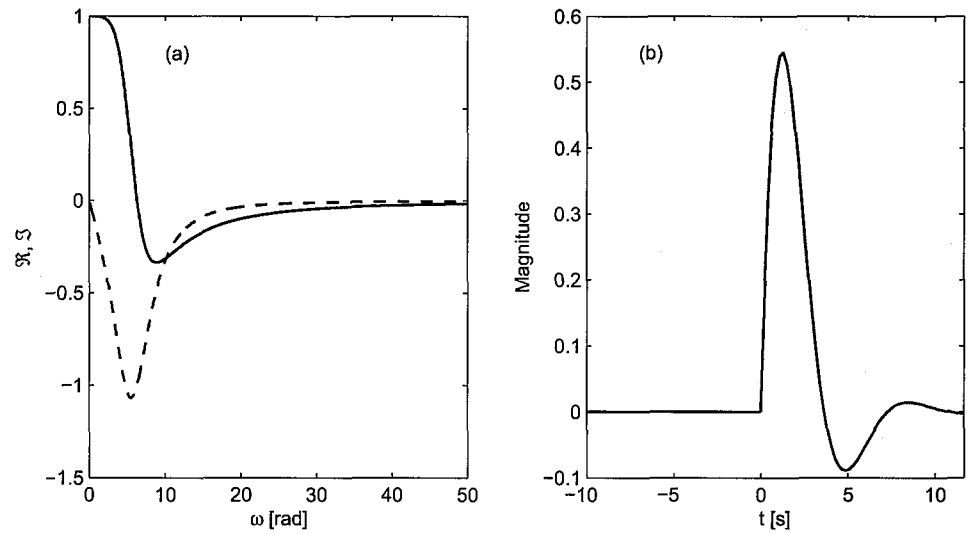


Figure 3.1: Second-order mass-spring-damper system with constant coefficients; (a) Transfer function, $H(\omega)$: —— $\Re\{H(\omega)\}$, – – $\Im\{H(\omega)\}$ and (b) Impulse response function h(t)

or likewise

$$H(\omega) = \int_{-\infty}^{\infty} h(t)e^{-i\omega t}dt. \tag{3.6}$$

Figure 3.1 concerns both the frequency response or transfer function, $H(\omega)$ in part (a), and the impulse response function, $h(t)$ in part (b), for a second-order mass-spring-damper system with constant coefficients. In the frequency domain, the transfer function $H(\omega)$ is presented in two parts: a real part $\Re\{H(\omega)\}$, and an imaginary part $\Im\{H(\omega)\}$. In the time domain, figure 3.1 (b), it is important to note that $h(t) = 0$ for $t < 0$; the relevance of this property being discussed later on. The differential equation for such a system may be expressed by

$$f(t) = m\ddot{x} + d\dot{x} + kx, \tag{3.7}$$

where f denotes a force, x denotes position and the constants for mass (m), damping (d) and spring (k) have been set to unity in the case shown in figure 3.1. The differential equation in the time domain is readily transformed to yield the system's frequency domain transfer function, $H(\omega)$, which may be expressed as the

ratio of velocity, $U(\omega) = i\omega X(\omega)$, and force, $F(\omega)$

$$H(\omega) = \frac{U(\omega)}{F(\omega)} = \frac{1}{i\omega m + d + k/(i\omega)}. \tag{3.8}$$

Applying the convolution theorem, the velocity of the oscillator, $u(t)$, in response to an incident force, $f(t)$, is given by

$$u(t) = \int_{-\infty}^{\infty} f(\tau)h(t-\tau)d\tau. \tag{3.9}$$

This integral equation is interpreted as follows: for an arbitrary system with impulse response function $h(t)$, the system's velocity in response to an arbitrary incident force can be calculated by evaluating the convolution of $f(t)$ and $h(t)$. With the integral ranging from $-\infty$ to ∞ the future values of the incident force could, at least in theory, affect the current oscillator velocity; this solely depending on the characteristic of $h(t)$. Clearly this theoretical construct is non-physical and further clarified in the following example.

Assume the velocity for $t = 0$ is sought: the integral written as a sum evaluates to

$$u(0) = f(-\infty)h(\infty) + ... + f(1)h(-1) + ... + f(\infty)h(-\infty), \tag{3.10}$$

where $\tau = 1s$ is chosen as an arbitrary element of the infinite sum. If the value of the impulse response function for $\tau = 1s$, that is $h(-1)$, is non-zero, it follows that the product $f(1)h(-1)$ contributes to $u(0)$. The same argument applies for all other values of $0 < \tau < \infty$. As a result, future values of the incident force, $f(\tau > 0)$, would be required in order to evaluate the velocity for $t = 0s$; such a system being referred to as a-causal. In contrast, a causal system is characterized by an impulse response function where all values of $h(t)$ are zero for $t < 0$. In considering these arguments, the relevance of the characteristic of $h(t)$ for the mass-spring-damper system (figure 3.1 b) becomes clear; with $h(t) = 0$ for $t < 0$

the velocity for $u(t)$ may be simplified to

$$u(t) = \int_{-\infty}^{0} f(\tau)h(t-\tau)d\tau \tag{3.11}$$

and, as a result, future values of the force do not affect the oscillator's current velocity.

Following these arguments causality is best judged in the time domain and, in so doing, the impulse response function for various wave maker problems has been shown to be non-causal (Chatry et al. 1998) or at least a-causal (Naito 2006). A non-causal system is defined as a system where the output solely depends on future input values. This is in contrast to an a-causal system where the output depends on some future input values but is also affected by input values from the past or present. In either case, a non- or a-causal system is identified by non-zero values of the impulse response function for $t < 0$. Both systems obviously represent a problem for the control task where future values of the input signal are unknown.

The non- or a-causality problems have been overcome in a variety of ways all based on some approximation of the optimum controller. In seeking an alternative formulation for the optimum controller, particular attention is paid to : (i) the choice of input signal, (ii) the controller architecture and (iii) the absorption filter implementation and optimisation. In the sections that follow, the physical model for the absorbing wave maker is first introduced. This builds upon the work presented in Chapter 2. Second, the various options for (i), (ii) and (iii) are considered. Subsequently some of those options are applied to the wave making problem and a controller optimisation method is sought. Two previously published methods are summarized and a controller based on infinite impulse response (IIR) filters is presented. Although this latter method has been employed in the field of wave absorption for some time (Salter et al. 1976), it has never been explicitly mentioned in the literature. The relative merits of this latter approach are compared to the two published methods. The IIR approach is found to outperform the other two methods.

3.3 Physical Model

3.3.1 Wave Field Solution

This section builds directly on Chapter 2 and seeks to summarise the theoretical formulation for the well known wave making problem coupled with the associated conditions for optimum absorption. Once again a potential flow solution is adopted in which the velocity potential $\Phi = \Phi(x, z, t)$ in Cartesian coordinates (x, z) is defined such that the velocity components are given by $(u, w) = (\partial\Phi/\partial x, \partial\Phi/\partial z)$ and the corresponding water surface elevation is given by $\eta = \eta(x, t)$. In the present case, the wave field within the flume is now assumed to be described by three linear wave potentials:

(i) A generated wave potential $\Phi^{(g)}$ resulting from the motion of the wave maker

(ii) An incident wave potential, $\Phi^{(i)}$, propagating in the negative x-direction and having arisen from some location well downstream of the wave board

(iii) A reflected wave potential, $\Phi^{(r)}$, resulting from the perfect reflection of $\Phi^{(i)}$ at $x = 0$ (on the wave board)

Figure 3.2 defines both the wave maker geometry and the three potentials; the notation being identical to that adopted in Chapter 2 (figure 2.1). Furthermore, the boundary conditions appropriate to the linearised problem are exactly as outlined in Chapter 2:

(a) The bottom boundary condition with $w = 0$ at $z = -h$.

(b) The Kinematic Free Surface Boundary Condition (KFSBC) whereby the water surface profile is a streamline, $w = \partial\eta/\partial t$ at $z = 0$.

(c) The Dynamic Free Surface Boundary Condition (DFSBC) defining the pressure acting on the water surface as constant (atmospheric), $-g\eta = \partial\Phi/\partial t$.

(d) The fluid velocity perpendicular to the wave board must be equal to the velocity of the wave board, $\partial\Phi/\partial x = f(z)dX_0/dt$.

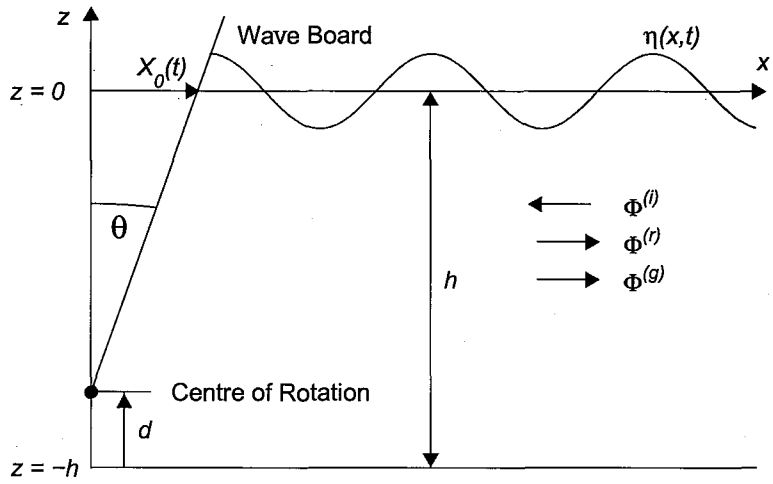


Figure 3.2: Wave maker geometry and definition of notation

Assuming perfect reflection on the wave board occurs, the superposition of incident and reflected wave potential forms an anti-node on the wave paddle and condition (d) only applies to the velocity potential generated by the wave maker, $\Phi^{(g)}$. Applying the solution of $\Phi^{(g)}$ given in Chapter 2 yields

$$\Phi^{(g)} = \sum_{n=1}^{N} \frac{1}{2} \left\{ \frac{igX_n}{\omega_n} \sum_{j=0}^{\infty} c_{jn} \frac{\cosh k_{jn}(z+h)}{\cosh k_{jn}h} e^{i(\omega_n t - k_{jn}x)} + c.c. \right\}. \tag{3.12}$$

Building on this result, a related solution for the velocity potentials $\Phi^{(i)}$ and $\Phi^{(r)}$, that satisfies the boundary conditions (a) - (c) at first-order, is given by

$$\Phi^{(i)} = \sum_{n=1}^{N} \frac{1}{2} \left\{ \frac{igA_n^{(i)}}{\omega_n} \frac{\cosh k_{0n}(z+h)}{\cosh k_{0n}h} e^{i(\omega_n t + k_{0n}x)} + c.c. \right\} \tag{3.13}$$

and

$$\Phi^{(r)} = \sum_{n=1}^{N} \frac{1}{2} \left\{ \frac{igA_n^{(r)}}{\omega_n} \frac{\cosh k_{0n}(z+h)}{\cosh k_{0n}h} e^{i(\omega_n t - k_{0n}x)} + c.c. \right\}, \tag{3.14}$$

where A_n is the complex amplitude of component n and *c.c.* denotes the complex conjugate of the preceding term. From the considerations above it follows that $A_n^{(r)} = A_n^{(i)}$ for all $n = 1..N$. This, in turn, confirms the condition of an anti-node on the wave board with the combined horizontal velocity, given by $u^{(i)} + u^{(r)} = \partial\Phi^{(i)}/\partial x + \partial\Phi^{(r)}/\partial x$, being zero at $x = 0$. This latter condition is, of course, essential to ensure that the earlier definition of $\Phi^{(g)}$ (equation 3.12) is correct.

Summing the three velocity potentials for each wave component n in the frequency domain yields

$$\Phi_n(\omega) = \Phi_n^{(i)}(\omega) + \Phi_n^{(r)}(\omega) + \Phi_n^{(g)}(\omega) = \frac{igA_n^{(i)}}{\omega_n}\frac{\cosh k_{0n}(z+h)}{\cosh k_{0n}h}e^{ik_{0n}x} + \left[\frac{igA_n^{(r)}}{\omega_n} + \frac{gU_n c_{0n}}{\omega_n^2}\right]\frac{\cosh k_{0n}(z+h)}{\cosh k_{0n}h}e^{-ik_{0n}x} + \frac{gU_n}{\omega_n^2}\sum_{j=1}^{\infty} c_{jn}\frac{\cosh k_{jn}(z+h)}{\cosh k_{jn}h}e^{-ik_{jn}x}, \quad (3.15)$$

where the wave board's displacement amplitude, X_n, has been replaced by the board's complex velocity, U_n. From (3.15) it is clear that the wave board's velocity must satisfy

$$U_n = -\frac{iA_n^{(r)}\omega_n}{c_{0n}} = -\frac{iA_n^{(i)}\omega_n}{c_{0n}}, \quad (3.16)$$

so that the progressive parts of $\Phi_n^{(g)}$ and $\Phi_n^{(r)}$ cancel each other out. For piston-type board geometries, U simply relates to the translational motion of the piston. In contrast, the wave boards angular velocity, Ω, is more meaningful when flap-type geometries are considered. In this latter case, the translational and angular velocities at the still water level are related by

$$\Omega \approx \tan\Omega = \frac{U}{h-d}, \quad (3.17)$$

where the small angle approximation, $\tan\Omega \approx \Omega$, has been introduced.

3.3.2 Added Mass and Hydrodynamic Damping

When investigating the dynamic behaviour of any hydrodynamic system the frequency dependent coefficients for the added mass, $m(\omega)$, and the hydrodynamic damping, $d(\omega)$, are crucial. Whilst a numerical solution is required for plunger-type wave makers (Wu 1991), these coefficients are readily derived by considering the hydrodynamic force for piston-type machines or torque for hinged wave board geometries. In order to evaluate the total hydrodynamic force or torque, Bernoulli's equation, given by

$$p(z,t) = -\rho\frac{\partial\Phi}{\partial t} - \rho g z - \frac{1}{2}\rho\left[\left(\frac{\partial\Phi}{\partial x}\right)^2 + \left(\frac{\partial\Phi}{\partial z}\right)^2\right], \tag{3.18}$$

is applied throughout the wave field and integrated over the surface of the wave board, where ρ is the density of the fluid and $p(z,t)$ is the fluctuating, depth dependent pressure. Within this equation three distinct contributions may be identified:

(i) An unsteady term: $-\rho\partial\Phi/\partial t$

(ii) A hydrostatic term: $-\rho g z$

(iii) Two velocity head terms: $-1/2\rho(u^2 + w^2)$

Of these, only the first term, the unsteady contribution, generates a first-order fluctuating force or torque. The hydrostatic term induces a mean term, whilst the velocity head terms contribute higher order components. As a result, the fluctuating first-order hydrodynamic force acting on a piston-type machine is given by

$$F^{(1)} = -\int_{-h+d}^{0} \rho\frac{\partial\Phi^{(1)}(z,t)}{\partial t}dz. \tag{3.19}$$

Substituting the wave field solution given in equation (3.12), this force evaluates to

$$F^{(1)} = \sum_{n=1}^{N}\frac{1}{2}\left\{\rho g X_n \sum_{j=0}^{\infty}\frac{c_{jn}}{k_{jn}}\frac{\sinh k_{jn}h - \sinh k_{jn}d}{\cosh k_{jn}h}e^{i\omega_n t} + c.c.\right\}. \tag{3.20}$$

Similarly, the first-order hydrodynamic torque acting on a flap-type machine is given by

$$T^{(1)} = -\int_{-h+d}^{0} \rho \frac{\partial \Phi^{(1)}(z,t)}{\partial t}(h-d+z)dz \tag{3.21}$$

and again substituting from equation (3.12) evaluates to

$$T^{(1)} = \sum_{n=1}^{N} \frac{1}{2} \left\{ \rho g X_n \sum_{j=0}^{\infty} \frac{c_{jn}}{k_{jn}^2} \frac{k_{jn}(h-d)\sinh k_{jn}h - \cosh k_{jn}h + \cosh k_{jn}d}{\cosh k_{jn}h} e^{i\omega_n t} + c.c. \right\}. \tag{3.22}$$

Recalling the real ($j = 0$) and complex ($j = 1..\infty$) nature of the wave field coefficients, c_j, and the wave numbers, k_j, the force and torque expressions may be separated into real and imaginary contributions. Considering the frequency domain relation between the force, $F(\omega)$, and the velocity, $U(\omega)$, for a system with added mass, $m(\omega)$, and hydrodynamic damping, $d(w)$,

$$F(\omega) = d(\omega)U(\omega) + i\omega m(\omega)U(\omega), \tag{3.23}$$

these latter coefficients are readily derived as

$$d(\omega) = \frac{\rho g}{\omega} \frac{c_0}{k_0} \frac{\sinh k_0 h - \sinh k_0 d}{\cosh k_0 h} \tag{3.24}$$

and

$$m(\omega) = \frac{\rho g}{\omega^2} \sum_{j=1}^{\infty} \frac{c_j}{k_j} \frac{\sinh k_j h - \sinh k_j d}{\cosh k_j h} \tag{3.25}$$

in the piston case. As discussed in §3.2, the convolution term has been neglected. Following similar arguments, the hydrodynamic damping and the added mass for flap-type wave makers are given by

$$d(\omega) = \frac{\rho g(h-d)}{\omega} \frac{c_0}{k_0^2} \frac{k_0(h-d)\sinh k_0 h - \cosh k_0 h + \cosh k_0 d}{\cosh k_0 h} \tag{3.26}$$

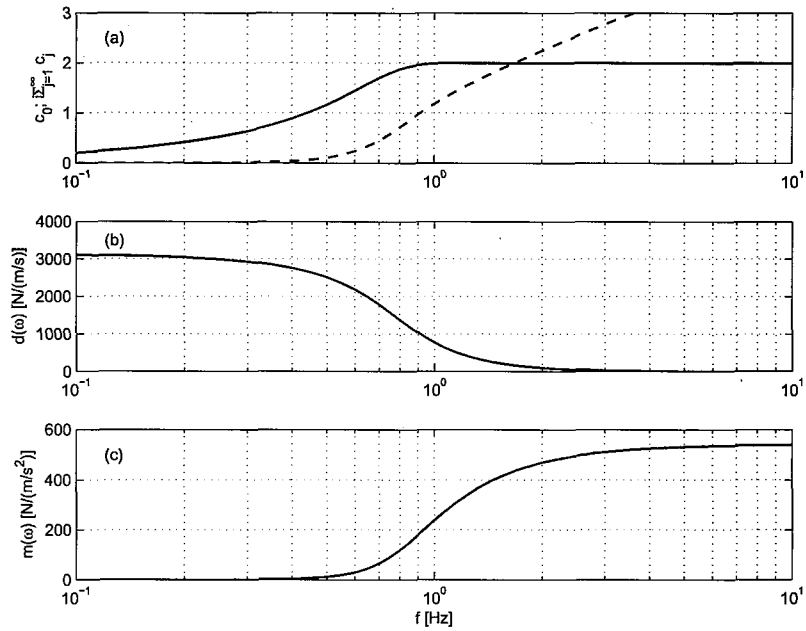


Figure 3.3: Hydrodynamic coefficients for a piston-type wave machine; (a) first order coefficients —— c_0, – – $i\sum_{j=1}^{\infty} c_j$; (b) hydrodynamic damping, $d(\omega)$; (c) added mass, $m(\omega)$

and

$$m(\omega) = \frac{\rho g(h-d)}{\omega^2} \sum_{j=1}^{\infty} \frac{c_j}{k_j^2} \frac{k_j(h-d)\sinh k_j h - \cosh k_j h + \cosh k_j d}{\cosh k_j h}. \tag{3.27}$$

Figures 3.3 and 3.4 show the hydrodynamic coefficients for piston- and flap-type wave machines. Within this chapter all graphs representing bottom hinged flap-type wave machines correspond to a $0.5m$ wide paddle operating at $1.0m$ water depth. In contrast, piston-type machines are evaluated for a $0.5m$ wide board operating at a water depth of $0.5m$. These dimensions are believed to be representative for many existing wave machines and allow to investigate a broad range of wave forms. In both cases the frequency in the plots is given in the physical dimension of Hz and none of the axes are normalized.

Introducing dimensional quantities is regarded necessary as most of the theory and application deals with physical wave machines for which non-dimensionalising is inappropriate. This is in stark contrast to numerical wave tanks that operate

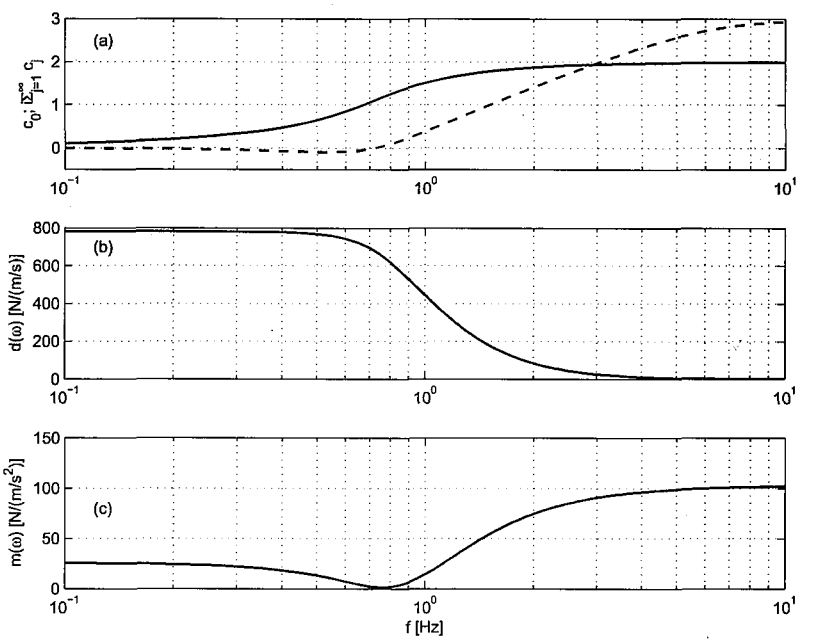


Figure 3.4: Hydrodynamic coefficients for a bottom hinged flap wave machine; (a) first order coefficients —— c_0, – – $i\sum_{j=1}^{\infty} c_j$; (b) hydrodynamic damping, $d(\omega)$; (c) added mass, $m(\omega)$

with idealised massless paddles. The characteristics of the added mass and hydrodynamic damping shown within figures 3.3 and 3.4 are very relevant to the problem in the following section and will be discussed in more detail. At this stage, the wave making system at first-order is now fully specified. The following section investigates how the condition for optimum absorption, equation (3.16), can be realised in practice.

3.4 Control of Absorbing Wave Makers

There are several key aspects that need consideration when designing an absorbing wave making system, the most important being (i) the choice of input signal, (ii) the controller architecture and (iii) the absorption filter implementation and optimisation. In respect of (i), there are several physical quantities that may be employed in order to determine the wave field on the paddle front; the two most commonly adopted approaches are the measurement of the surface elevation using

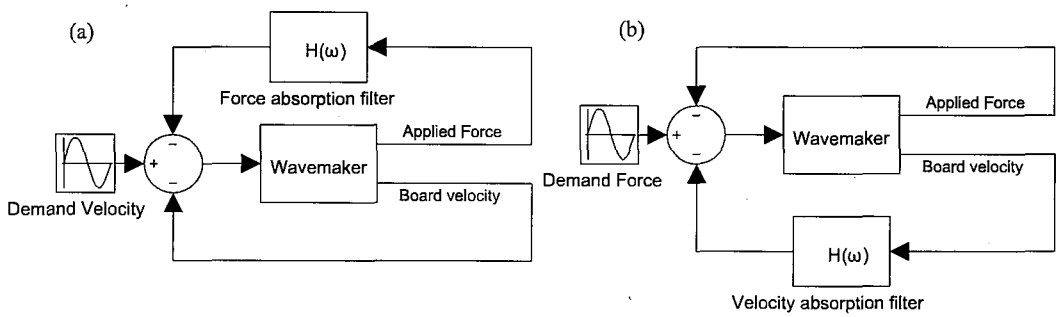


Figure 3.5: Schematic of controller model for absorbing wave maker; (a) Force based absorption filter and (b) Velocity based absorption filter

a wave gauge and the measurement of the applied force using a load cell. This present chapter, indeed the thesis as a whole, focuses on the latter, the applied force. An ideal absorption controller would maintain the optimum condition between the wave board's velocity and the applied force across all frequencies. It should be noted at this stage that an ideal controller cannot be implemented in practice; the principle causes for this apparent shortcoming being explained in the following discussion.

Figure 3.5 considers the controller architecture and suggests that this can be approached in two different ways. In figure 3.5 (a) the measured force signal is filtered and fed into a velocity summing junction; the demand being specified in terms of velocity. Alternatively, in figure 3.5 (b), the measured velocity signal is filtered and fed into a force summing junction; the demand being specified in terms of force. As discussed earlier, the optimum absorption filter for the wave making system is a-causal and hence unrealistic or unachievable. This applies to either approach, (a) and (b) above. Causal approximations for both options need to be considered; the details of which are largely dependent upon the absorption filter implementation. With regard to the absorption filter implementation, there are at least four options:

(i) A look up table with discrete frequencies

(ii) A finite impulse response (FIR) filter based on the ideal impulse response

function

(iii) A constant multiplication factor applied to the position- and velocity signals (given that controller architecture (b) is chosen)

(iv) An infinite impulse response (IIR) filter approximating the ideal transfer function

The first method, based on a look up table, would require estimating the frequency of the incident waves. In those cases where the wave maker is generating regular waves, this frequency is known *a priori*; the filter could hence be tuned for the given incident wave frequency. An alternative method is to automatically determine the instantaneous wave frequency. This has been discussed in Chatry et al. (1998) using an extended Kalman filter as a frequency estimator. However, this technique was developed for a numerical wave tank and has never been reported for a physical device where the controller's robustness is of prime concern.

Frigaard & Christensen (1994) studied a wave maker using the second method, based on a FIR filter in an open-loop control path. FIR filters have the advantage that the ideal impulse response function can be matched exactly. Strictly speaking, this is only true for an indefinitely deep filter (Smith 1998). The depth of a FIR filter expresses the length of the approximate impulse response function in the time domain. In practice, a high filter depth is required to implement a reasonable accurate estimate of the impulse response function. The time delay (more accurately: dead time) introduced by any FIR filter is directly proportional to the filter depth. This, in turn, prohibits the design of a robust closed-loop control system excluding the FIR filter from the application in real time wave absorption.

The third approach, a constant multiplication factor applied to both the position signal and the velocity signal has been mentioned in Naito (2006). Although being the most straightforward method to implement, it compromises the absorption efficiency when compared to the theoretical optimum. Nevertheless, this approach does provide a viable option and will be further discussed below.

The final approach, the IIR filter, appears to be the most balanced solution. A frequency estimate as in the case of the look up table is not required. Whilst introducing a phase shift or time delay to the signal, this only becomes significant at higher frequencies. This is in marked contrast to FIR filters where the same time delay applies to all frequency components. Furthermore, the effect of the IIR phase shift on a control system's design and stability is well understood. As a result, the development of an optimum controller based on IIR filters will also be considered below.

In developing these arguments some common notation will be employed: The tilde ($\tilde{}$) symbol placed above a letter is used to express the optimum condition. However, the respective quantity will not necessarily be causal. Furthermore, γ denotes the power absorption coefficient; the more effective the controller, the higher the absorption coefficient.

For the sake of simplicity all theoretical formulations and graphs that follow are given for mass-less and spring-less wave boards in which damping due to friction is also neglected. These assumptions are entirely appropriate when considering numerical wave makers and, in the case of the present study, facilitate the inter comparison between the different methods.

3.4.1 Absorption Based on a Filtered Force Signal

Chatry et al. (1998) discussed an absorbing numerical wave maker based on a filtered force signal, figure 3.5 (a). The optimum wave board velocity in the frequency domain, $\widetilde{U}(\omega)$, can be related to the force signal, $F(\omega)$, by

$$\widetilde{U}(\omega) = \widetilde{H}(\omega)F(\omega) \tag{3.28}$$

where $\widetilde{H}(\omega)$ is shown to be

$$\widetilde{H}(\omega) = \frac{1}{d(\omega) - i\omega m(\omega)}. \tag{3.29}$$

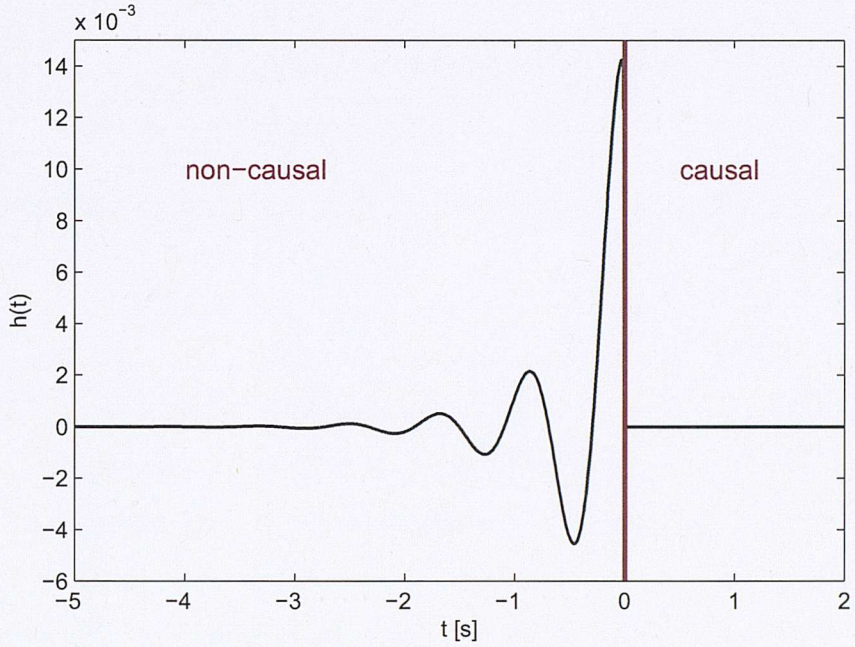


Figure 3.6: Impulse response function, $h(t)$, for a controller with filtered force signal after Chatry et al. (1998) and calculated for a piston-type wave machine

Applying the convolution theorem to (3.28) yields the optimum velocity in the time domain

$$\widetilde{u}(t) = \int_{-\infty}^{\infty} f(\tau)\widetilde{h}(t-\tau)d\tau. \tag{3.30}$$

Figure 3.6 shows the optimum impulse response function, $\widetilde{h}(t)$, for a piston-type wave machine. This impulse response function clearly is non-causal and, hence, not realizable in a practical controller. Chatry et al. (1998) showed that by introducing an auxiliary complex function $K(\omega)$ given by

$$K(\omega) = 1 + \frac{d(\omega) - i\omega m(\omega)}{d(\omega) + i\omega m(\omega)} \tag{3.31}$$

and two feed-forward transfer functions $\widetilde{Q}(\omega)$ and $\widetilde{P}(\omega)$ defined as

$$\widetilde{P}(\omega) = \begin{cases} \Re[\widetilde{P}(\omega)] = -\frac{1}{\pi}\int_{-\infty}^{\infty} \frac{\Im[\widetilde{P}(\omega')]}{\omega'-\omega} d\omega' \\ \Im[\widetilde{P}(\omega)] = \Im[K(\omega)] \end{cases} \tag{3.32}$$

and

$$\widetilde{Q}(\omega) = \begin{cases} \Re[\widetilde{Q}(\omega)] = \Re[K(\omega)] - \Re[\widetilde{P}(\omega)] \\ \Im[\widetilde{Q}(\omega)] = 0 \end{cases} \tag{3.33}$$

the relation between force and optimum velocity may be rewritten as

$$\widetilde{U}(\omega) = \widetilde{P}(\omega)\widetilde{U}(\omega) + \widetilde{Q}(\omega)\widetilde{U}(\omega) - \widetilde{H}^*(\omega)F(\omega). \tag{3.34}$$

The feed-forward function $\widetilde{P}(\omega)$ was defined to satisfy the Kramers-Krönig[1] relation and is hence causal. With $\widetilde{H}(\omega)$ being non-causal, $\widetilde{H}^*(\omega)$ is, by definition, causal. In contrast, $\widetilde{Q}(\omega)$ is a real function in the frequency domain which results in a real and even, thus a-causal, transform $\widetilde{q}(t)$. Due to the peaky shape and nature of $\widetilde{q}(t)$, Chatry et al. (1998) decided to approximate it by a scaled Dirac delta function such that $\widetilde{q}(t) \approx q(t) = \alpha\delta(t)$ where α is a variable coefficient. For any given tuning frequency ω_0, the factor α is chosen to be $\alpha = \widetilde{Q}(\omega_0)$. Using a frequency tracking technique, Chatry et al. (1998) also showed that the parameter α can be automatically adjusted to the instantaneous incident wave frequency. However, as discussed earlier, the present study only considers fixed coefficient systems; hence regards α to be a constant for each tuning frequency. The realizable controller in the frequency domain, $H(\omega)$, is given by

$$H(\omega) = \frac{U(\omega)}{F(\omega)} = \frac{\widetilde{H}^*(\omega)}{\widetilde{P}(\omega) + \widetilde{Q}(\omega_0) - 1} \tag{3.35}$$

and illustrated in figure 3.7 for the special case of $\alpha = \widetilde{Q}(0)$; this latter case giving optimum absorption at low frequencies. The theoretical power absorption coefficient, γ, for a piston-type machine and a variety of tuning frequencies ω_0, with $\alpha = \widetilde{Q}(w_0)$, is shown in figure 3.8. In this case the absorption characteristic

[1]For complex functions that are analytic in the upper half plane (positive imaginary part), the Kramers-Krönig relation connects the real and the imaginary part. Toll (1956) investigated the relation between the causality of a function and the analytic condition. Based on his results, the causality of a function implies that the analytic condition is satisfied and, as a result, the Kramers-Krönig relation applies. The real and imaginary parts for such functions are not independent.

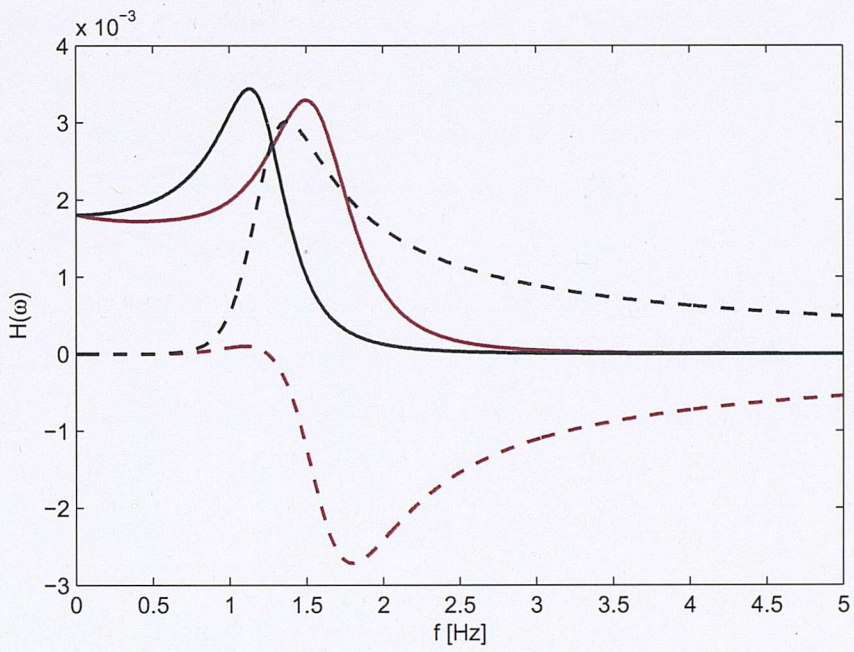


Figure 3.7: Ideal non-causal, $\widetilde{H}(\omega)$, and optimum causal low frequency approximation, $H(\omega)$, for controller with filtered force signal, based upon Chatry et al. (1998) and applied to a piston-type wave machine; —— $\Re(\widetilde{H}(\omega))$, – – $\Im(\widetilde{H}(\omega))$, —— $\Re(H(\omega))$, – – $\Im(H(\omega))$

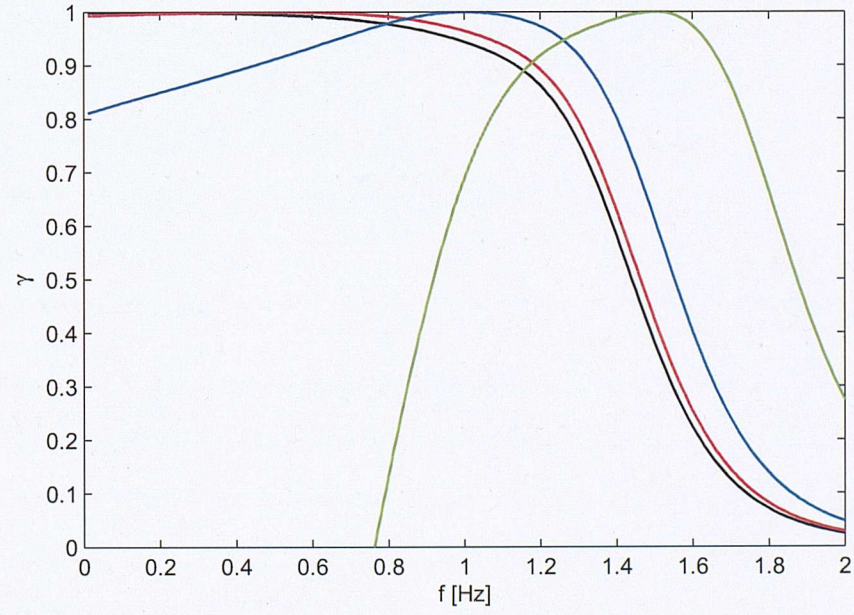


Figure 3.8: Power absorption coefficient, γ, for a piston-type wave machine and a variety of tuning frequencies, ω_0, based upon Chatry et al. (1998); —— $f_0 = 0Hz$, —— $f_0 = 0.5Hz$, —— $f_0 = 1.0Hz$, —— $f_0 = 1.5Hz$

is very good for low frequencies, but becomes less satisfactory for increasing values of ω_0. The optimum absorption range is directly linked to the match of the ideal and the approximate controller shown in figure 3.7; the data for $\omega_0 = 0$ in figure 3.8 confirming that the match is only reasonable at the lower frequencies.

It should also be stressed that, although $\widetilde{H}^*(\omega)$ is a causal function, Chatry et al. (1998) made no suggestion as to its implementation. For the characteristic plotted in figure 3.8 it was assumed that $\widetilde{H}^*(\omega)$ can be implemented perfectly, e.g. using a look up table and an instantaneous frequency estimation technique. This assumption is probably optimistic when considering a physical wave making system. As a result, it follows that realistic absorption characteristics suboptimal to the ones shown are likely to be achieved. It is also worthwhile noting that higher tuning frequencies, e.g. $f_0 = 1.5Hz$ in figure 3.8, lead to negative power absorption coefficients for low frequencies, $f < 0.75Hz$ in this particular case. This would be impractical for a physical wave making system where the fiume's seiche wave would be amplified rather than absorbed.

An analogy to wave energy applications may be drawn here. The curves in figure 3.8 are similar to bandwidth curves for a wave energy converter (Falnes 2002). As for the absorbing wave maker, a wave energy converter only performs well over a limited range of frequencies. Optimising this range of frequencies to match the incident wave conditions remains a major challenge.

3.4.2 Absorption Based on a Filtered Velocity Signal

An actively absorbing wave making system based on a filtered velocity signal was first reported by Salter (1982). More recently, Naito (2006) describes an advanced circular wave basin using a similar technique. Naito (2006) also discusses the problem arising due to the a-causality of such a system; his comments being directly related to earlier work on wave power extraction presented in Naito & Nakamura (1985).

Adopting the notation and assumptions stated earlier, the ideal control force

in terms of wave board velocity is given by

$$\widetilde{F}(\omega) = [d(\omega) - i\omega m(\omega)]U(\omega) = \widetilde{H}(\omega)U(\omega), \tag{3.36}$$

where the ideal transfer function $\widetilde{H}(\omega)$ is the inverse of the one shown in the previous section. For both piston- and flap-type wave boards the value for the added mass, $m(\omega)$, approaches a constant as the wave frequency approaches infinity; $m(\omega \rightarrow \infty) = m(\infty) =$ constant. This is clearly indicated in figures 3.4 and 3.3 presented earlier. Observing equation (3.36), it is clear that the term $i\omega m(\omega)$ approaches infinity for $\omega \rightarrow \infty$. This behaviour prohibits analysing the the transfer function and the impulse response as shown for the case of a filtered velocity signal. However, in an attempt to isolate the causal and a-causal parts of the optimum control force, and then approximate the latter, Naito (2006) adopted the following interpretation for this case

$$\widetilde{f}(t) = m(\infty)\dot{u}(t) - \int_{-\infty}^{0} L(-\tau)u(t-\tau)d\tau, \tag{3.37}$$

where the function $L(t) = L_e(t) + L_o(t)$ may be expressed by its even

$$L_e(t) = \frac{1}{\pi}\int_0^{\infty} d(\omega)\cos(\omega t)d\omega \tag{3.38}$$

and odd

$$L_o(t) = -\frac{1}{\pi}\int_0^{\infty} \omega[m(\omega) - m(\infty)]\sin(\omega t)d\omega \tag{3.39}$$

components. In the context of oscillating bodies in waves, a modelling approach based on the impulse response function is now commonly adopted. Such an approach is based upon the work originally outlined by Cummins (1962).

The optimum control force is now separated into its causal and a-causal components; only the integral part in equation (3.37) being a-causal. In seeking a causal approximation for this a-causal integral, Naito (2006) performed calcula-

tions based on the Bode [2] relation and concluded that the integral in (3.37) may be substituted by

$$\int_{-\infty}^{0} L(-\tau)u(t-\tau)d\tau \rightarrow \int_{0}^{\infty} L(\tau)u(t-\tau)d\tau \tag{3.40}$$

leading to the causal control force

$$f(t) = m(\infty)\dot{u}(t) - \int_{0}^{\infty} L(\tau)u(t-\tau)d\tau. \tag{3.41}$$

Applying the above control force, $f(t)$, to the system, the power absorption coefficient, γ, is given by

$$\gamma(\omega) = \frac{d^2(\omega)}{d^2(\omega) + \omega^2\left[m(\omega) - m(\infty)\right]^2}. \tag{3.42}$$

Recalling the nature of the added mass for piston- and flap-type wave machines (figures 3.3 and 3.4), it is clear that γ is less than unity for all frequencies suggesting that perfect absorption cannot be achieved. This is in contrast to the plunger type wave maker studied by Naito (2006) where theoretical perfect absorption was shown for one frequency ω_0 with $m(\omega_0) = m(\infty)$.

Naito (2006) also derived the power absorption coefficient for a controller with constant control parameters, γ_c. For a system where the condition $m(\omega_0) = m(\infty)$ is not realizable this coefficient may be re-derived as

$$\gamma_c(\omega) = \frac{4\omega^2 d(\omega)d(\omega_0)}{\omega^2\left[d(\omega) + d(\omega_0)\right]^2 + \left[2\omega_0^2 m(\infty) - \omega_0^2 m(\omega_0) - \omega^2 m(\omega)\right]^2}, \tag{3.43}$$

which simplifies to the expression given by Naito (2006) for $m(\omega_0) = m(\infty)$. The coefficient γ_c for various tuning frequencies ω_0 and the operation of a piston-type wave machine is shown in figure 3.9. For low tuning frequencies the absorption characteristic is very good. However, for increasing values of ω_0 the absorption

[2] Bode (1945) independently derived the Kramers-Krönig relation. In contrast, his form of representation concerns the magnitude and phase of the signal rather than the real and imaginary parts. A direct comparison of the two representations is given in Lichten (1985).

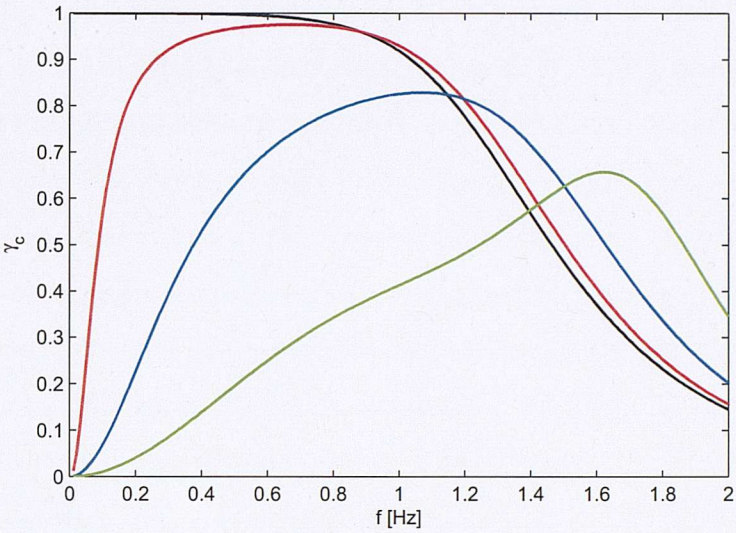


Figure 3.9: Power absorption coefficient for a system with constant control parameters, γ_c, for a variety of tuning frequencies, based upon Naito (2006) and applied to a piston-type wave machine; — $f_0 = 0Hz$, — $f_0 = 0.5Hz$, — $f_0 = 1.0Hz$, — $f_0 = 1.5Hz$

particularly at low frequencies becomes less satisfactory. It is important to note that, due to the mismatch of $m(\omega_0)$ and $m(\infty)$ in the piston case, the peak of the absorption curves shown in figure 3.9 does not occur at f_0. This is particularly evident for $f_0 = 1.5Hz$.

3.4.3 Absorption Based on Infinite Impulse Response Function Filters

Infinite Impulse Response Function Filters

The absorption techniques discussed thus far are based on an approximation of the impulse response function in the time domain. This approach is coherent in the sense that the causality of the impulse response function is a necessary condition. However, any approximation will lead to a less than perfect absorption characteristic. A direct mapping of the trade-off made in the impulse response to the absorption characteristic over frequency is extremely difficult; hence some sort of iterative or experience based procedure has to be applied in order to find the opti-

mum controller. For example, although approximating the a-causal feed-forward function $\widetilde{q}(t)$ by a scaled Dirac impulse (Chatry et al. 1998) seems reasonable, this has severe implications on the absorption characteristic, especially for higher tuning frequencies ω_0. Evidence of this effect was previously shown in figure 3.8.

The technique introduced in this subsection is based on a direct optimisation of the power absorption coefficient. Rather than seeking a causal approximation for the a-causal optimum, the procedure is based on functions that satisfy the causality relation by definition. To illustrate this, consider the characteristics of two infinite impulse response (IIR) filters; a first-order low pass filter, $H_{LP}(\omega)$, and a bandpass filter, $H_{BP}(\omega)$, defined by

$$H_{LP}(\omega) = \frac{k}{1 + i\omega/\omega_0} \tag{3.44}$$

and

$$H_{BP}(\omega) = \frac{k2\zeta(i\omega/\omega_c)}{(i\omega/\omega_c)^2 + 2\zeta(i\omega/\omega_c) + 1}, \tag{3.45}$$

where k, ζ, ω_0 and ω_c are the filter gain, bandwidth, cut off frequency and centre frequency respectively. These filters are most commonly viewed in the frequency domain using the Bode plot representation. A Bode plot illustrates the magnitude and the phase of the complex transfer function as two separate subplots. Moreover, the magnitude is expressed in decibel (dB) which is defined as $A_{dB} = -20 \log A_{lin}$ where A_{dB} is the signal amplitude in dB and A_{lin} is the linear signal amplitude. As a result, a linear amplitude gain of unity is equivalent to $0dB$, a gain of 0.1_{lin} equivalent to $-20dB$, a gain of 0.01_{lin} equivalent to $-40dB$ and so forth. The Bode plot representation for the first-order low pass and the bandpass are given in figure 3.10.

Applying the inverse Fourier transform to these functions yields their impulse response functions, $h(t)$, shown in figure 3.11. Observing this latter figure it is clear that both filters are strictly causal ($h(t) = 0$ for $t < 0$). Therefore, the output of such filters does not depend on future input signals.

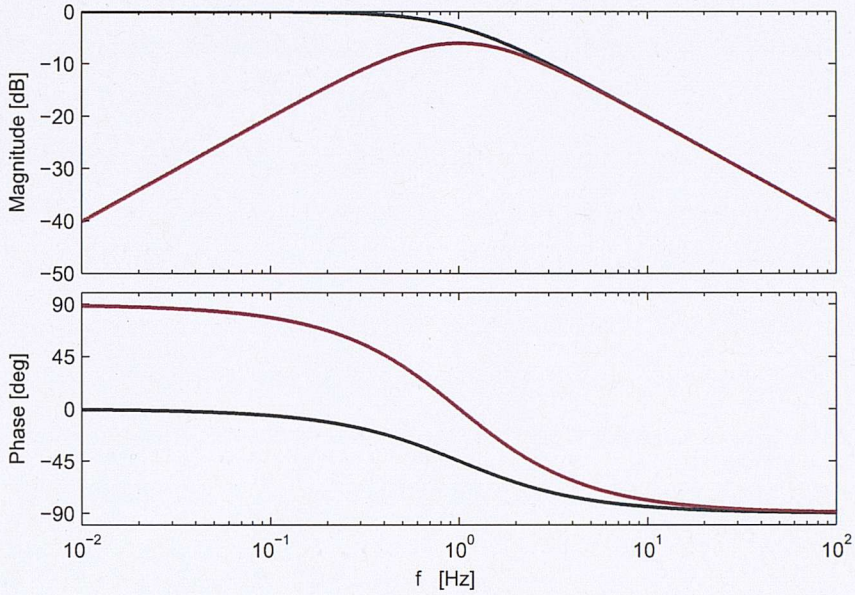


Figure 3.10: Bode plot representation for two IIR filters, one a first-order low pass filter, $H_{LP}(\omega)$, and the other a bandpass filter, $H_{BP}(\omega)$. See text for further explanation and discussions; — $H_{LP}(\omega)$, — $H_{BP}(\omega)$

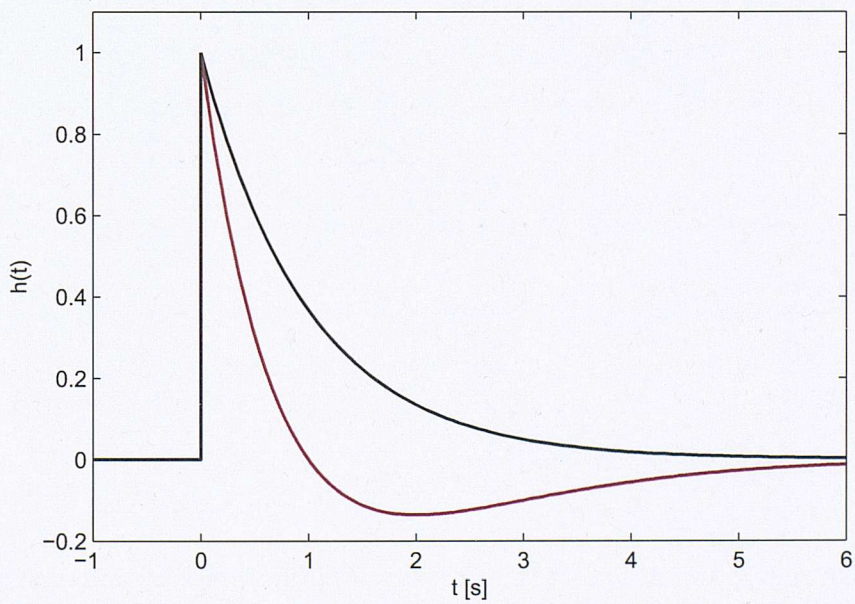


Figure 3.11: Impulse response function of the two IIR filters considered in figure 3.10; — $h_{LP}(t)$, — $h_{BP}(t)$

Absorption Viewed in the Frequency Domain

A first extensive theoretical analysis of wave power absorption by oscillating bodies was developed by Evans (1976). Later on, Falnes (1993) states two conditions for maximum power absorption: the condition for optimum phase and the condition for optimum amplitude. In the special case of a single oscillator system, in the present case a wave maker with one degree of freedom, Falnes (1980) has shown that the optimum oscillation velocity for maximum absorption is in phase with the excitation force. Furthermore, maximum power is absorbed from the wave when the destructive interference between the incident wave and the radiated wave is largest. Combining the two conditions gives the expression for maximum power absorption

$$Z_f = Z_d^*, \tag{3.46}$$

where the impedance Z can be decomposed into $Z = R + iX$, with R being the radiation resistance and X the radiation reactance. Furthermore, Z^* denotes the complex conjugate of Z, while the subscripts f and d denote filter and dynamic respectively. For any given hydrodynamic system with transfer function $H_d(\omega) = R_d(\omega) + iX_d(\omega)$ and absorption filter with transfer function $H_f(\omega) = R_f(\omega) + iX_f(\omega)$, Falnes (2002) showed that the absorbed power, P_a, is given by

$$P_a = \frac{R_f/2|F_e|^2}{(R_f + R_d)^2 + (X_f + X_d)^2}, \tag{3.47}$$

where F_e is the excitation force. Applying the optimum phase and amplitude conditions, (3.47) evaluates to

$$P_{a,max} = \frac{|F_e|^2}{8R_d} \tag{3.48}$$

for the maximum absorbed power. Introducing the power absorption coefficient,

γ, and substituting (3.47) and (3.48) yields

$$\gamma = \frac{P_a}{P_{a,max}} = 4\frac{R_f R_d}{(R_f + R_d)^2 + (X_f + X_d)^2}, \tag{3.49}$$

from which it is clear that $\gamma = 1$, or full absorption is achieved, for $R_f = R_d$ and $X_f = -X_d$; defining the two conditions for a complex conjugate impedance. Complex-conjugate control in the context of wave energy converters has been discussed by Nebel (1992).

For a controller based on the filtered velocity signal, figure 3.5 (b) and equation (3.36), the real and imaginary parts of $H_d(\omega)$ are given by $R_d = d(\omega)$ and $X_d = \omega m(\omega)$. Observing equation (3.49) it is clear that maximum power is absorbed when two conditions are satisfied:

i. The filter's real part is equal to the real part of the fluid's dynamic response (hydrodynamic damping).

ii. The filter's imaginary part is of equal magnitude and opposite sign to the imaginary part of the fluid's response (added mass).

Based on these conditions, the ideal fllter transfer function $H_f(\omega)$ is now specified; the remaining part of this section discusses the optimisation of the IIR filter to this ideal specification.

Considering conditions (i) and (ii) in terms of their practical relevance, a statement often adopted in wave power applications is: *A good wave generator is also a good wave absorber and vice versa.* This is best observed in the match of R_f and R_d, where the former is the power take off damping and the latter is the damping due to the radiation problem. For power to be extracted, the body must be capable of generating a significant amount of radiation damping.

IIR Filter Optimisation

The IIR filter optimisation process can be structured in two parts. In a first step, a filter type and order (e.g. first- or second-order low pass, band pass, high pass)

is chosen that closely reassembles the desired frequency domain characteristic. In a second step, the filter parameter (gain, cut off frequency, bandwidth) need to be optimised for the particular hydrodynamic system. All filter responses shown within this thesis were optimised using a nonlinear least-square fitting method. For a small number of independent coefficients (two in the case of a first order low pass) the `lsqnonlin` Matlab routine showed excellent convergence and was employed throughout. It is however appreciated that for a larger number of coefficients, a more sophisticated routine may be required. Such a procedure permits optimising for any given output parameter, one possibility being the power absorption coefficient, γ. Alternatively, one could optimise for the conditions (i) and (ii) above, the match of real and imaginary part between the filter and the hydrodynamic system. Several numerical tests have shown that the results for the two approaches vary only marginally and the power absorption coefficient was chosen.

The optimisation has to be limited to a particular frequency range or bandwidth. Figure 3.12 shows the power reflection coefficient, γ, for three different optimisation ranges where a piston-type wave board geometry and a first-order low pass filter were assumed. Even for this relatively simple filter excellent absorption over a wide range of frequencies can be achieved.

3.4.4 Comparing the Approaches

All the techniques outlined within this chapter require the specification of a tuning frequency or frequency band of interest. An approach that considers a frequency band is favoured. This allows for the absorption characteristic to be optimised over a range of frequencies rather than at a single point. The absorption characteristics shown in figure 3.13 were optimised for low frequencies and the piston-type geometry discussed earlier. In considering this figure it is important to note that the constant coefficient approximation derived by Naito (2006) performs almost identically to the IIR filter which is a likely outcome: for very low frequency range optimisation on a piston-type machine the evanescent modes (or the imaginary

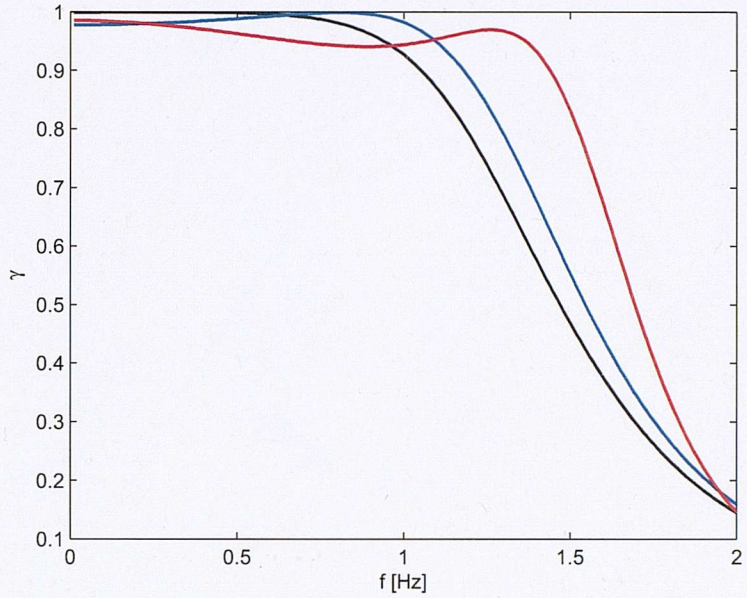


Figure 3.12: Power absorption coefficient, γ, for a piston-type wave machine and a variety optimum frequency bands using a first-order low pass (IIR) filter; the optimisation ranges being: — $0Hz \leq f \leq 0.5Hz$, — $0Hz \leq f \leq 1.0Hz$ and — $0Hz \leq f \leq 1.5Hz$

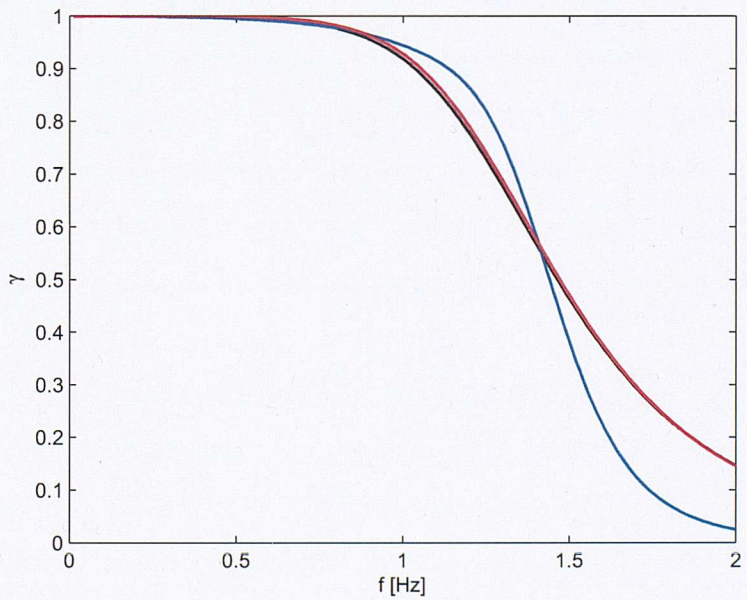


Figure 3.13: Power absorption coefficient, γ, optimised for low frequency range, — Naito (2006), — Chatry et al. (1998), — IIR filter

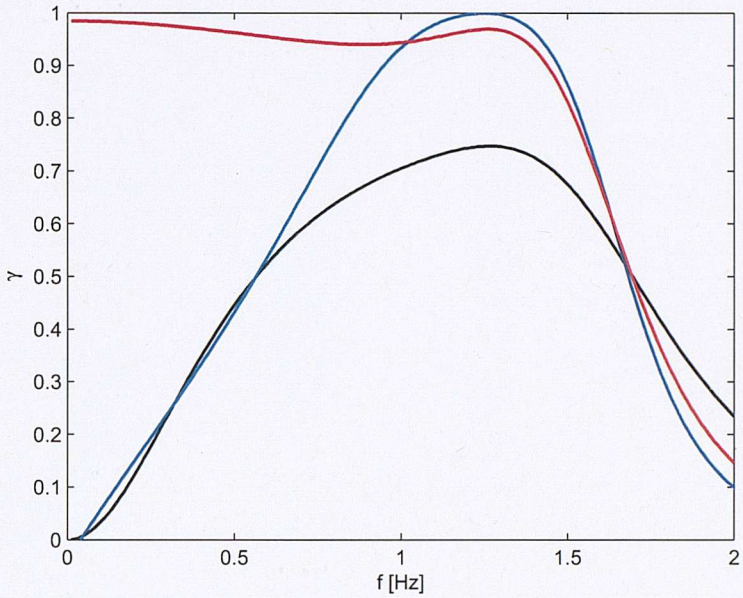


Figure 3.14: Power absorption coefficient, γ, optimised for intermediate frequency range, —— Naito (2006), —— Chatry et al. (1998), —— IIR filter

contributions) are virtually irrelevant. In this case the low pass filter optimisation routine results in a filter with a very high cut off frequency; thus effectively acting as a real and constant multiplication factor to the velocity signal. This particular scenario is identical to the constant factor technique presented by Naito (2006). The controller developed by Chatry et al. (1998) performs somewhat better at intermediate frequencies but shows poor high frequency behaviour. Given that the complex conjugate impedance, $\widetilde{H}^*(\omega)$, for this latter method may not be implemented exactly, the apparent advantage at intermediate frequencies may vanish in practice.

Figure 3.14 shows the absorption characteristic for all methods where an optimum for higher frequencies was sought. Whilst performing comparably to the method derived by Chatry et al. (1998) at high frequencies, the IIR filter approach also shows excellent absorption at low frequencies. In the context of a wave flume, this low frequency range remains important in order to prevent the build up of a seiche wave. In fact, a wave flume with the dimensions as outlined earlier is most

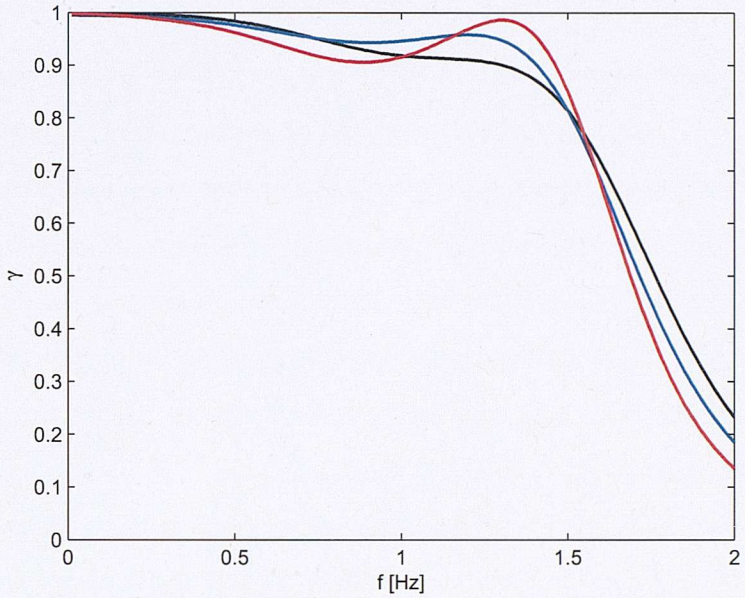


Figure 3.15: Power absorption coefficient, γ, for a bottom hinged flap-type wave machine and a variety of optimum frequency bands using a first-order low pass (IIR) filter; the optimisation ranges being: — $0Hz \leq f \leq 0.5Hz$, — $0Hz \leq f \leq 1.0Hz$ and — $0Hz \leq f \leq 1.5Hz$

likely to be used for the generation of waves with periods ranging from $T = 0.5s$ to $T = 3.0s$. As a result, the low to intermediate frequency range is crucial.

In addition to the aforementioned benefits, the IIR technique also shows great flexibility where different wave board geometries are involved (or other systems). This is illustrated in figure 3.15 where the application to a bottom hinged flap-type wave board is shown. As before (figure 3.12) a simple low-pass filter was used and very good absorption over a wide frequency range can be achieved. Overall, the simplicity and performance of the IIR filter technique makes it the ideal tool for any practical application including numerical wave tanks. The application of this technique to a physical wave making device will be demonstrated in Chapter 4.

3.5 Conclusions

An inherently causal control approach for absorbing wave making systems has been discussed. The technique is based on infinite impulse response filters and optimisation of the controller leads to a very good overall absorption characteristic. A direct comparison with two previously published techniques shows enhanced performance. Many parallels with wave power applications have been identified. In particular, the equation of motion for an absorbing wave maker and a generic wave energy converter are identical. It has also been shown that a good wave absorber must inevitably be a good wave generator. In the chapters that follow, an experimental validation of the method will be sought (Chapters 4 and 5) and the approach expanded to a 3-D wave making environment (Chapter 6).

4

Nonlinear Wave Generation and Absorption Using Force-feedback Control: Flap-type Wave Machines

4.1 Chapter Overview

The previous two chapters provide all the background information required to model an absorbing wave maker system; the key points being:

(i) Formulation of the boundary condition problem

(ii) Presentation of a potential solution that satisfies these boundary conditions at first- and second order

(iii) Formulation and discussion of an ideal controller for force-driven absorbing wave machines

Building upon this work, the present chapter develops a force-feedback wave maker model up to second order. Second-order wave maker theory has long been established; the most extensive and detailed approach given by Schäffer (1996). However, all existing theories assume the wave paddle is driven by a position-feedback

motion controller. In contrast, the present thesis is concerned with force-controlled wave paddles; the justification for this interest being that they provide excellent absorption and appear to introduce very little spurious harmonic content when driven with a first-order command signal.

The first part of this chapter provides a mathematical model for the operation of wave makers using force-feedback control and seeks to explain this apparent advantage. The model is developed to second order so that a command signal compensating for the remaining spurious wave is also provided. Due to the complexity of the problem, the model has initially been limited to flap-type wave machines and the generation of regular waves. A variety of numerical tests in force-control mode have been conducted, indicating that the spurious wave content is greatly reduced when compared to the position-control mode.

The second part of the present chapter concerns the experimental validation of the new theory. When the wave maker is controlled by a first-order force command signal, comparisons between the theory and experimental observations confirm two key points: (i) The first-order behaviour is crucial for the absorption characteristics of the machine. (ii) The second-order behaviour leads to a spurious, or unwanted, freely propagating second harmonic that is substantially smaller in amplitude when compared to an identical wave paddle operating with first-order position control. Both aspects of this work, effective absorption and reduced second-order spurious wave generation, are investigated over a broad range of wave frequencies and shown to be widely applicable. Furthermore, the theory also provides a force command signal correct to second order. This is introduced in a separate set of experiments and shown to provide further improvement in the quality of the wave generation.

Part I: A new Theory for Regular Wave Generation

4.2 Introduction

Position-feedback has traditionally been used for controlling the behaviour of wave machines. Indeed, the dominance of this approach is such that the term *'first-order control signal'* has almost become synonymous with *'first-order position control signal'*. In the context of force-controlled wave machines, the understanding of the control quantity needs to be broadened. Throughout this thesis *'position-controlled'* refers to machines where the wave board position is the only control parameter, while *'force-controlled'* refers to machines where the force acting on the wave board is one of the controlled quantities; the others being position, velocity and acceleration.

The behaviour of position-controlled wave machines is well understood. A first-order theory was initially derived by Havelock (1929). Second-order effects such as long waves in laboratory models have been discussed by Ottesen-Hansen et al. (1980), Sand (1982) and Sand & Donslund (1985). In addition, Flick & Guza (1980) and Sulisz & Hudspeth (1993) addressed the effects of spurious super-harmonic waves. In seeking an explanation of these effects, Schäffer (1996) derived a complete mathematical model for position-controlled wave makers including the sub- and super-harmonic effects arising at second order. This latter second-order solution has been presented in Chapter 2 and will be discussed in more detail herein.

With advances in laboratory wave generation techniques, wave makers are increasingly required to provide active absorption in order to avoid spurious reflection and reduce the flume or basin stilling time. Reviews of this extensive topic are given by Schäffer & Klopman (2000) and Naito (2006). Historically, Milgram (1970) pioneered this field for both theory and practical application. Although

his final experimental apparatus used a signal based on the surface elevation measured some distance from the absorbing terminal, he also suggested using the wave-induced force acting on the face of the wave board to implement active absorption. However, due to concerns regarding the resonant excitation of the fluid behind the wave paddle, he decided it would be impractical to use the force signal.

Research in the wave power field (Salter et al. 1976) led to a detailed investigation of the forces acting on various oscillating bodies. Because this work was often carried out by electrical engineers, the concept of an impedance was commonly adopted. In essence, the impedance describes a frequency dependent function between the incident force and the oscillator velocity; the latter being the mechanical analogies to voltage and current. Impedance in the context of hydrodynamics has been discussed in McCormick et al. (1981) and McCormick (1983). Falnes (1980) showed that for the special case of a single oscillator system, the optimum oscillation velocity for maximum absorption is in phase with the excitation force. This condition can be achieved using an impedance matching controller as outlined in Chapter 3; further discussion of this being given in §4.6. To overcome the problematic resonant fluid motion behind the paddle, described by Milgram (1970), Salter (1982) engineered a dry-backed paddle so that the measured force solely depends on the wave-induced pressure acting on the paddle face and the dynamics of the wave board.

In addition to operating as excellent absorbers, the dry-backed force-controlled wave machines have a significant benefit over position-controlled machines in that they seem to introduce very little spurious harmonic content. As a result, in excess of 500 force-controlled wave paddles are operating today in many laboratory facilities worldwide. Even though these devices have been used for more than three decades, a complete theory, linking the demand signal to the generated wave field, has not been derived. In practice, the machines are set up using an empirical tank transfer function. The successful application of this method, as well as an improved calibration technique, has been reported by Masterton & Swan (2008).

The main objective of the present chapter is to derive a mathematical model

predicting the behaviour of force-controlled wave machines up to second order. This incorporates aspects of the theory already derived in Chapters 2 and 3. At first order, this model seeks to link the linear demand signal to the linear or first-order wave field; hence, at the very least, providing an initial estimate for the empirical transfer function mentioned above. At second order, the model aims to explain the machine's success in terms of the absence of spurious wave modes.

The proposed model will build upon existing wave maker theories: the wave field generated by a given sinusoidal paddle motion is identical for both position- and force-controlled machines. However, a single harmonic force-control signal does not inevitably lead to a paddle motion at this harmonic alone. Indeed, all the nonlinear processes in the generated wave field will contribute to the applied force and hence feed back into the generation process. A full explanation of this effect is given in §4.3. Once the behaviour up to second order is fully understood, an additional command signal for the suppression of the remaining spurious super-harmonic may be evaluated.

Unlike for position-controlled machines, absorption is integral to the operation of force-controlled machines. As such, the second-order model derived here, includes all effects introduced by the absorption mechanism. Schäffer & Jakobsen (2003) (see also Zhang (2005)) derived a new theory of nonlinear wave generation in position control with active absorption. However, for large reflections, they state that the theory is not fully consistent with regard to non-linearity. The full impact of absorption filters on nonlinear wave generation in position-control has not yet been explained. Consequently, the force-feedback model developed herein is compared to non-absorbing position-controlled machines.

In a variety of numerical tests in force-control mode (§4.10) it is shown that the spurious wave content introduced in the wave flume is greatly reduced when compared to the position-control mode. A set of experiments substantiating the numerical tests is presented in Part II of this chapter, §4.12 onwards.

4.3 Physical Model

For position-controlled machines, the control quantity is easily defined: the mechanics of the paddle and, more importantly, the generated wave field do not affect the board motion. In contrast, with a force-controlled wave machine the control quantity is not so straightforward. Even though the force is a crucial part of the control, the position, velocity and acceleration of the wave machine are also important. In order to fully understand this concept, the wave machine has to be considered as a coupled mass-spring-damper system; the forces appropriate to such a system being dependent on position, velocity and acceleration. In addition to the forces related to the generated wave field, hereafter referred to as the hydrodynamic feedback, the paddle spring, damping and inertia also have to be modelled precisely.

To understand the complexity of the hydrodynamic feedback, it is important to appreciate the following. Applying a single-frequency, sinusoidal force to the paddle will cause it to move and generate a wave field. This wave field, in turn, induces a force on the wave board which is sensed by a force transducer. The nature of this force is dependent on the full non-linearity of the waves and it is this nonlinear force that determines, via the paddle controller, the force to be applied in the next time step. Consequently, exciting a force-controlled wave machine at one frequency, will cause a nonlinear or multiple frequency paddle motion. For waves of small steepness, a force controlled wave machine acts as a linear system. However, when generating steeper waves, the higher-order wave effects produce a nonlinear forcing and hence a nonlinear paddle motion. This is in marked contrast to a position-controlled wave machine.

Furthermore, absorption is achieved using an impedance-matching digital filter network as outlined in Chapter 3. These filters compute the wave board velocity signal or the first derivative of the board position. In accordance with the discussion above, the velocity signal may contain harmonics of the primary generation signal which will contribute to the total feedback signal. With these two simulta-

neous feedback paths (force and filtered velocity), force-controlled wave machines cannot be modelled considering only one process quantity at a time; hence the earlier comment that absorption is an integral part of a force-controlled system. As a result, a complete frequency domain model, including hydrodynamic feedback, wave board dynamics as well as absorption filters, must be derived. Each of these aspects are considered in the following sections.

4.4 Hydrodynamic Feedback

4.4.1 Generated Wave Field

Based upon the discussion in Chapter 2, the potential solution for a wave field generated by a second-order force signal can be separated into four components:

(i) *The first-order velocity potential* - $\Phi^{(1)}$

This describes the progressive wave to be generated as well as the associated evanescent modes arising at, or near, the wave paddle. It must satisfy the boundary condition on the wave maker, requiring the fluid velocity normal to the wave board to be equal to the wave board velocity. The velocity potential can be expressed in terms of the wave board motion following Schäffer (1996). Relating the first-order force input to the first-order wave board motion, hence the first-order wave amplitude, is one of the key objectives of the work presented herein.

(ii) *The wave-wave interaction potential* - $\Phi^{(21)}$

In the general case of an irregular sea state, the various first-order waves and their evanescent modes described by $\Phi^{(1)}$ will interact with each other; $\Phi^{(21)}$ describes these cross interaction terms as well as the self interaction or Stokes terms. With the present study limited to regular waves, only the self- and evanescent interaction terms are important. The wave-wave interaction terms are bound to the first-order components. Consequently, these

contributions are referred to as a *bound waves* or *bound modes* throughout the thesis.

(iii) *The spurious free wave potential* - $\Phi^{(22)}$

Although $\Phi^{(1)}$ and $\Phi^{(21)}$ together satisfy the second-order free surface boundary conditions, they do not fully satisfy the second-order boundary condition at the wave maker. This leads to the generation of an unwanted free wave which is expressed as $\Phi^{(22)}$. For the special case of a regular wave, the spurious content at some distance from the paddle, where the evanescent modes have decayed, is a pure super-harmonic of the primary wave. The spurious waves are freely propagating wave components that satisfy the dispersion equation. As a result, these contributions are referred to as *free waves* or *free modes* throughout the thesis.

(iv) *Feedback involving a second-order second harmonic correction* - $\Phi^{(23)}$

The sum of all the forces at second harmonic is measured by the machine's force transducer. Even if there is no second harmonic specified in the command signal, the feedback excites the paddle at this frequency. The resulting paddle motion generates another freely propagating spurious wave. In order to generate the desired wave only $(\Phi^{(1)} + \Phi^{(21)})$, the contributions $\Phi^{(22)}$ and $\Phi^{(23)}$ must cancel each other out. The additional second-harmonic command force must be evaluated to satisfy this condition.

The solution of the first three potentials is identical to that presented in Chapter 2. In contrast, $\Phi^{(23)}$ results from the wave maker moving at the second harmonic caused by the nonlinear feedback and the additional correction force. In order to determine the complex amplitude of the feedback-induced motion, the entire system has to be modelled.

To remove any ambiguity, the amplitude of the spurious wave mode will be referred to as $A^{(2s)}$ hereafter. In first-order position control, $A^{(2s)}$ arises due to $\Phi^{(22)}$ alone. In contrast, $A^{(2s)}$ in first-order force control refers to the spurious

content due to the combination of $\Phi^{(22)}$ and the nonlinear force feedback included in $\Phi^{(23)}$.

4.4.2 Wave Field at Second-harmonic in First-order Position Control

To illustrate the relevance of the second-order potentials discussed above, figure 4.1 shows the dimensionless ratio between the spurious free wave amplitude, $A^{(2s)}$ (arising from $\Phi^{(22)}$ alone), and the Stokes second-order wave amplitude, $A^{(21)}$, at some distance from the wave paddle for the two flap wave machines discussed previously, figure 2.3. Recalling the nature of the wave machine geometries, figure 2.3 (a) concerned a bottom hinged flap ($d/h = 0$) whereas figure 2.3 (b) concerned a flap where the hinge is place half way between the bed and the free surface ($d/h = 0.5$).

The curves in figure 4.1 are based on the second-order solution given within Chapter 2 (equations 2.28 and 2.31), hence considering the case of first-order position control; the effect of the hydrodynamic feedback, giving rise to $\Phi^{(23)}$, is neglected and only regular waves are considered herein. In the case of a bottom hinged wave machine ($d/h = 0$) the spurious wave may be as large as the Stokes second-order content and peaks at $h/L_0 \approx 0.15$. This is a relatively shallow water wave and the Stokes contribution is hence significant, leading to a sizable spurious free wave. In contrast, the minimum occurs at $h/L_0 \approx 0.06$. However, the latter point is only of theoretical interest as it would be inappropriate to operate a flap machine in this regime; the small first-order coefficient c_0 in figure 2.3 (a) indicates that a very large stroke would be required to generate a wave of practical amplitude. In this case, a piston-type wave maker would be required.

Similar arguments apply in the second wave maker case ($d/h = 0.5$). The minimum $A^{(2s)}/A^{(21)}$ occurs in very shallow water $h/L_0 \approx 0.03$; whilst the maximum again occurs at $h/L_0 \approx 0.15$. In this latter case, a spurious free wave of up to four times the Stokes content arises. This is clearly undesirable because this region is

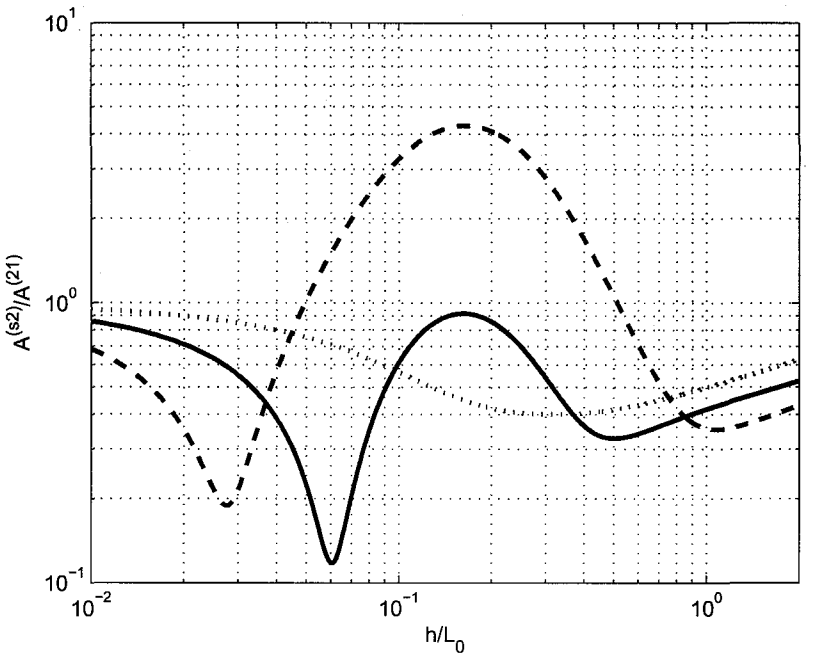


Figure 4.1: Dimensionless ratio between spurious free wave amplitude, $A^{(2s)}$, and Stokes second-order wave amplitude, $A^{(21)}$, based on first-order position control; —— wave maker hinged at $d/h = 0$, – – wave maker hinged at $d/h = 0.5$, · · · · piston-type wave maker

of interest for wave generation (figure 2.3 b).

As the water depth increases, the dimensionless spurious wave ratio becomes small for both paddle configurations. However, this may be of little practical importance, since the Stokes second-order effects are less pronounced in this regime unless extremely steep waves are generated.

Even though the second-order behaviour of piston-type wave machines is not discussed within this section, the corresponding dimensionless ratio $A^{(2s)}/A^{(21)}$ is given in figure 4.1 allowing a direct comparison to be made. Further discussion of this result is given in §5.4.

4.4.3 Hydrodynamic Torques on Flap-type Wave Machines

In the case of a flap-type wave machine, the origins of the feedback potential $\Phi^{(23)}$ are best described by considering the applied torque, T. A wave-induced

pressure acting at the hinge of the flap makes no contribution to the measured hydrodynamic torque, whilst a pressure acting at or above still water level has a very large effect. In order to evaluate the total hydrodynamic torque, Bernoulli's equation, given by

$$p(x,z,t) = -\rho\frac{\partial\Phi}{\partial t} - \rho g z - \frac{1}{2}\rho\left[\left(\frac{\partial\Phi}{\partial x}\right)^2 + \left(\frac{\partial\Phi}{\partial z}\right)^2\right], \tag{4.1}$$

is applied throughout the wave field, evaluated at $x = 0$ and integrated over the surface of the wave board, where ρ is the density of the fluid and $p(x,z,t)$ is the depth dependent pressure fluctuation. In contrast to the discussion in Chapter 3 where only first-order terms were retained, the interest in the present study lies in torques up to second order; terms of higher order being neglected. Separating the total wave induced torque into its first- and second-order components gives

$$T_\Phi^{(1)} = -\int_{-h+d}^{0} \rho\frac{\partial\Phi^{(1)}}{\partial t}(h-d+z)dz \tag{4.2}$$

and

$$\begin{aligned} T_\Phi^{(2)} = &-\int_0^{\eta^{(1)}} \rho g z(h-d+z)dz - \int_0^{\eta^{(1)}} \rho\frac{\partial\Phi^{(1)}}{\partial t}(h-d+z)dz \\ &-\int_{-h+d}^{0}\frac{\rho}{2}\left(\frac{\partial\Phi^{(1)}}{\partial x}\right)^2(h-d+z)dz - \int_{-h+d}^{0}\frac{\rho}{2}\left(\frac{\partial\Phi^{(1)}}{\partial z}\right)^2(h-d+z)dz \\ &-\int_{-h+d}^{0}\rho\frac{\partial\Phi^{(21)}}{\partial t}(h-d+z)dz - \int_{-h+d}^{0}\rho\frac{\partial\Phi^{(22)}}{\partial t}(h-d+z)dz, \end{aligned} \tag{4.3}$$

where the subscript Φ indicates wave-induced quantities and the superscript () denotes the order of the term involved. All torques are derived as torques per unit paddle width. Further detail concerning the derivation of these results is given in Appendix B.

In addition to the wave-induced contributions to the torque, flap-type machines also experience a torque caused by the varying effective water depth associated with departures from the mean or vertical position. The total hydrostatic torque

is given by

$$T_h = -\frac{1}{6}\rho g(h-d)^3 \frac{1}{\cos^2\theta} \approx -\frac{1}{6}\rho g(h-d)^3(1+\theta^2) \tag{4.4}$$

which may be approximated as the sum of a static term and a second-order contribution, $T_h^{(2)}$. With flap-type wave machines typically being operated in the range of ± 0.3 radians, the second-order approximation introduces an error of less than one percent for the maximum stroke. The total second-order torque is now given by

$$T^{(2)} = T_\Phi^{(2)} + T_h^{(2)}, \tag{4.5}$$

where $T^{(2)}$ is the forcing term leading to the generation of the additional second-order wave potential $\Phi^{(23)}$. However, the systems transfer function, incorporating the wave board dynamics and the absorption filter, needs to be known before the impact of $T^{(2)}$ can be evaluated.

4.5 Wave Board Dynamics

The torques discussed thus far are all induced by the generated wave field. In practice, a transducer would sense three torque components: the hydrodynamic feedback torque, the wave board inertia torque and the wave board gravity torque. When modelling the behaviour of the wave machine, the paddle is regarded as an inverted pendulum with inertia, r, and a gravity induced component, $-Mgh_m$, where h_m is the distance from the hinge to the centre of gravity and M is the paddle's mass. Considering a physical pendulum, the gravity induced component varies with $\sin\theta$. However, with flap-type wave machines typically being operated in the range of ± 0.3 radians, the first-order approximation, $sin\theta \approx \theta$, introduces an error of less than two percent over the full range, neglecting terms at third order and above. This gravity induced torque is crucial for very low frequencies, whereas the inertia torque may become dominant towards the higher frequencies.

The equation of motion for this system is given by

$$[r + m(\omega)]\,\ddot{\theta} + d(\omega)\dot{\theta} - Mgh_m\theta = T, \tag{4.6}$$

where the mechanical damping, d, is assumed to be negligible compared to the hydrodynamic damping, $d(\omega)$. The coefficients for hydrodynamic damping and added inertia, $m(\omega)$, for a flap-type wave machine have already been derived in Chapter 3, equations (3.26) and (3.27) respectively. In contrast, the wave board induced torque $(r\ddot{\theta} - Mgh_m\theta)$, hereafter referred to as wave board dynamic torque, was not considered previously.

4.6 Absorption Filter Design

The various control strategies for absorbing force-controlled wave makers have been discussed in Chapter 3. Throughout the thesis, an absorption strategy based on infinite impulse response (IIR) filters will be applied; the relative merits of this approach having been presented in Chapter 3. Building upon this earlier work, the power absorption coefficient, γ, for any given hydrodynamic system with transfer function $H_d(\omega) = R_d(\omega) + iX_d(\omega)$ and absorption filter with transfer function $H_f(\omega) = R_f(\omega) + iX_f(\omega)$ was shown to be

$$\gamma = \frac{P_a}{P_{a,max}} = 4\frac{R_f R_d}{(R_f + R_d)^2 + (X_f + X_d)^2}, \tag{4.7}$$

where P_a is the absorbed power and $P_{a,max}$ is maximum power that can be absorbed. The subscripts d and f denote dynamic and filter respectively. It is also important to note that the terms X_f and X_d must not be confused with the wave board amplitude X_n.

The analysis in Chapter 3 focused on mass-less and spring-less paddles appropriate to the operation of numerical wave tanks. With the present study concerning physical absorbing wave machines, the mass and spring cannot be neglected.

Rewriting the equation of motion (4.6) in the frequency domain gives

$$T(\omega) = \left[i \left(\omega(r + m(\omega)) + \frac{Mgh_m}{\omega} \right) + d(\omega) \right] \Omega(\omega) = H_d(\omega)\Omega(\omega), \qquad (4.8)$$

where $H_d(\omega)$ is the complex transfer function relating flap torque and the paddle angular velocity. Examining (4.8) further, shows that some of the components of torque are in phase with the velocity (real part), whilst others are 90 degree out of phase (imaginary part). The optimum absorption filter will have the same real part, while the imaginary part will be of equal magnitude and opposite sign (complex conjugate filter). This is equivalent to Falnes (1980) finding that the optimum oscillator velocity is in phase with the excitation force and confirms the expression in equation (4.7) with $\gamma = 1$ (full absorption is achieved) for $R_f = R_d$ and $X_f = -X_d$.

Figure 4.2 (a) shows the real and imaginary parts of the dynamic transfer function $H_d(\omega)$ compared to the real and imaginary parts of the absorption filter transfer function $H_f(\omega)$; both terms being evaluated for an existing bottom hinged wave maker.

Figure 4.2 (a) also shows the two conditions for optimum absorption, $R_d(\omega) - R_f(\omega) = 0$ and $X_d(\omega) + X_f(\omega) = 0$. Towards the higher frequencies, the imaginary part of the dynamic impedance, $X_d(\omega)$, increases rapidly. This is mainly due to the increasing contribution of the evanescent modes in this regime, evidence of which is provided in figure 2.3. In this case it becomes difficult to provide sufficient negative filter reactance, resulting in a non-zero sum of the two imaginary parts. [1]

Figure 4.2 (b) shows the resulting power absorption coefficient γ. The absorption becomes poor when the filter fails to match the machine's reactance. Nonetheless, very good power absorption is achieved over a wide band of interest.

[1] An increased imaginary part in the filter impedance results in an additional phase shift in the processed velocity signal. From basic control theory it is well known that sufficient phase margin (63 degrees for optimum step response, but at least 30 degrees for a reasonable overshoot characteristic) must be maintained to ensure system stability. Therefore, absorption has to be traded off against stability.

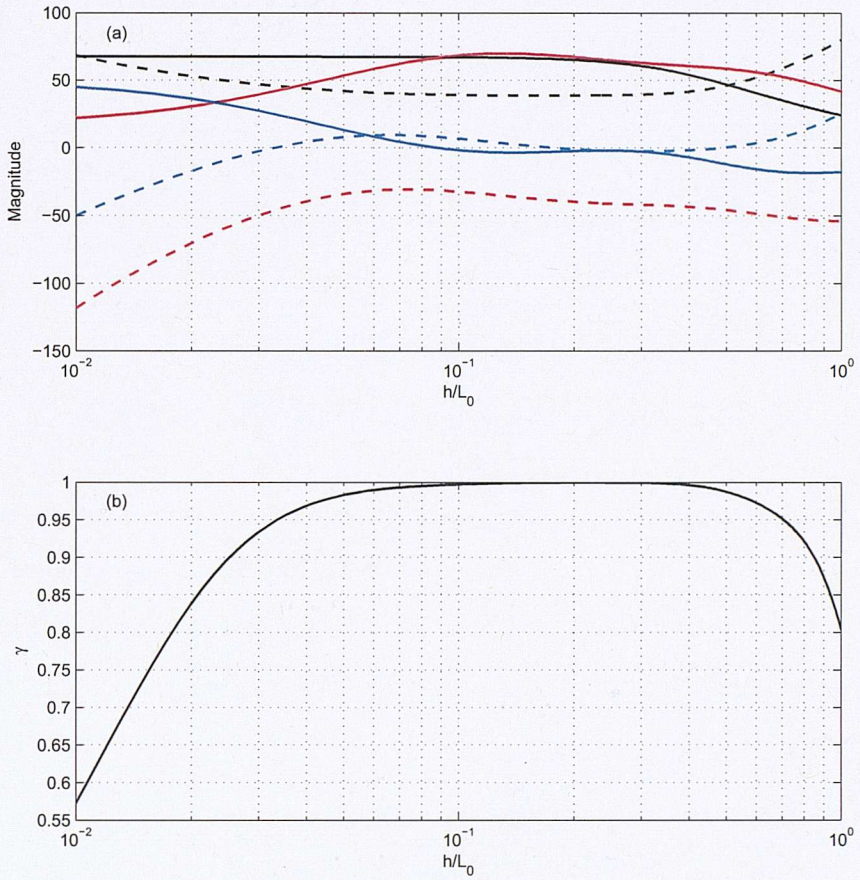


Figure 4.2: Impedance matching for a bottom hinged wave maker; —— $R_d(\omega)$, – – $X_d(\omega)$, —— $R_f(\omega)$, – – $X_f(\omega)$, —— $R_d(\omega) - R_f(\omega)$, – – $X_d(\omega) + X_f(\omega)$

4.7 Frequency Domain Model

All system components have now been discussed. Figure 4.3 shows a block diagram of the entire wave machine, the four contributions being: $C(\omega)$ - the machine controller, $G(\omega)$ - the wave board and water transfer function, $H_f(\omega)$ - the absorption filter and $H_d(\omega)$ - the dynamic torque feedback.

Any real wave machine needs a controller to minimize the error between demand and measured feedback, a process commonly referred to as *closing the loop*. Even though the controller has to be included in the simulation process, it will not be discussed here. An ideal closed-loop discrete-time controller of a hinged wave maker is discussed in Hodge & Cherchas (1988). However, their approach is only partially applicable here since they adopt the paddle position as the control

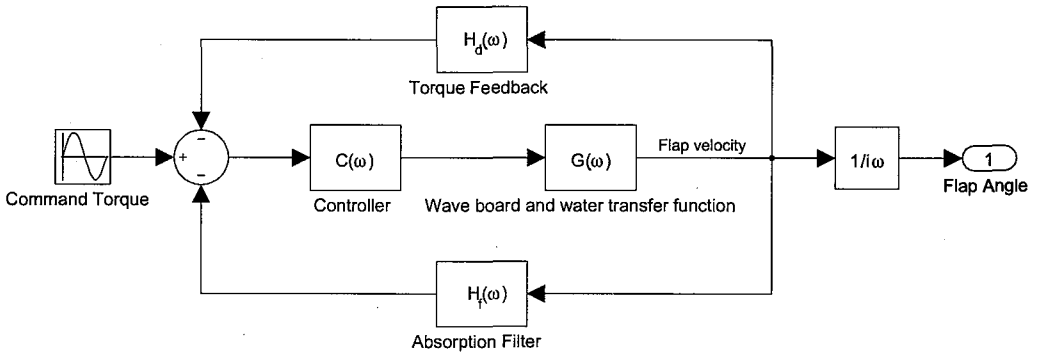


Figure 4.3: Schematic for general system model

quantity. The transfer function $G(\omega)$ relates the drive motor torque to the flap angular velocity and is the inverse of $H_d(\omega)$.

Applying standard frequency domain methods (see Appendix D for a note on closed-looped control systems), the block diagram in figure 4.3 may be expressed as a single transfer function

$$H_s(\omega) = \frac{\Theta(\omega)}{T(\omega)} = \frac{1}{i\omega} \frac{C(\omega)G(\omega)}{1 + C(\omega)G(\omega)\left[H_f(\omega) + H_d(\omega)\right]}, \tag{4.9}$$

where $H_s(\omega)$ relates the command torque, $T(\omega)$, to the flap angle, $\Theta(\omega)$, for a closed-loop control system; the subscript s denoting system. The transfer function $H_s(\omega)$ can now be used to model and simulate the behaviour of the wave machine.

4.8 Wave Generation at Second Harmonic and Second-order Correction

Equation (4.5) defines the second-order torque $T^{(2)}$. This is the forcing term for a wave board motion at second harmonic $X_1^{(2)}$. Using the system's transfer function $H_s(\omega)$ this motion can be related directly to the second-order torque,

$$X_{1,a}^{(2)} = (h - d)H_s(2\omega_n)T_a^{(2)}, \tag{4.10}$$

where $H_s(2\omega_n)$ is the frequency response of the transfer function $H_s(\omega)$ evaluated at frequency $2\omega_n$; ω_n being the frequency of the primary progressive wave. The additional subscript a indicates that the complex amplitudes of the respective terms are considered. For any given second-order paddle displacement, the time history and the complex amplitude are related by

$$X^{(2)} = \frac{1}{2}\left\{-iX_a^{(2)}e^{i2\omega t} + c.c.\right\} \tag{4.11}$$

where the factor $-i$ was kept for consistency with Schäffer (1996). Similarly, any given second-order torque time history is related to the complex amplitude by

$$T^{(2)} = \frac{1}{2}\left\{-iT_a^{(2)}e^{i2\omega t} + c.c.\right\}. \tag{4.12}$$

In order to eliminate the spurious free wave content, the second-order wave board motion is given by

$$X_{0,a}^{(2)} = \frac{F^+c_0^2}{h}X_a^2, \tag{4.13}$$

where the transfer function F^+ is found (Schäffer 1996) by ensuring that the progressive part of the spurious free wave and the progressive part of the additionally generated wave cancel out; the definition of F^+ being given in Appendix A. Introducing a second-order compensation torque with complex amplitude $T_{c,a}^{(2)}$, leading to an additional paddle motion $X_{2,a}^{(2)}$, the desired second-order paddle motion $X_{0,a}^{(2)}$ may now be expressed as the sum of $X_{1,a}^{(2)}$ and $X_{2,a}^{(2)}$

$$X_{0,a}^{(2)} = X_{1,a}^{(2)} + X_{2,a}^{(2)} = (h-d)H_s(2\omega_n)\left(T_a^{(2)} + T_{c,a}^{(2)}\right). \tag{4.14}$$

Comparing (4.13) and (4.14) yields

$$T_{c,a}^{(2)} = \frac{F^+c_0^2X_a^2}{h(h-d)H_s(2\omega_n)} - T_a^{(2)}, \tag{4.15}$$

which is the second-order compensation torque required to eliminate the spurious free wave. Equations (4.10) and (4.15) are the two main outcomes of this

theory. Whilst the former enables us to understand the behaviour of existing first-order controlled force-feedback machines, the latter provides an expression for full second-order compensation. Both results are evaluated in the following section. The additional second-order potential, $\Phi^{(23)}$, is given by

$$\Phi^{(23)} = \frac{1}{2}\left\{\frac{ig}{2\omega}X_a^{(2)}\sum_{p=0}^{\infty}c_p^{(23)+}\frac{\cosh K_p^+(z+h)}{\cosh K_p^+ h}e^{i(2\omega t - K_p^+ x)} + c.c.\right\} \tag{4.16}$$

where $c_p^{(23)+}$ is given in Appendix A and the second-order paddle displacement amplitude at still water level, $X_a^{(2)}$, is defined as

$$X_a^{(2)} = \begin{cases} X_{1,a}^{(2)} & \text{for first-order force control} \\ X_{0,a}^{(2)} & \text{for second-order force control.} \end{cases} \tag{4.17}$$

4.9 Simulation Models

Many control systems can be modelled and simulated using a transfer function approach in the frequency domain. Such a transfer function expresses the frequency dependent ratio of output to input, involving both magnitude and phase. The coefficients characterising a model are often constant, or frequency independent, and as a result it is easily possible to obtain step responses using control system toolboxes. However, in the present case the hydrodynamic coefficients characterising the second-order mass-spring-damper system are strongly frequency dependent. Consequently, a transfer function evaluated for a particular wave frequency is only valid at this frequency. Exciting the transfer function with either an impulse or a step function would lead to meaningless results, as both correspond to an infinite series of frequency components. When modelling the given system this had to be considered: each time- or frequency-domain simulation is limited to one particular point and the effect of the second-order components in the feedback path need to be evaluated in a separate simulation with adopted hydrodynamic coefficients.

Two different methods were used to simulate the behaviour of the machine: a time-domain simulation using Matlab Simulink and a frequency-domain simulation. The simple Simulink model (figure 4.3) requires differentiation in order to evaluate paddle acceleration from its angular velocity. An ideal differentiator has an infinite gain for very high frequencies. For any real differentiator, some form of gain limitation at higher frequencies must be included. Since this was found to affect the simulation results, especially at the second harmonic frequencies of the shorter wave components, the model had to be reformulated. Using this modified model, the Simulink time-domain simulation and the frequency-domain response model produced identical results.

4.10 Second-order Content for Flap-type Machines

For flap-type machines, the wave board and water transfer function is given as

$$G(\omega) = \frac{\Omega(\omega)}{T(\omega)} = \frac{1}{(r + m(\omega))i\omega + d(\omega) - Mgh_m/(i\omega)}. \tag{4.18}$$

This is the ratio of angular velocity to input torque and follows directly from the equation of motion (4.6). Using $G(\omega)$ allows the evaluation of the system transfer function $H_s(\omega)$ for a matched absorption filter and closed-loop control.

The model evaluation has two main objectives. First, the model should provide an improved understanding of the operation for existing force-controlled flap-type machines, or machines driven with a first-order force control signal. Second, the new second-order force command signal should be verified. Whilst the latter may perhaps be more readily demonstrated via experimental observations (§4.16), the first point requires careful consideration.

Figure 4.4 provides a dimensionless plot of the spurious wave content for a bottom hinged wave maker operating in both position-control and force-control mode. The curve relating to position control is identical to that shown in figure 4.1, the only difference being that the frequency band is now limited to the region

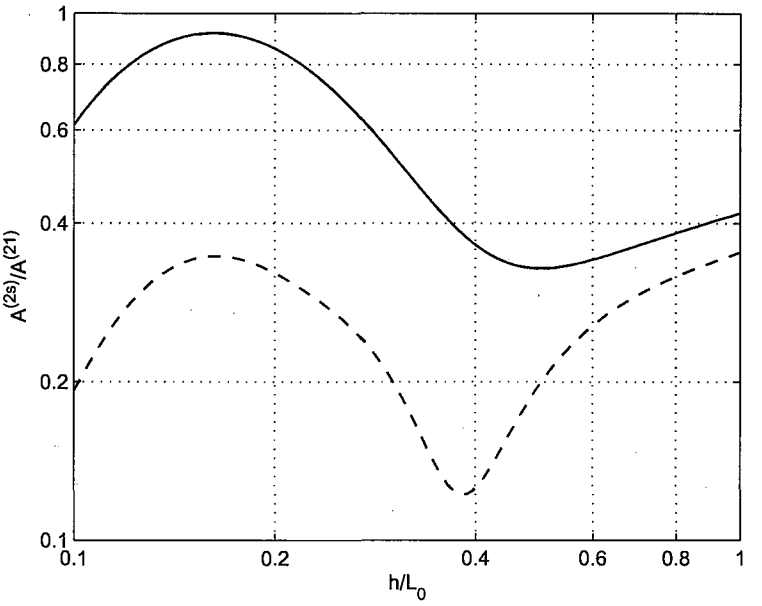


Figure 4.4: Dimensionless spurious wave content, $A^{(2s)}/A^{(21)}$, for a flap-type machine hinged at $d/h = 0$, based on —— first-order position control, – – first-order force control

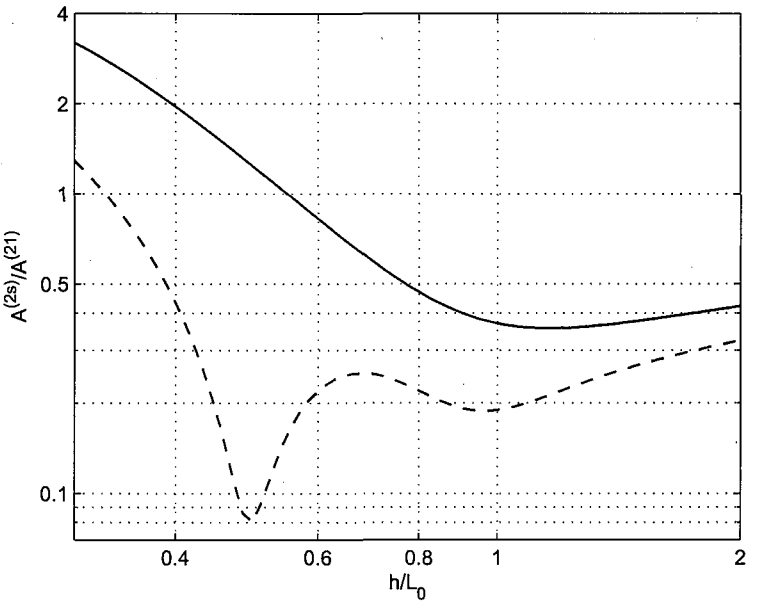


Figure 4.5: Dimensionless spurious wave content, $A^{(2s)}/A^{(21)}$, for a flap-type machine hinged at $d/h = 0.5$, based on —— first-order position control, – – first-order force control

of interest appropriate to wave generation using a flap wave machine (figure 2.3 a). A detailed discussion concerning the spurious wave characteristic in position-control mode was previously given in §4.4.2.

In force-control mode the total spurious wave is given by the sum of the original spurious wave and the wave generated by the feedback-induced paddle motion at second harmonic, $X_1^{(2)}$. Figure 4.4 clearly shows that this latter component, the feedback-induced wave, cancels out a significant proportion of the original spurious wave. For example, the maximum value of the dimensionless ratio, $A^{(2s)}/A^{(21)}$, occurring at $h/L_0 \approx 0.15$ is cut to about one third of its original value. Indeed for most of the region of interest, the spurious wave content is reduced considerably. It is only towards higher relative frequencies, corresponding to deeper water, that the difference between the two approaches reduces. In practice, this effect is hardly noticeable as second-order effects, notably the Stokes second-order contribution to the wave profile, $\eta^{(21)}$, are very weak in this regime.

Figure 4.5 shows the same dimensionless ratio, $A^{(2s)}/A^{(21)}$, for a wave machine hinged half way between the still water level and the bed. This is an important case because a bottom hinged wave maker becomes impractical in deep water test tanks. Once again, the frequency band has been limited to the region of practical wave generation (figure 2.3 b). As was the case for the bottom-hinged wave maker, a considerable cut in spurious wave content is observed across a broad range of frequencies. In the first-order force control case, two minima exist. The first minimum, at $h/L_0 \approx 0.5$, occurs where the cancellation between the spurious free wave in position control and the force-induced free wave is largest. In contrast, the second minimum, at $h/L_0 \approx 0.95$ is closely related to the minimum in first-order position control. At this location the infiuence of the force-induced free wave becomes progressively less pronounced.

In the present study, the optimum absorption filters were estimated using a best fit technique as discussed in §4.6 and shown in figure 4.2; the curves given in figures 4.4 and 4.5 being evaluated using the estimated filter transfer function, $H_f(\omega)$. This force control strategy is identical to that implemented on most operating

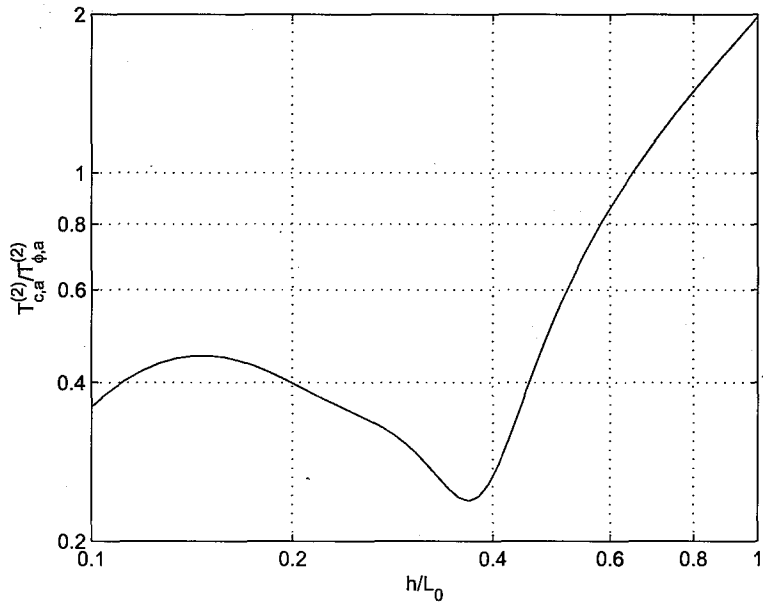


Figure 4.6: Dimensionless second-order correction torque for a flap-type machine hinged at $d/h = 0$

force-controlled wave machines. As a result, the dashed lines given in figures 4.4 and 4.5 will be representative of the performance of these machines, the detail being dependent upon the specific geometry of the machine involved.

When simulating the second-order content produced by a force-driven wave machine, values for paddle inertia and the paddle's gravity induced torque component (Mgh_m) are required. In the present study these values are based upon estimates for two existing wave machines. For other configurations, these values will vary. However, as long as the filter impedance provides a good match to the dynamic impedance, further simulations have shown that the characteristic of the spurious wave content only varies marginally. Nonetheless, a detailed analysis of the wave board's dynamic properties may be required for each practical application.

Similar arguments apply to the second-order correction torque shown in figure 4.6; the absolute value of this torque varying between different wave machines. Nevertheless, the characteristic shown in figure 4.6 gives a comprehensive insight

in the operation of force-controlled machines. Within this figure, the second-order correction torque amplitude, $T^{(2)}_{c,a}$, is plotted normalised over the second-order wave-induced torque amplitude, $T^{(2)}_{\Phi,a}$, producing a graph that is steepness independent. However, it is important to note that $T^{(2)}_{\Phi}$ is not the only second-order torque acting on the machine; indeed, the feedback torque arising due to the wave machine's inertia may become dominant at higher frequencies. Nevertheless, the minimum value of this ratio, $T^{(2)}_{c,a}/T^{(2)}_{\Phi,a}$, occurs at $h/L_0 \approx 0.37$. This is closely related to the second-order spurious wave minimum noted in figure 4.4. Given the magnitude of the terms presented in figure 4.6, it is clear that in the proximity of this minimum a second-order correction is not required. Indeed, for a relatively large frequency bandwidth, the second-order correction torque is small, indicating that first-order force-control may be appropriate for the operation of flap wave machines.

4.11 Conclusions

A second-order force-feedback wave making theory has been established. Application of the theory has demonstrated that over the frequency range where the absorption mechanism is effective a first-order force-controlled flap-type wave machine gives much reduced spurious second-harmonic waves when compared to a position-controlled machine. Indeed, over a substantial frequency bandwidth the spurious second-order wave is significantly reduced and a second-order correction may not be required. The theory outlined is limited to flap-type wave machines, generating waves of a single frequency. The experimental validation of the results outlined thus far is presented in the second part of this chapter. The expansion of the model to incorporate random waves, particularly wave groups, and piston-type wave boards is discussed in Chapter 5.

Part II: An Experimental Verification of Regular Wave Generation

4.12 Introduction to Experimental Investigation

The first part of this chapter, hereafter referred to as Part I, developed a second-order wave maker theory incorporating force-feedback control. The motivation for this work was the need for an improved understanding of wave generation, driven by a desire to accurately control the wave forms produced within a laboratory environment. Indeed, recent research has demonstrated that the precise control of a generated wave field is fundamental to the analysis of:

i. The nonlinear wave-wave interactions associated with the evolution of the largest or most extreme wave events (Baldock et al. 1996, Johannessen & Swan 2001, Johannessen & Swan 2003).

ii. The nonlinear wave-structure or wave-vessel interactions associated with the imposition of the largest loads, the loss of an air-gap, or the occurrence of wave impacts (Swan et al. 1997, Sheikh & Swan 2005).

In this context, it must be borne in mind that the theory is developed to the second order of wave steepness; the associated limitations of the work being discussed in §2.5. However, since the wave events described in (i) and (ii) involve the focussing of wave components, the waves generated at the paddle will be only weakly nonlinear and therefore appropriately modelled using a second-order wave maker theory. Given the motivation of this work, it is clear that several aspects of the theory developed in Part I require experimental validation. First, the active absorption of wave components by a wave maker controlled by force-feedback is dependent upon first-order impedance matching. Although the underlying theory has been known for several decades and has been adopted in many applications,

including wave generation, it has not been thoroughly discussed in the context of actively absorbing wave machines. The success of this approach is addressed in §4.14, with comparisons between the theory and the absorption characteristics of a flap-type wave maker.

Second, the spurious second-order wave content produced when a force controlled machine is driven with a first-order command signal requires investigation. The theory developed in Part I suggests that first-order force control can greatly enhance the wave quality when compared to first-order position control. This proposition is carefully examined in §4.15, with direct comparisons between the different control strategies.

Third, the theory developed in Part I also provides a second-order correction to the command signal. The success of this approach and the improvement it provides over a broad range of wave conditions is examined in §4.16. The chapter concludes in §4.17 with an overview of the experimental validation and a discussion of future work.

4.13 Experimental Conditions

The experiments were undertaken in a narrow wave flume located in the hydrodynamics laboratory in the Department of Civil and Environmental Engineering at Imperial College London. The wave making facilities at Imperial College London were manufactured and commissioned by Edinburgh Designs Ltd. The control system and methodology driving the wave maker used in the present study are identical to those widely installed by Edinburgh Designs. As such, the results will be directly relevant to the operation of many wave machines and provide guidance as to the effective operation of others.

The wave flume employed in the present investigation is $0.3m$ wide, $27m$ long and equipped with wave boards on either end. Both paddles are bottom hinged and mechanically identical. The water depth was maintained constant at $h = 0.7m$ throughout the wave flume. This arrangement is illustrated in figure 4.7; a more

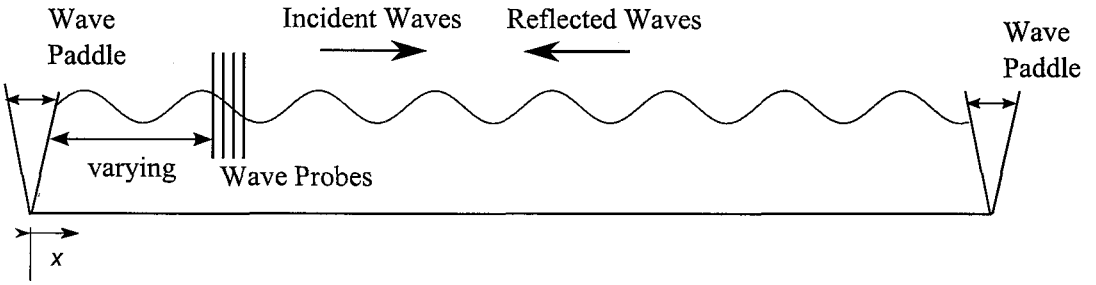


Figure 4.7: Definition sketch for the double ended flume at Imperial College

detailed description of the experimental facility being provided in Appendix G. Operating a wave maker on either side requires a rigorous definition of the terms incident wave and reflected wave. Unless stated otherwise, the wave maker on the left hand side was used to generate waves whereas the wave maker on the right hand side was used to absorb waves. Consequently, the incident wave propagates in the positive x-direction. The origin at $x = 0$ is defined as the mean position of the left hand side wave maker. The position of the wave probes relative to the origin is defined in the relevant subsections.

As further discussed in Appendix G, a precision force transducer and a high resolution motor shaft encoder were used to measure the physical quantities of wave board torque and angular position. A flexible digital control system allowed for an uncomplicated and fast change of the system's control program. This reads the digitized signals for torque and position and can process them in any required fashion. As a result, the paddle can be operated in position-control or force-control mode. Furthermore, digital absorption filters were implemented and could be rapidly altered. The test cases chosen for the experimental verification cover a fairly broad range of frequencies.

In shallow water conditions, it is well known that Stokes theory over predicts the magnitude of the second-order components. Schäffer (1996) introduced the non-linearity parameter S; a value of $S = 1$ corresponding to the 'limiting' case where second-order Stokes theory predicts secondary peaks in the trough of the primary wave. As a result, for $S > 1$ the theory fails to predict the correct second-order content. With the force-feedback model outlined in Part I utilizing the wave

Wave frequency, $f[Hz]$	Dimensionless water depth, h/L_0	Dimensionless water depth, kh	Wave height, $H[mm]$	Wave steepness, $Hk/2$	Wave non-linearity, S
32/64	0.11	0.95	148	0.10	0.60
34/64	0.13	1.03	150	0.11	0.57
36/64	0.14	1.11	164	0.13	0.59
38/64	0.16	1.19	176	0.15	0.60
40/64	0.18	1.28	174	0.16	0.57
42/64	0.19	1.38	162	0.16	0.52
44/64	0.21	1.48	150	0.16	0.47
46/64	0.23	1.58	142	0.16	0.45
48/64	0.25	1.70	132	0.16	0.42
50/64	0.27	1.81	124	0.16	0.40
52/64	0.30	1.94	116	0.16	0.38
54/64	0.32	2.07	108	0.16	0.36
56/64	0.34	2.21	102	0.16	0.35
58/64	0.37	2.36	96	0.16	0.34
60/64	0.39	2.51	92	0.16	0.34
62/64	0.42	2.67	88	0.17	0.35
64/64	0.45	2.84	82	0.17	0.34

Table 4.1: Laboratory test cases

field solution derived by Schäffer (1996), the non-linearity factor S will also be applied herein. The implications of large values of S have already been discussed in Chapter 2, §2.5.

For the lowest wave frequencies, the steepness is limited by the maximum available stroke of the wave machine. When driven in force-control mode, the maximum wave-generating angle has to be further limited to allow for the additional superimposed motion necessary for the absorption of reflected waves. Overall, a maximum steepness of $Hk/2 = 0.1$ was adopted for the longest wave having a period of $T = 2.0s$. This wave condition lies well within the applicability region of the theory ($S = 0.60$).

Details of the regular wave cases for which the second-order content was investigated are given in table 4.1. For each case the wave frequency f, the normalised water depths h/L_0 and kh, the dimensionless steepness $Hk/2$ and the non-linearity parameter S are shown; where $L_0 = 2\pi g/\omega^2$ is the deep water wave length. In

addition to the wave cases outlined in table 4.1, the machine's behaviour at first order was further investigated. This is described in detail within the following section; second order effects being discussed in §4.15 and §4.16

The theoretical development in Chapter 2 and Part I of the present Chapter were based upon the Still Water Level (SWL). It is important to note that this may differ from the Mean Water Level (MWL) in the wave flume. However, within the present experimental investigation, the variation between MWL and SWL was found to be insignificant and this difference is not further considered.

4.14 First-order Control and Wave Absorption

With position-controlled wave machines, the first-order behaviour is well understood; the amplitude of the generated progressive wave being readily evaluated from the position command signal. In contrast, force-controlled wave machines require an empirically determined transfer function; details of which are discussed by Masterton & Swan (2008). Whilst an empirical transfer function may remain the preferred approach for the calibration of a wave flume and, in particular, a 3-D wave basin, in the short term, the model developed in Part I provides a first theoretical transfer function linking the demand signal and the first-order surface elevation for force-controlled wave machines. Although this demand signal has the dimension of a torque it actually represents the input signal appropriate to the summation of the hydrodynamic feedback torque and the filtered velocity. As a result, it must not be confused with the actual torque acting on the wave machine. This latter summation may appear dimensionally inconsistent. However, the measured velocity signal passes through the impedance matching absorption filter, $H_f(\omega)$. The transfer function $H_f(\omega)$ has the dimension of torque divided by angular velocity (Falnes 2002), and hence the SI unit of $Nm/(rad/s)$. Consequently, the filtered velocity (which in effect is an angular velocity) has the dimension of torque with a unit of Nm.

Figure 4.8 compares the theoretical first-order transfer function with experi-

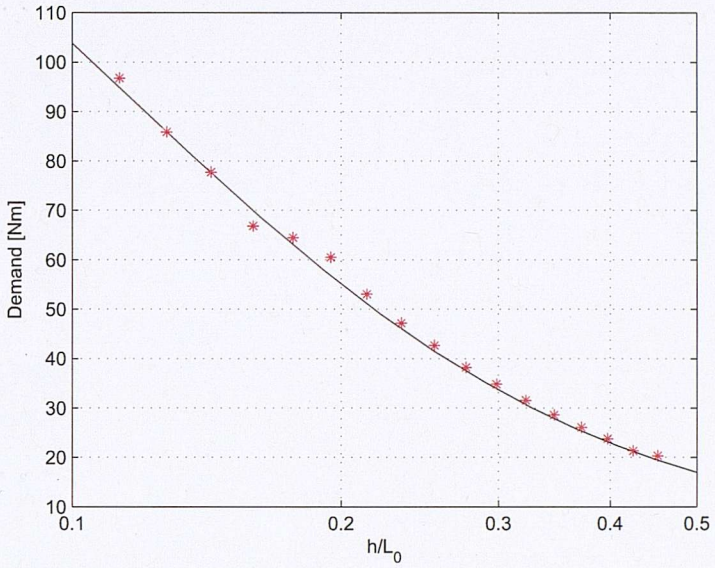


Figure 4.8: Demand signal at first order to generate a wave of steepness $Hk/2 = 0.1$ for a bottom hinged wave machine; —— Force-control theory; $*$ Experimental transfer function

mental data relating to a bottom hinged wave machine. Each experimental data point indicates the magnitude of the demand signal required to generate a wave with steepness $Hk/2 = 0.1$. Within these tests, the wave amplitude $(H/2)$ in the flume was obtained by means of a Fourier analysis of the recorded time trace. For this purpose, the initial ramp-up period was neglected and a time window that excludes reflections from the opposite side was adopted. The agreement between the theoretical model and the experimental data is excellent across the broad range of wave cases investigated. On the basis of these results it is clear that, at the very least, the theoretical transfer function provides a very good input for a first iteration of a wave maker calibration. The most likely explanation for the departures apparent around $h/L_0 \approx 0.18$ is a spurious oscillation of the wave flume's side walls. Each glass wall section is approximately 1.5m long and a resonant motion was identified for $f \approx 42/64Hz...46/64Hz$ or $h/L_0 \approx 0.19...0.23$; the wave length for these components being approximately $3m$.

Part I also derived a first-order impedance matching approach to implement

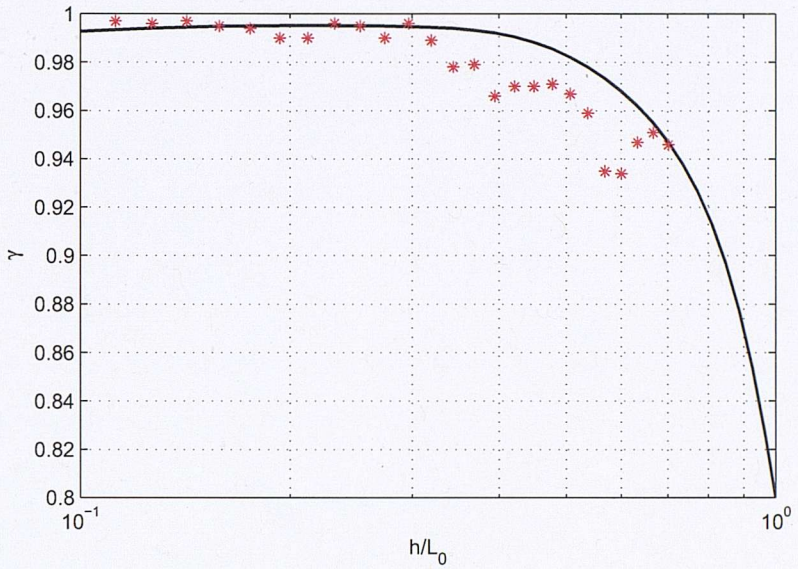


Figure 4.9: Absorption coefficient for a bottom hinged flap-type wave machine; —— Theoretical power absorption coefficient γ, $*$ Experimental data

active absorption with flap-type wave boards. Full absorption is achieved if the absorption filter provides a complex conjugate impedance, or negative reactance, to the combined wave-board and wave-field impedance. For the experimental validation a network of digital filters was designed and implemented in the machine's controller. With the filter and the wave-board-water impedance known, the theoretical power absorption coefficient, γ, can be calculated; refer to Part I for further details. Figure 4.9 compares the theory with the experimental observations; the data presented in terms of γ vs normalised water depth, or h/L_0. Overall, the agreement between the theory and the experiment is generally good but becomes less satisfactory for higher frequencies. Moreover, there appears to be a slight oscillation of the experimental data about the predicted theoretical curve. The origin of both the oscillatory behaviour and the larger departures at the highest frequencies are not understood at present and need further investigation.

In the experimental study the absorption coefficient was calculated using *Method I* proposed by Isaacson (1991); the wave gauge array consisting of 8 gauges with individual gauges spaced at a fixed distance in all test cases. For the data points shown in figure 4.9 the dimensionless probe spacing angle varied between 20° and

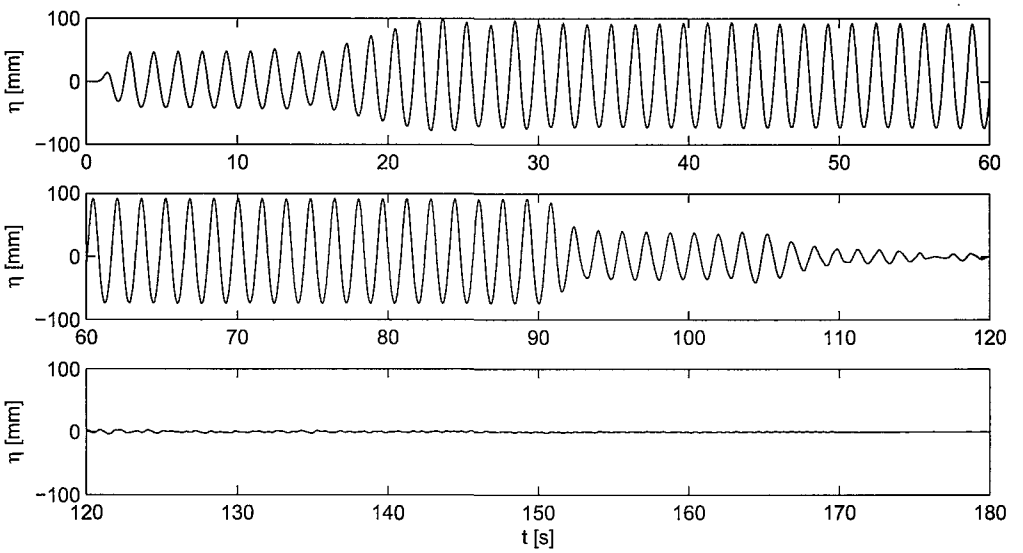


Figure 4.10: Water surface elevation $\eta(t)$ corresponding to two waves, each with $f = 40/64Hz$ and steepness $Hk/2 = 0.08$, travelling in opposite directions. Wave generation commenced at $t = 0s$ and stopped at $t = 90s$; the wave gauge being located at the first anti-node adjacent to one wave maker. Note: Although the figure is presented as three sub-plots, they are sequential defining one continuous time-history, $\eta(t)$.

110°. On the basis of Isaacson's (1991) figure 4, this relates to analysis errors of approximately 20%. Within figure 4.9, the larger deviations occurring towards the higher frequencies may be due to an inaccurate estimate of the paddle's inertia since this becomes dominant, or at least progressively more important, in this region. Another key issue neglected in the theoretical model, is the impact of a finite loop gain in the controller. The gain roll off at higher frequencies may affect the machine's response and lead to a non-ideal absorption characteristic. Nevertheless, in spite of these difficulties, the data presented in figure 4.9 is in generally good agreement with the theory.

In a double ended wave flume the success of active wave absorption based on force-feedback, with simultaneous wave generation, can be demonstrated by the generation of a standing wave of constant shape. The water surface profile, $\eta(t)$, recorded by a single wave gauge placed at the first anti-node adjacent to one wave maker is shown in figure 4.10. In this example both wave makers commence

wave generation simultaneously at $t = 0s$. The generated waves are of identical frequency and amplitude; the resulting interference pattern creating a standing wave. With the wave gauge located much closer to one wave paddle than the other, the entire data record can be sub-divided into the following intervals. During the first time interval $0s \leq t \leq 15s$ the wave probe records the wave generated by the adjacent wave maker only; a regular wave train being quickly established and maintaining a constant shape and wave height. Subsequently, the wave generated at the opposite end arrives and the standing wave profile progressively develops, becoming fully developed by $t \approx 25s$. In the time interval $25s \leq t \leq 90s$ both wave makers must absorb and generate concurrently in order to maintain the standing wave profile. The resulting surface profile within this interval (figure 4.10) is almost perfectly constant. The mean wave height in the interval $25s \leq t \leq 90s$ is $H = 165.1mm$ with a standard deviation of $\sigma = 0.33mm$. Expressed as a ratio, the standard deviation accounts for 0.2% of the mean wave height. The largest departure from the mean wave height is $0.53mm$ or $H = 165.6mm$. This indicates that the simultaneous generation and absorption using force-feedback control is both practical and effective. At time $t = 90s$ the wave generation was stopped and both wave makers are absorbing only; the surface profile recorded in the interval $90s \leq t \leq 105s$ is the wave approaching from the opposite end with almost no reflection occurring from the adjacent wave maker. Almost all of the wave energy in the flume is absorbed by $t = 180s$.

4.15 Errors Arising from a First-order Command Signal

In addition to operating as excellent absorbers, force-feedback (or impedance matching) wave machines appear to introduce very little spurious harmonic content when driven with a first-order command signal. For the first time, the model developed in Part I explains this apparent advantage, but there is a complete

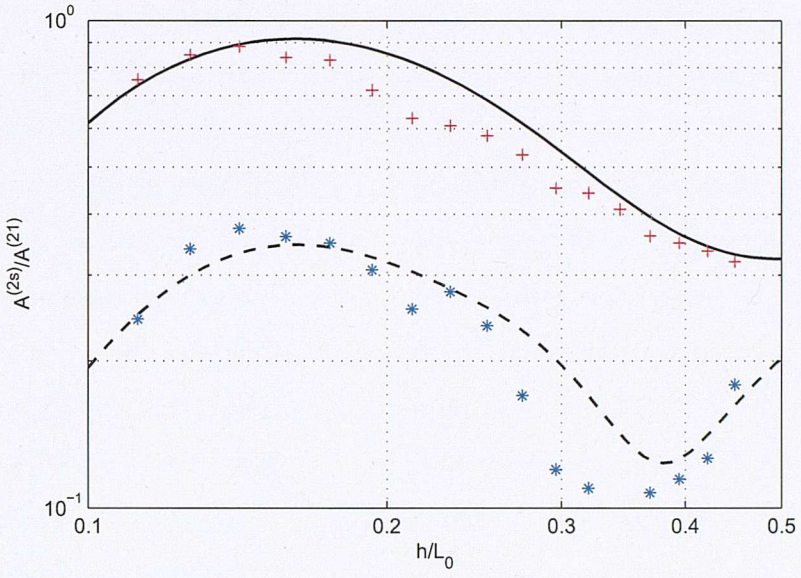


Figure 4.11: Dimensionless spurious wave content, $A^{(2s)}/A^{(21)}$, for a bottom-hinged wave maker; —— Position-control theory, + First-order position-control experiment, – – Force-control theory, $*$ First-order force-control experiment

absence of laboratory data investigating this effect. To correct this, the spurious wave content was measured for all of the test cases noted in table 4.1. In each case the wave maker was run in both first-order position control and first-order force control. The resulting data is presented in figure 4.11: the spurious second-order wave amplitude, $A^{(2s)}$, being normalised with respect to the second-order Stokes amplitude, $A^{(21)}$, so that the form of the presentation is independent of wave steepness.

In both control modes (position- and force-control) the agreement between the theoretical results and the experimental data is good across a broad range of frequencies. The observed deviation at the higher frequencies may have arisen for several reasons. First, the impact of the finite loop gain may be partially responsible. Second, when generating very short regular waves a small spurious cross-tank resonance was observed introducing additional measurement errors. Third, given the moderate steepness of the waves, the amplitude of the high frequency waves is relatively small. This, in turn, means that the absolute amplitude of the spurious second-order waves is extremely small (within the sub millimetre range) and

this has obvious implications for the relative errors associated with the data acquisition. Nevertheless, despite these difficulties, the experimental data clearly demonstrates that the operation of a flap-type wave machine with a first-order force-control signal yields a significantly smaller second-order spurious wave content when compared to an identical paddle operating in first-order position-control mode. It should also be noted that both sets of experimental data appear to lie on curves that are displaced slightly to the left of the theoretical curves. The origin of this small effect is not understood at present and requires further investigation.

However, it must be stressed that for most test cases the relative magnitude of the spurious wave is small. Indeed, the largest values are measured for shallow water waves where the second-order Stokes content is relatively large. Figure 4.12 concerns the longest wave case investigated in the present study and contrasts first-order position control (a) with first-order force control (b). In both modes the measured water surface profile is compared to second-order Stokes theory. Comparison between these cases demonstrates the much improved wave quality achieved using first-order force control. This is further established in figure 4.13 which provides a detailed view of an adjacent wave crest and wave trough in both modes of operation; the location of these points being noted as (1) to (4) in figure 4.12. With the data sampled at $128Hz$, individual data points are best shown by taking every third measured point. Absolutely no further filtering has been applied to the data in these examples, or any others presented within this chapter. In comparing the plots given in figure 4.13, the errors associated with the description of the wave trough are much reduced when the wave generation is based on the force controlled mode.

Figure 4.14 shows the surface profile for a much shorter wave ($f = 0.875Hz$) for which the wave steepness has been increased to $Hk/2 = 0.23$, highlighting the discrepancies in the wave shape arising at second order and above. Figure 4.14 (a) shows the water surface profile arising from first-order position control, while figure 4.14 (b) presents the corresponding profile produced by first-order force control; in both cases two wave crests are highlighted, numbered (1)-(4),

and these are further considered in figure 4.15. The wave profile generated using first-order position control (figure 4.14 a) is initially in very close agreement with a second-order Stokes' solution; evidence of this being provided at location (1) in figure 4.15. However, this agreement is misleading because, given the frequency of the wave involved, any spurious second-harmonic wave evolving in the vicinity of the paddle will have had insufficient time to propagate to the measuring section some $2.5m$ downstream of the paddle. The significance of this effect becomes clear in subsequent wave cycles. For example at location (2) in figure 4.14 (a), the measured data shows marked departure from the Stokes theory, confirming the presence of significant spurious second-order wave components. In contrast, the wave profile generated by first-order force control is in near-perfect agreement with the Stokes solution, showing no evidence of the delayed arrival of unwanted or spurious wave components. Evidence of this is provided by the crest elevation at locations (3) and (4) in figure 4.15; the contrast between locations (2) and (4) being the key issue.

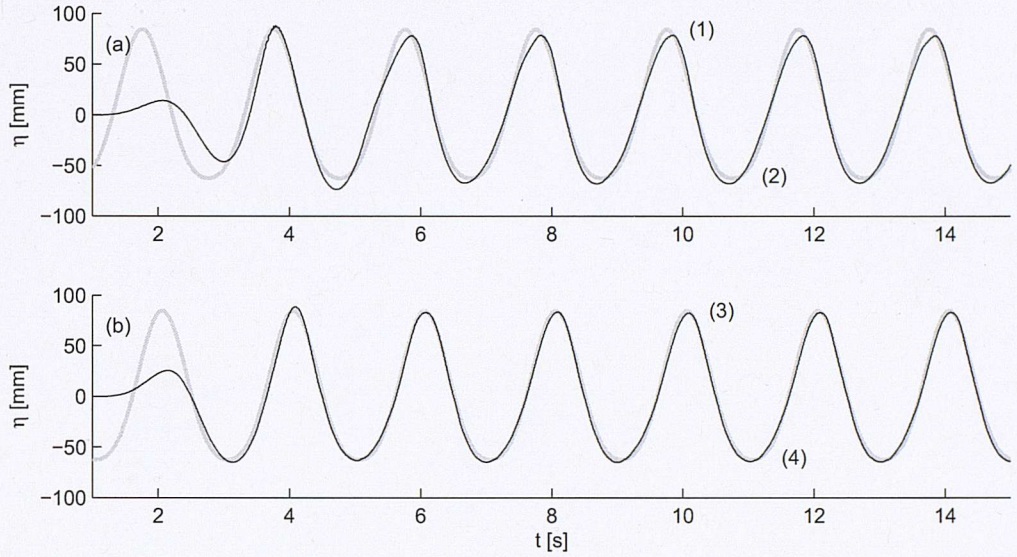


Figure 4.12: Surface elevation for wave case $f = 32/64Hz$, $Hk/2 = 0.10$; (a) First-order position control, (b) First-order force control; —— Experiment, —— Second-order Stokes solution; Note: the numbers (1) to (4) refer to locations that are considered in detail in figure 4.13

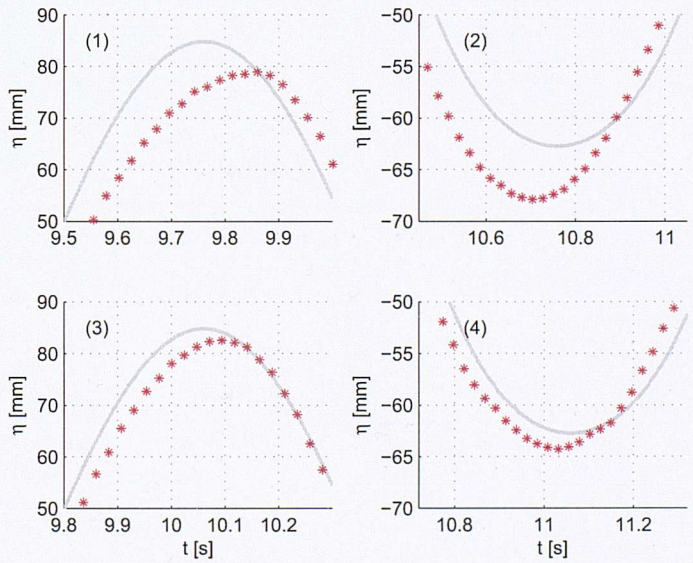


Figure 4.13: Close-up of the water surface elevation at locations (1) to (4) for wave case $f = 32/64Hz$, $Hk/2 = 0.10$ as labelled in figure 4.12; $*$ Experiment, —— Second-order Stokes solution

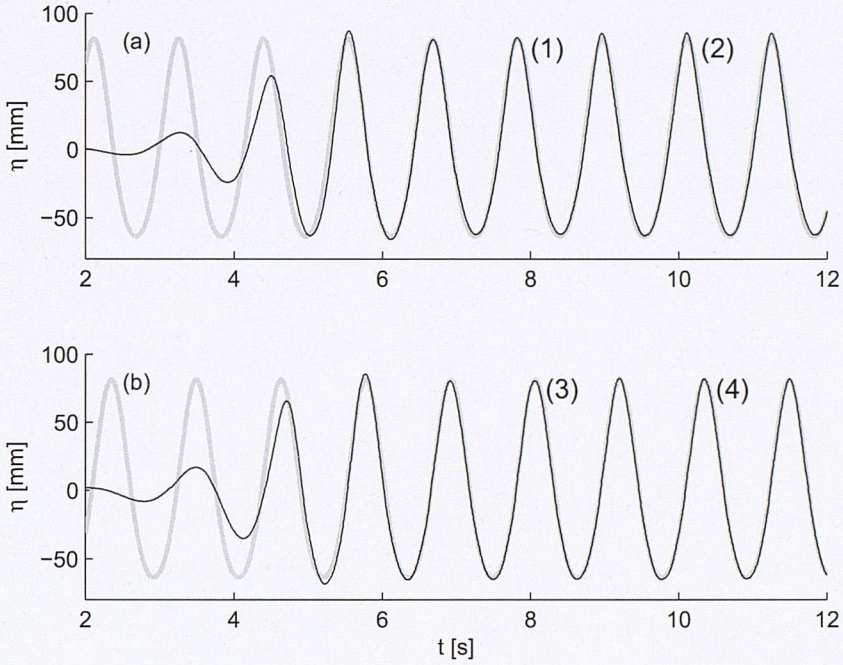


Figure 4.14: Surface elevation for wave case $f = 56/64Hz$, $Hk/2 = 0.23$; (a) First-order position control, (b) First-order force control; —— Experiment, —— Second-order Stokes solution; Note: the numbers (1) to (4) refer to locations that are considered in detail in figure 4.15

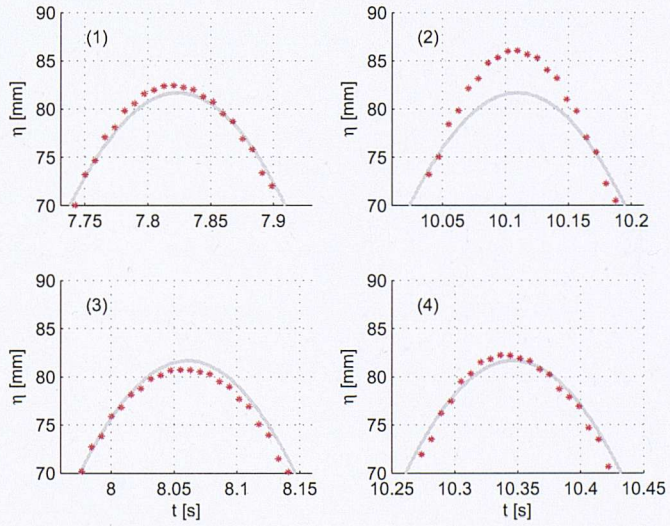


Figure 4.15: Close-up of the water surface elevation at locations (1) to (4) for wave case $f = 56/64Hz$, $Hk/2 = 0.23$ as labelled in figure 4.14; $*$ Experiment, —— Second-order Stokes solution

4.16 Second-order Control

Comparisons between the Part I theory and the present experiments have shown that using a first-order force control signal introduces very little spurious wave content over a broad frequency range. However, in the shallow water wave cases, where the second-order Stokes contributions is more pronounced, the wave profile remains less than ideal; see, for example, figure 4.12 (b) or more specifically location (4) in figure 4.13. In order to correct for the remaining spurious wave, the Part I theory provides an expression for the second-order control signal. The applicability of this correction term is considered in this section.

Figure 4.16 illustrates the benefits of second-order force control. Figure 4.16 (a) concerns the second-order spurious wave amplitude, $A^{(2s)}$, non-dimensionalised with respect to the second-order Stokes amplitude, $A^{(21)}$. For reference purposes the results of the first-order command signal are reproduced and it is clear from these comparisons that the second-order command signal significantly reduces the spurious wave content for most wave cases. Alternatively, figure 4.16 (b) defines the spurious wave amplitude based on second-order force control, $A_2^{(2s)}$, as a ratio of the corresponding value arising from first-order force control, $A_1^{(2s)}$. In this latter case, ratios less than unity define the relative merit of second-order force control.

According to the theory outlined in Part I, the amplitude of the spurious second-order wave should reduce to zero with the adoption of a second-order command signal. However, in practice the experimental error associated with the measurement of the water surface elevation becomes similar in magnitude to the spurious wave component, particularly as the wave frequency increases. For example, in wave case $f = 48/64Hz$ with a steepness of $Hk/2 = 0.16$ (table 1), the 10% dimensionless spurious wave ratio (figure 4.16 a) corresponds to $0.8mm$ of spurious wave amplitude. This is not substantially larger than the absolute experimental error of $\pm 0.5mm$ associated with the wave gauges.

It has already been noted in relation to the first-order force control experiments

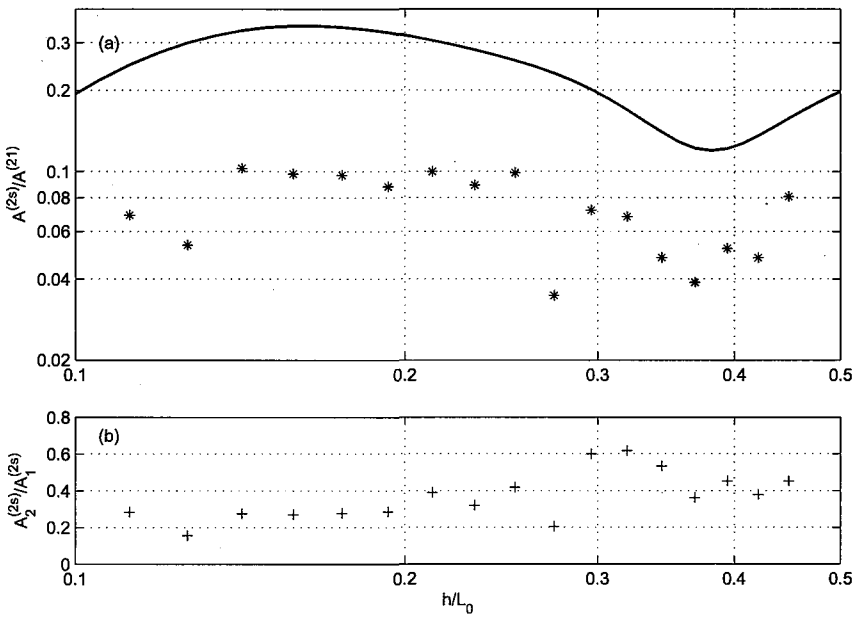


Figure 4.16: (a) Dimensionless, second-order, spurious wave content using second-order force control; —— First-order force-control theory (for reference), $*$ Second-order force-control experiment; (b) Ratio of spurious wave in second- and first-order force control experiment, $+$ $A_2^{(2s)}/A_1^{(2s)}$.

that the results are less satisfactory for higher frequencies. The results presented in figure 4.16 suggest that this is equally true for second-order force control. In addition to the arguments outlined in §4.15, the second-order correction may also be affected by the fact that the system's drive mechanics are not considered in the theoretical model; this includes the motor with mechanical inertia and electrical inductance, the gearing system with inertia and the power amplifier. These components will add a small phase shift to the compensation signal and this may become larger at higher frequencies. These effects will be considered in future work, but given the absolute magnitude of the second-order spurious wave in the higher frequency range they were not considered to be of primary importance to the present study.

Figures 4.17 to 4.20 show the wave profiles (or close-ups thereof) of two waves cases in which second-order force control has been applied successfully. Figure 4.17 concerns a wave frequency of $f = 34/64Hz$, with a steepness of $Hk/2 = 0.11$,

and compares the wave profile arising from (a) first-order force control and (b) second-order force control with the Stokes second-order solution. Although the data relating to first-order force control (figure 4.17 a) are in reasonable agreement with the Stokes solution (comparable to figure 4.12 b), some important departures remain. Whilst these are not entirely eliminated by the adoption of second-order force control, they are substantially reduced (figure 4.17 b); evidence of this being provided by the close-ups of the data records at locations (1)-(4) given in figure 4.18. Figures 4.19 and 4.20 provide a similar sequence of plots relating to a wave frequency of $f = 48/64Hz$ and a steepness of $Hk/2 = 0.16$. Once again, these results demonstrate that there is a small but noticeable improvement in the wave quality following the adoption of second-order force control.

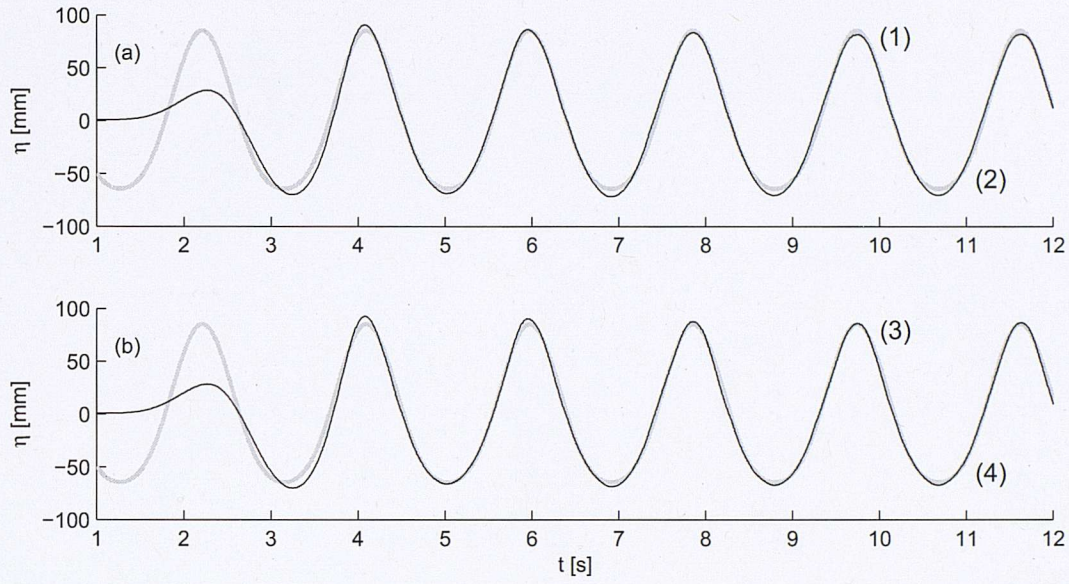


Figure 4.17: Surface elevation for wave case $f = 34/64Hz$, $Hk/2 = 0.11$; (a) First-order force control, (b) Second-order force control; —— Experiment, —— Second-order Stokes solution; Note: the numbers (1) to (4) refer to locations that are considered in detail in figure 4.18

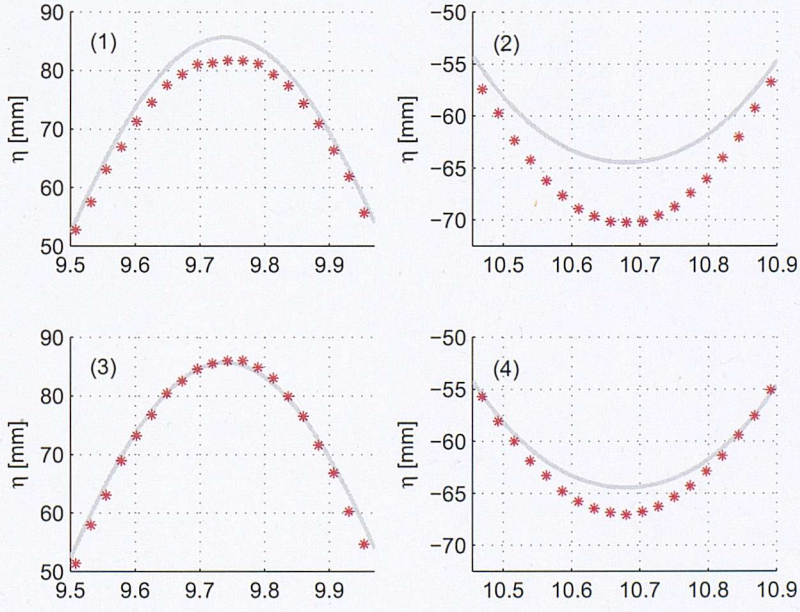


Figure 4.18: Close-up of the water surface elevation at locations (1) to (4) for wave case $f = 34/64Hz$, $Hk/2 = 0.11$ as labelled in figure 4.17; $*$ Experiment, —— Second-order Stokes solution

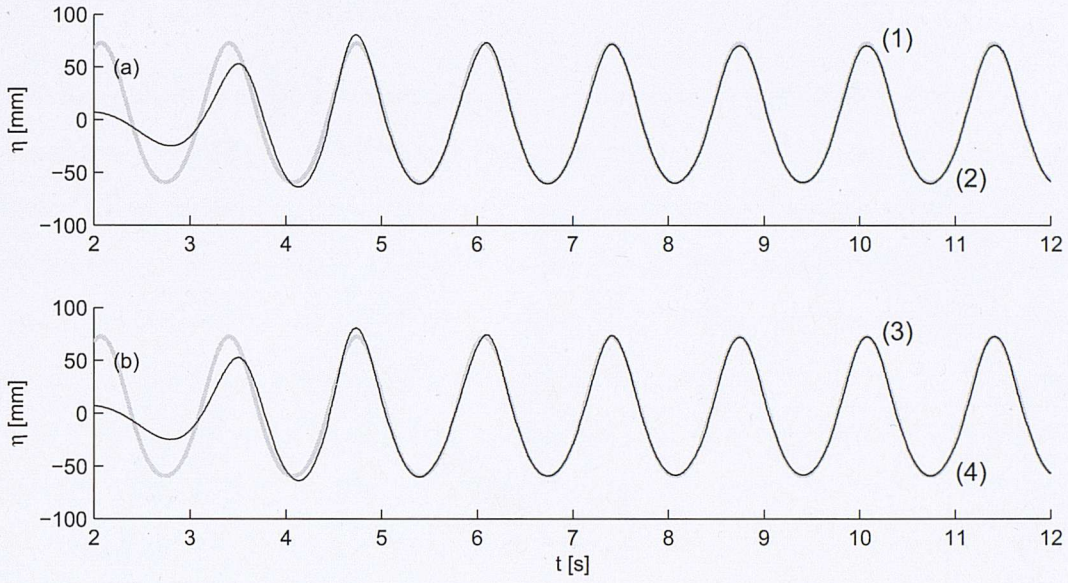


Figure 4.19: Surface elevation for wave case $f = 48/64Hz$, $Hk/2 = 0.16$; (a) First-order force control, (b) Second-order force control; —— Experiment, —— Second-order Stokes solution; Note: the numbers (1) to (4) refer to locations that are considered in detail in figure 4.20

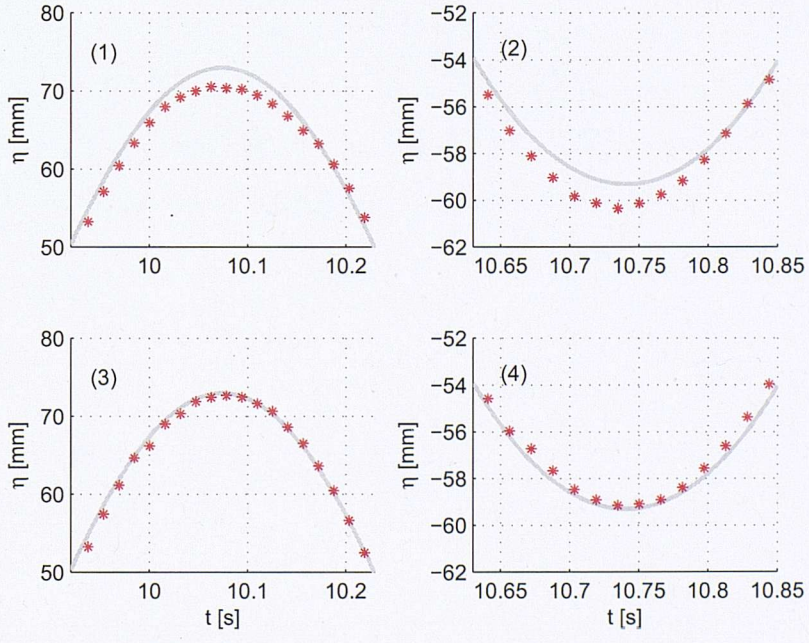


Figure 4.20: Close-up of the water surface elevation at locations (1) to (4) for wave case $f = 48/64Hz$, $Hk/2 = 0.16$ as labelled in figure 4.19; $*$ Experiment, —— Second-order Stokes solution

4.17 Conclusions

The force-feedback theory developed in Part I has been compared to experimental observations and three key features of the theory verified. First, active absorption based upon first-order impedance matching has been shown to work well over a broad frequency band, and especially for low frequencies where traditional passive absorbers perform poorly. Second, a bottom-hinged flap-type wave maker driven by first-order force control produces significantly smaller second-order spurious waves when compared to an identical wave maker driven by first-order position control. This highlights the inherent advantages of a system driven with force-feedback control. Third, the validity of a second-order correction signal has been proven, leading to a further significant reduction in the spurious wave content. However, in respect of the latter, some deviations from the theory remain for higher frequency waves and the model may need to be expanded to include the drive system's dynamics. Moreover, the influence of higher harmonics has not been investigated; the discussion being limited to second-order effects. Given the moderate steepness of the generated waves, this is regarded acceptable. Within the present chapter, these results were limited to flap-type wave makers generating regular waves. The next chapter will consider random or irregular waves and expands the analysis to address piston-type wave machines.

5

Nonlinear Wave Generation and Absorption Using Force-feedback Control: Piston-type Wave Machines and Irregular Waves

5.1 Chapter Overview

In the course of the PhD thesis, the behaviour of flap-type wave boards was investigated first. The incentive for this was the dominance of this type when considering the number of installed machines worldwide. The purpose of the present chapter is to apply the work presented in Chapters 3 and 4, effective wave absorption and consistent second-order control, to the operation of piston-type wave machines. In so doing, a second-order theory for piston-type board geometries incorporating a force based absorption controller is presented. In addition, the theory is applied, for the first time, to the generation of multi-component or irregular waves.

In accordance with Chapter 4, the present study is divided into two parts. Part I discusses the theoretical aspects of the work. First, the second-order spurious wave modes arising in position control are reviewed; this review being based upon the theory presented in Chapter 2. Subsequently, the hydrodynamic feedback path for a piston-type machine is investigated and all forces up to second order

are evaluated. Finally, the effect of the nonlinear feedback on the spurious modes is discussed in detail and a second-order compensation signal is derived.

In contrast, Part II of the present chapter provides an experimental verification of the key aspects of the developed theory. In particular, laboratory data will be provided to demonstrate that: (i) a very good absorption characteristic can be achieved over a wide range of frequencies, (ii) unlike for position-controlled wave machines, the start phase for each wave component needs to be modified to achieve a deterministic surface profile in the flume and (iii) applying a second-order force-control signal leads to a significant improvement in wave quality.

In presenting this data, some additional comments are made concerning the difficulties of overcoming the problem of spurious wave generation at the back of the immersed piston. Despite a rather complex paddle design, very good agreement between the developed theory and the experimental data is achieved.

Part I: A new Theory for Irregular Wave Generation

5.2 Introduction

Piston-type wave generators are well suited to relatively shallow water wave generation. Given that they produce a depth-uniform velocity profile, they provide an ideal match to the horizontal velocity under a progressive shallow water wave. This condition ensures that most of the board's motion results in the generation of a progressive wave mode; the evanescent modes being small in shallow water. The first-order progressive wave field and the evanescent mode distribution have already been illustrated in figure 2.4; with further information relating to shallow water conditions given in figure 2.5.

Historically, much of the work on second-order effects and spurious wave modes in laboratory wave generation has focused on piston-type machines (Madsen 1971, Ottesen-Hansen et al. 1980, Sand 1982, Schäffer 1996) and hence relatively shallow water conditions. This may be attributed to the fact that the nonlinear wave-wave interaction terms (including the wave self-interaction or Stokes terms) are more pronounced in shallow water. Furthermore, the relative magnitude of the spurious wave modes associated with first-order position control are also substantially larger accounting for 40% to 100% of the wave-wave interaction terms; evidence of this being provided by Sulisz & Hudspeth (1993).

Given the undoubted importance of these spurious wave modes, a theory for the operation of absorbing piston-type machines correct up to second order is developed. The effect of the second-order feedback is investigated for regular, bi-chromatic and irregular or random waves. In each of these cases, the second-order effects are shown to be significant; the theoretical aspects of the work being substantiated in an experimental study presented as Part H of this chapter.

5.3 Wave-wave Interaction

Thus far, only regular waves and their self-interaction or Stokes terms were considered (Chapter 4). However, the theory presented in Chapter 2 applies to the general case of irregular waves. Indeed, equations for both the wave-wave interaction potential, $\Phi^{(21)\pm}$, and the spurious wave potential arising due to the presence of the wave maker, $\Phi^{(22)\pm}$, were given. In both cases the definition of these terms is such that the superscript + denotes the super-harmonics and the superscript − denotes the sub-harmonics.

Within most of the figures in this thesis, the spurious free wave amplitude, $A^{(2s)\pm}$, is normalised with respect to the wave-wave interaction amplitude, $A^{(21)\pm}$. However, to illustrate the relative importance of the latter term in various water depths, figures 5.1 and 5.2 give a comparison of first- and second-order quantities. In both cases, the contours represent the dimensionless ratio of $A_{nm}^{(21)\pm}/(A_n^{(1)} + A_m^{(1)})$ evaluated for a steepness of $Hk/2 = 0.05$. The curves are directly based on equation (2.34) with only the progressive component ($j = 0$, $l = 0$) being considered. For each pair of terms (ω_n, ω_m) taken from the series of a N component wave spectrum, the wave-wave interaction term $A_{nm}^{(21)\pm}$ at $\omega_{nm}^{\pm} = \omega_n \pm \omega_m$ may be identified as the intersection of ω_n on the x-axis and ω_m on the y-axis, where both axes are expressed in terms of h/L_0 and L_0 is the deep water wave length corresponding to a given frequency. The terms n and m may be interchanged as the plots are symmetric about the x-y diagonal. Note that in this and all the following contour plots the colours shown correspond to a range of values as indicated on the adjacent colourbar.

In the context of first- and second-order quantities it is important to note that for a non-linearity factor of $S = 1$ (the limiting case for regular waves) the amplitude of the second-order term is one fourth of the primary wave amplitude. Adopting the same condition to the ratio of $A_{nm}^{(21)\pm}/(A_n^{(1)} + A_m^{(1)})$, all values exceeding 0.25 have been limited to 0.25. As a result, figures 5.1 and 5.2 also provide an indication of the limited range of applicability.

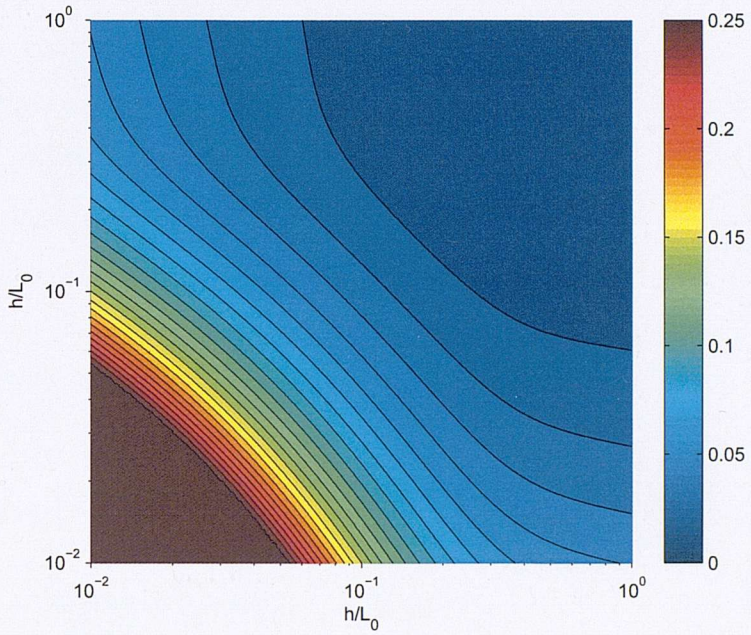


Figure 5.1: Contours defining the ratio of the second-order super-harmonic and the first-order amplitude, $A_{nm}^{(21)+}/(A_n^{(1)}+A_m^{(1)})$, evaluated for a steepness of $Hk/2 = 0.05$

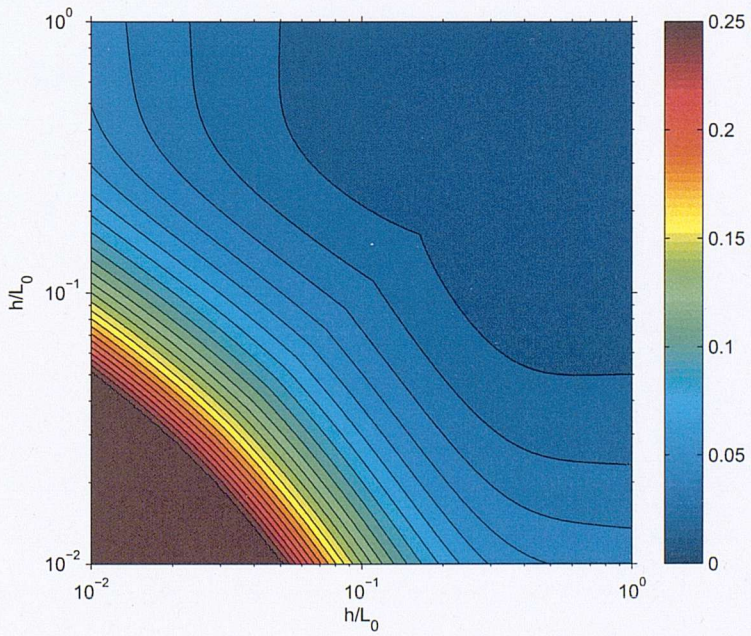


Figure 5.2: Contours defining the ratio of the second-order sub-harmonic and the first-order amplitude, $A_{nm}^{(21)-}/(A_n^{(1)}+A_m^{(1)})$, evaluated for a steepness of $Hk/2 = 0.05$

The contours lines given in both figures are provided at equally spaced intervals. As the water depth reduces, the ratio of first- and second-order quantities increases significantly; the rate of increase being indicated by the decreasing spacing between adjacent contour lines. This applies to both, the super-harmonic and the sub-harmonic amplitudes alike. When considering the dimensionless ratio of $A_{nm}^{(2s)\pm}/A_{nm}^{(21)\pm}$ in the following discussion, the increase in the absolute magnitude of both terms must be borne in mind. Furthermore ,to improve the clarity of both text and figures, the subscripts (n, m) are omitted hereafter.

5.4 Application of Position-control Theory

This section illustrates the results of the second-order theory presented in Chapter 2 and seeks to explain the importance of the spurious wave modes arising from first-order position control. All graphs are based on the operation of a piston-type wave machine. The effect of the nonlinear hydrodynamic feedback introduced in force control is omitted until Section 5.5.

5.4.1 Regular Waves

In the special case of regular wave generation, a single super-harmonic at twice the fundamental frequency arises and the sub-harmonic represents a mean or time-averaged term. Figure 5.3 shows the dimensionless ratio between the spurious free wave amplitude, $A^{(2s)+}$, and the second-order wave-wave interaction amplitude, $A^{(21)+}$, at some distance from the wave board; the curve being based on equations (2.28) and (2.31).

For full depth piston-type wave machines ($l = \infty$, $d = 0$), this ratio varies between approximately 0.4 and 0.96 for the range shown; the largest values occurring in shallow water. Given the discussion in the previous section, this is of very significant practical interest since piston-type wave machines are most commonly employed in the shallow water regime where the wave-wave interaction terms may

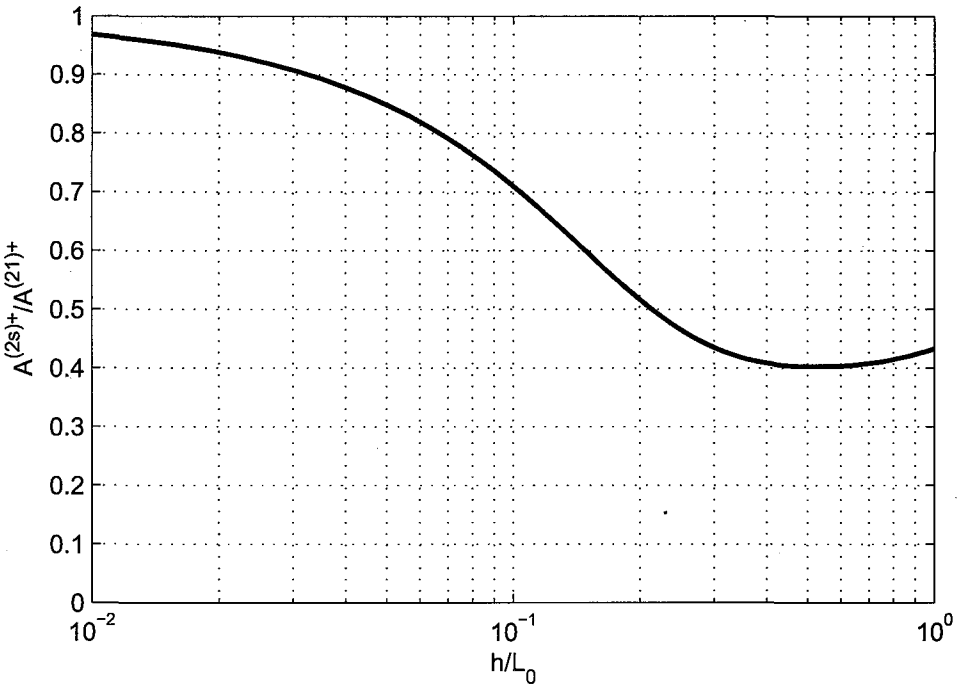


Figure 5.3: Dimensionless spurious wave content, $A^{(2s)+}/A^{(21)+}$, based on first-order position control and the operation of a piston-type wave machine

become very large (figure 5.1). The curve given in figure 5.3 may be directly related to figure 4.1; the latter giving the equivalent theory for flap-type wave machines. For a direct comparison between different wave board geometries the reader is directed to Sulisz & Hudspeth (1993).

5.4.2 Irregular Waves

Figures 5.4 and 5.5 present the spurious super- and sub-harmonic terms arising due to the interaction of two waves at different frequencies in the presence of the wave maker; the magnitude of the normalised spurious terms being presented as a contour plot of $A^{(2s)\pm}/A^{(21)\pm}$. Relating the super-harmonic terms given in figure 5.4 to the previous discussion, the single line shown within figure 5.3 represents the diagonal values corresponding to $n = m$. To put this normalized ratio into context, the absolute values for the wave-wave interaction amplitude given in figure 5.1 should be considered.

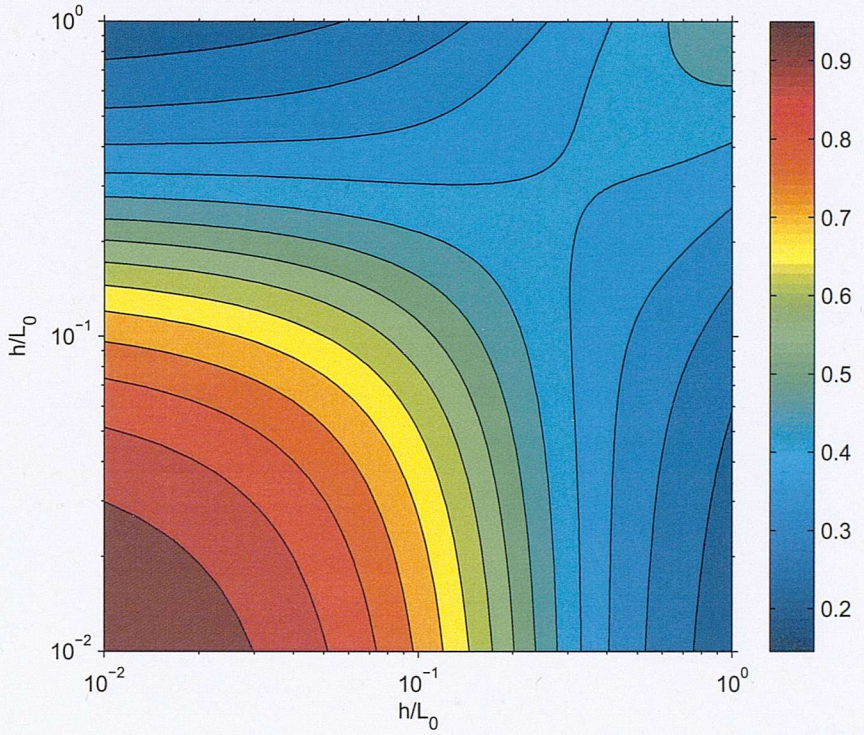


Figure 5.4: Dimensionless spurious super-harmonic content, $A^{(2s)+}/A^{(21)+}$, based on first-order position control and the operation of a piston-type wave machine

Within figure 5.4, the largest terms occur in shallow water conditions where the magnitude of the free mode may be up to 0.9 times the magnitude of the bound interaction term. Given the large absolute values of the bound modes in shallow water, this corresponds to a large spurious wave which is of significant practical importance.

In accordance with the presentation of the super-harmonic terms, figure 5.5 shows the spurious sub-harmonic amplitude, $A^{(2s)-}$, normalized with respect to the bound mode amplitude, $A^{(21)-}$. Absolute values for $A^{(21)-}$ were previously given in figure 5.2. As before, the largest relative values occur in shallow water conditions and are of comparable magnitude to the spurious super-harmonics in this regime.

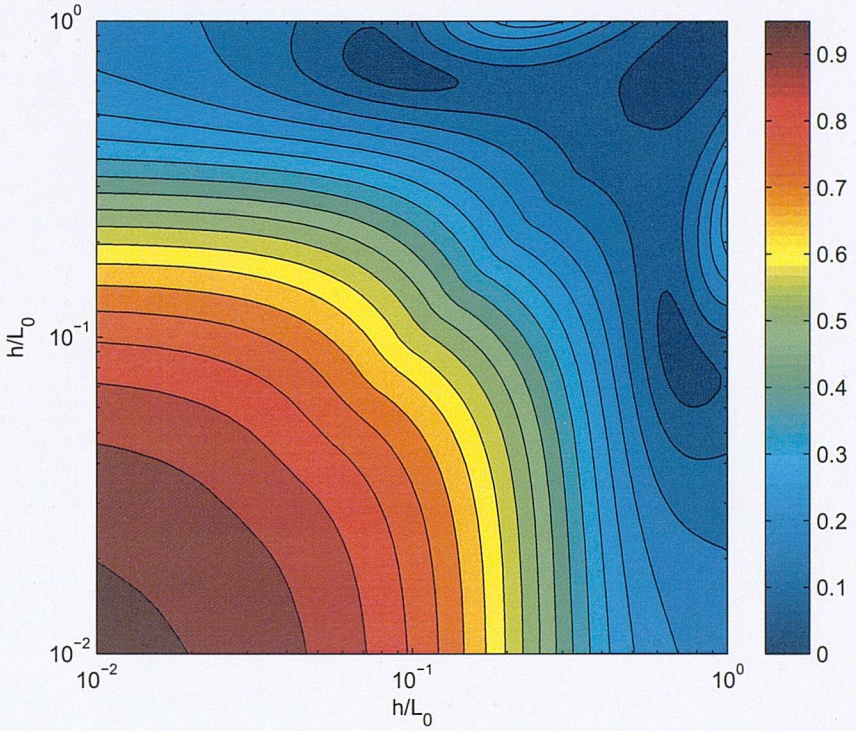


Figure 5.5: Dimensionless spurious sub-harmonic content, $A^{(2s)-}/A^{(21)-}$, based on first-order position control and the operation of a piston-type wave machine

5.5 Application of Force-control Theory

This section investigates the effect of the nonlinear hydrodynamic feedback for piston-type wave machines. The absorption strategy for the flap-type wave machines presented in Chapter 4 is based on controlling the applied torque and the wave board's angular velocity. In contrast, absorbing piston-type wave makers utilize the applied force and the board's translational velocity.

5.5.1 Forces at First and Second Order

In order to derive the total hydrodynamic force acting on a piston-type machine, Bernoulli's equation (4.1) is again evaluated on the wave board and integrated over depth. This procedure is very similar to that presented for flap-type machines (Section 4.4.3); the only difference being the lever arm in the flap case.

Within the present study, interest lies in forces up to second order; terms of

higher order being neglected. Separating the total wave-induced force into its first- and second-order components gives

$$F_{\Phi}^{(1)} = -\int_{-h+d}^{0} \rho \frac{\partial \Phi^{(1)}}{\partial t} dz \tag{5.1}$$

and

$$F_{\Phi}^{(2)} = -\int_{0}^{\eta^{(1)}} \rho g z dz - \int_{0}^{\eta^{(1)}} \rho \frac{\partial \Phi^{(1)}}{\partial t} dz - \int_{-h+d}^{0} \frac{\rho}{2} \left(\frac{\partial \Phi^{(1)}}{\partial x} \right)^2 dz$$
$$- \int_{-h+d}^{0} \frac{\rho}{2} \left(\frac{\partial \Phi^{(1)}}{\partial z} \right)^2 dz - \int_{-h+d}^{0} \rho \frac{\partial \Phi^{(21)}}{\partial t} dz - \int_{-h+d}^{0} \rho \frac{\partial \Phi^{(22)}}{\partial t} dz, \tag{5.2}$$

where the subscript Φ indicates wave-induced quantities and the superscript () denotes the order of the term involved. All forces are derived as forces per unit paddle width. Further details concerning the derivation of these second-order results are given in Appendix C. The total wave-induced force at first order, equation 5.1, evaluates to

$$F_{\Phi}^{(1)} = \frac{1}{2} \left\{ \rho g X_a \sum_{j=0}^{\infty} \frac{c_j}{k_j} \frac{\sinh k_j h - \sinh k_j d}{\cosh k_j h} e^{i\omega t} + c.c. \right\}. \tag{5.3}$$

This term has already been evaluated within Chapter 3 where the absorption characteristic of the machine was considered. Chapter 3 also identified two coefficients related to this force: the added mass, $m(\omega)$ given in equation (3.24), and the hydrodynamic damping, $d(\omega)$ given in equation (3.25). In contrast to the ideal wave machines discussed in Chapter 3, the present work concerns physical wave machines. The equation of motion for such devices being given by

$$[M + m(\omega)]\ddot{X} + d(\omega)\dot{X} + kX = F, \tag{5.4}$$

where the additional terms represent the wave board's mass (M) and the spring rate (k) of the machine. This spring rate is dependent upon the exact geometry of the wave board and will be discussed where appropriate.

5.5.2 Nonlinear Feedback and Second-order Correction

Following the discussion presented in Chapter 4, the hydrodynamic feedback path affects the machine's behaviour at second order. The second-order force on the wave paddle, $F_{\Phi}^{(2)}$, acts as an additional input to the controller and imposes a wave board motion at second order. This motion creates a free travelling wave in addition to that evaluated as $\eta^{(22)\pm}$ arising from $\Phi^{(22)\pm}$. Adopting the notation as presented in Chapter 4, the wave board motion due to the nonlinear feedback may be expressed by

$$X_{1,nm}^{(2)\pm} = H_s(\omega_{nm}^{\pm}) F_{\Phi,nm}^{(2)\pm} \tag{5.5}$$

where $H_s(\omega_{nm}^{\pm})$ is the system's transfer function evaluated at $\omega_{nm}^{\pm} = \omega_n \pm \omega_m$ and $F_{\Phi,nm}^{(2)\pm}$ is the hydrodynamic second-order force. For piston-type machines the transfer function is given as the ratio of wave board position and demand force

$$H_s(\omega) = \frac{X(\omega)}{F_d(\omega)} \tag{5.6}$$

and incorporates both the absorption filter and the hydrodynamic feedback path.

In seeking an expression for the correction force required to eliminate the second-order spurious wave, $\eta^{(22)\pm}$, a procedure similar to that outlined in §4.8 is applied. This yields the second-order correction force as

$$F_{c,nm}^{(2)\pm} = \frac{F^{\pm} A_n A_m^{-*}}{h H_s(\omega_{nm}^{\pm})} - F_{\Phi,nm}^{(2)\pm}. \tag{5.7}$$

Observing this equation, it is important to note that $F^{\pm}$ must not be confused with a force term, but is the transfer function derived by Schäffer (1996) given in Appendix A. Applying the force $F_{c,nm}^{(2)\pm}$ as an additional input to the machines controller eliminates the freely travelling unwanted wave $\eta^{(22)\pm}$. Within the following discussion the effect of the nonlinear feedback is considered. The benefits of applying the second-order force correction term are outlined in the experimental investigation presented in Part II of this chapter.

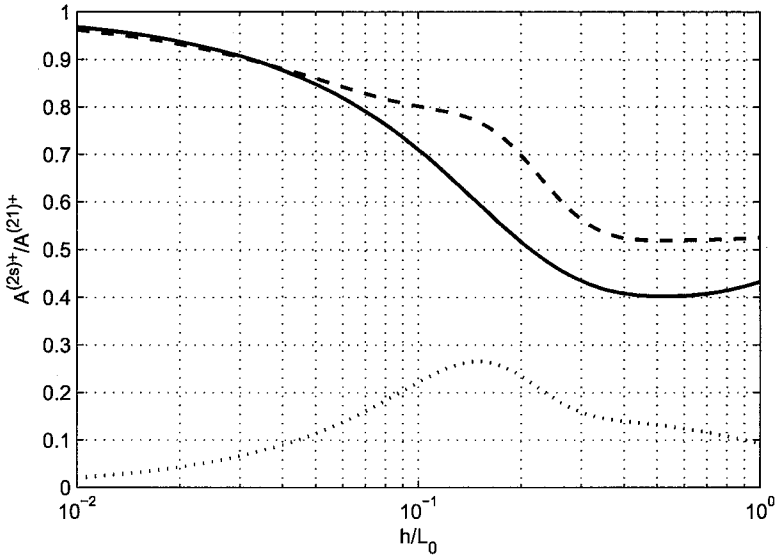


Figure 5.6: Dimensionless spurious wave content, $A^{(2s)+}/A^{(21)+}$, for regular waves and the operation of a piston-type machine; —— First-order position control, – – First-order force control, · · · · Nonlinear hydrodynamic feedback alone

5.5.3 Second-order Effects for Regular Waves

Figure 5.6 shows the theoretical second-order spurious wave content for the piston-type machine used in the experimental study presented in Part II of this chapter. Further details concerning the machine's geometry and absorption filter implementation are given later on. The graph is evaluated for the generation of regular waves only and a direct comparison to the spurious wave content in position control is made. Moreover, the additional free wave content introduced by the nonlinear feedback is shown.

Comparing figure 5.6 with figures 4.4 and 4.5, the latter two figures giving the corresponding data for flap-type wave makers, an interesting result is seen. In both flap cases the theoretical spurious wave content in first-order force control is significantly reduced when compared to first-order position control. This characteristic clearly indicates that the additional force-induced second harmonic partially cancels with the geometry related spurious free wave. Considering the data in figure 5.6, it is apparent that, unlike for flap-type wave machines, the spurious wave content in first-order force control is not reduced when compared to

first-order position control; the additional free wave due to $F_{\Phi}^{(2)+}$ is superimposed on, or adds to, the magnitude of the spurious free wave in position control. In contrast to flap-type machines, the spurious wave content is now significant and a first-order force control signal is not adequate. As a result, consistent second-order correction for force-controlled piston-type wave machines is very important and needs to be properly formulated.

5.5.4 Second-order Effects for Irregular Waves

Given the importance of the free super-harmonic term when generating regular waves, the spurious modes arising as a result of the interaction of waves at different frequencies must also be investigated. Figure 5.7 shows the spurious super-harmonic amplitude, $A^{(2s)+}$, normalised with respect to the wave-wave interaction amplitude, $A^{(21)+}$. Comparing this figure to the earlier results concerning first-order position control (figure 5.4) confirms the findings for regular waves; far from improving the quality of the generated waves a significant amount of additional spurious wave content is introduced in force control. Indeed, the dimensionless ratio of $A^{(2s)+}/A^{(21)+}$ is in the order of 0.5 for deep water and reaches values of up to 0.9 in shallow water. In particular, the values for deep water and intermediate water are larger than those arising in equivalent position-controlled machines.

Figure 5.8 shows the sub-harmonic terms based on first-order force control. Observing this figure in detail, these free long wave components are small for the interaction of two waves in the deep water range but become large as the water depth reduces.

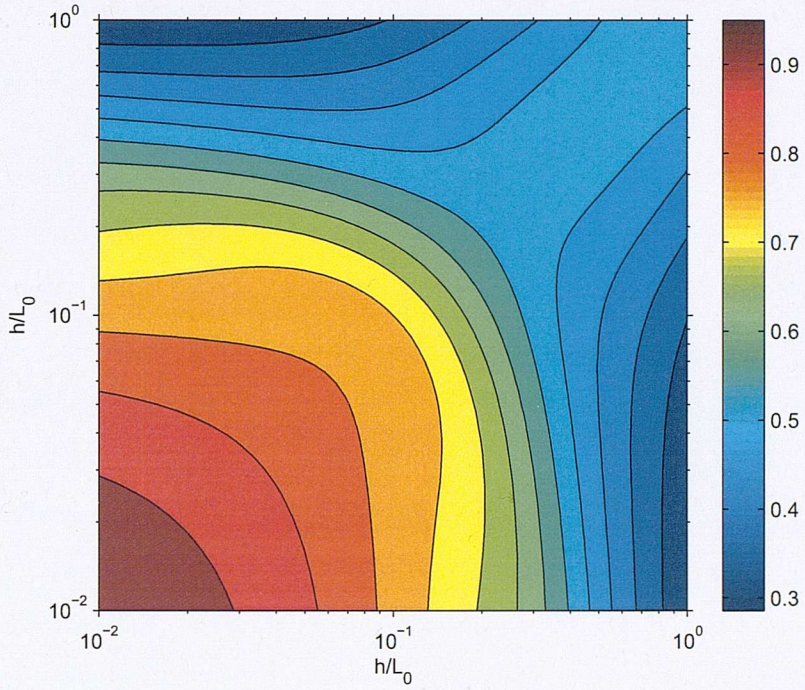


Figure 5.7: Dimensionless spurious super-harmonic content, $A^{(2s)+}/A^{(21)+}$, based on first-order force control and the operation of a piston-type wave machine

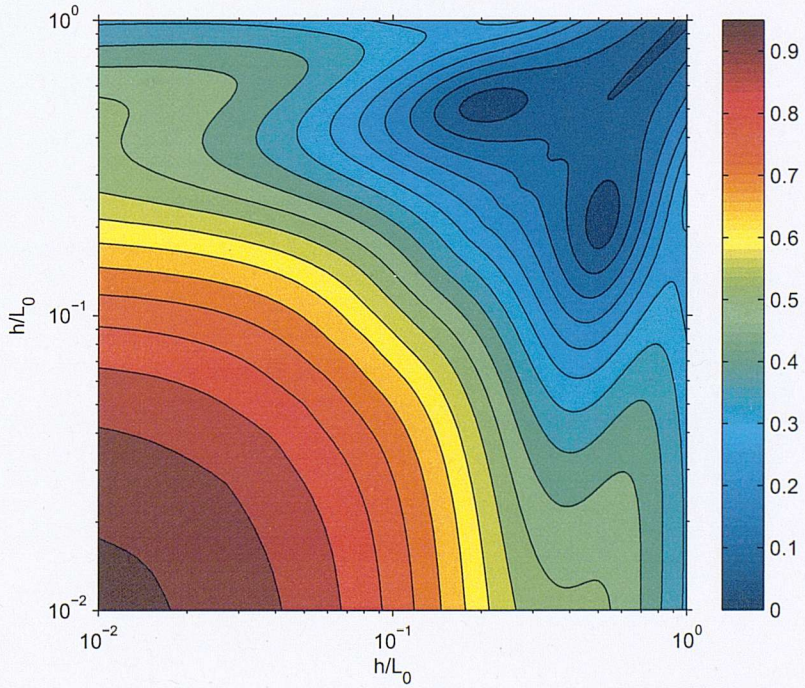


Figure 5.8: Dimensionless spurious sub-harmonic content, $A^{(2s)-}/A^{(21)-}$, based on first-order force control and the operation of a piston-type wave machine

5.6 Comparison of First-order Position and First-order Force Control

Thus far, the spurious modes have been presented as non-dimensional quantities. To further illustrate their importance, dimensional data is presented as part of a direct comparison between position control and force control. At this stage the data is evaluated from the proposed solutions and relates to a piston-type wave machine operating at a water depth of $h = 0.6m$. Both regular waves and a JONSWAP spectrum are considered. In addition, the effects arising from a pseudo-random generation technique for irregular waves are investigated. This latter investigation has important implications for the experimental validation presented in Part II.

5.6.1 Regular Waves

Figure 5.6 illustrated the spurious wave effects for a wide range of wave frequencies. To illustrate the relative importance of these terms, three values of h/L_0 are considered in detail. For small values of h/L_0, the effect of the nonlinear hydrodynamic feedback is small. A wave case with $h/L_0 = 0.05$ is chosen to represent this regime. In contrast, the departure between position and force control increases significantly with increasing values of h/L_0. To represent both the intermediate water regime and the deep water regime, values of $h/L_0 = 0.15$ and $h/L_0 = 0.5$ were chosen.

The presence of free and bound modes creates an interference pattern at second harmonic. Figure 5.9 (a) - (c) illustrates this pattern for the three cases noted above and directly compares position and force control. The curves presented are evaluated as the time averaged ratio of $\overline{(A^{(2s)} + A^{(21)})/A^{(21)}}$. The time averaging ensures that the combined amplitude will be fixed for a particular location. However, this value will vary over space. In the non-dimensional form given, a value of 1.0 corresponds to a second-harmonic content equal to that of the bound

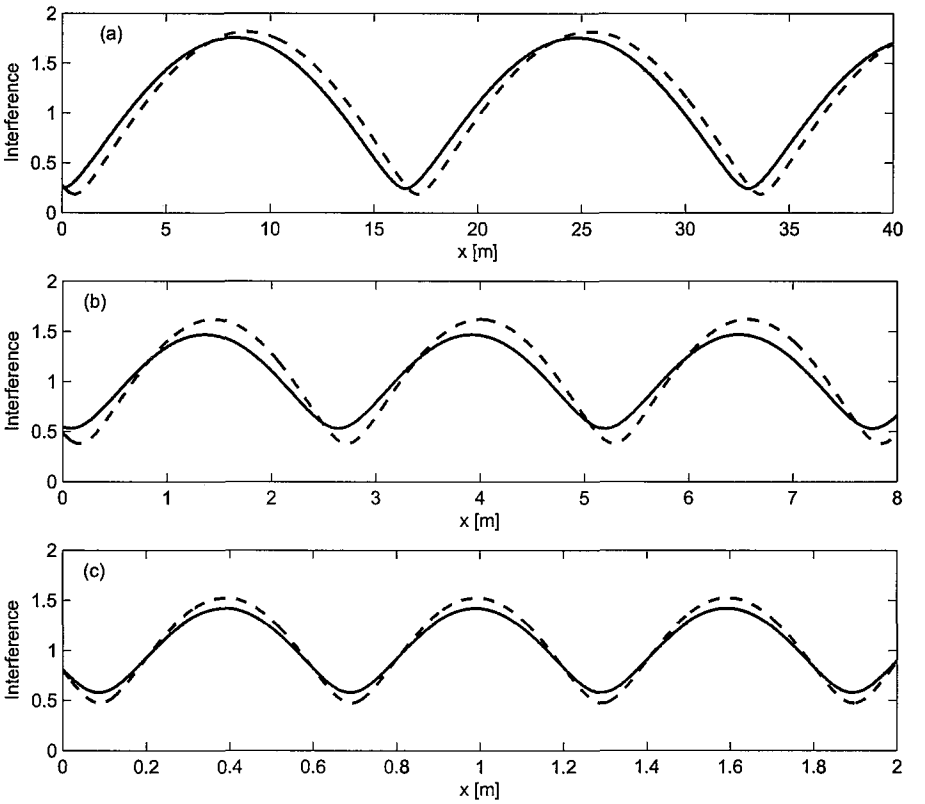


Figure 5.9: Time averaged spatial interference pattern arising from the bound and free travelling harmonics at second order, $\overline{(A^{(2s)} + A^{(21)})/A^{21}}$, evaluated for $h = 0.6m$; (a) $f = 23/64Hz$ $(h/L_0 = 0.05)$, (b) $f = 40/64Hz$ $(h/L_0 = 0.15)$ and (c) $f = 73/64Hz$ $(h/L_0 = 0.5)$; —— First-order position control, – – First-order force control

harmonic content alone. For ratios smaller than 1.0, too little second-harmonic content is present at the particular location. Based on this interference pattern, spatial locations in close proximity to the maxima and minima observed in figure 5.9 (a) - (c) are chosen for each wave case. The small phase and amplitude difference between position control and force control arises due to the presence of the additional free wave in the force controlled case.

The wave case illustrated in figure 5.10 corresponds to a value of $h/L_0 = 0.05$. A steepness of $Hk/2 = 0.055$ was adopted to represent a non-linearity value of $S = 1$ (the limiting case for regular waves). The surface profile shown in sub-plot (a) is evaluated at $x = 8.5m$, representing the first maximum of the

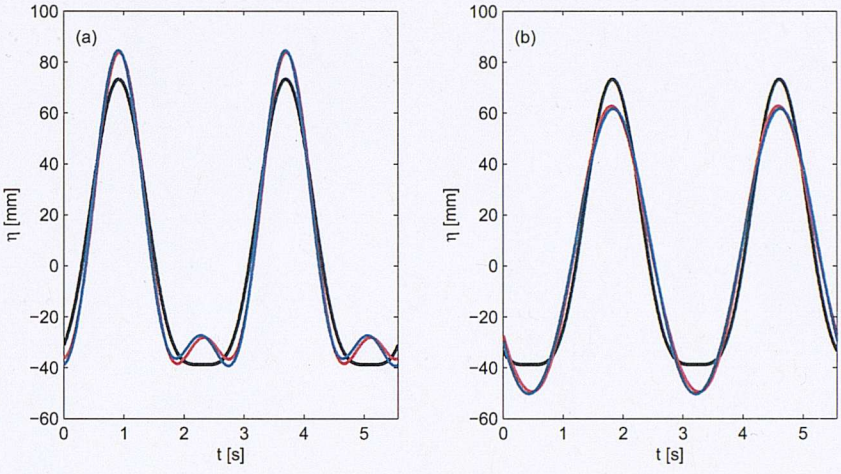


Figure 5.10: Surface profile evaluated for $h = 0.6m$, $f = 23/64Hz$ $(h/L_0 = 0.05)$ and $Hk/2 = 0.055$ $(S = 1)$; —— Second-order Stokes solution, —— First-order position control, —— First-order force control; (a) $x = 8.5m$, (b) $x = 17m$

spatial interference pattern (figure 5.9 a). In contrast, sub-plot (b) shows the surface profile at $x = 17m$ corresponding to a distinctive minimum in total second-harmonic content. Comparing the two sub-plots directly, a significant difference between the two spatial locations is observed. This has a considerable effect on the experimental testing environment. A model placed at $x = 8.5m$ (figure 5.10 a) would be exposed to a wave with much larger second harmonic content when compared to $x = 17m$ (figure 5.10 b). This is particularly relevant with respect to: (i) the maximum crest elevation and (ii) the dynamic response of a fixed or oscillating body subjected to waves.

The wave case presented in figure 5.11 corresponds to a value of $h/L_0 = 0.15$. As before, two spatial locations are shown, representing the maximum (sub-plot (a), $x = 1.4m$) and minimum (sub-plot (b), $x = 2.7m$) second-harmonic content. It is important to note that the spurious wave effect is of comparable magnitude to that observed in the previous case. This is despite the fact that the steepness has been increased to $Hk/2 = 0.2$; nearly fourfold the previous one. The similarity in terms of non-linearity is also reflected by a comparable value of S ($S = 1$ in the former and $S = 0.85$ in the latter case).

Finally, a deep water wave case $(h/L_0 = 0.5)$ is considered in figure 5.12. As

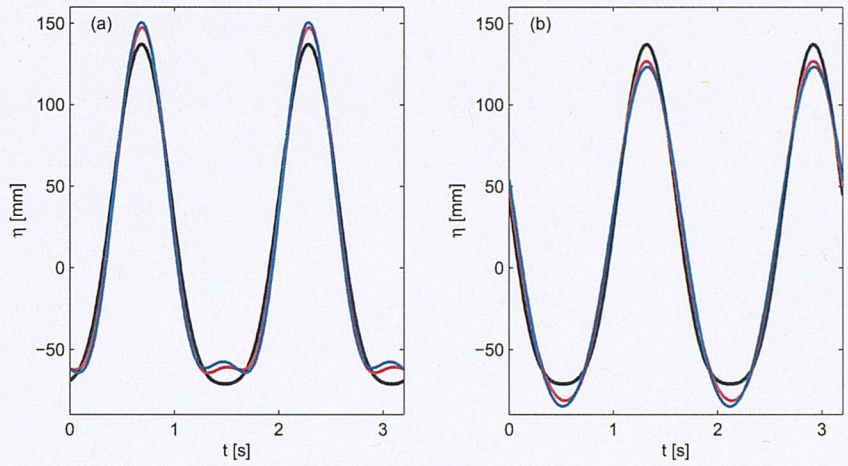


Figure 5.11: Surface profile evaluated for $h = 0.6m$, $f = 40/64Hz$ $(h/L_0 = 0.15)$ and $Hk/2 = 0.2$ $(S = 0.85)$; —— Second-order Stokes solution, —— First-order position control, —— First-order force control; (a) $x = 1.4m$, (b) $x = 2.7m$

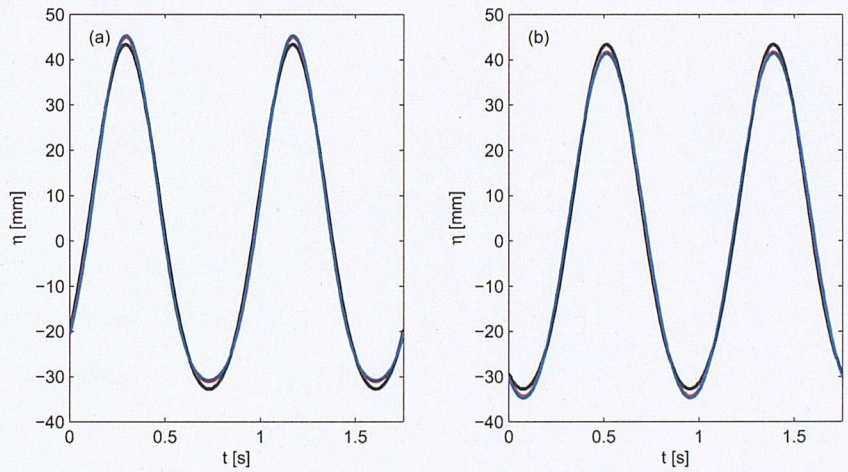


Figure 5.12: Surface profile evaluated for $h = 0.6m$, $f = 73/64Hz$ $(h/L_0 = 0.5)$ and $Hk/2 = 0.2$ $(S = 0.4)$; —— Second-order Stokes solution, —— First-order position control, —— First-order force control; (a) $x = 0.4m$, (b) $x = 0.7m$

before, a steepness of $Hk/2 = 0.2$ has been adopted. In contrast to the previous case, the non-linearity factor is reduced significantly $(S = 0.4)$. The relatively small spurious wave effect observed at both locations reflects this decrease in non-linearity. Overall, it is important to note that the magnitude of the second-order effects is not only a function of wave steepness but, to a large extent, dependent upon the relative water depth.

5.6.2 Irregular waves

In the most realistic laboratory wave testing, multi-component or irregular wave spectra are generated. A commonly adopted energy distribution, $S_{\eta\eta}(\omega)$, is given by the JONSWAP spectrum which may be expressed as

$$S_{\eta\eta}(\omega) = \frac{\alpha g^2}{\omega^5} e^{-\frac{5}{4}\left(\frac{\omega_p}{\omega}\right)^4} \gamma^{\beta}, \tag{5.8}$$

where β is defined as

$$\beta = e^{-\frac{(\omega-\omega_p)^2}{2\sigma^2\omega_p^2}}, \tag{5.9}$$

with

$$\sigma = \begin{cases} 0.07 & \text{for } \omega \leq \omega_p \\ 0.09 & \text{for } \omega > \omega_p. \end{cases} \tag{5.10}$$

Furthermore, g is the acceleration due to gravity, $\omega_p = 2\pi f_p$ is the circular peak frequency and γ is the peak enhancement factor.

Like many other spectra, the JONSWAP energy distribution is a fit to field data and there is an ongoing debate whether such a modelling approach correctly accounts for higher order wave effects. In the context of the present study, all components included in $S_{\eta\eta}(\omega)$ are regarded as freely propagating first-order waves. As a result, all components contributing to $S_{\eta\eta}(\omega)$ correspond to the terms $A_n^{(1)}$ and $S_{\eta\eta}(\omega)$ will subsequently be referred to as the *'first-order spectrum'*. In contrast, the term *'ideal second-order spectrum'* is used to refer to the combination of the freely propagating waves, $A_n^{(1)}$, and the bound wave-wave interaction terms arising at second order, $A_{nm}^{(21)\pm}$.

The first-order spectrum is shown in figure 5.13 and was evaluated in the range of $f_{min} = 16/64Hz$ to $f_{max} = 96/64Hz$ with a peak frequency of $f_p = 32/64Hz$ and a peak enhancement factor of $\gamma = 3.3$, the latter being a commonly adopted value. In defining the spectrum, the last five wave components were reduced linearly to zero to avoid a discontinuity in the tail of the spectrum. Furthermore, the spectrum was computed at discrete frequencies with a spacing of $\Delta f = 1/64Hz$.

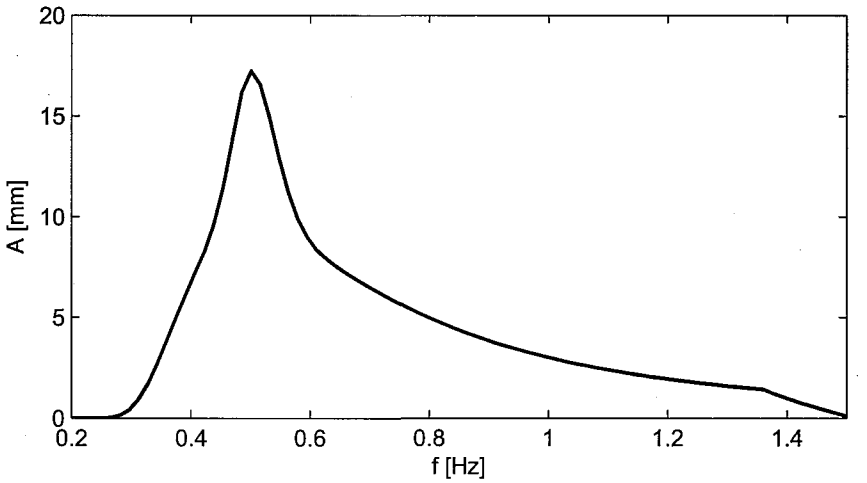


Figure 5.13: First-order JONSWAP amplitude spectrum with peak enhancement factor $\gamma = 3.3$, peak frequency $f_p = 32/64Hz$ and gain $\alpha = 0.001$

With all frequency components being periodic within a time frame of $T_r = 64s$, the entire spectrum is periodic in this interval; the time frame, T_r, often being referred to as the *repeat time.*

Assuming the absence of reflections, the first-order spectral content (figure 5.13) is constant throughout the wave flume, including the distribution of wave energy in the tail of the wave spectrum. This is in marked contrast to the ideal theoretical second-order spectrum ($A^{(1)}+A^{(21)}$) presented in figure 5.14 and shown for three spatial locations, $x_1 = 2m$, $x_2 = 4m$ and $x_3 = 10m$. The variation of the amplitudes observed in this latter plot may seem counter-intuitive at first sight and requires further consideration. In the laboratory, each primary wave component is generated with a random start phase which remains constant throughout the experiment.[1] The phasing of the second-order components is directly related to this start phase. This is evident when observing the expression for the second-order potential $\Phi^{(21)\pm}$ given in Chapter 2, equation (2.34).

As a direct result of applying discrete uniformly spaced frequencies ($\Delta f = 1/64Hz$), each bin in the frequency domain carries information for a number of

[1]In generating random sea states it is important to note that a best possible representation of a real sea state should incorporate both random phase and random amplitude. However, for the purpose of the present study, in which we are seeking to examine and improve the performance of the wave generation and absorption, it is sufficient to incorporate random phases alone.

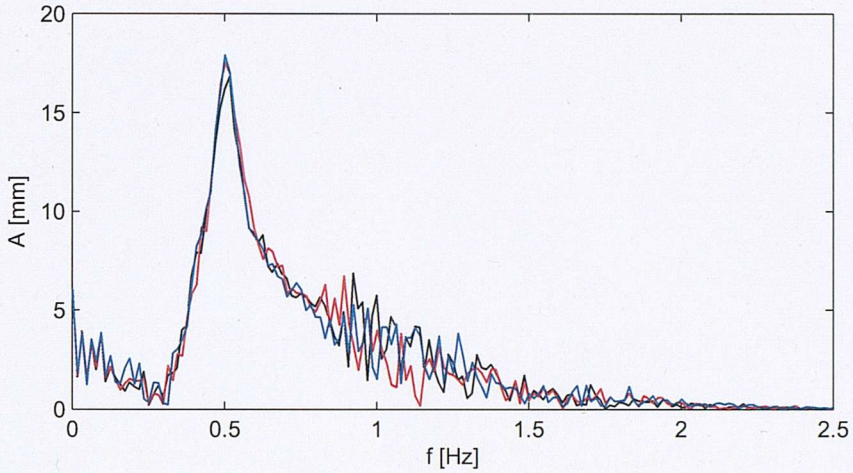


Figure 5.14: Ideal second-order JONSWAP amplitude spectrum $(A^{(1)} + A^{(21)})$ with $\gamma = 3.3$, $f_p = 32/64Hz$ and $\alpha = 0.001$; — $x_1 = 2m$, — $x_2 = 4m$, — $x_3 = 10m$

wave-wave interaction terms. As an example, the bin at $f = 1.25Hz$ or $f = 80/64Hz$ represent the super-harmonic term for the interaction of components $(40/64Hz$ and $40/64Hz)$, $(39/64Hz$ and $41/64Hz)$, $(38/64Hz$ and $42/64Hz)$ and so forth. Assuming that the majority of these interaction terms are approximately in phase at one spatial location, they would superimpose creating a large spike at one frequency bin. On the contrary, a scenario where they would cancel out is also possible. In reality, this superposition depends on the initial random phase of the primary wave components.

This concept is further examined in figure 5.15 where the same spectrum as before has been evaluated at a single spatial location, $x = 2m$. In contrast to the previous figure, the various curves illustrated in figure 5.15 represent several computational runs; the start phasing of the first-order components being randomised each time. As a result, the second-order components also change their phasing creating different patterns of superposition.

The above considerations have obvious implications for the experimental verification of the theory: for a representative study, the same spectrum needs to be run a number of times, each run having a unique random phase with uniform distribution. The averaged spectrum may then be evaluated to give a true repre-

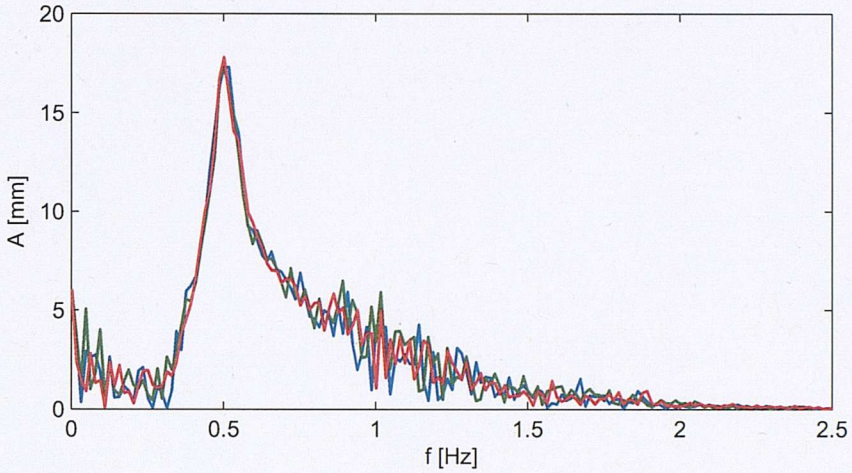


Figure 5.15: Ideal second-order JONSWAP amplitude spectrum $(A^{(1)} + A^{(21)})$ with $\gamma = 3.3$, $f_p = 32/64Hz$ and $\alpha = 0.001$; three runs with independent and random start phasing computed at $x = 2m$

sentation of the second-order spectral content. This process is complicated even further if reflections are present in the flume. Numerical simulations have shown that in the order of 100 runs are required to achieve a satisfactory smoothness in the spectral representation.

Alternatively, the surface elevation may be compared qualitatively to the theoretical solution. This latter approach is adopted in the experimental investigation presented as Part II of this chapter. Moreover, some common spectral properties may be considered. The spectral properties for the wave cases investigated within figure 5.15 are shown in table 5.1.

For all three runs the following properties are presented: average up-crossing period (T_z), significant wave height (H_s), maximum wave height (H_{max}), maximum crest elevation (η_{max}) and maximum surface slope ($\dot{\eta}_{max}$). These properties are evaluated for four different computations based on the proposed solutions of: (i) first order, (ii) ideal second order, (iii) first-order position control and (iv first-order force control.

Observing table 5.1 the values for T_z and H_s are seen to be very similar for all three runs. This is in marked contrast to the values for η_{max}. The departure between the ideal second-order solution and the computation including the spuri-

Quantity		First order	Ideal second order	Position control	Force Control
			Run 1		
T_z	$[s]$	1.652	1.694	1.605	1.604
H_s	$[m]$	0.146	0.149	0.149	0.149
H_{max}	$[m]$	0.190	0.189	0.194	0.197
η_{max}	$[m]$	0.092	0.102	0.115	0.116
$\dot{\eta}_{max}$	$[m/s]$	0.412	0.483	0.499	0.520
			Run 2		
T_z	$[s]$	1.659	1.671	1.611	1.617
H_s	$[m]$	0.146	0.162	0.163	0.164
H_{max}	$[m]$	0.190	0.199	0.219	0.224
η_{max}	$[m]$	0.092	0.143	0.155	0.154
$\dot{\eta}_{max}$	$[m/s]$	0.412	0.706	0.717	0.710
			Run 3		
T_z	$[s]$	1.651	1.823	1.729	1.725
H_s	$[m]$	0.146	0.149	0.149	0.149
H_{max}	$[m]$	0.190	0.179	0.179	0.174
η_{max}	$[m]$	0.092	0.106	0.114	0.116
$\dot{\eta}_{max}$	$[m/s]$	0.412	0.652	0.666	0.685

Table 5.1: Spectral properties for JONSWAP amplitude spectrum with $\gamma = 3.3$, $f_p = 32/64Hz$ and $\alpha = 0.001$; three runs with independent and random start phasing computed at $x = 2m$

ous modes is in the order of 10% for all three cases. These departures increase to approximately 20% when compared to the first-order computation.

Part II: An Experimental Verification of Irregular Wave Generation

5.7 Introduction

The first part of this chapter, referred to as Part I, discussed a new theory concerning the generation and absorption of irregular waves using piston-type machines. In fact, most of the underlying theory had been presented in Chapter 4 where the focus was set on flap-type wave machines subjected to regular waves. The major conclusions related to flap-type wave machines were:

i. A very good absorption characteristic can be achieved over a wide range of frequencies.

ii. A first-order transfer function has been established; this transfer function has the potential to replace or, at the very least, provide a starting point for an empirical flume calibration.

iii. The wave quality when applying a first-order force control signal is very good. Indeed is was so good that second-order correction may often not be required. Nevertheless, in some cases applying a second-order force-control signal showed a further enhancement in the wave quality.

With the expansion of the theory in Part I, these key factors (absorption characteristic, first-order transfer function and second-order control) remain important and require experimental verification. With the current chapter building upon the previous work, some aspects are not repeated herein. This, in turn, allows other more important aspects to be thoroughly discussed. As an example, the first-order transfer function reported in Chapter 4 only considered the magnitude of the demand signal. Unfortunately, given the complex frequency domain characteristic of

an absorbing wave machine, this information is strictly speaking insufficient; the phase of the signal being equally important.

This becomes particularly relevant in the generation of irregular waves using a pseudo-random wave generation approach. In this latter case the initial phasing for each wave component is random but known *a priori* in the experiment. As a result, the surface elevation in the flume can be predicted. In this context, the correct application of the phase information will be discussed. In particular, the start phasing of individual wave components is compared to the theory for position-controlled machines. This comparison is very important and highlights some stark contrasts in the operation of position- and force-controlled machines.

The study concerning flap-type wave boards did not explicitly mention the wave board design. Operating flap-type wave machines in force control is relatively straightforward. A simple membrane or gusset attached to the wave board and the flume's side walls prevents any water from leaking or seeping behind the machine. With zero displacement at the machine's hinge, a gusset is relatively easy to install in practice. As a result, the force acting on the paddle is excited by waves generated on the front face only.

For piston-type wave machines a simple sealing arrangement is not easily installed; a problem first encountered by Milgram (1970) who proposed using the hydrodynamic force for his novel active absorption mechanism. Due to a resonant fluid excitation at the back of his piston-type absorber, he opted to rely on a wave gauge based absorption technique instead. The problem of wave excitation at the rear of the paddle has been overcome by introducing the so called '*sector-carrier*' wave machine which seeks to generate a wave at the paddle front only. To achieve this, the rear part of the machine is designed as part of a circular arc centred on its axis of rotation (Salter 1982). Two photographs showing implementations of this arrangement are provided in figure 5.16.

Even though this paddle type shows good performance for most wave cases, some of the small deviations between the theory and the experimental observations may be attributed to fluid forces acting on the carrier part of the machine and

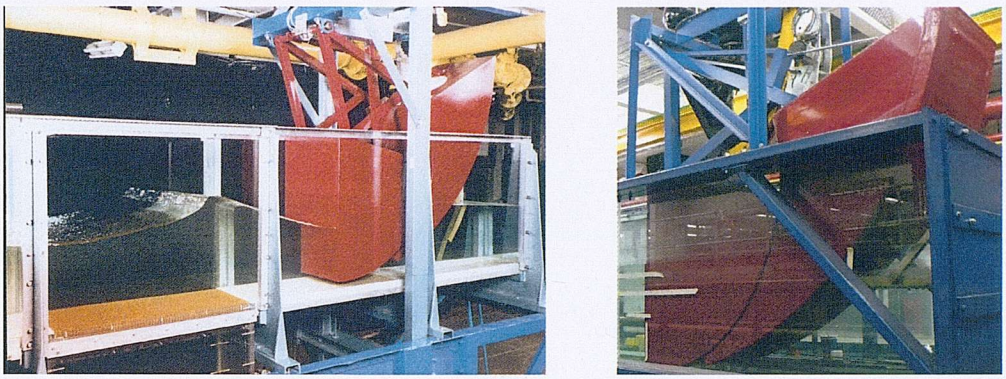


Figure 5.16: Two implementations of a sector-carrier piston-type wave machine: University College London (left) and Imperial College London (right)

fluid trapped between the two segments. Additional comments concerning the geometry of the machine are made where it is believed to influence the quality of the experimental comparisons.

Building upon experience gained during the first test programme presented in Part II of Chapter 4, the standard conductive wave gauges (diameter 1.5mm to 3.0 mm) were replaced by a tensioned wire arrangement (diameter 0.5mm). Utilizing this type of gauge significantly reduces the measurement inaccuracies especially when gauge arrays with closely spaced probes are employed; the latter being required when seeking to separate incident and reflected wave spectra or free and bound travelling harmonics. The major benefits of tensioned wire gauges are: (i) reduced meniscus effect, (ii) reduced wave scattering, (iii) very exact and consistent probe spacing and (iv) exactly parallel wires. Further analysis of the errors associated with standard conductive wave gauging techniques can be found in Payne et al. (2009).

The experimental investigation is divided into two parts covering first-order and second-order control. Within the first part, regular wave trains (§5.8.2), focused wave events (§5.8.4) and irregular waves (§5.8.5) of small amplitude are considered. Both the theoretical first-order transfer function and the absorption characteristic are discussed; particular attention being paid to the phasing of the individual wave components. The section on second-order control investigates the generation of steep regular waves (§5.9.1), bi-chromatic waves (§5.9.2) and irreg-

ular sea states (§5.9.3). The chapter concludes by summarising the key findings in §5.10.

5.8 Effects Arising at First Order

5.8.1 First-order Transfer Function

The theoretical work presented in Part I of this chapter focused on the second-order effects arising in position and force control. Some additional comments concerning the theoretical aspects of the machine's first-order transfer function are made here. As discussed previously, the term *'force-controlled wave machine'* refers to devices where the force acting on the paddle is one of the control quantities; the others being position, velocity and acceleration of the wave board. In particular, the velocity of the machine needs to be controlled in order to maintain maximum power absorption. This has been discussed in detail in Chapter 3 and was applied to a flap-type wave maker in Chapter 4

From this earlier discussion it may be concluded that, even theoretically, an ideal absorption controller ensuring perfect power absorption at all incident wave frequencies does not exist. Accordingly, a controller optimisation procedure has to be adopted which takes into account parameters such as the controller complexity and the frequency range of interest. As a result, the first and second-order characteristics cannot be generalized to a generic wave machine. However, these characteristics indicate the properties common to all force-controlled wave machines and provide guidance as how to evaluate the performance given a particular controller implementation.

With the absorption controller for a wave machine having been established, the first-order transfer function, relating the demand signal to the progressive wave amplitude, may be evaluated. This requires careful consideration not least because some contrasts to position-controlled machines arise. For a position-controlled wave machine, the first-order transfer function relates the wave board amplitude

to the progressive wave amplitude. It is often referred to as the Biesel transfer function, equation (2.22), and denoted as c_0 herein. This coefficient has the dimensions of $[m/m]$ and is therefore presented as a dimensionless quantity.

For force-controlled wave machines, the demand signal represents the input signal appropriate to the summing junction for the system shown in figure 3.5 (b) and has the physical dimension of force. This demand signal should not be confused with the simple wave induced force acting on the paddle front, $F_{\Phi}^{(1)}$, since it also includes the filtered velocity term which may be considered in the units of force once it has passed the absorption filter. The force transfer function may thus be defined as

$$c_f = \frac{A}{F_d}, \tag{5.11}$$

where A is the complex amplitude of the progressive wave mode and F_d is the complex amplitude of the force demand signal.

It is important to note that the coefficient c_f is also complex. This is in marked contrast to the coefficient c_0 for position-controlled wave machines which is real for all frequencies. In this latter case, a real coefficient c_0 expresses the fact that the generated progressive wave measured on the wave board is always in phase with the wave board velocity, or 90 degree out of phase with the wave board position. In the case of force-controlled wave machines, a frequency dependent phase shift between the demand signal and the generated progressive wave is introduced. This has important implications especially when generating focused wave events or irregular waves in which the start phase for each wave component needs to be known.

Moreover, it is particularly important that the complex coefficient c_f is not confused with the real (progressive wave) and imaginary (evanescent modes) contributions to the sum $\sum_{j=0}^{\infty} c_j$; where c_j is real for $j = 0$ and imaginary for $j > 0$. The complex coefficient c_f only relates to the progressive wave amplitude. To remove any ambiguity, c_f is presented as a magnitude and phase plot in the following discussion.

The phase shift introduced in the first-order transfer function for force-controlled machines is best understood by considering the hydrodynamic force acting on the paddle

$$f(t) = m(\omega)\ddot{x}(t) + d(\omega)\dot{x}(t), \tag{5.12}$$

where $m(\omega)$ and $d(\omega)$ are the added mass and the hydrodynamic damping. Given the frequency dependent characteristics of $m(\omega)$ and $d(\omega)$ (Chapter 3, figure 3.3), the phasing between the paddle position, $x(t)$, and the hydrodynamic force, $f(t)$, is also frequency dependent. With the force acting on the machine being one feedback path, the other being the filtered velocity, the phasing between the total demand signal and the progressive wave mode will be frequency dependent.

5.8.2 Validation of the First-order Transfer Function

The parameters used to evaluate the characteristics shown herein are based upon an existing wave machine located in the Hydrodynamics Laboratory at Imperial College London. Indeed, all the experimental results shown within this study are based on the operation of this machine. The piston-type wave generator is $0.57m$ wide and the gap between the bed and lower edge of the wave board is $d = 0.04m$ on average; the range of d for the largest paddle motions being approximately $d = 0.03m$ to $d = 0.05m$. The gap on either side of the piston-type panel is approximately 15mm. As a result, the wave board occupies approximately 89% of the flume's cross sectional area. This is regarded as a resonabley good fit for most wave conditions. However, the various gaps are believed to introduce experimental erros for some wave conditions and this is highlighted where appropriate. All results are evaluated for a water depth of $h = 0.6m$. The paddle mass and spring rate (the latter representing the buoyancy force on the back part of the sector-carrier) are estimated to be $189kg$ and $1000N/m$ respectively. A first-order low pass filter with a cut-off frequency of $f_c = 1.3Hz$ was found to be an optimum absorption controller. Further detail concerning the experimental setup is given in Appendix G.

To illustrate the first-order transfer function, figure 5.17 (a)-(c) shows the surface profile for regular waves of steepness $Hk/2 = 0.05$ and a wave frequency of $f = 26/64Hz$, $f = 36/64Hz$ and $f = 46/64Hz$. The data was taken from a single wave probe located at $x = 2.15m$ downstream of the wave maker. In all three cases very good agreement between the demanded and the measured wave amplitude and phase is observed. Further analysis of the data illustrated in sub-plot (a) showed that the departures from the expected surface profile are due to nonlinear wave effects; the amplitude and the phase of the first harmonic being in good agreement with the theory. It is only for the highest frequency shown in sub-plot (c), that the phase agreement becomes less satisfactory.

This observation is substantiated in figure 5.18 which contrasts the amplitude and phase information for a large number of regular wave cases. Within this figure, sub-plot (a) shows the magnitude of the first-order transfer function, $|c_f|$, expressed in $[mm/N]$. Observing this sub-plot it is clear that, for this particular wave machine and the range of frequencies shown, one Newton of demand signal yields a progressive wave with an amplitude between approximately $0.1mm$ and $0.25mm$. Considering the data points in detail, a small oscillatory behaviour about the expected theoretical curve is noted. In fact, this characteristic shows some similarity to the experimental data concerning the absorption characteristic in the fiap case (figure 4.9). As stated in the discussion relating to this latter figure, the origin of this oscillatory behaviour is not understood at present and needs further investigation.

The phase relation between this progressive wave (evaluated on the paddle, at $x = 0$) and the demand signal is shown in sub-plot (b). To obtain this phase information, the phase recorded at $x = 2.15m$ was related to the phase at $x = 0$ by $-k\Delta x$, where Δx is the distance between the measurement point and the paddle face. This calculation is based on the assumption that the influence of the evanescent modes is negligible at $x = 2.15m$; evidence of which has been provided in Chapter 2, figure 2.9.

The occurrence of large phase deviations, but very good agreement in terms of

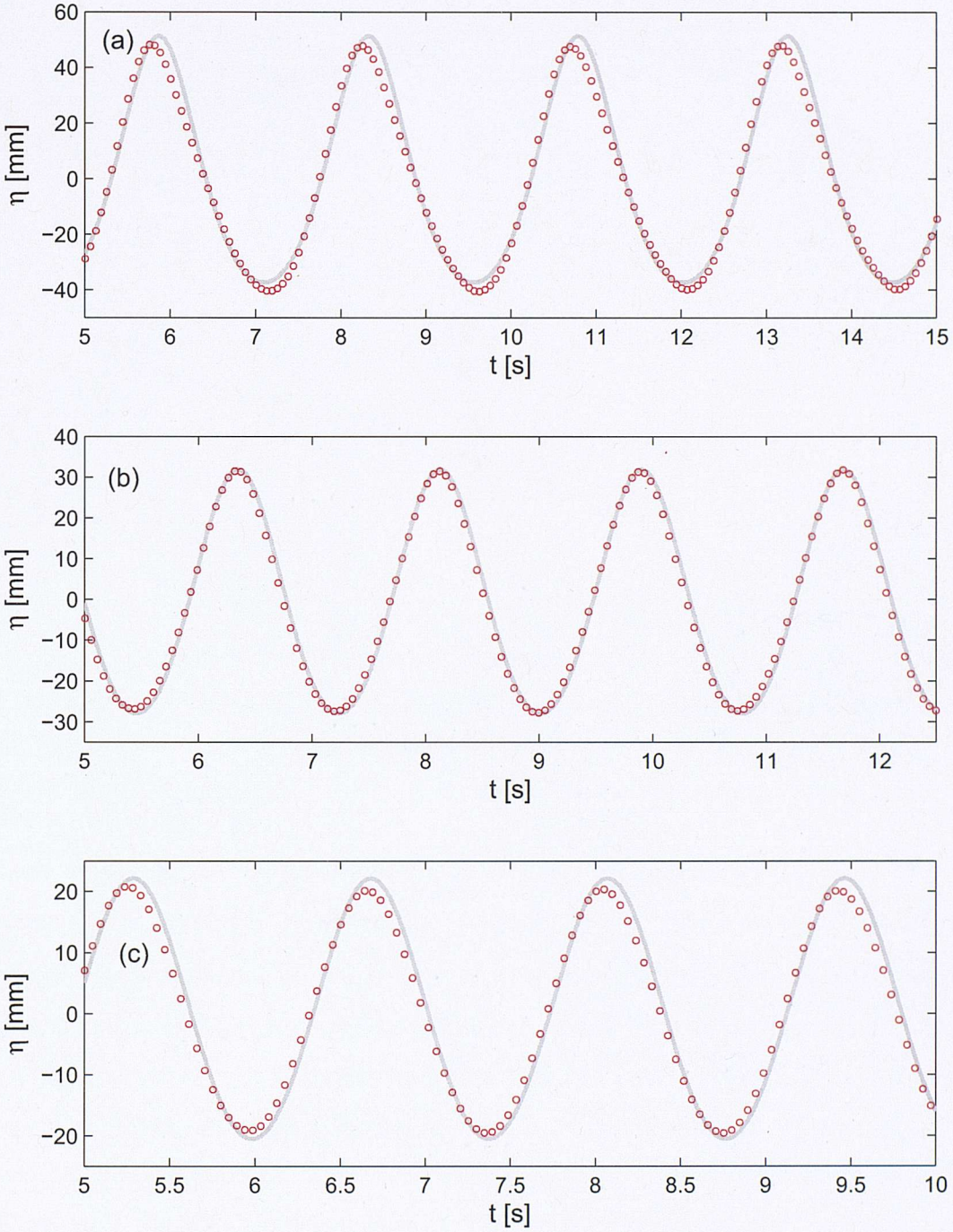


Figure 5.17: Surface elevation for a wave steepness of $Hk/2 = 0.05$; (a) $f = 26/64Hz$, (b) $f = 36/64Hz$, (c) $f = 46/64Hz$; —— Theoretical second-order Stokes solution at $x = 2.15m$, ○ Experimental data recorded at $x = 2.15m$. Note: the scales adopted on each sub-plot differ significantly.

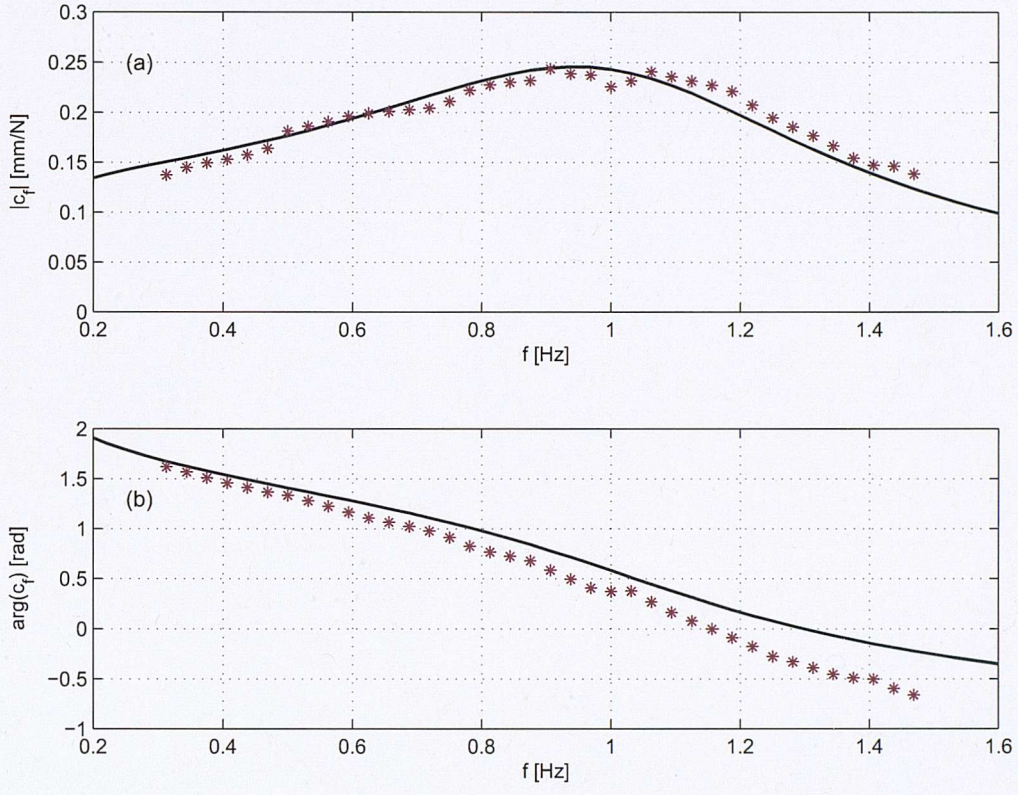


Figure 5.18: Complex first-order force-control transfer function, c_f, relating the demand signal to the generated progressive wave mode; (a) Magnitude of c_f, (b) Phase of c_f

wave amplitude seem contradictory at first sight. To fully understand this effect, a simple first-order low pass filter may be considered. For an excitation frequency where the input signal to such a filter is attenuated by only 5%, the phase shift introduced is as large as 18.3 degrees. Given a realistic wave machine, the drive system (power amplifier, motor inductance, motor inertia) introduces numerous low pass filters. In order to further reduce the phase deviation, a modelling approach that incorporates these components would have to be adopted. However, given that the maximum departure between predicted phase and measurement shown in figure 5.18 is in the order of 24 degree for the highest frequency considered, the model is regarded as sufficiently exact at this stage.

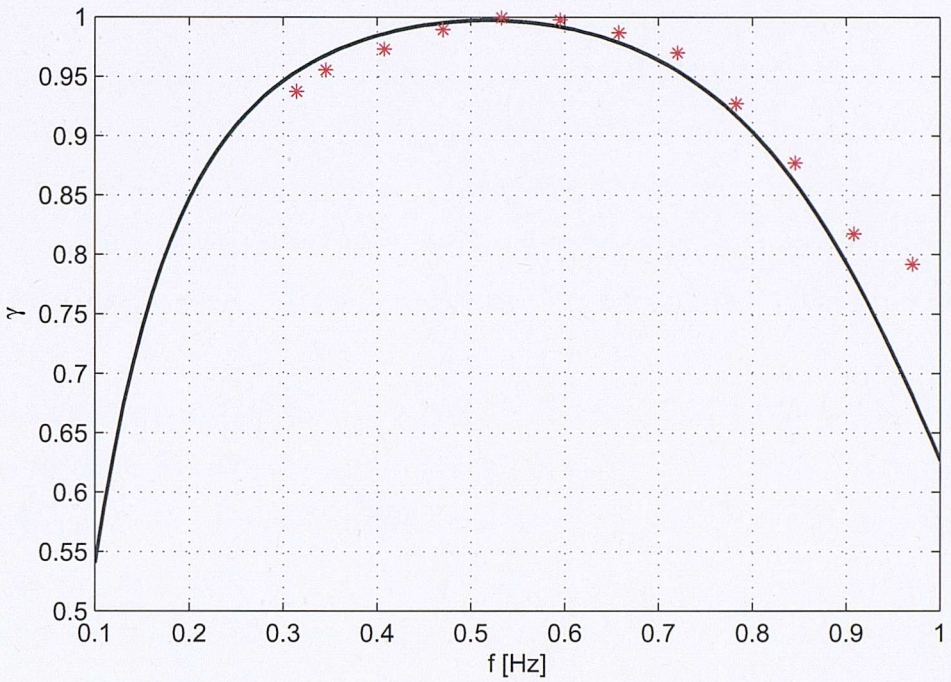


Figure 5.19: Power absorption coefficient for piston-type wave machine based on a low pass filter (IIR) optimised for the frequency range of $0.1Hz \leq f \leq 1Hz$; —— Theoretical absorption coefficient, $*$ Experimental data

5.8.3 Absorption Coefficient

In order to verify the absorption characteristic of the wave machine, the downstream beach was removed and hence full reflection occurred at the far end of the wave flume. The wave maker was programmed to generate a group of regular waves; once reflected at the end wall, these waves could be considered as incident waves to the wave maker which were to be absorbed. This notation is consistent with the definition of the velocity potentials in figure 3.2. Using a wave gauge array consisting of eight probes, with an individual spacing of $0.2m$, the resulting wave field was separated into its incident and reflected parts. The data was processed applying the method described in Lin & Huang (2004), modified to use data from all eight wave probes. The resulting power absorption coefficient, γ, is shown in figure 5.19.

The theoretical curve incorporates the finite mass and spring rate of the wave

machine; hence the difference when compared to the idealised curves shown in Chapter 3, figure 3.12. The absorption characteristic given in figure 5.19 results from a first-order low pass filter (IIR) optimized for the frequency range of $0.1Hz \leq f \leq 1Hz$; the absorption mechanism being most effective in the frequency range of $0.4Hz \leq f \leq 0.7Hz$ where the machine is operated most commonly. Even for frequencies as low as $0.1Hz$ and as high as $1Hz$, the power absorption coefficient exceeds 0.5.

The data points in figure 5.19 appear to lie on a curve that is slightly shifted to the right when compared to the theoretical result. Nevertheless, the agreement between the theory and the experimental data is very good; the small deviations at either end of the frequency range probably being due to an inaccurate estimate of the paddle's mass and spring terms. In addition, the gap at either side of the wave board as well as the gap between the wave board and the bed may also contribute to this error.

5.8.4 Focused Wave Event

A focused wave event is easily generated in the laboratory by demanding a spectrum where the initial phasing of all wave components has been predetermined. In order to illustrate the importance of the additional phase shift discussed in §5.8.2 (figure 5.18), an experiment was undertaken in two parts: (i) the additional phase shift was neglected and all phases set to $\pi/2$ and (ii) the additional phase shift was incorporated when calculating the initial phase for each wave component.

In both cases a tophat spectrum, comprised of wave components with equal amplitude, was chosen. The spectrum consists of wave frequencies between $f_{min} = 32/64Hz$ and $f_{max} = 64/64Hz$ with a spacing of $\Delta f = 1/64Hz$. The combined amplitude at the focused event was chosen to be $10.0mm$ so that the wave motion remains linear. As a result, the amplitude of the individual frequency components is $A_n = 0.3mm$. Moreover, the initial phases were calculated with the focal time set to $t_{focal} = 32s$ and the focal position to $x_{focal} = 6m$. The surface profiles

recorded in parts (i) and (ii) above are shown in figure 5.20 (a) and (b); in both sub-plots the experimental data is directly compared to the theoretical (linear) solution. The data shown was obtained using a single wave probe located at $x = 6m$.

In the first case, figure 5.20 (a), it is clear that, even though the recorded data is in reasonably agreement with theory, some of the wave components are out of phase. Incorporating the additional phase information eliminates this shortcoming and leads to a more symmetrical wave event in better agreement with linear theory; evidence of this being provided in figure 5.20 (b). The remaining small departures from the theoretical solution can be directly attributed to the small phase and magnitude errors apparent in figure 5.18.

5.8.5 Irregular Waves

Amplitude Spectrum

The final set of experiments concerning first-order effects investigates the machine's behaviour when generating and absorbing linear (small) random waves. The distribution of energy in the wave flume was observed for two cases. In a first test an absorbing beach was installed at the flume's far end and the generation capabilities of the machine are observed. In a second test the downstream beach was removed and replaced by a reflecting vertical wall. In this latter case, the machine has to simultaneously generate and absorb waves. Before considering the data, the terms incident- and reflected spectra need to be redefined when compared to those given in figure 3.2. The incident spectrum is now defined as incident to the wave gauges (propagating in the positive x-direction), whereas the energy reflected by the beach or wall (propagating in the negative x-direction) is regarded as the reflected spectrum; this is further clarified in figure 5.21 which also shows the experimental setup.

In both cases a JONSWAP target spectrum, as defined by equation (5.8), with a peak frequency of $f_p = \omega_p/(2\pi) = 38/64Hz$ and a peak enhancement factor of

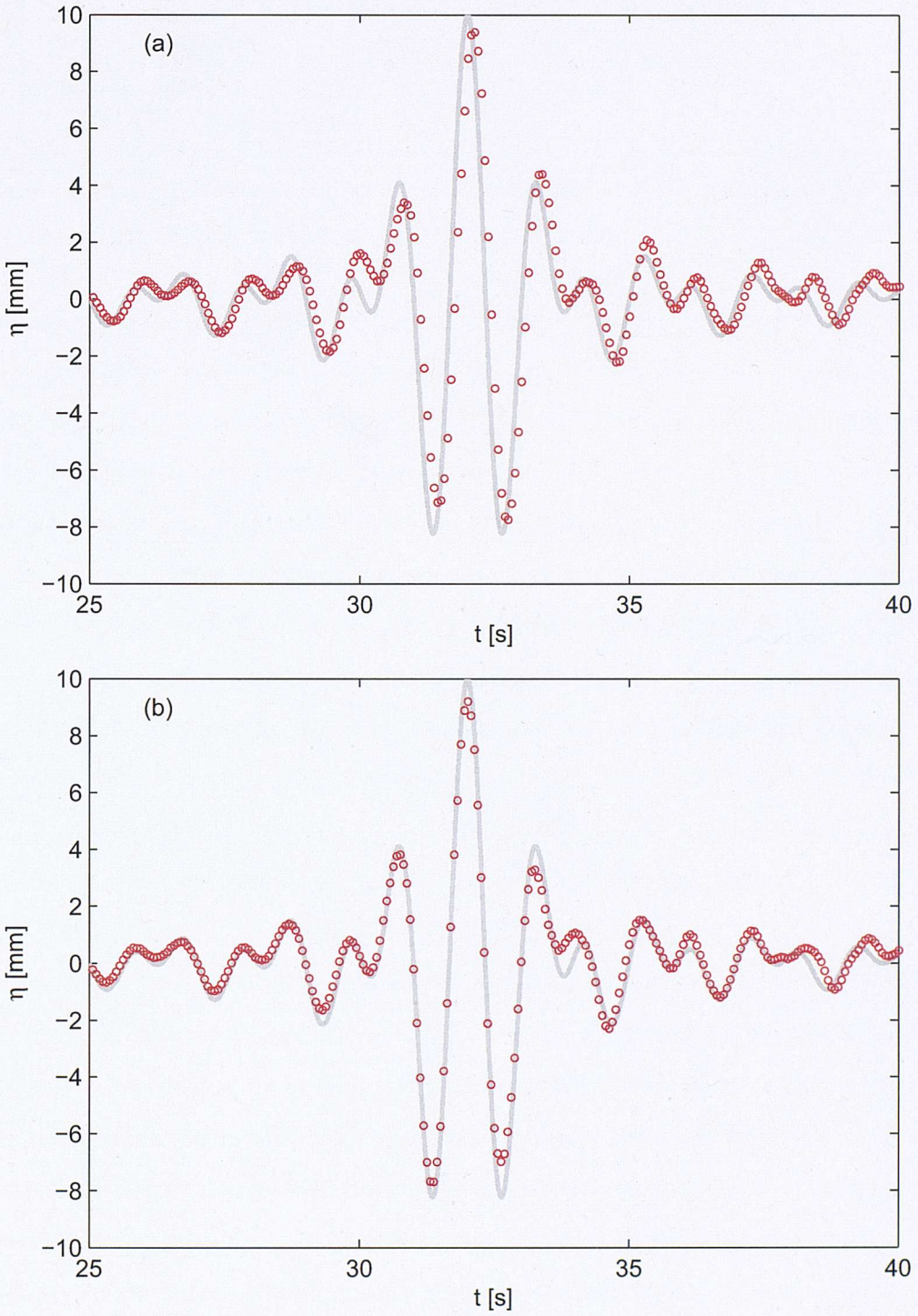


Figure 5.20: Surface profile for focused wave event at $t = 32s$ and $x = 6m$; (a) additional phase information neglected, (b) additional phase information incorporated; —— Theoretical (linear) solution; ○ Experimental data

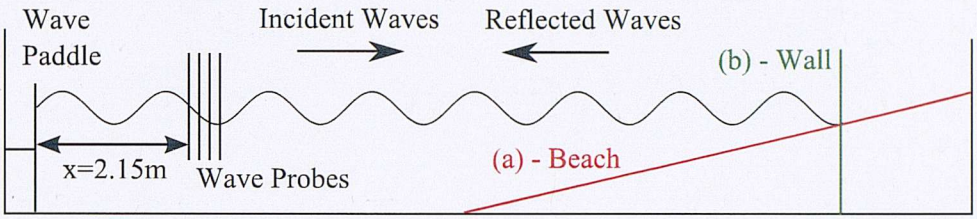


Figure 5.21: Experimental setup for the investigation of (a) wave generation only and (b) simultaneous wave generation and absorption

$\gamma = 3.3$ was adopted. As before, the water depth was kept constant at $h = 0.6m$. The term *target spectrum* is defined as the desired incident wave spectrum. In the first part of the measurements the target spectrum was generated (using the theoretical first-order transfer function described in §5.8.2) and dissipated by the downstream beach. Figure 5.22 (a) shows the theoretical target spectrum as well as the measured incident and reflected spectra. In this case the incident and reflected spectra were separated using the method described by Mansard & Funke (1980); the data taken from a $64s$ interval preceded by $256s$ of initial wave generation to obtain a fully developed sea state (including sufficient time for reflections to be generated at the beach / end wall and propagate back to the wave maker).

For this purpose, three wave gauges with a spacing of $0.2m$ were located in the vicinity of the wave generator; the distance between the wave board and the first probe being $2.15m$. This distance is sufficiently large to neglect the influence of any evanescent wave modes. The agreement between theoretical and measured incident spectrum in figure 5.22 (a) is very good. Furthermore, the beach performs very well over a broad range of frequencies; the low frequency components introduced in the reflected spectrum ($f \approx 0.2Hz$) being effectively absorbed by the wave maker. A detailed description of the frequency-dependent beach reflection coefficient is provided in Appendix G. Data taken after $1024s$ of continuous wave generation (not presented herein) shows equally good agreement with the spectra presented in figure 5.22 (a).

In the second set of measurements, with a vertical wall present, a demand signal identical to that used in the initial test was sent to the wave generator.

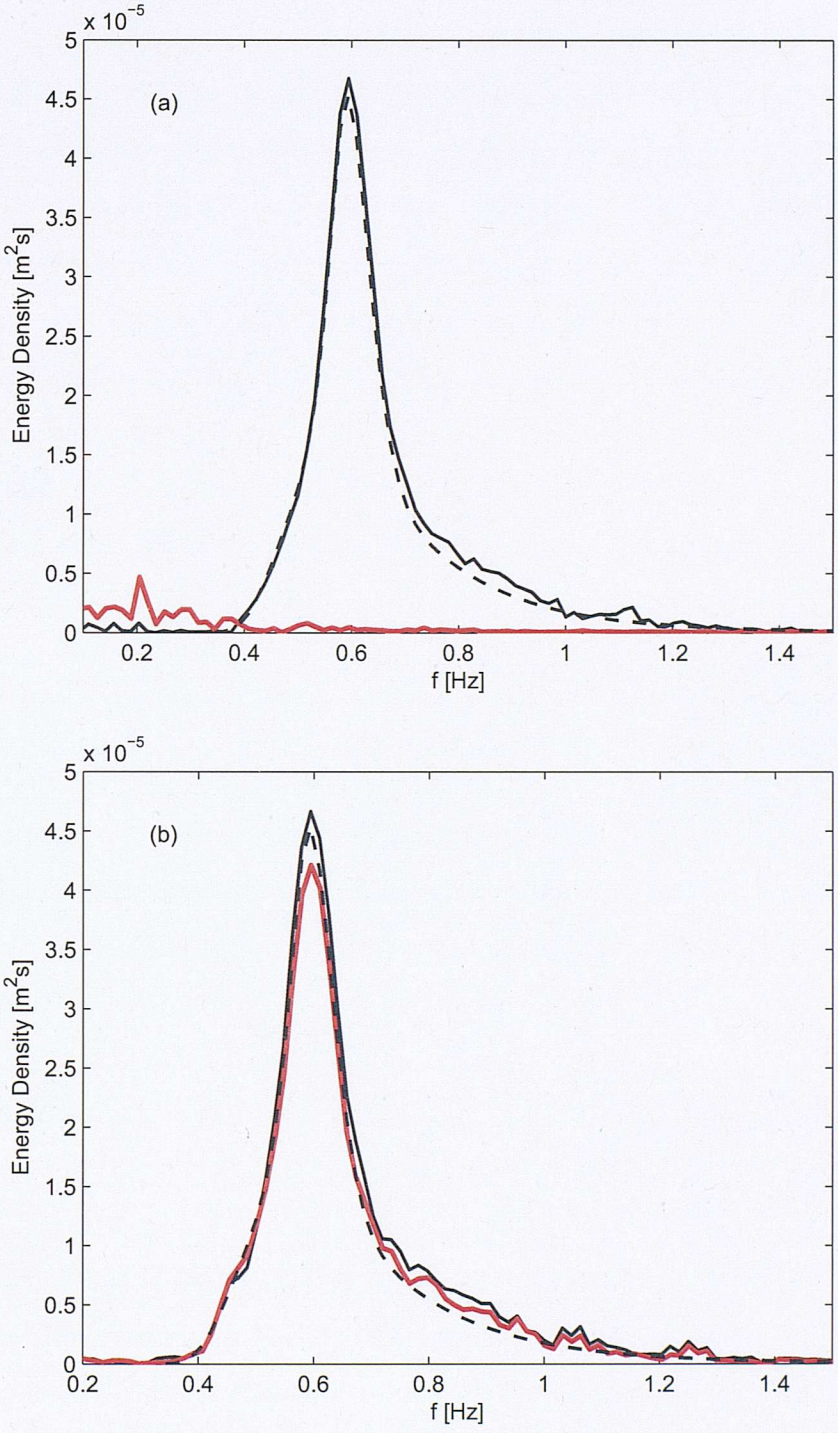


Figure 5.22: Irregular wave generation and absorption: (a) with absorbing beach, (b) with reflecting vertical wall; – – Target JONSWAP spectrum, —— Measured incident spectrum, —— Measured reflected spectrum

Figure 5.22 (b) shows the resulting incident and reflected spectra; the curves being computed applying the same procedure as outlined above. It is apparent from the plot that almost all the energy is reflected back to the wave maker; the measured reflected spectrum being almost equal to the incident spectrum. However, it is important to note that, apart from the deviations at the higher frequencies, the measured incident spectrum closely resembles the target spectrum. It can therefore be concluded that the wave maker absorbs most of the reflected wave energy whilst still generating the desired incident wave spectrum. Furthermore, the low frequency components appearing in the reflected spectrum within the first test, figure 5.22 (a), do not occur in the second test. This confirms that these modes were excited by the wave breaking process and are not introduced by the wave generator.

Amplitude and Phase Distribution

Figure 5.22 showed the incident and reflected energy spectra computed using the data recorded from an array of wave gauges. This procedure may be regarded as a best fit over multiple spatial locations. In this case the absolute phase is irrelevant. Indeed, any random start phase applied to each of the spectra's wave components would yield an energy distribution identical to that shown in figure 5.22 (a) and (b).

In contrast, the surface elevation recordings provided in figures 5.23 and 5.24 correspond to two different random sets of phases and are therefore very different. In each case the data is obtained using a single probe located at $x = 2.15m$. The measured surface elevation is directly compared to the theoretical first-order computation. In considering these results it is important to note that, even though both figures are presented as four sub-plots, these are representations of a continuous recording ranging from $t = 0s$ to $t = 256s$. In fact, the sub-plots are divided into blocks of $64s$ which is the repeat period for the generated spectrum; the four sub-figures should hence be exact repetitions of the same surface profile.

For both cases considered, a JONSWAP target spectrum with $f_p = 26/64Hz$,

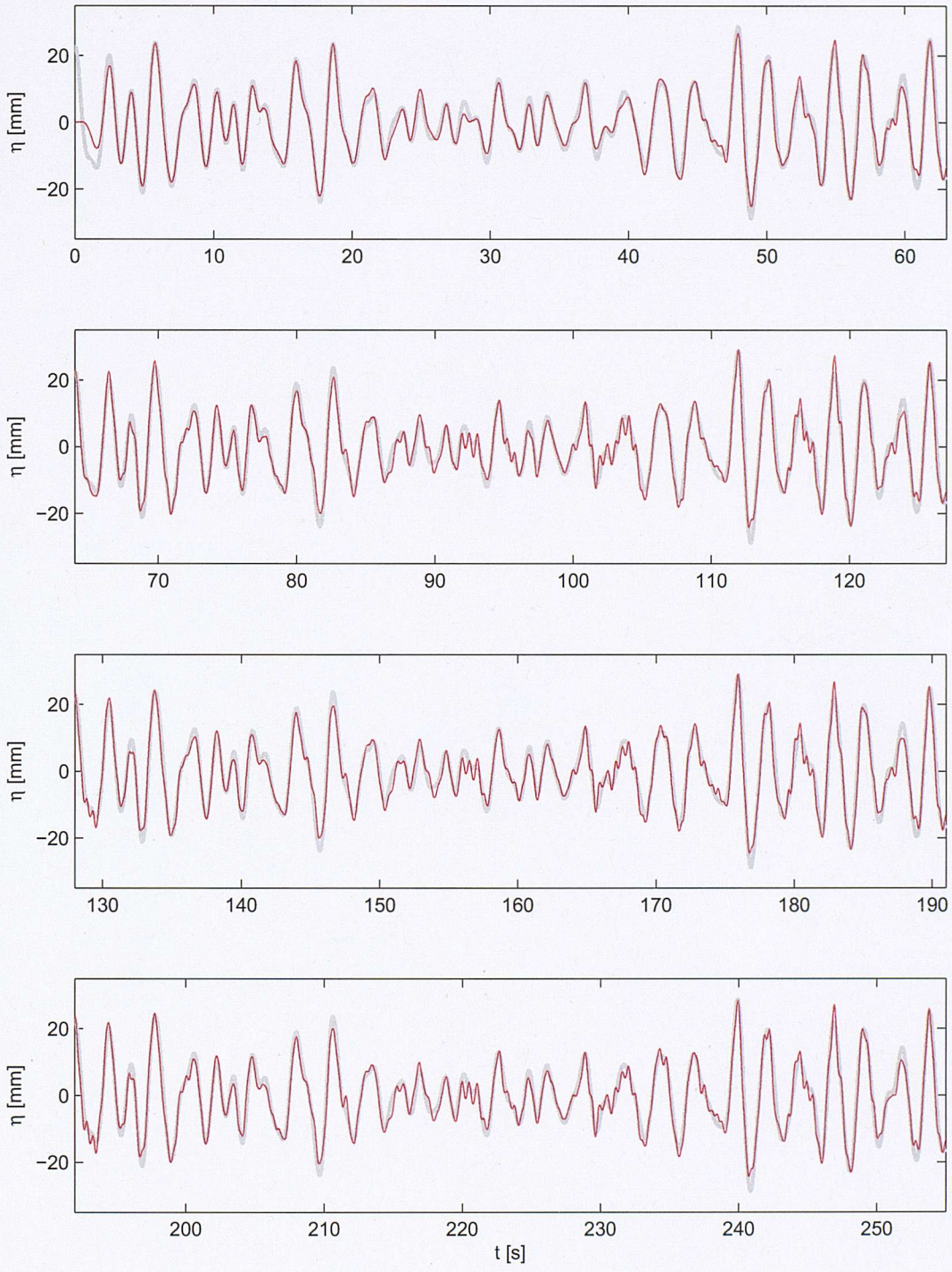


Figure 5.23: Surface elevation data at $x = 2.15m$, JONSWAP target spectrum, randomised phase set 1; Theoretical surface elevation, Measured surface elevation; Note: The four sub-plots are representations of a continuous recording ranging from $t = 0s$ to $t = 256s$

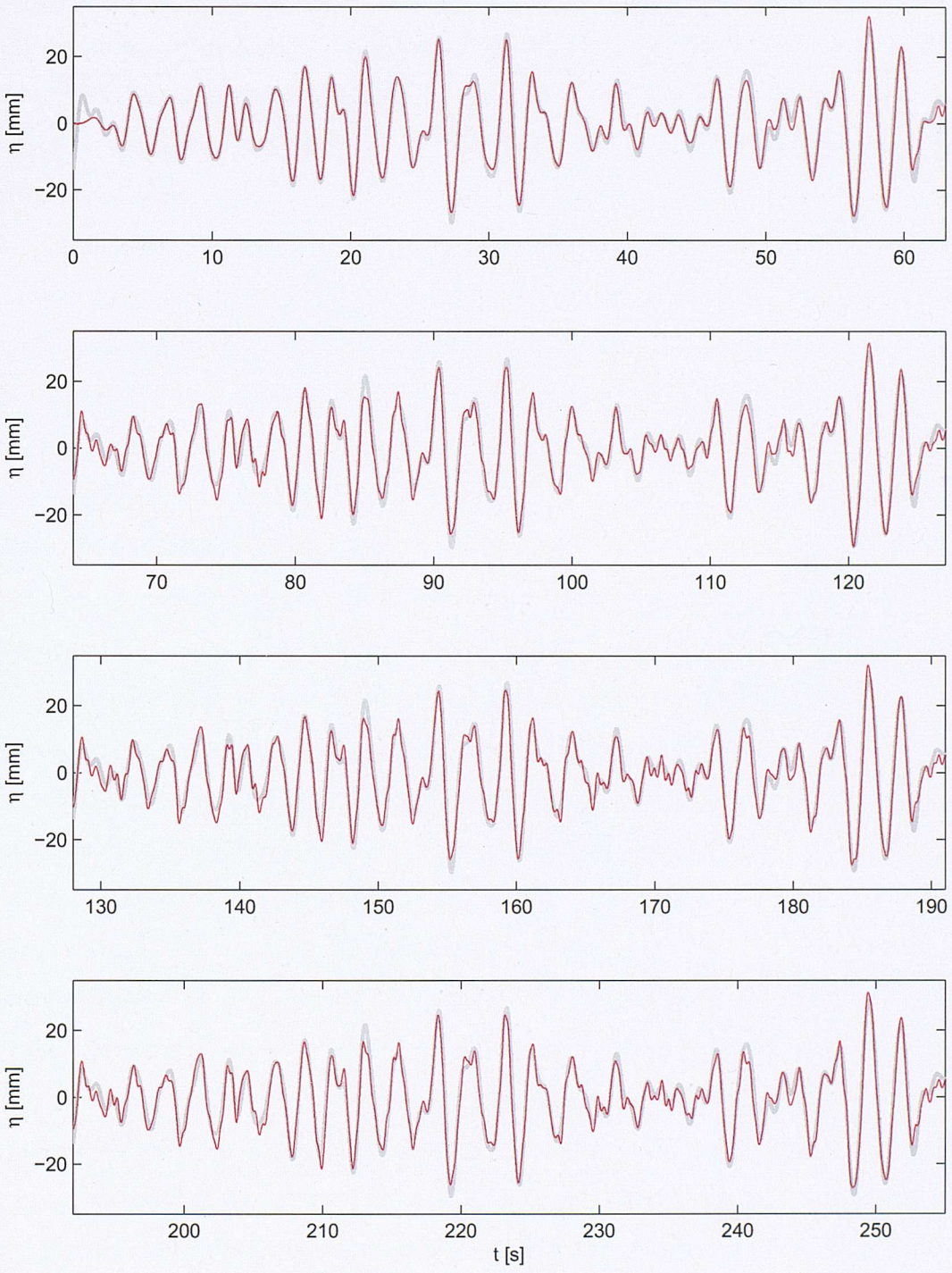


Figure 5.24: Surface elevation data at $x = 2.15m$, JONSWAP target spectrum, randomised phase set 2; Theoretical surface elevation, Measured surface elevation; Note: The four sub-plots are representations of a continuous recording ranging from $t = 0s$ to $t = 256s$

$\gamma = 3.3$ and $H_s \approx 0.02m$ was adopted; the only difference between the recordings shown in figures 5.23 and 5.24 being the initial phasing of the wave components. The start phase for each component is set to a random value varying between $-\pi$ and $+\pi$. Subsequently, the first-order force demand signal incorporating the theoretical phase shift (§5.8.2 and figure 5.18) is evaluated.

Observing these two figures it is clear that a different set of start phases leads to very different surface elevations in the flume. However, since the wave machine's behaviour is fully modelled, this surface elevation may be computed *a priori*. In both cases the agreement between this calculated profile and the measured data is very good; minor deviations being due to: (i) reflections from the beach present in the record after $t \approx 25s$, (ii) higher order effects including small nonlinear wave-wave interactions and (iii) small amplitude and phase errors in the theoretical transfer function. In these and the following figures representing the surface elevation at $x = 2.15m$, the initial $5s$ of data must be excluded from the discussion. This interval includes the ramp-up time of the wave maker and the initial time taken for the propagation of energy to the wave probe location.

Even though some energy is reflected back from the beach, careful observation of the surface profile recorded between $t = 64s$ and $t = 256s$ shows near-perfect steady state condition. However, some build-up of energy is observed at high frequencies. The most likely explanation for this lies in the fact that the wave maker absorption characteristic is poor at high frequencies (figure 5.19). As a result, high frequency components reflected from the beach are not effectively absorbed. Nevertheless, the combination of a beach and an absorbing wave maker prevents a build-up of energy at most frequencies. This latter observation is an important feature of the present study: a model placed in the flume would be subject to almost identical wave conditions for a large number of repeat periods.

5.9 Effects Arising at Second Order

5.9.1 Regular Waves

In the previous section (figure 5.17 a), a shallow water wave ($f = 26/64Hz$, $h = 0.6m$, $Hk/2 = 0.05$) generated using a first-order force demand signal showed a noticeable departure from the theoretical Stokes solution. With an increase in the wave steepness to $Hk/2 = 0.1$, the experimental data provided in figure 5.25 indicates that the departure from the expected theoretical solution becomes more significant. Furthermore, figure 5.26 suggests that similar arguments apply to the wave case with a frequency of $f = 32/64Hz$ and a steepness $Hk/2 = 0.1$.

Unlike previously argued for force-controlled flap-type wave machines (Chapter 4), a first-order control signal is clearly not appropriate to the operation of absorbing piston-type machines. Indeed, a sinusoidal signal applied to a piston-type machine results in significantly distorted waves; the mechanisms underlying this effect being discussed in Part I of the present chapter.

The benefits of applying a demand signal correct up to second order are clearly visible in figures 5.27 and 5.28. These figures concern exactly the same wave cases and show that the agreement between the experimental data and the theoretical Stokes solution has been improved considerably. Indeed, the present study has shown that applying a second-order signal provides a significant improvement in wave quality for nearly all the wave cases observed. A summary of the test results is given in figure 5.29 where the spurious free wave amplitude, $A^{(2s)+}$, is plotted normalised with respect to the second-order Stokes amplitude, $A^{(21)+}$, thereby producing a non-dimensional representation of the problem. Figure 5.29 directly contrasts the non-dimensional data arising from second-order control with that produced using first-order control. In addition, the theoretical ratio based on first-order control is also included.

The first notable feature of the data shown in figure 5.29 is that the measured second-order content in first-order position control is considerably smaller than the expected values. In this context, it should be noted that, even though the

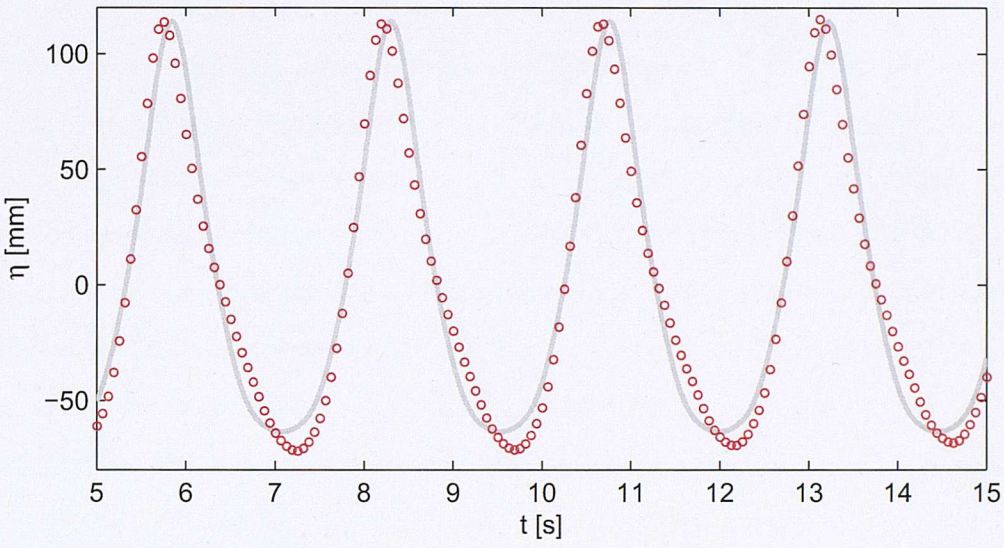


Figure 5.25: Surface profile for wave case $f = 26/64Hz$ with a steepness of $Hk/2 = 0.1$ at $x = 2.15m$ based on first-order force control; —— Theoretical second-order Stokes solution, ○ Experimental data

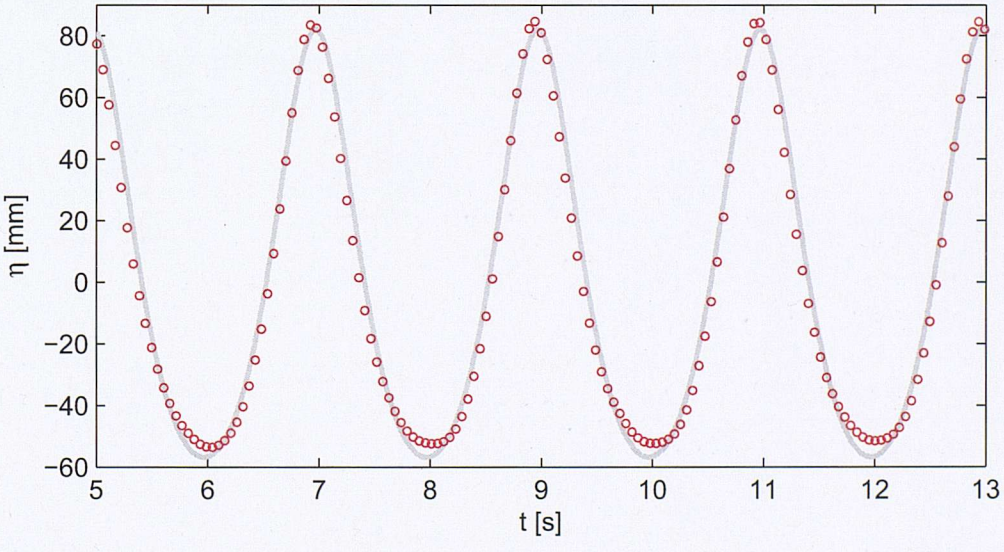


Figure 5.26: Surface profile for wave case $f = 32/64Hz$ with a steepness of $Hk/2 = 0.1$ at $x = 2.15m$ based on first-order force control; —— Theoretical second-order Stokes solution, ○ Experimental data

development of second-order position-control theory has been established for some time, very little experimental evidence is available for comparison. With the force-control theory building directly upon the development of position control, the match in the former case can only be as good as in the latter. Nevertheless, it is in relatively shallow water, where the second-order effects are highly pronounced, that the agreement is reasonable. In deeper water, or with higher frequencies, the agreement becomes less satisfactory; the most likely explanation for this being the complex wave board geometry and/or the various gaps around the boundary of the paddle discussed earlier. Likewise, applying a control signal correct to second order is most effective at low and medium frequencies. Indeed, it is shown to have little influence with some of the highest frequencies observed.

This latter issue may be attributed to two principal causes. First, in deep water, the second-order content in first-order control is much smaller than expected; hence the compensation signal will be too large. Second, the deviation between the theoretical and measured phase at higher frequencies (figure 5.18) leads to an erroneous start phase for the second-order compensation. Nevertheless, for all the relevant wave cases considered, especially those in shallow water, the second-order control signal improved the wave quality considerably and must therefore be recommended.

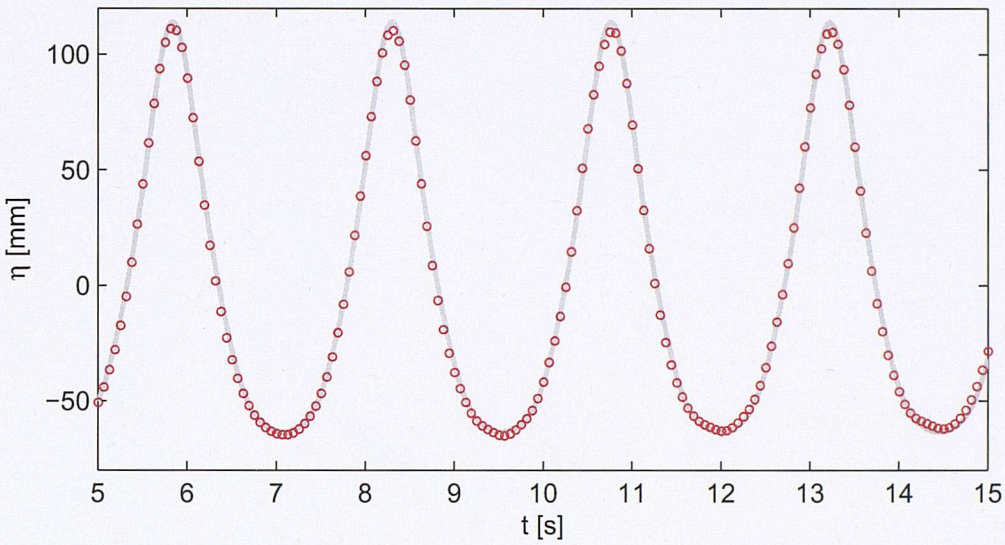


Figure 5.27: Surface profile for wave case $f = 26/64Hz$ with a steepness of $Hk/2 = 0.1$ at $x = 2.15m$ based on second-order force control; —— Theoretical second-order Stokes solution, ○ Experimental data

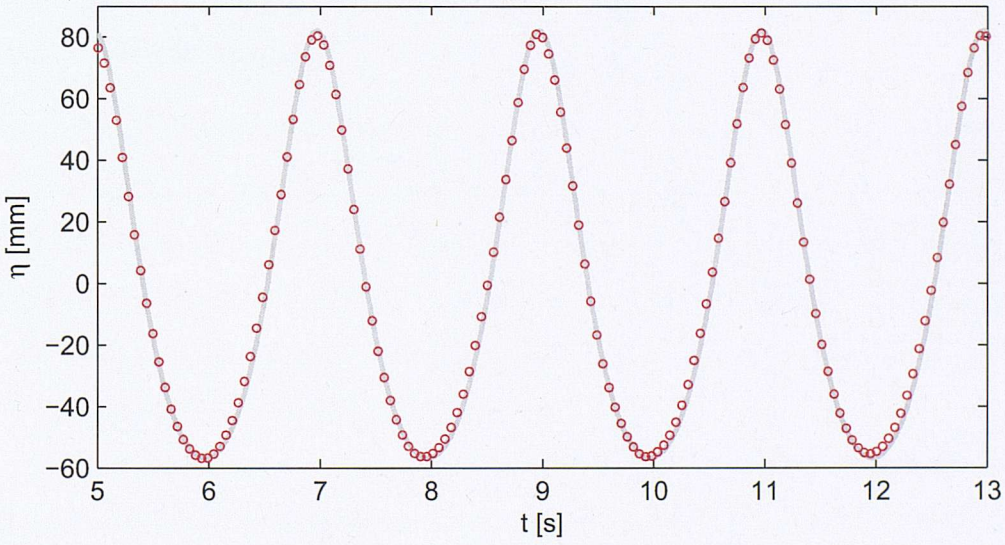


Figure 5.28: Surface profile for wave case $f = 32/64Hz$ with a steepness of $Hk/2 = 0.1$ at $x = 2.15m$ based on second-order force control; —— Theoretical second-order Stokes solution, ○ Experimental data

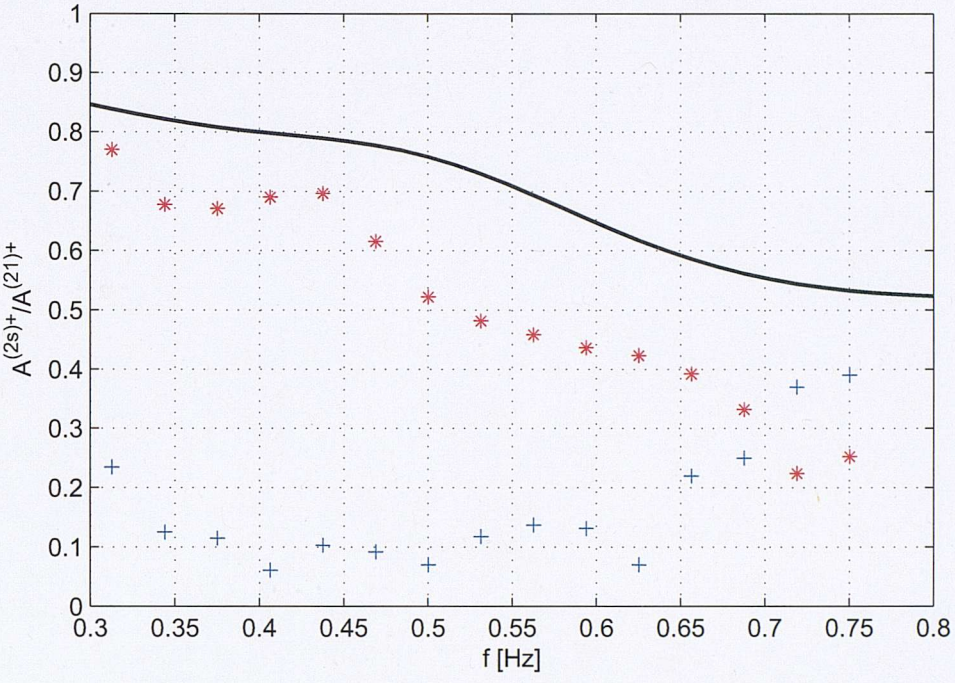


Figure 5.29: Dimensionless ratio of spurious free wave amplitude, $A^{(2s)+}$, and the Stokes second-order amplitude, $A^{(21)+}$; $*$ Experimental data based on first-order force control, $+$ Experimental data based on second-order force control and —— Theoretical solution based on first-order force control.

5.9.2 Bi-chromatic Waves

The generation of multi-component sea states also introduces freely propagating spurious waves. In fact, with a realistic spectrum in the laboratory consisting of many tens of wave components, the large number of wave-wave interaction terms gives rise to a large number of spurious waves. With this complex sea state present in the wave tank, the data processing and the interpretation of the data becomes very difficult.

As a result, the wave-wave interaction terms and their spurious counterparts are best visualized by generating a two component or bi-chromatic sea state in which the frequency components are very close in frequency. In this case the two primary waves give rise to a total of four wave-wave interaction terms: one at the double frequency of each primary wave, one at their frequency sum and one at their frequency difference. All of these wave components are bound to the p imary

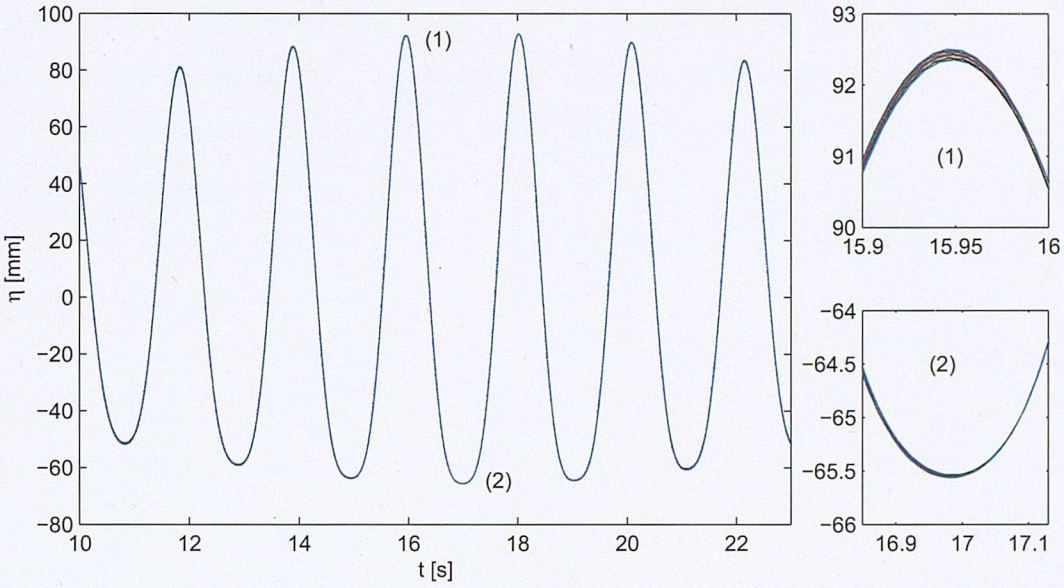


Figure 5.30: Theoretical second-order surface profile for a bi-chromatic wave train, eight gauges located at $2.15m \leq x \leq 3.55m$ with a spacing of $0.2m$. Note that the data recorded by gauges 2 to 8 is time shifted to overlap with the data recorded at $x = 2.15m$.

waves. In contrast, the associated spurious wave modes are freely propagating and therefore satisfy the dispersion relation in their own right.

With the two components in the bi-chromatic sea state being very close in frequency, the primary waves (and hence their bound modes) propagate with approximately the same phase velocity. As a result, the evolution of the combined surface profile in space is insignificant for small spatial variations. This is illustrated in figure 5.30 where a theoretical second-order bi-chromatic surface profile (no spurious modes) is compared at eight spatial locations lying in the range $2.15m \leq x \leq 3.55m$ with individual gauges spaced $0.2m$ apart.

Within this figure, the data for each gauge is time shifted to create an overlap with the data predicted at the first gauge ($x = 2.15m$). The sea state was evaluated for the two wave components $f_1 = 26/64Hz$ and $f_2 = 28/64Hz$, both with an amplitude of $a = 40mm$. Given the similarity in the phase velocity of the two waves ($c_1 = 2.26m/s$ and $c_2 = 2.24m/s$), the spatial variation in the predicted surface profile is very small and hence difficult to identify; the largest deviation

being in the order of $0.2mm$. The extent of this variation is further clarified in the inserts labelled (1) and (2) which provide close-ups at the wave crest and the wave trough respectively. If the plots presented in figure 5.30 related to measured data rather than theoretical solutions, the match in the surface profiles at different spatial locations would provide the clearest possible evidence of the absence of freely propagating spurious wave modes.

Considering these arguments, the measured surface profiles presented in figure 5.31 confirm the presence of significant spurious wave content. This data was generated using a first-order force-control signal and relates to exactly the same wave conditions as described in the previous theoretical case. Indeed, everything about the comparisons is identical, including the spatial locations of the measuring points and the time shift applied to the recorded data. However, in contrast to the theoretical case, the time shifted wave gauge signals do not match well, evidence of this being particularly clear in inserts (1) and (2) again relating to adjacent crest and trough positions. It is noted once more that figure 5.31 relates to experimental data whereas figure 5.30 relates to a numerical simulation. The apparent smoothness of the curves in figure 5.31 is a result of the high sample rate and very low noise, full details of which are given in Appendix G.

Adopting the second-order force-control signal derived in Part I, leads to a significant improvement in wave quality; evidence of this being provided in figure 5.32. In this case the eight time histories of the water surface elevation are in close agreement indicating much reduced spatial variation. This, in turn, confirms a substantial reduction in the freely propagating spurious wave modes.

Adopting exactly the same procedure, a second bi-chromatic wave case is considered. In this second case the frequencies generated are $f_1 = 30/64Hz$ and $f_2 = 32/64Hz$, both with an amplitude of $a = 40mm$. The surface profiles for first- and second-order control are shown in figures 5.33 and 5.34 respectively. As before, the improvement in wave quality when applying a second-order control signal is very significant. However, there clearly remains some departure from ideal behaviour and this may be due to spurious effects arising at higher orders,

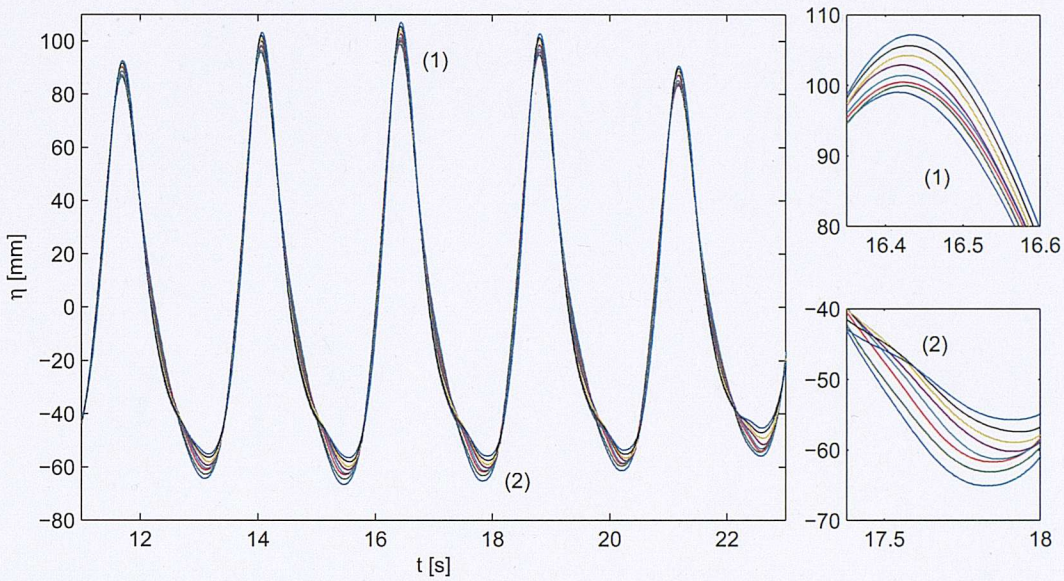


Figure 5.31: Measured surface profile for a bi-chromatic wave train with $f_1 = 26/64Hz$ and $f_2 = 28/64Hz$ based on first-order force control. Note that the data recorded by gauges 2 to 8 is time shifted to overlap with the data recorded at $x = 2.15m$.

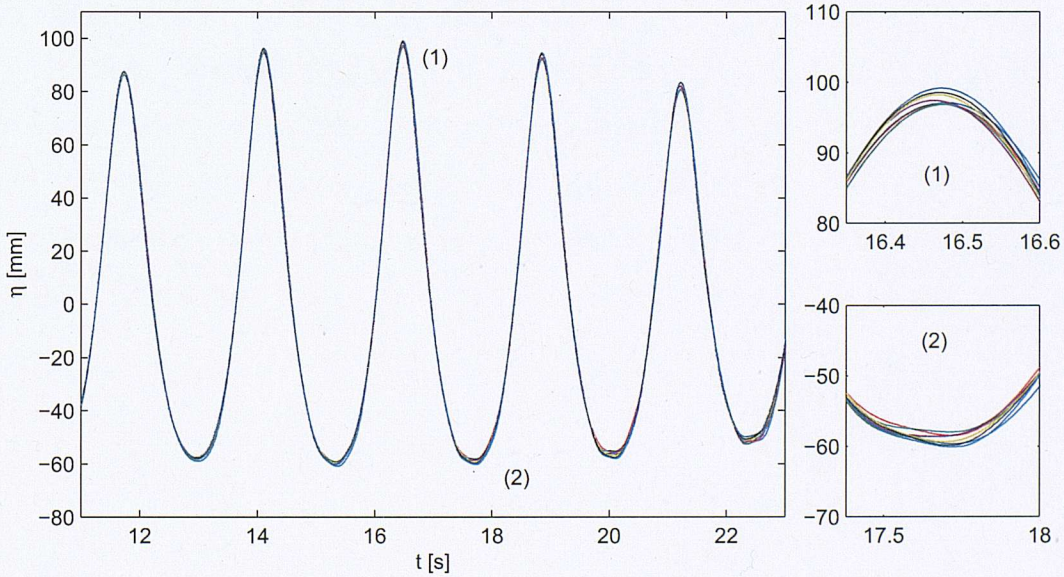


Figure 5.32: Measured surface profile for a bi-chromatic wave train with $f_1 = 26/64Hz$ and $f_2 = 28/64Hz$ based on second-order force control. Note that the data recorded by gauges 2 to 8 is time shifted to overlap with the data recorded at $x = 2.15m$.

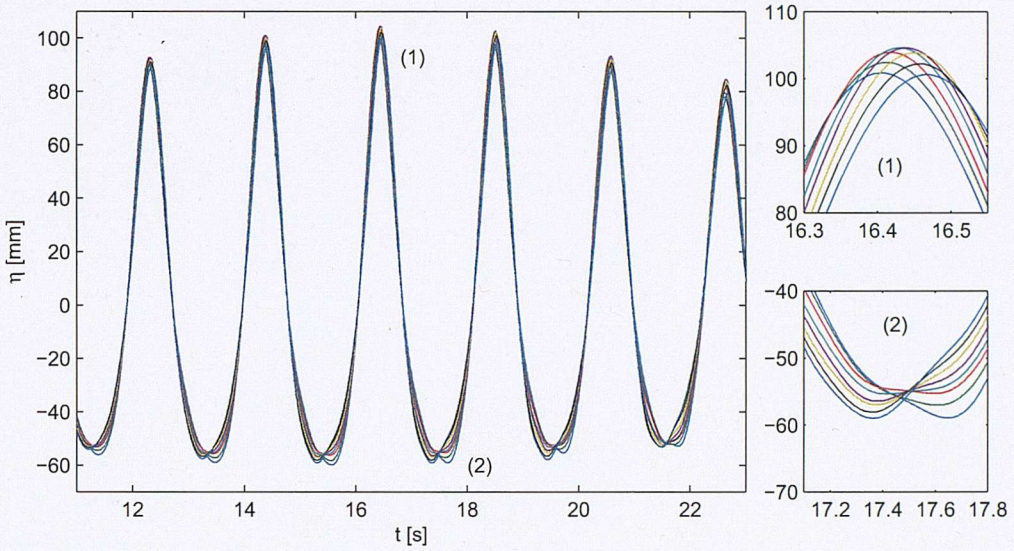


Figure 5.33: Measured surface profile for a bi-chromatic wave train with $f_1 = 30/64Hz$ and $f_2 = 32/64Hz$ based on first-order force control. Note that the data recorded by gauges 2 to 8 is time shifted to overlap with the data recorded at $x = 2.15m$.

particularly at the third harmonic. Evidence of this being given by the difference in the spread of data at the crest and the trough.

It should be noted that, in all cases considered above, the sub-harmonic term has not been corrected for. With a difference term of $f_{nm}^{-} = 2/64Hz$, a spurious sub-harmonic wave with a wave length of approximately $77m$ is predicted. Given the dimensions of the flume, it is questionable whether this wave mode would develop in practice.

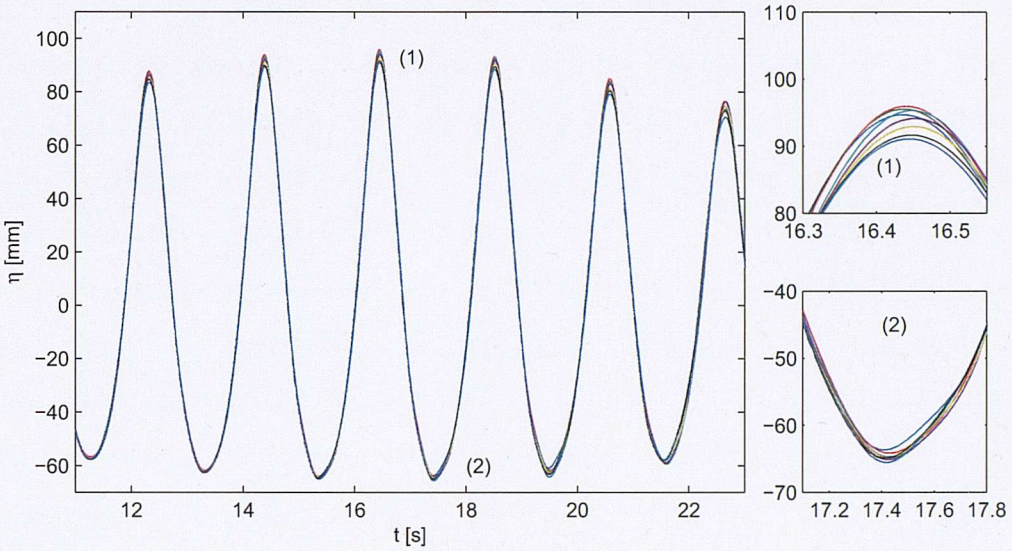


Figure 5.34: Measured surface profile for a bi-chromatic wave train with $f_1 = 30/64Hz$ and $f_2 = 32/64Hz$ based on second-order force control. Note that the data recorded by gauges 2 to 8 is time shifted to overlap with the data recorded at $x = 2.15m$.

5.9.3 Irregular Waves

The final set of experiments concerns the generation of steep irregular or random waves with simultaneous wave absorption. Based on the discussion in Part I, it seems advantageous to illustrate the experimental results in the time domain. To be consistent with the earlier first-order experiments, a JONSWAP spectrum with peak enhancement factor $\gamma = 3.3$ and peak frequency $f_p = 26/64Hz$ was adopted.

Two cases are considered, the first with a significant wave height of $H_s \approx 0.13m$ (referred to as case 1) and the second with $H_s \approx 0.16m$ (referred to as case 2). Both cases correspond to a JONSWAP energy spectrum, but have independent random start phases and hence very different surface profiles. All the surface profiles shown were recorded at $x = 2.15m$ and are directly compared to the expected second-order solution evaluated for this location. A location in close proximity of the wave maker was chosen to maximise the time window without reflections from the downstream beach.

Figure 5.35 concerns case 1 based on a first-order force demand signal. In con-

trast to the linear cases shown previously (figures 5.23 and 5.24), some significant departures from the theoretical second-order water surface profile arise. This is particularly pronounced for the largest waves in the intervals $5s \leq t \leq 15s$ and $35s \leq t \leq 50s$; with equivalent positions in each sub-plot reflecting the fact that the sea state has a repeat period of $64s$.

Figure 5.36 again concerns case 1, but based on a second-order force demand signal. Comparing figures 5.35 and 5.36 in detail, it is clear that a significant enhancement in wave quality is observed; the latter case providing a much improved fit to the theoretical second-order surface profile. This is further clarified when considering the close-ups provided in figures 5.37 and 5.38. These figures show the surface profiles in the initial interval of $1s \leq t \leq 20s$ and therefore exclude any reflections from the downstream beach. Despite the fact that some small departures from the expected surface profile remain when a second-order control signal is applied (figure 5.38), the contrast with the data generated using first-order control (figure 5.37) is clearly established. However, given the influence of reflections from the far side beach (Appendix G), some significant departures from the expected surface profile remain for $t > 50s$ (figure 5.36). This is particularly pronounced in the regions of relatively small wave height such as $50s < t < 64s$ where the reflected energy of the large preceding waves ($35s < t < 50s$) contaminates the record.

In addition the the comments above it is important to note that the significant wave height achieved using first- and second-order control varies slightly. Based on the same first-order input spectrum, the first-order control signal led to a significant wave height of $H_s = 0.132m$, whereas the second-order signal created as sea state with $H_s = 0.137m$. Moreover, the maximum crest elevation under first-order control is $\eta_{c,max} = 92.43mm$ and increased to $\eta_{c,max} = 101.5mm$ under second-order control. This latter increase, representing nearly 10%, is very important when considering model tests where the maximum crest elevation is crucial; a typical example being the occurrence of impact loads on decks of offshore structures.

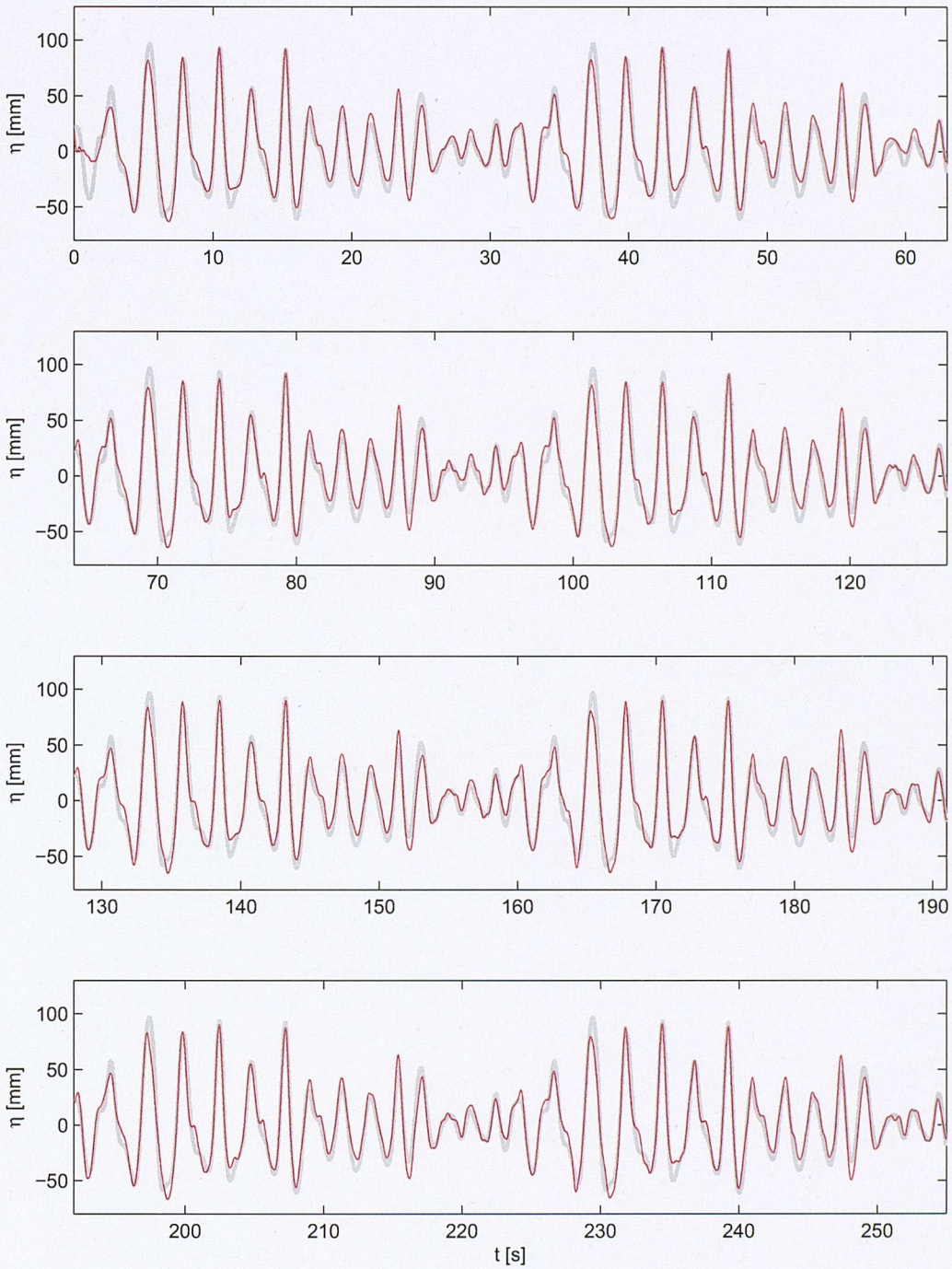


Figure 5.35: Case 1: Surface elevation at $x = 2.15m$ based on first-order force control, JONSWAP spectrum with $\gamma = 3.3$, $f_p = 26/64Hz$ and $H_s = 0.132m$; Theoretical second-order surface elevation, Measured surface elevation; Note: the four sub-plots are representations of a continuous recording ranging from $t = 0s$ to $t = 256s$; the sea state having a repeat period of $T_r = 64s$.

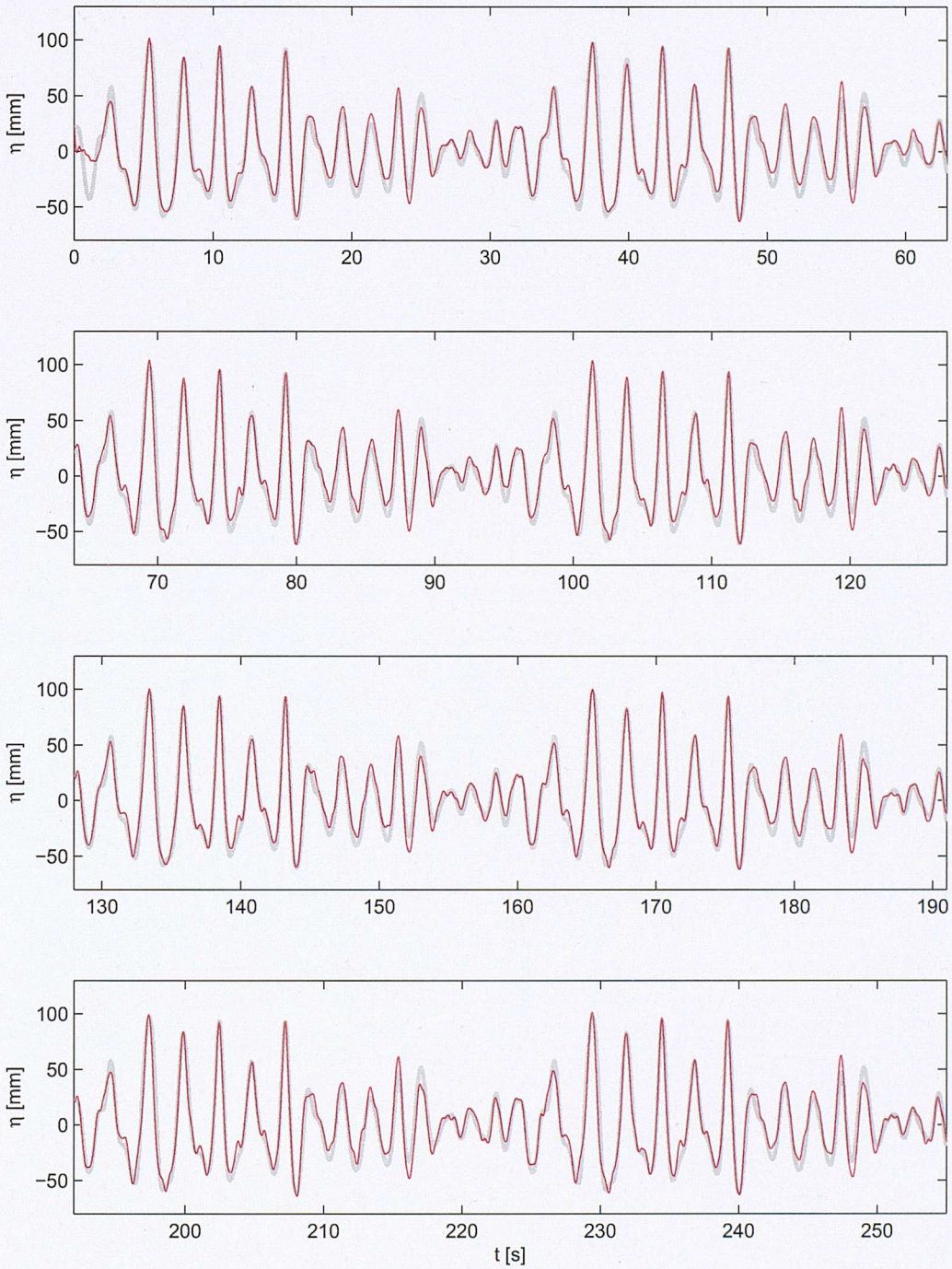


Figure 5.36: Case 1: Surface elevation at $x = 2.15m$ based on second-order force control, JONSWAP target spectrum with $\gamma = 3.3$, $f_p = 26/64Hz$ and $H_s = 0.137m$; —— Theoretical second-order surface elevation, —— Measured surface elevation; Note: the four sub-plots are representations of a continuous recording ranging from $t = 0s$ to $t = 256s$; the sea state having a repeat period of $T_r = 64s$.

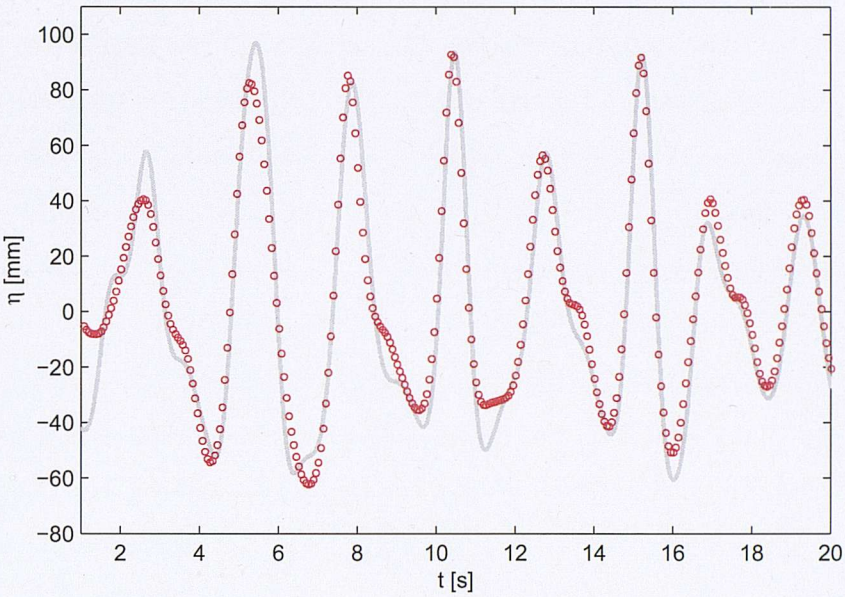


Figure 5.37: Case 1 based on first-order force control, close-up of the surface elevation shown in figure 5.35; data lying in the range $1s \leq t \leq 20s$; —— Theoretical second-order surface elevation, ○ Measured surface elevation

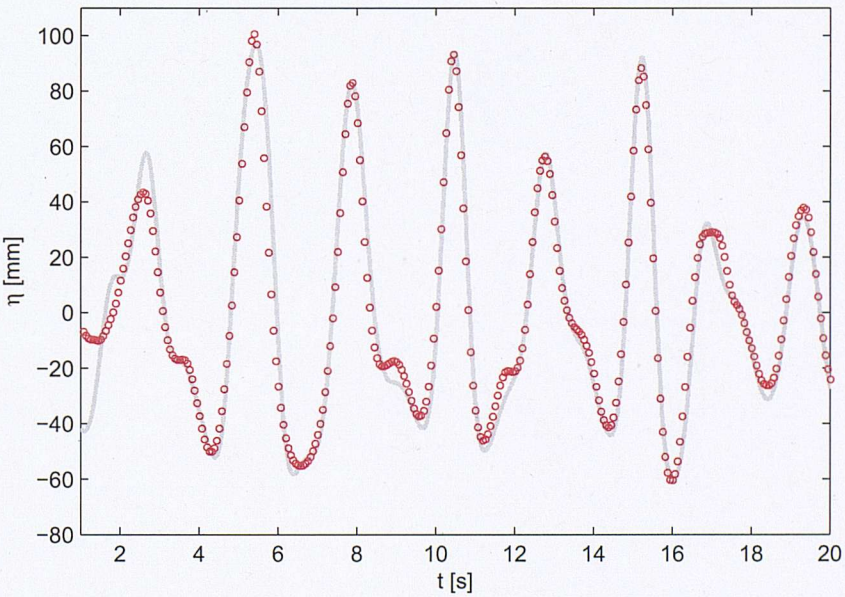


Figure 5.38: Case 1 based on second-order force control, close-up of the surface elevation shown in figure 5.36; data lying in the range $1s \leq t \leq 20s$ —— Theoretical second-order surface elevation, ○ Measured surface elevation

The second test case concerns a sea state in which the significant wave height has been increased to $H_s \approx 0.16m$. The surface elevation based on a first-order force-control signal is shown in figure 5.39. Figure 5.40 concerns the same wave spectrum based on a second-order force-control signal. As before, close-ups of the initial interval ($1s \leq t \leq 20s$) are provided in figures 5.41 and 5.42.

This second case was chosen to illustrate the effect of spurious sub-harmonics when generating irregular waves. Considering the surface elevation under first-order force control in the interval $8s \leq t \leq 12s$ (this is best seen in figure 5.41), a significant departure from the expected surface profile is observed. This is despite the relatively small waves in the interval and is hence readily identified as a free travelling sub-harmonic wave. Considering the same time interval, but based on second-order force control (figure 5.42), much better agreement between the predicted and the measured data is observed. Similar arguments apply to the two following wave troughs at $t \approx 14s$ and $t \approx 16.5s$.

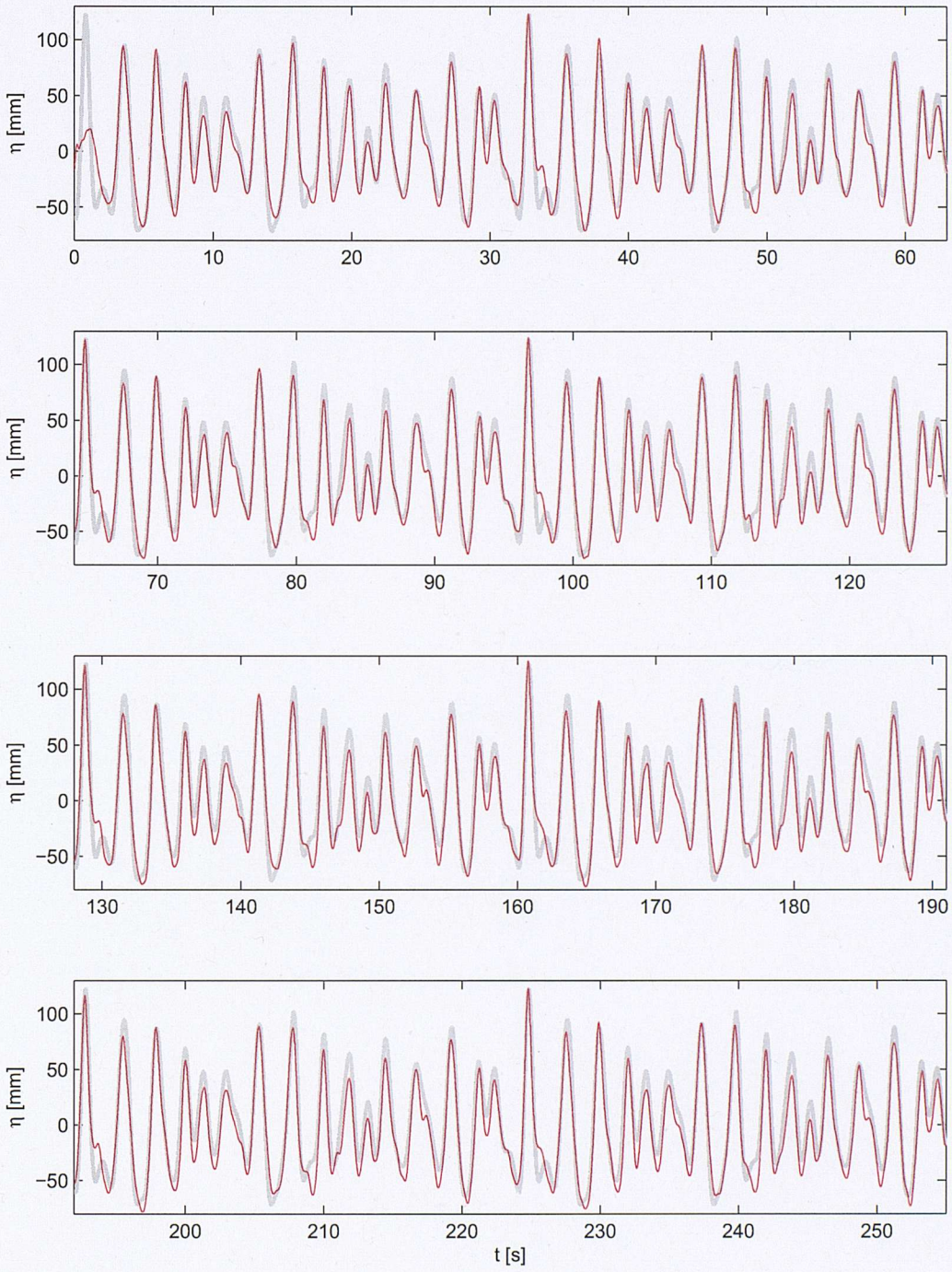


Figure 5.39: Case 2: Surface elevation at $x = 2.15m$ based on first-order force control, JONSWAP spectrum with $\gamma = 3.3$, $f_p = 26/64Hz$ and $H_s = 0.159m$; Theoretical second-order surface elevation, Measured surface elevation; Note: the four sub-plots are representations of a continuous recording ranging from $t = 0s$ to $t = 256s$; the sea state having a repeat period of $T_r = 64s$.

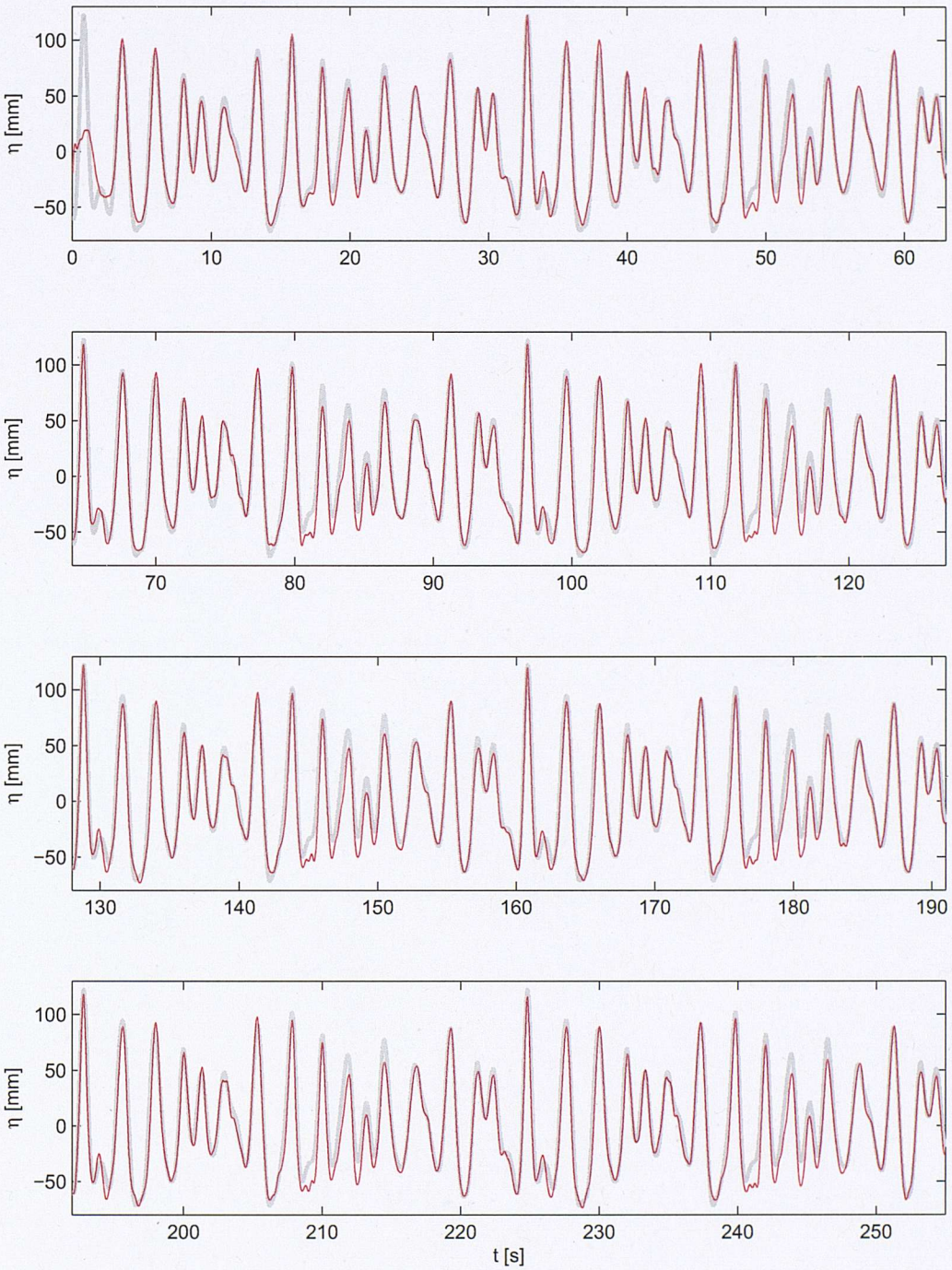


Figure 5.40: Case 2: Surface elevation at $x = 2.15m$ based on second-order force control, JONSWAP spectrum with $\gamma = 3.3$, $f_p = 26/64Hz$ and $H_s = 0.163m$; Theoretical second-order surface elevation, Measured surface elevation; Note: the four sub-plots are representations of a continuous recording ranging from $t = 0s$ to $t = 256s$; the sea state having a repeat period of $T_r = 64s$.

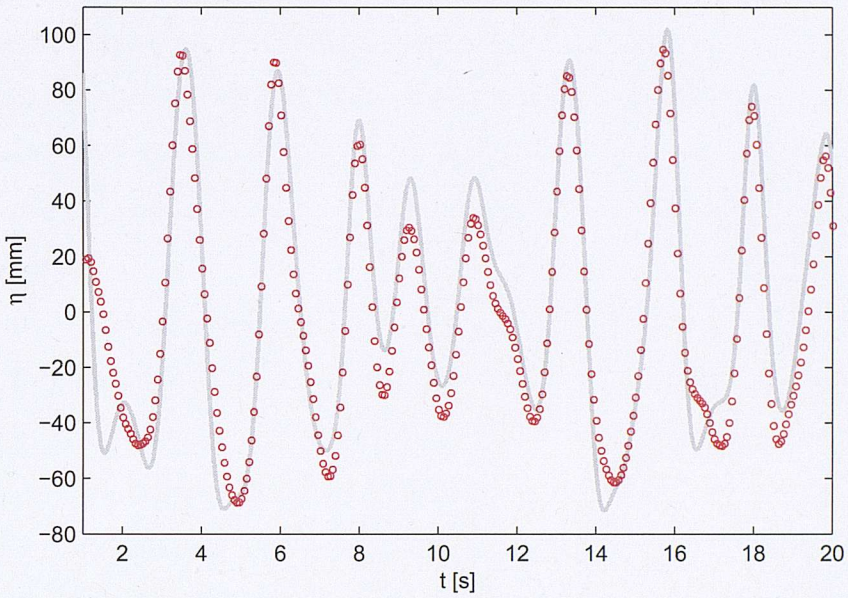


Figure 5.41: Case 2 based on first-order force control, close-up of the surface elevation shown in figure 5.39; data lying in the range $1s \leq t \leq 20s$; —— Theoretical second-order surface elevation, ○ Measured surface elevation

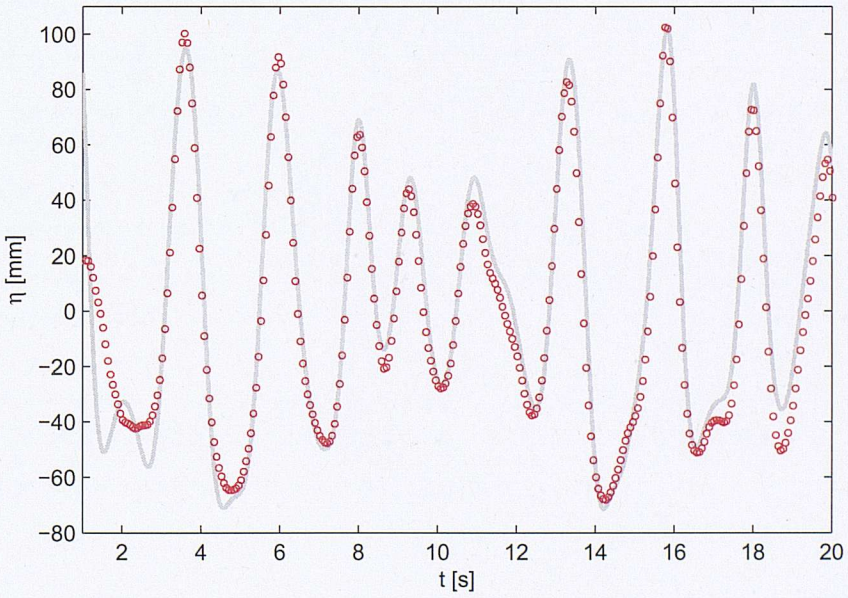


Figure 5.42: Case 2 based on second-order force control, close-up of the surface elevation shown in figure 5.40; data lying in the range $1s \leq t \leq 20s$; —— Theoretical second-order surface elevation, ○ Measured surface elevation

To quantify the departures in each case, the minimum and maximum surface elevations were determined; this data being based on a zero up-crossing analysis. Table 5.2 gives the root mean square (RMS) deviation between the predicted and the measured results for an analysis in the interval $5s \leq t \leq 64s$. In both cases the errors are significantly reduced when the generation is based on a second-order control signal.

Overall, the benefits of second-order force control are clearly visible in all these figures. Furthermore, in addition to the points already noted, the wave quality remains superior to that under first-order control when consecutive cycles of the spectrum are considered. With the repeat period of the spectrum being $T_r = 64s$, each of the four sub-plots in figures 5.35, 5.36, 5.39 and 5.40 represents the same spectral content. Based on a second-order force-control signal (figures 5.36 and 5.40), the departures from the theoretical second-order surface profile remain small in consecutive cycles; any minor deviations probably being due to reflections from the downstream beach.

Quantity		First-order force control	Second-order force control
		Case 1	
RMS (η_{max})	$[mm]$	12.4	4.5
RMS (η_{min})	$[mm]$	9.9	5.4
		Case 2	
RMS (η_{max})	$[mm]$	9.9	6.6
RMS (η_{min})	$[mm]$	8.5	5.2

Table 5.2: RMS deviation of maximum and minimum surface elevation with the data being based on a zero up-crossing analysis

5.10 Conclusions

A second-order force-control theory appropriate to piston-type wave machines and irregular waves has been presented. Even though large parts of this theory are based on earlier chapters, some additional comments concerning the phasing of the individual wave components were made. An extensive experimental investigation covering both regular and irregular wave generation under first- and second-order control was presented. In most wave cases, the agreement between the theoretical results and the experimental data is very good; the benefits of adopting second-order force control being clearly noted.

In contrast to the flap-type machines considered within Chapter 4, the spurious wave modes when based on a first-order force-control signal are very significant. The application of a second-order control signal greatly reduces these spurious modes and enables the generation of waves of high quality. The combination of active absorption and second-order force control established a sea state that is in very close agreement with the second-order prediction for a large number of repeat periods.

6

Multi-directional Wave Generation using Force Control

6.1 Chapter Overview

The present chapter concerns the generation and absorption of directional waves in a facility where the absorption mechanism is based on force-control. In contrast to the previous chapters, only first-order effects are considered. To put the present work into context, the chapter begins with a brief introduction covering some of the theoretical aspects of wave generation in a three-dimensional wave basin. The hydrodynamic coefficients for an infinitely long wave maker are then derived and a first-order transfer function presented.

Based on this first-order transfer function, preliminary experimental data suggested some significant departures from the expected wave content. This was particularly pronounced for the generation of short wave components at large angles. In seeking an explanation for those departures, a theory for wave makers of finite length as well as a theory concerning the finite-segment width were revised.

The present results show that by incorporating the effects of finite-segment width within the theoretical transfer function, a significant improvement in the experimental data can be achieved. At present, the two theories are combined

in a somewhat *ad-hoc* manner; a consistent formulation being envisaged for future work. Whereas the comparison with the *ad-hoc* approach primarily concerns the amplitude content for random phase wave spectra, an extensive experimental validation of the phase information is also provided. For this purpose, a number of focused wave events are generated, including both uni-directional and multi-directional, or directionally spread, wave groups.

6.2 Introduction

In the context of wave making, the ultimate goal of any laboratory model testing apparatus must be the simulation of the ocean at scale. Even though many preliminary studies are performed in 2-dimensional (2D) wave flumes, most advanced testing is inevitably undertaken in 3-dimensional (3D) wave basins. Wave flumes are often built as very long channels at reasonable cost; reflections from the beach taking a relatively long time to influence the testing area. In contrast, in multi-directional wave basins it is often the case that only a few seconds remain before waves reflected from the beach contaminate the testing area. Absorbing these waves on the wave maker boundary is crucial in order to prevent the built-up of energy in the basin. This is particularly important for long wave components; a regime where beach absorption is inherently poor.

A multi-directional absorbing facility was first described by Salter (1982). More recently, the IAHR seminars '*Wave Analysis and Generation in Laboratory Wave Basins*' (1987) and '*Multi-directional Waves and their Interaction with Structures*' (1997) contributed a large number of publications in the field of multi-directional wave generation, some of which concern absorbing facilities. Notable publications include Mansard et al. (1997), giving a review on multi-directional wave making facilities, Schäffer & Klopman (1997) reviewing multi-directional absorption strategies (also Schäffer & Klopman (2000)) and Hald & Frigaard (1997), presenting a novel method for active absorption of multi-directional waves.

All the studies noted above are limited to first-order effects. In contrast,

Schäffer & Steenberg (2003) presented a second-order wave maker theory for multi-directional waves and propose a long term goal as the combination of this theory with active absorption. However, the author is unaware of any experimental evidence for this multi-directional second-order theory (even excluding active absorption); an indication for the challenges associated with such a generation technique.

Similar arguments apply to active absorption in multi-directional facilities; very limited experimental evidence of their 3D absorption characteristic having been provided over the past decades. To date there is only one as yet unpublished study that discussed the absorption performance of waves in a 3D environment, but this relates to numerical computations (Newman 2008).

The present study develops the theoretical aspects of multi-directional generation and absorption for a facility where the absorption technique is based on force control, as discussed by Salter (1982). The theoretical formulation of this particular strategy was given in Chapters 3 and 4. In contrast to the earlier work, the present chapter derives the hydrodynamic coefficients for the generation of oblique waves; their derivation being based on the assumption of an infinitely long wave maker [1]. In working towards this result, which is presented in §6.3.3, it becomes clear that this assumption places some restrictions on the accuracy of the results. In light of this, §6.3.1 argues the need for adopting such a solution and indicates the range of applicability. Moreover, the effects related to a 'snake-type' geometry with a finite wave maker segment width are investigated in §6.3.2.

Based on an optimal 2D absorption strategy for an infinitely long wave maker, the 3D absorption characteristic is evaluated and the relative merits of applying an advanced 3D strategy are discussed. With the absorption technique having been established, a theoretical transfer function for one particular wave basin is derived. However, the approach adopted is general and could equally be applied to other 3D wave basins.

[1] In the context of the present work the term '*wave maker*' refers to the entire wave generating boundary and not to individual segments thereof. Moreover, the term '*length*' will be used to illustrate the extent of this boundary. In contrast, the term '*width*' refers to the extent of the individual wave maker segments.

The validity of the theoretical model is investigated in an accompanying experimental study (§6.6). Within this aspect of the work, the theoretical transfer function is directly compared to a previously published empirical calibration approach developed in the same facility (Masterton & Swan 2008). In addition, experimental data relating to an *ad-hoc* approach, that seeks to combine the force-based theory and the theory concerning the finite segment width, is also presented.

6.3 Directional Wave Generation

6.3.1 Directional Wave Maker of Finite Length

A theory describing finite-length multi-directional wave makers has been developed by Dalrymple (1985) and was summarised in Naito (2006). To identify the effective basin usage area appropriate to the experimental study presented later on, a brief review is included here. In accordance with the notation in Chapter 2, the wave maker is oriented along the y-axis. The waves propagate in the positive x-direction; the x-axis being bound by $x = 0$, where the wave maker is located, and $x = +\infty$. For simplicity, side wall reflection is neglected and the basin extents to $y = \pm\infty$. Within this infinite basin, a finite wave maker of length $2b$ is located between $-b \leq y \leq b$. Furthermore, the contours of the wave crests and the y-axis define an angle α and the wave direction vector $\vec{k}$ may be expressed by $\vec{k} = (k_x, k_y) = k(\cos\alpha, \sin\alpha)$. The wave length of the progressive wave is denoted by λ_0; this symbol being chosen to avoid confusion with the deep water wave length, L_0. The schematic given in figure 6.1 illustrates this layout of a 3D wave basin and defines the terms involved.

Following Dalrymple (1985), the progressive part of the velocity potential in this domain may be expressed as

$$\Phi_p(x,y,z,t) = \Re\left\{-\frac{iR}{2}\cosh k(h+z)e^{-i\omega t}\int_{-b}^{b} e^{ik_{0y}\zeta}H_0^{(1)}\left[k\sqrt{x^2+(y-\zeta)^2}\right]d\zeta\right\}, \tag{6.1}$$

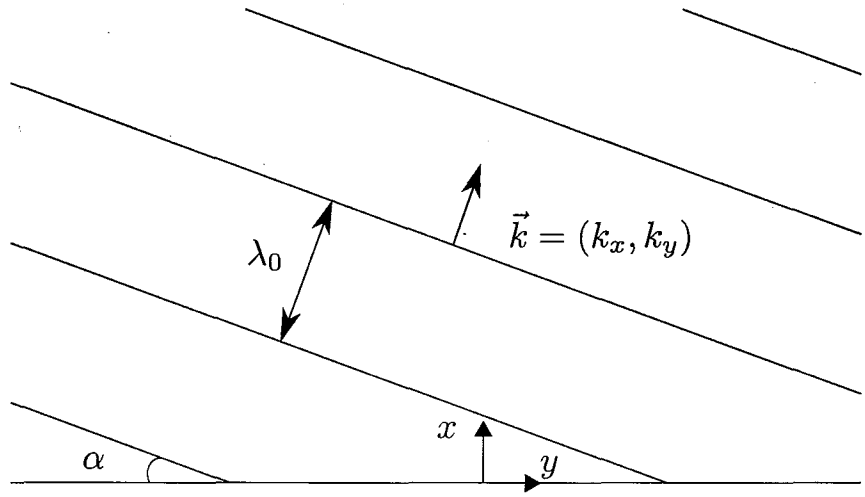


Figure 6.1: Layout of a 3D wave basin. Angled lines represent the crest contours of a progressive wave train propagating at an angle α.

where $H_0^{(1)}$ is the Hankel function of the first kind and R is a geometry dependent coefficient. Based on the expression of the velocity potential, the surface elevation in the wave basin may be computed. Further detail concerning the derivation of this result is given in Appendix E.

Figure 6.2 shows a contour plot of the surface elevation within a section of this infinite wave basin. Only the progressive wave component is shown; the evanescent modes having been neglected. The water depth was set to $h = 1.5m$ and a wave maker of length $2b = 0.5m$ is located between $-0.25m \leq y \leq +0.25m$. A water depth of $h = 1.5m$ was chosen as this corresponds to the nominal water depth of the wave basin at Imperial College; experimental data relating to this facility being presented in §6.6. At this stage, it is important to note that this finite wave maker consists of indefinitely small segments. The wave maker is generating a regular wave with frequency $f = 1.0Hz$ and a wave propagation direction of $\alpha = 0°$; the surface elevation having been normalised with respect to the maximum wave height (or trough-crest excursion). A radial diffraction pattern around the centre of the wave maker at $(x, y) = (0, 0)$ is readily identified. With increasing distance from the wave maker, the energy becomes progressively more spread out and the

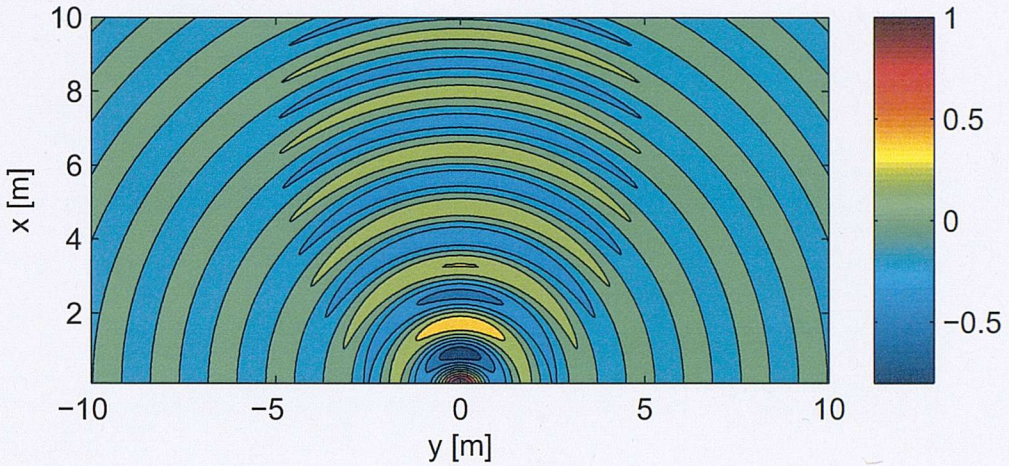


Figure 6.2: Normalised surface elevation contours for $h = 1.5m$, $f = 1.0Hz$ and $\alpha = 0\,°$; the wave maker being located at $-0.25m \leq y \leq 0.25m$.

maximum wave height decreases.

In contrast, figure 6.3 concerns the case where the wave maker length has been increased to $2b = 20m$. Furthermore, the normalised surface elevations shown in figure 6.3 are based on three different propagation directions: (a) $\alpha = 15\,°$, (b) $\alpha = 30\,°$ and (c) $\alpha = 45\,°$. The wave frequency and the water depth are both held constant at $f = 1.0Hz$ and $h = 1.5m$ as discussed above.

Observing figure 6.3, the surface elevation now defines a regular wave train propagating in a given direction. However, only part of the area of the wave basin may be used for model testing. This is particularly evident for the wave case shown in sub-plot (c) corresponding to $\alpha = 45\,°$. In this case, approximately two thirds of the basin is available for testing. Further observation of figure 6.3 (c) shows that a notable variation of wave height occurs along the crests which needs to be taken into account. In this regard, it is also important to note that the theoretical model does not include any side wall reflections which would further reduce the testing area. Nevertheless, the effect of diffraction and the effective basin usage area are now clearly identified.

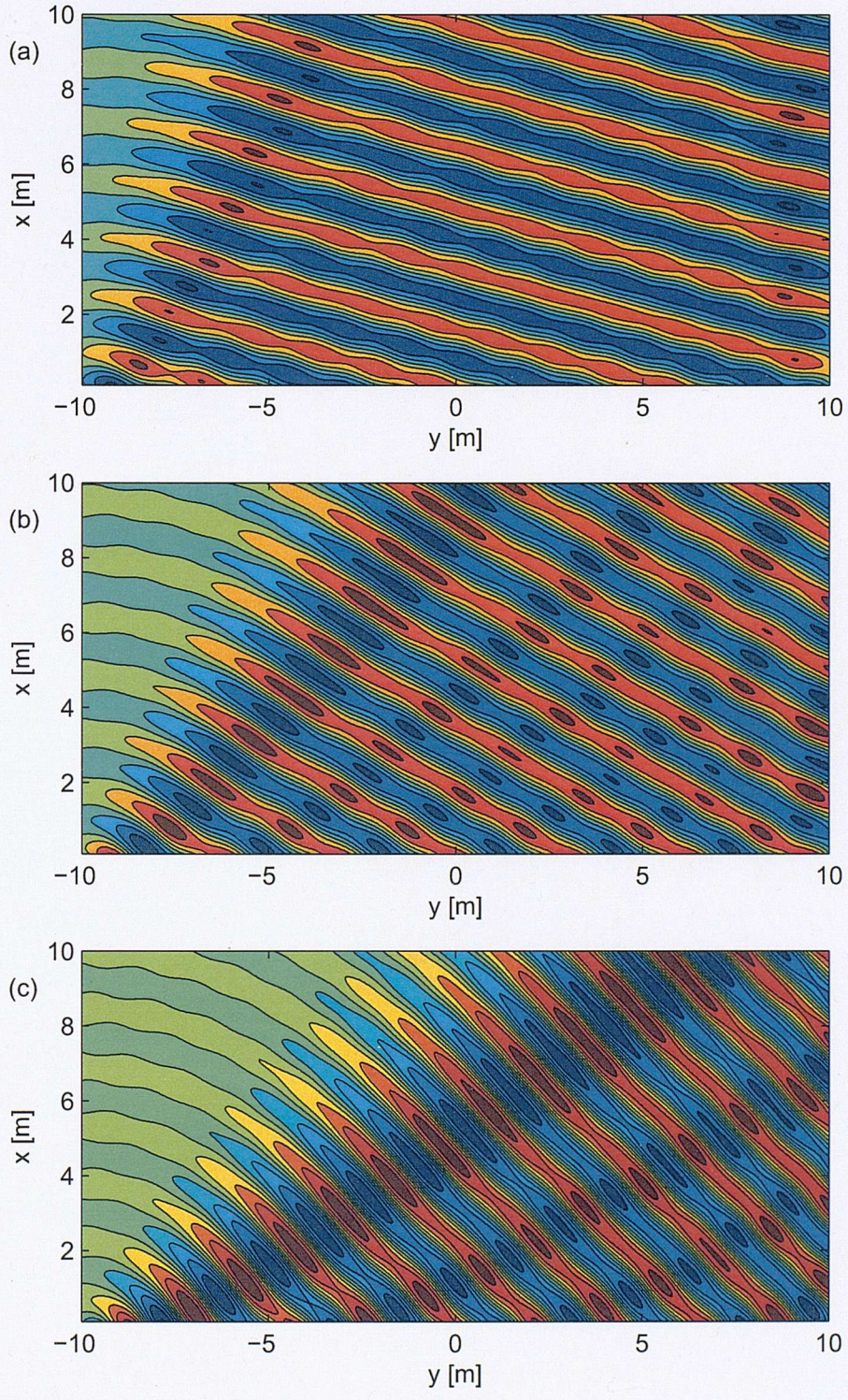


Figure 6.3: Normalised surface elevation contours for $h = 1.5m$ and $f = 1.0Hz$; (a) $\alpha = 15°$, (b) $\alpha = 30°$ and (c) $\alpha = 45°$; the wave maker being located at $-10m \leq y \leq 10m$.

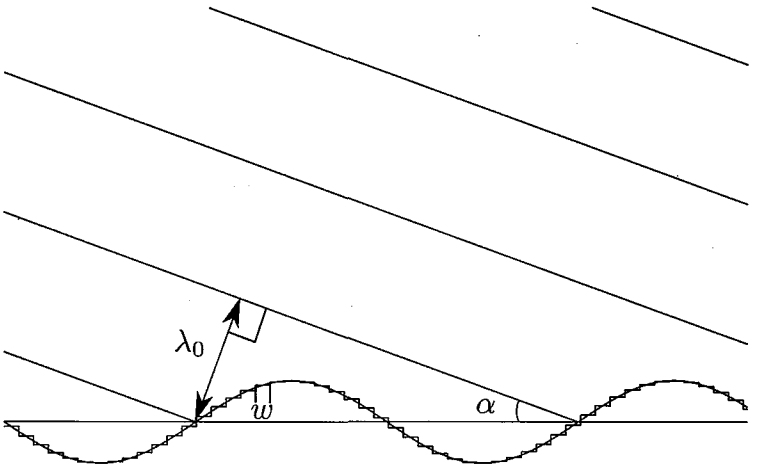


Figure 6.4: Motion approximated by a piecewise constant function as adopted in a realistic segmented-type wave maker

6.3.2 Segmented-type Wave Generators

In reality, a wave maker will consist of individual segments of finite width and the sinusoidal velocity distribution along the y-axis, appropriate to the generation of oblique waves, is approximated by a piecewise constant function. Figure 6.4 illustrates the wave maker motion and the crest lines of an oblique progressive wave train; the wave length of the progressive wave and the angle of wave propagation again being denoted as λ_0 and α respectively. Using the notation defined in figure 6.4, it is clear that

$$\sin\alpha = \frac{\lambda_0}{Nw}, \tag{6.2}$$

where w is the individual wave board width and the integer N is the number of wave boards in one oscillation in the y-direction. The demand signal phase shift between two adjacent wave makers is thus given by

$$\varphi = \frac{2\pi}{N} \tag{6.3}$$

and equation (6.2) may be rewritten as

$$\sin\alpha = \frac{\varphi\lambda_0}{2\pi w}. \tag{6.4}$$

In seeking an explanation for the existence of spurious waves when using finite width paddles, Sand & Mynett (1987) derived an expression for the wave modes created by a segmented-type wave maker. Their result has a similar form to equation (6.4) and is given by

$$\sin \alpha_p = \frac{(\varphi - 2\pi p)\lambda_0}{2\pi w}, \tag{6.5}$$

where p is an integer with the discrete values of $0, \pm 1, \pm 2...$; a full derivation of this result being given by Sand (1979). The mode $p = 0$ corresponds to the desired wave component (equation 6.5 reduces to equation 6.4) and values of $|p| > 0$ represent the unwanted or spurious waves. Sand & Mynett (1987) also showed that all valid values of p must lie within the interval

$$\frac{\varphi}{2\pi} - \frac{w}{\lambda_0} < p < \frac{\varphi}{2\pi} + \frac{w}{\lambda_0}. \tag{6.6}$$

Furthermore, the ratio between the spurious wave amplitudes and the amplitude of the primary desired wave was shown by Sand (1979) to be

$$a_p/a_0 = -\frac{\sin(\pi(pN-1)/N)}{(pN-1)\sin(-\pi/N)}. \tag{6.7}$$

Assuming that the wave board width, the wave frequency, the wave propagation angle and the water depth are given by $w = 0.36m$, $f = 1.8Hz$, $\alpha = 45\,^\circ$ and $h = 1.5m$, then p must lie in the range $-0.22 < p < 1.27$. Consequently, the valid values of p are 0 and 1. Substituting this result into equation (6.5) gives the two angles of wave propagation: in addition to the desired progressive wave at $\alpha_0 = 45\,^\circ$, a spurious progressive wave at $\alpha_1 = -39.2\,^\circ$ arises. Using equation (6.7), the amplitude of this latter component is found to be 112% of the primary wave amplitude; an unwanted or spurious wave mode having an amplitude larger than the desired wave is thus generated.

This set of equations is best illustrated as shown in figure 6.5; the dimensionless ratio λ_0/w being plotted against the angle of wave propagation α. Note that in

contrast to the representation given in figure 6.5, Sand & Mynett (1987) presented a related figure in which the ordinate was scaled by $\sin\alpha$. Observing the occurrence of spurious wave modes, four distinct regions may be identified within figure 6.5.

i. For values of $\lambda_0/w > 2$, waves with a propagation direction of up to $\alpha = 90\,°$ may be generated and spurious modes do not exist.

ii. For values of $\lambda_0/w < 2$, the solid line represents the limit of $p = 0$. On the right hand side of this line, only the desired progressive mode ($p = 0$) exists.

iii. In between the dashed line and the solid line, one or more spurious modes are generated ($p \geq 1$). Sand & Mynett (1987) give a more detailed representation of this region including the number of modes generated.

iv. The dashed line represents the limit of $\varphi = \pi$. In this case, two adjacent wave makers are exactly out of phase and the spurious wave is of equal magnitude when compared to the desired wave. For all cases on the left hand side of the dashed line, the spurious modes arising due to the finite segment width are larger than the desired wave.

The representation given in figure 6.5 is plotted with the dimensionless ratio λ_0/w. In contrast, figure 6.6 illustrates the spurious modes associated with the wave basin located in the Hydrodynamics Laboratory at Imperial College London (ICL); the calibration of this particular facility being presented by Masterton & Swan (2008). Given that figure 6.6 is plotted in terms of wave frequency f, the directional sense of the abscissa is inverted when compared to figure 6.5.

The wave maker at ICL consists of 56 individual segments and spans a total length of $20m$; the paddle width being approximately $w = 0.36m$. The wave basin is operated at a nominal water depth of $h = 1.5m$. Observing figure 6.6 in detail, it is important to note that the wave field is free of oblique spurious modes for frequencies $f < 1.5Hz$. This is in marked contrast to frequencies in the region of $f \approx 2Hz$. Even for wave propagation angles as small as $\alpha = 30\,°$, the spurious wave modes may be as large as the wanted primary wave.

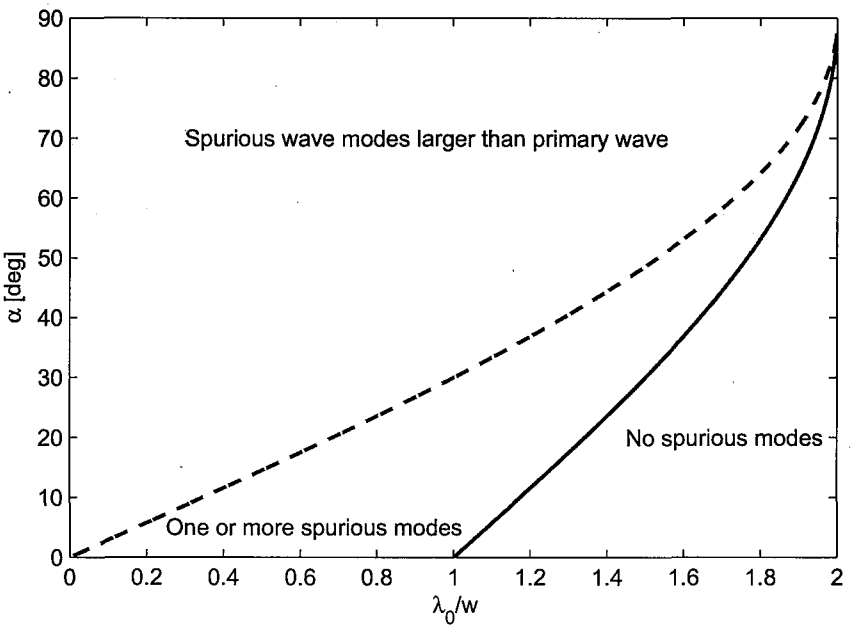


Figure 6.5: Spurious wave modes arising from the generation of oblique waves based on Sand & Mynett (1987); —— Boundary between $p = 0$ and $p \geq 1$, – – Limiting case with $\varphi = \pi$. Note this figure differs from that of Sand & Mynett in that they scaled their ordinate by $\sin\alpha$.

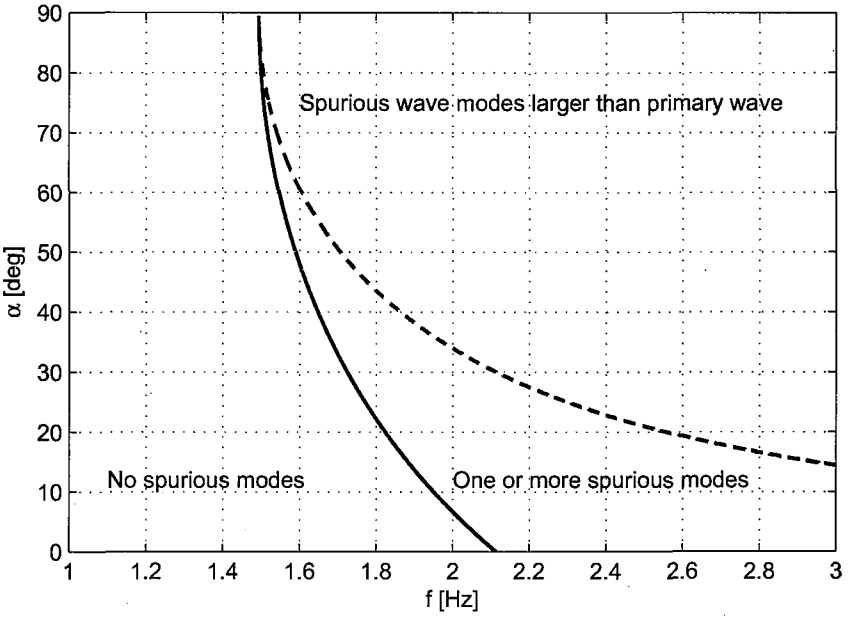


Figure 6.6: Spurious wave modes for the generation of oblique waves with $h = 1.5m$ and $w = 0.36m$; —— Boundary between $p = 0$ and $p \geq 1$, – – Limiting case with $\varphi = \pi$.

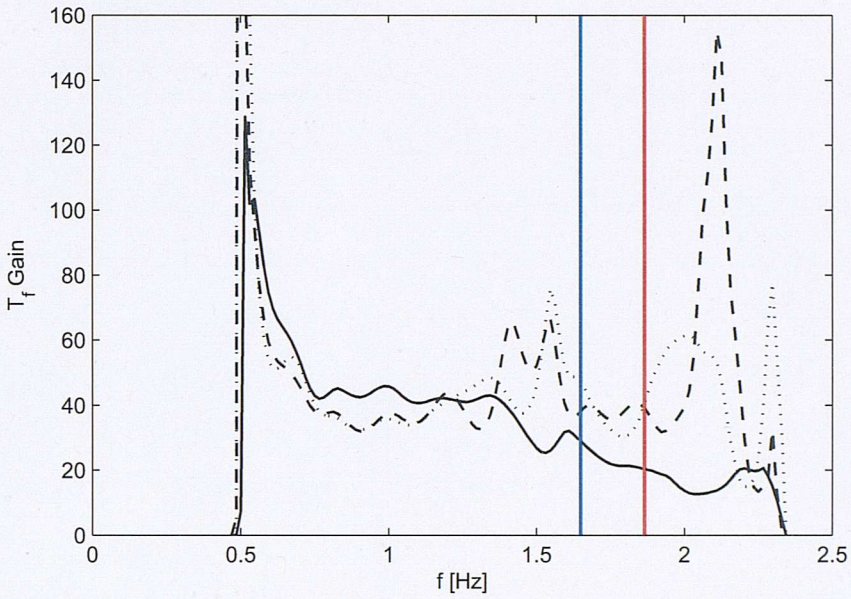


Figure 6.7: Empirical transfer function for a 3D wave basin, after Masterton & Swan (2008); —— $\alpha = 0\,°$, – – $\alpha = 40\,°$, · · · · $\alpha = -40\,°$; —— Limit for $p = 0$ and —— Limiting case with $\varphi = \pi$, both for $\alpha = \pm 40\,°$

Figure 6.7 shows the calibration data for the wave basin at ICL based on the results presented in Masterton & Swan (2008). The calibration curves for $\alpha = 0\,°$ and $\alpha = \pm 40\,°$ are shown. In addition to these calibration curves, the limits for $p = 0$ (solid line in figure 6.6) and $\varphi = \pi$ (dashed line in figure 6.6) are provided for a wave propagation angle of $\alpha = \pm 40\,°$. Relating to the above discussion, the calibration results for $\alpha = \pm 40\,°$ and frequencies on the right hand side of these lines must be questioned, particularly those on the right hand side of the line representing $\varphi = \pi$. A detailed discussion concerning the validity of the empirical transfer function shown in figure 6.7 is given in Appendix F.

6.3.3 Infinitely Long Wave Maker

The following discussion presents the theory for an infinitely long wave maker; the velocity distribution along the wave maker being assumed to vary as a continuous function. The derivation of the hydrodynamic coefficients and the theoretical force transfer function will be based upon this theory. However, the effects introduced by a wave maker of finite length and the finite segment width will be discussed further within the experimental validation of the force transfer function.

Adopting a formulation and notation identical to that presented in Chapter 2 and applying this to a 3D problem [2], yields the solution to the first-order velocity potential

$$\Phi^{(1)}(x,y,z,t) = \frac{1}{2}\left\{\frac{igX_a}{\omega}\sum_{j=0}^{\infty} e_j \frac{\cosh k_j(z+h)}{\cosh k_j h} e^{i(\omega t - \vec{k}_j\vec{x})} + c.c.\right\} \tag{6.8}$$

and the expression of the paddle motion

$$X_0^{(1)} = \frac{1}{2}\left\{-iX_a e^{i(\omega t - k_{0y}y)} + c.c.\right\}. \tag{6.9}$$

The wave number vector $\vec{k}_j = (k_{jx}, k_{jy}) = k_j(\cos\alpha_j, \sin\alpha_j)$ for the progressive wave mode with $j = 0$ is identical to that defined in figure 6.1. Comparing this latter solution for the velocity potential (equation 6.8) to that for the wave maker of finite length (equation 6.1), the benefits in terms of ease of solution are evident.

Following Schäffer & Steenberg (2003), the solution for the wave field coefficients appropriate to the generation of oblique waves, e_j, is readily shown to be

$$e_j = \frac{1}{\cos\alpha_j} c_j, \tag{6.10}$$

where the coefficients c_j are the solution to the 2D problem (Chapter 2). Furthermore, α_j is the direction of wave propagation generalized to complex wave modes.

[2] The boundary conditions in 3D are very similar to those presented for the 2D case. For brevity, the complete formulation is omitted here; the reader being referred to Schäffer & Steenberg (2003) for further details.

Further details concerning the derivation of this result is given in Appendix A. The expression for $\cos\alpha_j$ for this general complex case may be rewritten as

$$\cos\alpha_j = \sqrt{1 - \frac{k^2\sin^2\alpha}{k_j^2}} = \begin{cases} \cos\alpha \leq 1 & \text{for } j = 0 \\ \sqrt{1 - \frac{k^2\sin^2\alpha}{|k_j|^2}} \geq 1 & \text{for } j > 0 \end{cases} \tag{6.11}$$

Observing this latter representation for $\cos\alpha_j$, it is important to note that for the real solution ($j = 0$) the expression simply evaluates to $\cos\alpha_0$ which is always less than or equal to one. As a result, the coefficient for the generation of oblique waves, e_0, is larger than c_0. The relation between the amplitude of the paddle motion, X_a, and the amplitude of the oblique progressive wave mode is

$$A = e_0 X_a, \tag{6.12}$$

from which it is clear that, for a particular wave board amplitude, the progressive wave amplitude increases in the oblique case; the factor of proportionality being $1/\cos\alpha$ for all frequencies. At this stage it is important to note that in the remainder of this chapter the wave propagation angle α refers to the propagation direction of the progressive wave mode, the subscript 0 (as in α_0) being omitted.

The generation of the evanescent wave modes ($j > 0$) needs further consideration. For this purpose, the first-order coefficients for a range of wave propagation directions are presented in figures 6.8 and 6.9, concerning piston-type and flap-type wave machines respectively. In both figures the coefficient for the progressive wave mode, e_0, and the infinite sum $i\sum_{j=1}^{\infty} e_j$ are shown.

As noted above, the progressive wave amplitude for oblique waves obeys a $1/\cos\alpha$ relationship when compared to the 2D solution. This is particularly evident within figure 6.8 where the deep water limit of $c_0 = 2$ ($e_0 = c_0$ for $\alpha = 0°$) increases to $e_0 = 4$ for $\alpha = 60°$. On the contrary, considering the sum of the evanescent modes ($j = 1..\infty$), it is clear that their amplitude decreases with increasing wave propagation angle (figures 6.8 and 6.9). For example, the magnitude

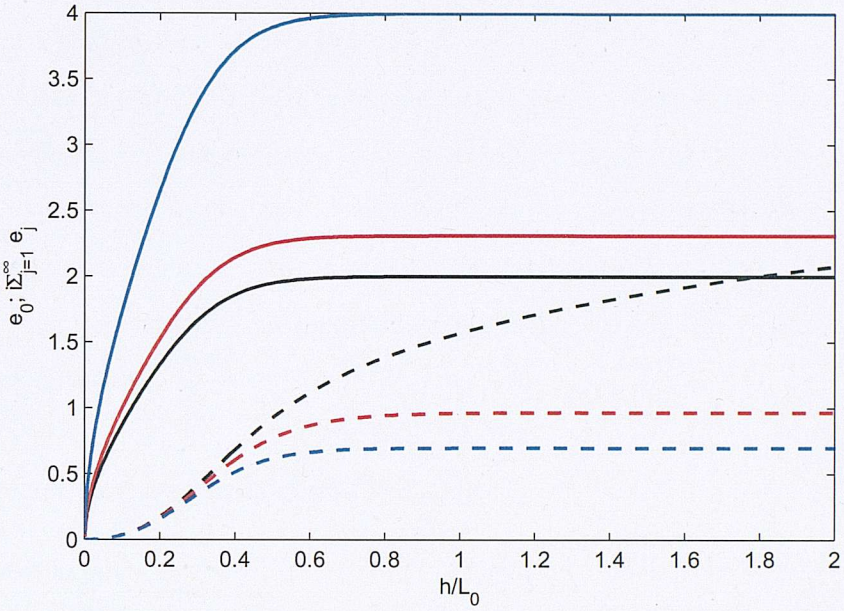


Figure 6.8: Dimensionless first-order coefficients for a piston-type wave maker. The solid lines represent e_0 and the dashed lines represent $i\Sigma_{j=1}^{\infty} e_j$; — $\alpha = 0\,°$, — $\alpha = 30\,°$, — $\alpha = 60\,°$

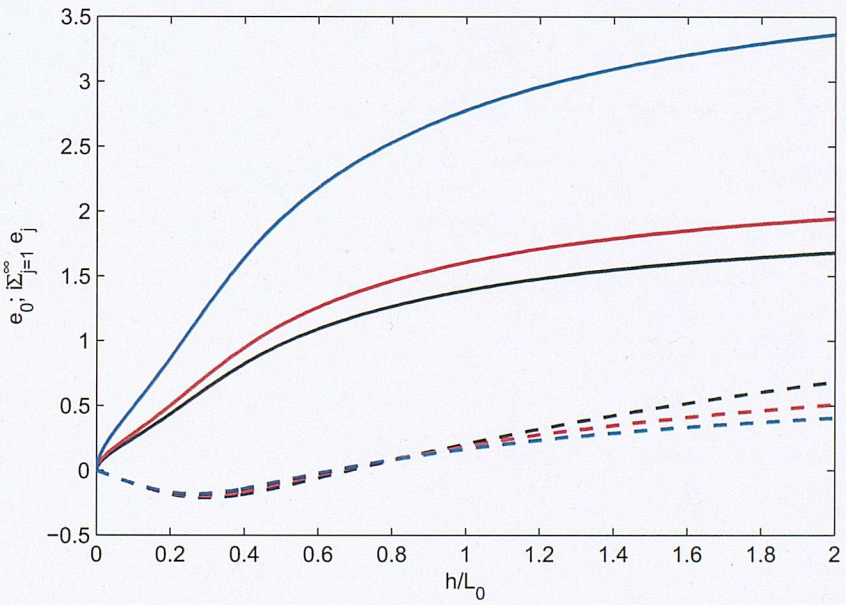


Figure 6.9: Dimensionless first-order coefficients for a flap-type wave maker ($d/h = 0.5$). The solid lines represent e_0 and the dashed lines represent $i\Sigma_{j=1}^{\infty} e_j$; — $\alpha = 0\,°$, — $\alpha = 30\,°$, — $\alpha = 60\,°$

of the evanescent mode sum for the piston-type machine shown in figure 6.8 decreases from $i\sum_{j=1}^{\infty} e_j \approx 2$ ($\alpha = 0°$) to $i\sum_{j=1}^{\infty} e_j \approx 0.7$ ($\alpha = 60°$) for $h/L_0 = 1.8$. As a result, the ratio of $(\sum_{j=1}^{\infty} e_j)/e_0$ reduces significantly when generating oblique waves. This directly affects the hydrodynamic coefficients and hence the machine's absorption characteristic and the first-order force transfer function. It should be noted that the increase in e_0 is anticipated and easily argued on physical grounds. In contrast, the decrease in the evanescent mode sum is far less intuitive and needs careful consideration.

6.3.4 Hydrodynamic Coefficients

Chapter 3 discussed optimum absorption strategies for wave making devices and showed that the hydrodynamic coefficients are crucial when adopting a force based absorption approach. The hydrodynamic coefficients in the oblique case are readily derived by replacing the 2D velocity potential (equation 3.12) with the expression presented in equation (6.8).

In so doing, the only difference arising between the 2D case and the 3D case is that the first-order wave field coefficients (c_j) must be replaced by the coefficients appropriate to the generation of oblique waves, e_j. Apart from this difference, the equations for the hydrodynamic coefficients (3.24 to 3.27) remain unchanged. Given the discussion relating to the coefficients e_j, the hydrodynamic damping and the added mass will also vary with wave propagation angle α.

Considering the hydrodynamic damping for the case of oblique wave generation first, it is important to note that this term varies with $1/\cos\alpha$ for all frequencies. This is an interesting result which may be explained as follows. The wave amplitude of the progressive wave component is proportional to $1/\cos\alpha$. As a result, the radiated energy density is proportional to $1/\cos^2\alpha$. Observing the component of the group velocity normal to a surface with $x = constant$, this component is proportional to $\cos\alpha$. Consequently, the rate of energy flux or damping must be proportional to $1/\cos\alpha$. It is also important to note once more that these

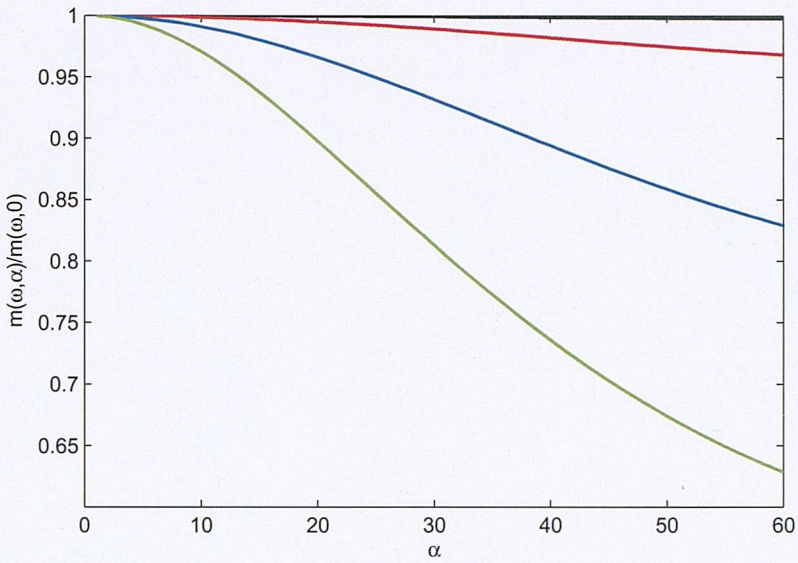


Figure 6.10: Added mass coefficient for a piston-type wave maker; —— $h/L_0 = 0.01$, —— $h/L_0 = 0.1$, —— $h/L_0 = 0.3$, —— $h/L_0 = 0.5$

arguments apply to an infinitely long wave maker.

In contrast, the added mass term does not obey such a simple relationship. Figures 6.10 and 6.11 illustrate $m(\omega, \alpha)$ for the wave machine geometries discussed earlier; the term $m(\omega, \alpha)$ for a particular wave propagation direction being presented normalised with respect to the added mass in the 2D case, $m(\omega, 0)$. The curves shown in both figures represent a variety of dimensionless water depth values h/L_0.

In the piston case (figure 6.10), values of $h/L_0 = 0.01$, $h/L_0 = 0.1$, $h/L_0 = 0.3$ and $h/L_0 = 0.5$ were adopted. The dependency of the added mass term on the wave propagation direction increased significantly in intermediate depth water ($h/L_0 = 0.3$ and $h/L_0 = 0.5$). In the case of $h/L_0 = 0.5$ the value for the added mass is less than 75% of the equivalent 2D value for angles of α exceeding approximately 40°. In shallow water ($h/L_0 = 0.01$ and $h/L_0 = 0.1$) the effect is relatively small.

For the flap-type wave machine ($h/d = 0.5$) considered in figure 6.11 values of $h/L_0 = 0.1$, $h/L_0 = 0.5$, $h/L_0 = 1.0$ and $h/L_0 = 1.5$ were adopted. In this case it is interesting to note that the ratio $m(\omega, \alpha)/m(\omega, 0)$ for $h/L_0 = 1.0$ is larger

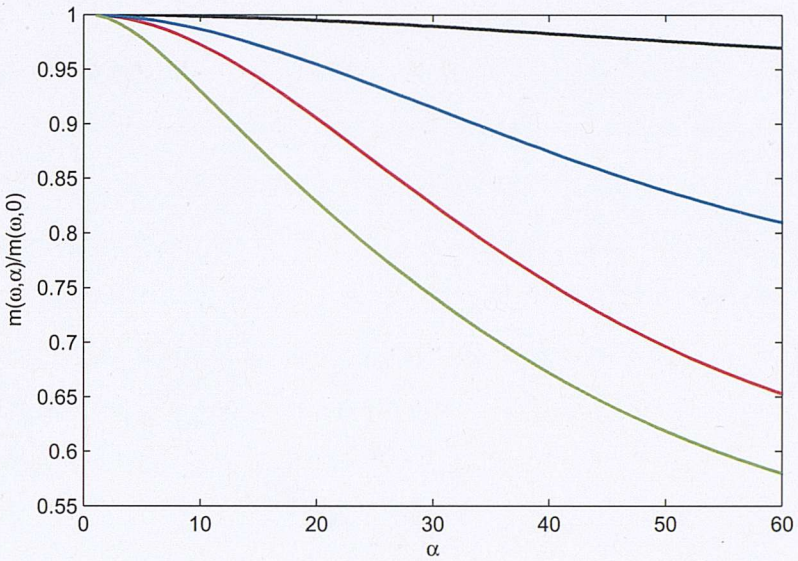


Figure 6.11: Added mass coefficient for a flap-type wave maker ($h/d = 0.5$); — $h/L_0 = 0.1$, — $h/L_0 = 0.5$, — $h/L_0 = 1.0$, — $h/L_0 = 1.5$

than the equivalent ratio for $h/L_0 = 0.5$. The origins of this characteristic are best understood by considering the first-order coefficients, e_j, in figure 6.9. In contrast to piston-type wave machines, the infinite sum $i\sum_{j=1}^{\infty} e_j$ is negative for small values of h/L_0 and has a zero crossing at $h/L_0 \approx 0.6$.

6.4 Absorption Characteristic of a Wave Basin

The variation of the added mass and hydrodynamic damping terms with the angle of wave propagation affects the wave machine's absorption characteristic. The power absorption coefficient, γ, is defined as the ratio of the absorbed power over the maximum power (Chapter 3, equation 3.49) and is restated here as

$$\gamma = \frac{P_a}{P_{a,max}} = 4\frac{R_f R_d}{(R_f + R_d)^2 + (X_f + X_d)^2}, \tag{6.13}$$

where R_d and X_d are the real and imaginary part of the dynamic system. Chapter 4 established the relation between R_d and X_d and the hydrodynamic coefficients $d(\omega)$ and $m(\omega)$; the absorption filter (R_f and X_f) being optimised to match R_d

and $-X_d$.

In contrast to the 2D case, such a matching approach proves difficult for the absorption of oblique waves. Given the variation of $m(\omega)$ and $d(\omega)$ with the angle of incidence α, the ideal absorption controller would need to incorporate this angular dependency and adjust (R_f, X_f) accordingly. This, in turn, requires an estimate (in real time) of the angle α based on the force and velocity signals of neighbouring paddles. The author is aware of the potential benefits of such a cross talk technique and these may be subject of future research. At present, the discussion will be limited to a controller with fixed coefficients.

Figure 6.12 shows the theoretical absorption characteristic for the wave machine installed in the wave basin at ICL. For this facility the nominal water depth is $h = 1.5m$ and the hinge is located at $d = 0.8m$ above the bed. The three cases shown within figure 6.12 represent the absorption characteristic for $\alpha = 0\,°$, $\alpha = 30\,°$ and $\alpha = 60\,°$; the controller being optimised for the 2D case ($\alpha = 0\,°$). Observing the figure in detail, it is clear that the absorption characteristic for oblique waves ($\alpha = 30\,°$ and $\alpha = 60\,°$) deteriorates for low to intermediate frequencies, but improves for the highest frequencies. Given the nature of the wave field coefficients, the deterioration in the intermediate frequency range may be related to the $1/\cos\alpha$ behaviour of the damping term; the filter failing to match the real part (damping) of the wave field. Whilst this remains the case at high frequencies, the decreasing evanescent mode amplitude for oblique waves in this regime (figure 6.9) leads to an improved absorption characteristic. The explanation for this lies in the fact that at $\alpha = 0\,°$ the controller fails to match the imaginary part (evanescent modes) for high frequencies. However, when considering oblique waves, the amplitude of the evanescent modes decreases and, consequently, the match is improved as is the absorption characteristic.

Overall, the 3D absorption characteristic based on a 2D optimisation is acceptable. This is further illustrated in figure 6.13 where the absorption coefficient γ is shown as a contour plot over f and α; the lines in figure 6.12 being a subset of the surface shown.

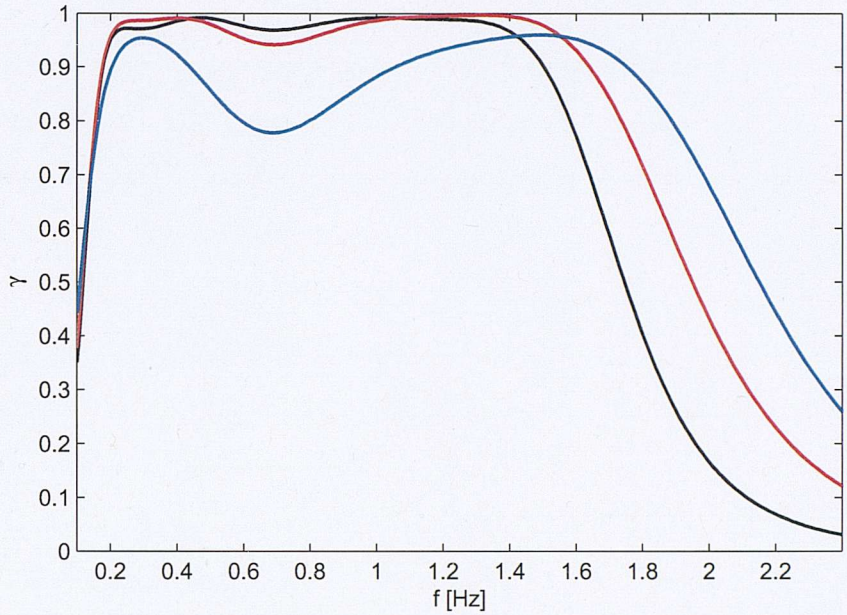


Figure 6.12: Power absorption coefficient for a flap-type wave maker ($d/h = 0.533$) in a wave basin with $h = 1.5m$; the controller being optimised for $\alpha = 0\,°$; $\alpha = 0\,°$, $\alpha = 30\,°$, $\alpha = 60\,°$

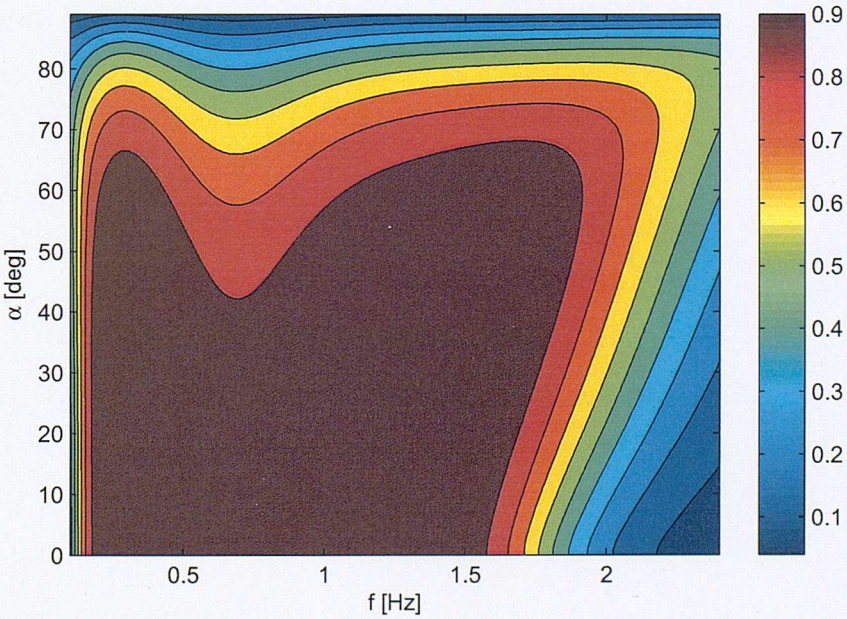


Figure 6.13: Contour plot representing the power absorption coefficient γ for the wave machine discussed in figure 6.12

6.5 Theoretical Transfer Function of a Wave Basin

With the absorption controller having been established, the transfer function for the force-controlled wave machine may be evaluated. As in the 2D case, this transfer function relates the force demand signal to the amplitude of the progressive wave mode and is of a complex nature. For a more detailed discussion concerning this first-order transfer function the reader is being referred to Chapter 5, §5.8. In contrast to the 2D scenario, the transfer function previously $c_f(\omega)$, must now be evaluated for each direction of wave propagation; the coefficient becoming $c_f(\omega, \alpha)$.

Figure 6.14 illustrates the magnitude and phase of the theoretical first-order transfer function for the wave basin at ICL; the curves relating to three angles of wave propagation ($\alpha = 0\,°$, $\alpha = 15\,°$ and $\alpha = 30\,°$). However, for a 3D wave basin the coefficient $c_f(\omega, \alpha)$ is best illustrated as shown in figures 6.15 and 6.16. Herein, the magnitude (figure 6.15) and phase (figure 6.16) are provided as contour plots as a function of the wave frequency, f, and the wave propagation direction, α; the lines in figure 6.14 being a subset of those contours.

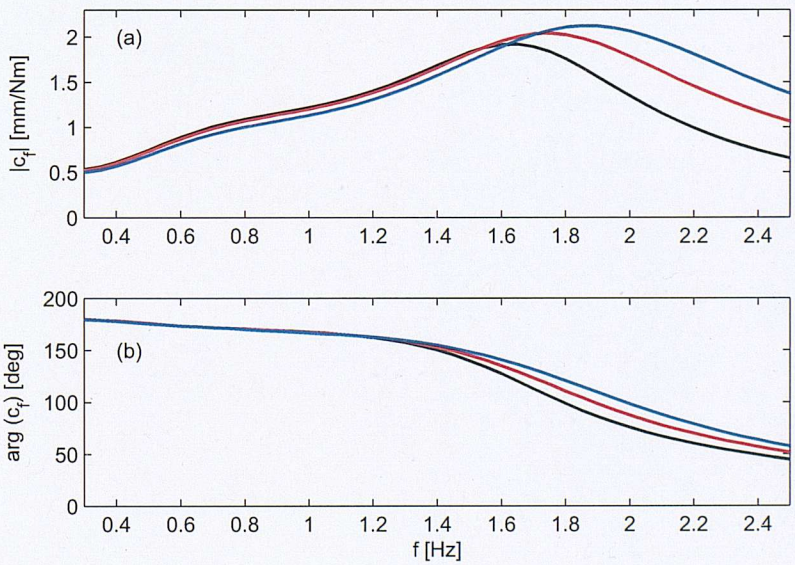


Figure 6.14: First-order force transfer function for a flap-type wave maker ($d/h = 0.533$) in a wave basin with $h = 1.5m$; (a) magnitude of $c_f(\omega, \alpha)$ and (b) phase of $c_f(\omega, \alpha)$; — $\alpha = 0\,°$, — $\alpha = 15\,°$, — $\alpha = 30\,°$

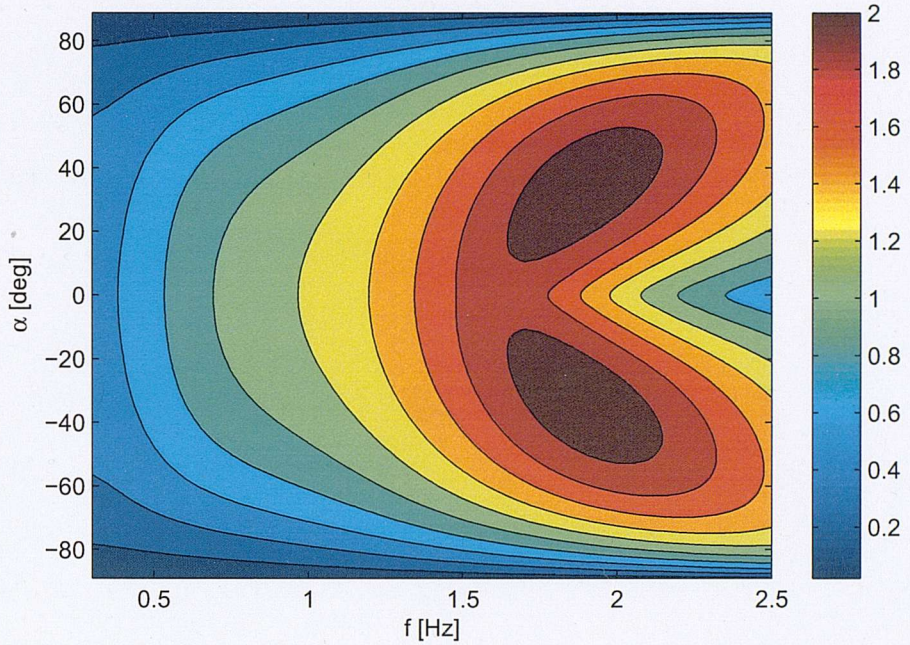


Figure 6.15: Contour plot representing the magnitude of the theoretical first-order force transfer function, $|c_f(\omega, \alpha)|$, in $[mm/Nm]$

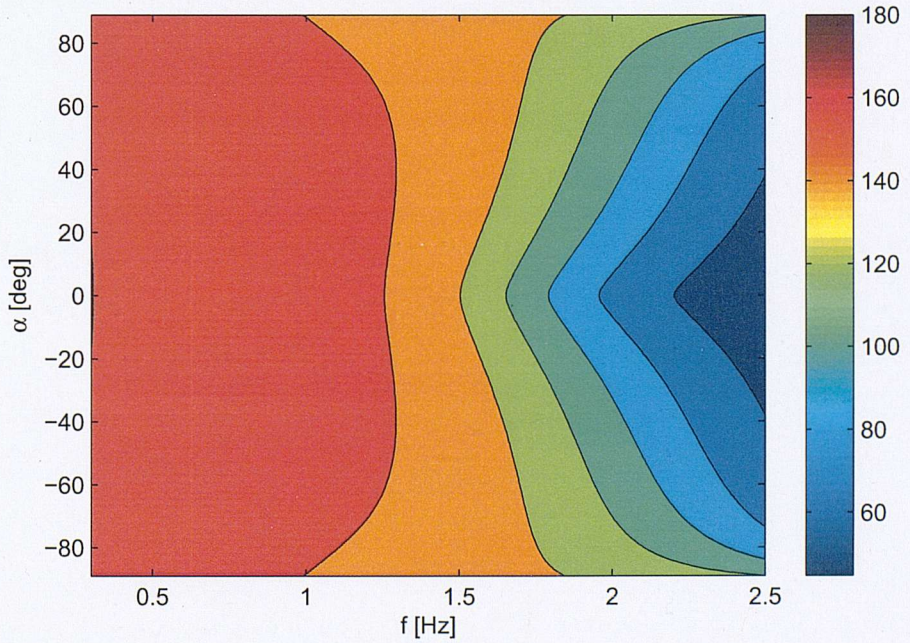


Figure 6.16: Contour plot representing the phase of the theoretical first-order force transfer function, $arg(c_f(\omega, \alpha))$, in $[deg]$

6.6 Experimental Investigation

This section concerns the generation of oblique waves in a 3D wave basin. In particular, the generation of a small amplitude JONSWAP spectrum is investigated where the data is based on four transfer functions:

i. The theoretical first-order force transfer function, $c_f(\omega, \alpha)$.

ii. An *ad-hoc* transfer function representing a combination of $c_f(\omega, \alpha)$ and the theory for a segmented-type wave generator outlined in §6.3.2.

iii. The empirical transfer function presented by Masterton & Swan (2008) (hereafter referred to as MS). The amplitude and phase information in this transfer function are based upon the generation of a small amplitude focused wave event.

iv. A recent empirical transfer function for the 3D wave basin. In this latter case, the amplitude information is based upon the generation of a random JONSWAP spectrum; the phase information in the transfer function being neglected.

All the experiments were undertaken in the wave basin located in the Hydrodynamics Laboratory at Imperial College London. The nominal water depth of this facility is $h = 1.5m$. However, in the context of ongoing work within this basin, the water depth was reduced to $h = 1.25m$ at the time of the present study. This change in water depth has been incorporated when evaluating (i), (ii) and (iv) above. In contrast, the empirical transfer function described by MS, (iii) above, was obtained for $h = 1.5m$, and this must be borne in mind when considering the results relating to (iii). However, with most wave components propagating in relatively deep water, the difference between $h = 1.25m$ and $h = 1.5m$ is insignificant. Indeed, to quantify the magnitude of the error, the theoretical transfer function, $c_f(\omega, \alpha)$, h s been evaluated for both water depths; the maximum difference in the transfer function gain for the range of interest being less than 1.6%.

The present experimental study seeks to demonstrate the applicability, or success, of the theoretical force transfer function developed within this chapter. In so doing, three important cases are considered.

1. The amplitude content for a random phase JONSWAP spectrum is considered. A direct comparison between (i) and (ii) above is made, §6.6.1.

2. To demonstrate the successful application of the phase information, a number of focused wave events are generated. This includes both uni-directional and multi-directional, or directionally spread, wave events. A direct comparison between (i) and (iii) above is made, §6.6.2

3. In an attempt to broaden our understanding of an empirical calibration approach, where the calibration routine is based on a random phase spectrum, the energy content in the wave basin is further investigated. A direct comparison between (i) and (iv) above is made, §6.6.3.

6.6.1 Amplitude Spectrum

The first set of experiments concerns the amplitude content when generating a spectrum with random phases. A uni-directional JONSWAP spectrum with $f_p = 51/64Hz$, $\gamma = 3.3$ and a significant wave height of $H_s \approx 0.02m$ has been adopted for all wave cases; the spectrum being evaluated in the range $16/64Hz \leq f \leq 128/64Hz$ with a spacing of $f = 1/64Hz$ between the individual wave components. As in the experimental study presented in Chapter 5, wave gauges consisting of a tensioned wire arrangement have been employed. The gauges were located along the centre of the wave basin to minimise any influence related to the finite length of the wave maker (figure 6.3).

Figure 6.17 illustrates the experimental data for this spectrum at a wave propagation angle of $\alpha = 0\,°$. Within this figure, the results for the transfer functions (i) and (ii) above are provided. The curves are based on a refiection analysis of the data recorded at eight spatial locations ($3.2m \leq x \leq 4.6m$; $y = 0m$) with

individual gauges spaced $0.2m$ apart. For this purpose, data from the time interval $64s \leq t \leq 128s$ was taken. The initial interval of $t = 64s$ is regarded to be sufficiently long to ensure that the beach reflections are fully developed. Moreover, to avoid spectral leakage in the frequency domain, the sample window was chosen to be equivalent to the repeat time of the wave spectrum ($T_r = 64s$).

Observing figure 6.17 in detail, both the theoretical force transfer function $c_f(\omega, \alpha)$ and the *ad-hoc* approach are in excellent agreement with the expected JONSWAP amplitude content; the departures apparent at the highest frequencies ($1.5Hz < f < 1.9Hz$) probably being due to the nonlinear wave-wave interaction between the wave components forming the peak of the spectrum. In fact, for a wave propagation direction of $\alpha = 0\,^\circ$, the force transfer function and the *ad-hoc* transfer function are effectively identical. As a result, the data shown in figure 6.17 provides evidence for the repeatability of the generation process.

Figures 6.18, 6.19 and 6.20 illustrate the experimental data for a JONSWAP spectrum propagating at $\alpha = 15\,^\circ$, $\alpha = 30\,^\circ$ and $\alpha = 45\,^\circ$ respectively. In considering this data, the wave propagation angle α must not be confused with the directional spreading σ_α; at this stage the wave spectra remain uni-directional. Observing the data based on $c_f(\omega, \alpha)$ first, the departures between the experimental measurements and the expected solution increase with the angle of wave propagation. This is particularly noticeable for frequencies exceeding $f \approx 1Hz$; the agreement in the range $1.5Hz < f < 2.0Hz$ being poor at large angles (figures 6.19 and 6.20). For this latter region the match with the expected content is much improved when considering the data based on the *ad-hoc* approach. Even at the largest angle, $\alpha = 45\,^\circ$, the agreement is now satisfactory. This improvement suggests that some of the departures from the expected content are related to the effect of the finite segment width; the remaining departures at large values of α probably being due to wave diffraction effects caused by the finite length of the wave maker.

Similar arguments apply to the experimental results where a wave propagation direction of $\alpha = -15\,^\circ$, $\alpha = -30\,^\circ$ and $\alpha = -45\,^\circ$ has been adopted (not shown

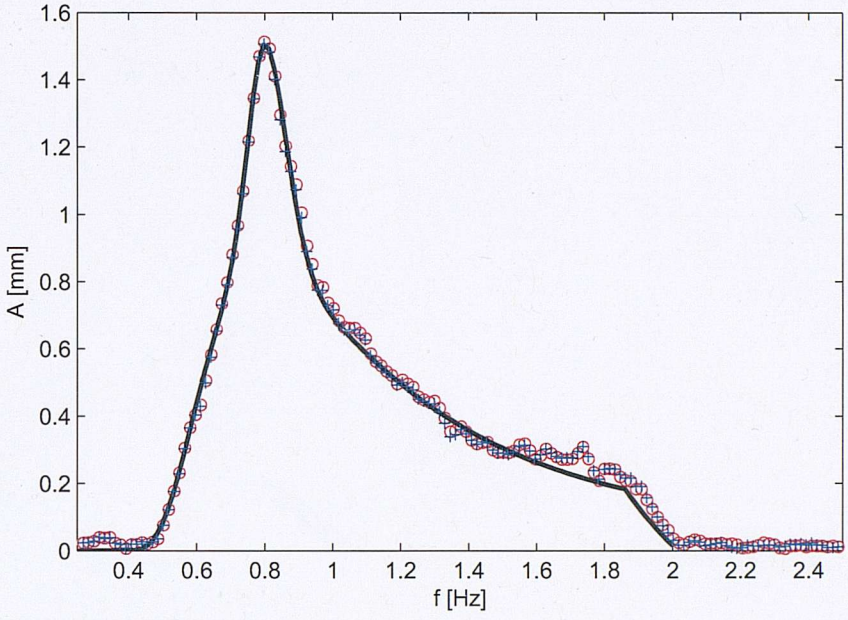


Figure 6.17: Amplitude content for a random phase uni-directional JONSWAP spectrum with $f_p = 51/64Hz$, $\gamma = 3.3$ and $H_s \approx 0.02m$ propagating at $\alpha = 0\,^\circ$ and based on ○ theoretical force transfer function $c_f(\omega, \alpha)$, + *ad-hoc* approach

herein). Overall, the data based on the *ad-hoc* approach give the most consistent agreement with the expected amplitude content. This is an unsurprising result as the *ad-hoc* approach combines aspects of two important theories. It remains a challenge for future work to formulate a theory that covers all aspects of the two theories. In particular, this relates to the amplitude of the evanescent modes for a wave maker of finite width. Nevertheless, the data relating to the theoretical force transfer function alone also show good agreement for a wide range of wave conditions.

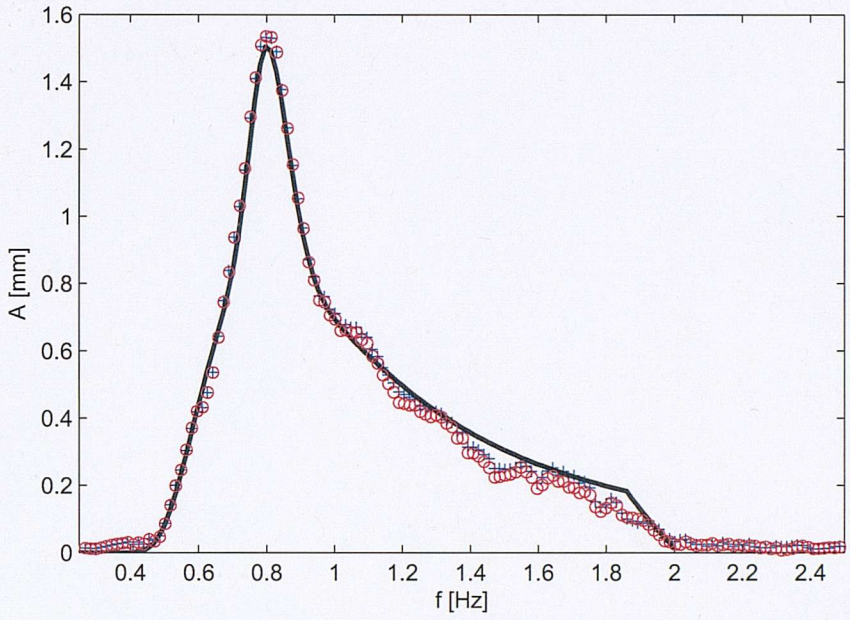


Figure 6.18: Amplitude content for a random phase uni-directional JONSWAP spectrum with $f_p = 51/64Hz$, $\gamma = 3.3$ and $H_s \approx 0.02m$ propagating at $\alpha = 15\,^\circ$ and based on ○ theoretical force transfer function $c_f(\omega, \alpha)$, + *ad-hoc* approach

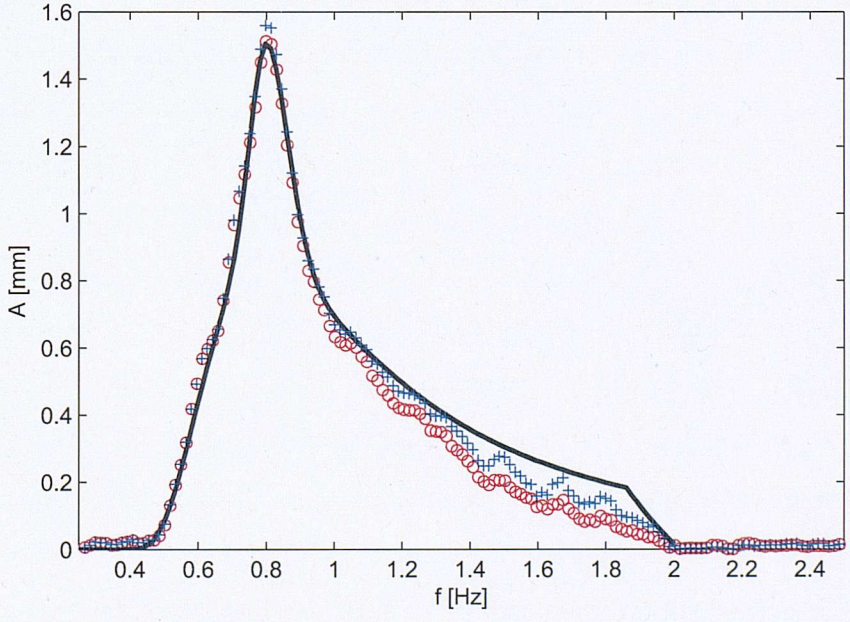


Figure 6.19: Amplitude content for a random phase uni-directional JONSWAP spectrum with $f_p = 51/64Hz$, $\gamma = 3.3$ and $H_s \approx 0.02m$ propagating at $\alpha = 30\,^\circ$ and based on ○ theoretical force transfer function $c_f(\omega, \alpha)$, + *ad-hoc* approach

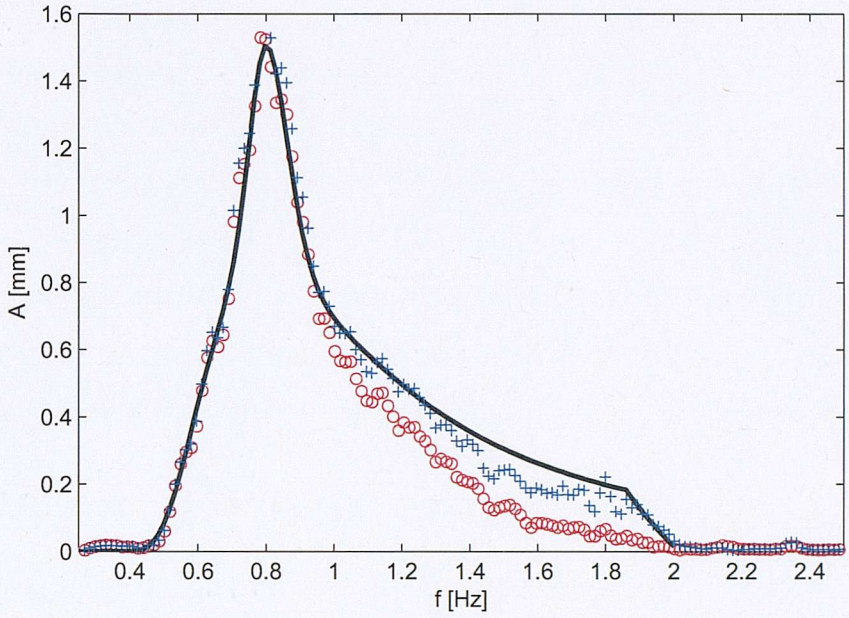


Figure 6.20: Amplitude content for a random phase uni-directional JONSWAP spectrum with $f_p = 51/64Hz$, $\gamma = 3.3$ and $H_s \approx 0.02m$ propagating at $\alpha = 45\,^\circ$ and based on ○ theoretical force transfer function $c_f(\omega, \alpha)$, + *ad-hoc* approach

6.6.2 Focused Wave Event

The previous discussion concerned the amplitude content within the wave basin. In contrast, the present case seeks to demonstrate the correct application of the phase information. For this purpose, a number of focused wave events are considered; the results being directly compared to experimental data based on the empirical calibration of MS. With the routine adopted by MS being optimised for the generation of focused wave events, this latter transfer function is believed to be the most suitable calibration for the present case. However, when considering the data in the figures that follow, the previously mentioned change in water depth must be borne in mind. Furthermore, as part of ongoing maintenance and improvement work within the wave basin at IC, some of the drive components and force transducers have been replaced since MS published their results. This also may have altered the optimum calibration slightly.

The generation of realistic large focused wave groups in the laboratory is best achieved by adopting a *NewWave* formulation (Tromans et al. 1991). In

a *NewWave* spectrum the amplitude of each component is directly proportional to the energy content of the desired spectral shape (as opposed to the square root of the energy content). Once again, a JONSWAP target spectrum has been adopted and, in accordance with MS, the peak frequency and peak enhancement factor have been set to $f_p = 53/64Hz$ and $\gamma = 2.5$ respectively. Furthermore, the amplitude A is introduced as the linear sum of all wave components. As a result, in a linear sea state the water surface elevation at the focal location and time, where all the wave components superimpose, reaches a maximum value of A.

Uni-directional NewWave Spectrum

The first set of cases considers a uni-directional JONSWAP *NewWave* spectrum measured and focused at $x = 4.0m$, $y = 0m$ and $t = 32s$. The amplitude sum has been set to $A = 12mm$ so that the particle motion remains linear. Figures 6.21, 6.22 and 6.23 illustrate the water surface elevation for the wave propagation directions $\alpha = 0\,°$, $\alpha = 15\,°$ and $\alpha = 30\,°$ respectively. Both the data based on the theoretical force transfer function and the empirical calibration after MS are shown. In all three cases and for both transfer functions the agreement between the experimental data and the theoretical (linear) solution is very good providing evidence that (i) the gain information in the transfer function yields the correct amplitude content and (ii) the correct application of the phase information leads to the focusing of the components at the desired time and location. However, some small departures remain and are noted as follows.

- In the vicinity of the main event both the empirical transfer function and the theoretical approach appear to provide a near exact match for most wave cases.

- In contrast, in the tail ($t \geq 33s$) of the event based on the empirical calibration the agreement with the theoretical solution becomes less satisfactory. This effect, particularly the conflict between the match in the vicinity of the

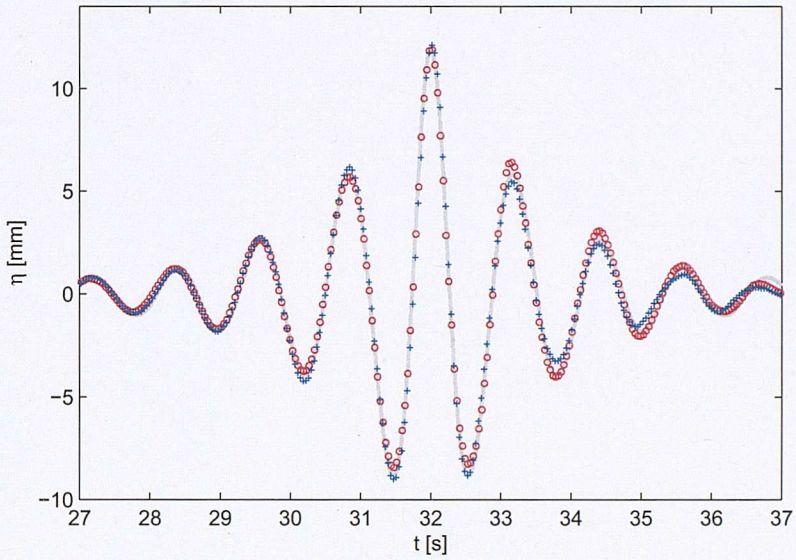


Figure 6.21: Surface profile for a uni-directional JONSWAP *NewWave* spectrum with $f_p = 53/64Hz$, $\gamma = 2.5$, $A = 12mm$ and $\alpha = 0\,°$; measured and focused at $x = 4.0m$, $y = 0m$; —— Theoretical (linear) solution; Experimental data based on ○ theoretical force transfer function, + empirical transfer function after MS

event and the mismatch in the tail, is not fully understood at present and requires further consideration.

- Based on the theoretical force transfer function, the amplitude sum in the oblique cases (figures 6.22 and 6.23) is slightly reduced when compared to the theoretical value. This decrease in amplitude is most probably related to the finite segment width of the paddle and the resulting reduction in amplitude content (figures 6.18 and 6.19).

- For the largest wave propagation angle ($\alpha = 30\,°$) the data concerning the theoretical transfer function suggest that some wave components are out of phase; evidence of which being provided by the slightly increased size of the trough and crest immediately following the largest crest.

Nevertheless, despite these small departures, the agreement is very good for all cases considered.

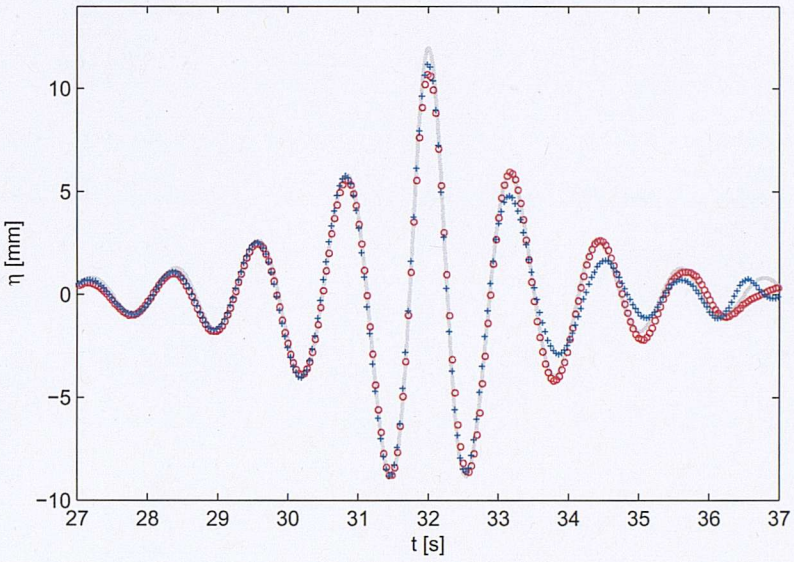


Figure 6.22: Surface profile for a uni-directional JONSWAP *NewWave* spectrum with $f_p = 53/64Hz$, $\gamma = 2.5$, $A = 12mm$ and $\alpha = 15\,°$; measured and focused at $x = 4.0m$, $y = 0m$; —— Theoretical (linear) solution; Experimental data based on ○ theoretical force transfer function, + empirical transfer function after MS

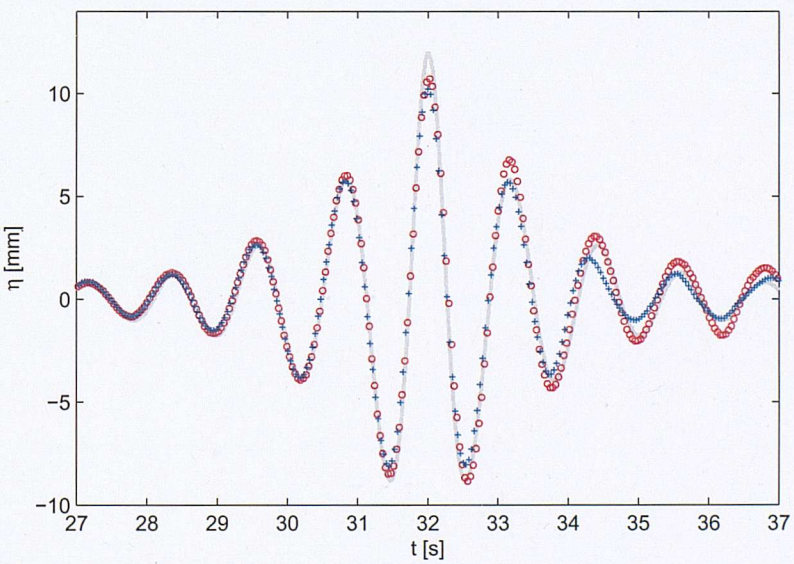


Figure 6.23: Surface profile for a uni-directional JONSWAP *NewWave* spectrum with $f_p = 53/64Hz$, $\gamma = 2.5$, $A = 12mm$ and $\alpha = 30\,°$; measured and focused at $x = 4.0m$, $y = 0m$; —— Theoretical (linear) solution; Experimental data based on ○ the theoretical force transfer function and + the empirical transfer function of MS

Multi-directional NewWave Spectrum

To evaluate the directional capabilities of both transfer functions, a multi-directional, or directionally spread, focused *NewWave* event has also been generated. A directional spreading factor of $\sigma_\alpha = 30\,^\circ$ has been adopted with all the wave components being generated at discrete intervals of $\Delta\alpha = 5\,^\circ$ in the range $-40\,^\circ \leq \alpha \leq +40\,^\circ$. Figure 6.24 shows the water surface elevation recorded by a single wave probe located at the focal position $x = 4.0m$ and $y = 0m$. As before, the experimental data relating to the two transfer functions is directly compared to the theoretical (linear) solution. Considering the figure in detail, the agreement between theory and experiment is found to be excellent for both transfer functions, (i) and (iii).

The directional spreading of this latter event is best illustrated as shown in figure 6.25 where the crest amplitude at the focal time ($t = 32s$) is shown in the traverse direction. For this purpose, nine wave gauges were located at $x = 4.0m$ and $-1.2m \leq y \leq 1.2m$ with a spacing of $\Delta y = 0.3m$ between individual probes. Overall, the agreement between the measured data and the linear prediction is good for both transfer functions. Indeed, the only significant departures between the two approaches is suspected to relate to a slight positioning error ($\Delta x = 0.1m$) in the calibration routine adopted by MS.

To further evaluate the directional capabilities of the wave basin at IC, a focused wave event identical to that above ($f_p = 53/64Hz$, $\gamma = 2.5$, $A = 12mm$ and $\sigma_\alpha = 30\,^\circ$) was generated at $(x, y) = (4.0m, +1.2m)$ and $(x, y) = (4.0m, -1.2m)$; the data being presented in figures 6.26 and 6.27 respectively. As before, the agreement between the experimental data and the linear theoretical solution is very good.

The ultimate goal of any experimental investigation concerning focused groups must be the correct generation of a very large wave event. The *NewWave* event shown in figure 6.28 is based on a linear amplitude sum of $A = 58mm$; all other parameters being identical to the spectrum considered above. As before, the experimental data are compared to the linear theoretical solution. In this context, it

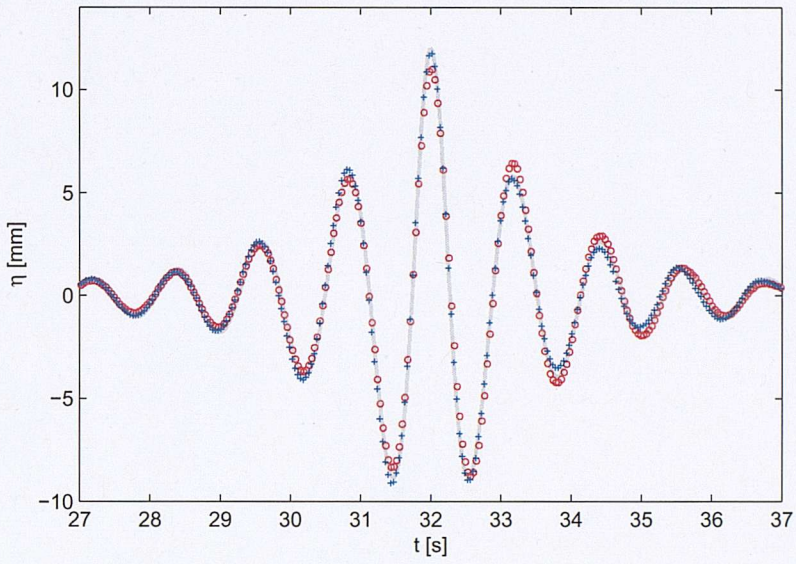


Figure 6.24: Surface profile for a multi-directional JONSWAP *NewWave* spectrum with $f_p = 53/64Hz$, $\gamma = 2.5$, $A = 12mm$ and $\sigma_\alpha = 30\,°$; measured and focused at $x = 4.0m$, $y = 0m$; —— Theoretical (linear) solution; Experimental data based on ○ the theoretical force transfer function and + the empirical transfer function of MS

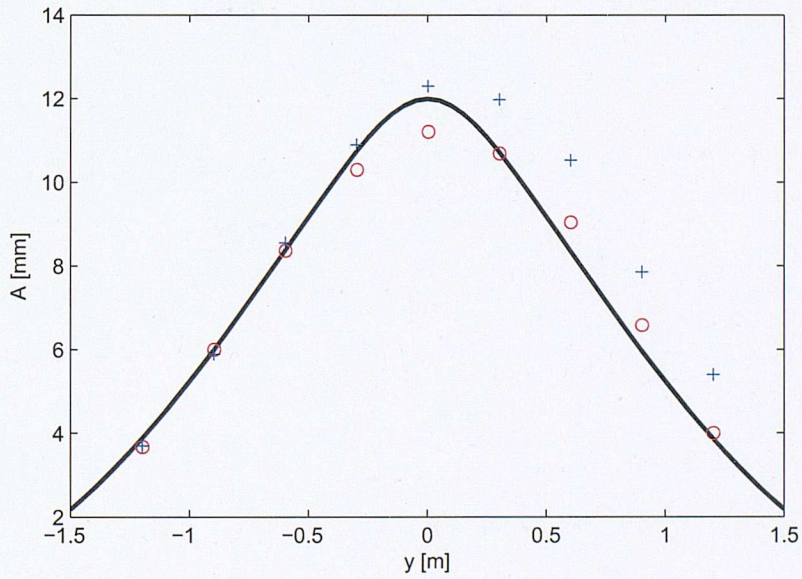


Figure 6.25: Spatial amplitude variation in the traverse direction at $t = 32s$ for a JONSWAP *NewWave* spectrum with $f_p = 53/64Hz$, $\gamma = 2.5$, $A = 12mm$ and $\sigma_\alpha = 30\,°$; focused at $x = 4.0m$, $y = 0m$ and $t = 32s$; —— Theoretical (linear) solution; Experimental data based on ○ the theoretical force transfer function and + the empirical transfer function of MS

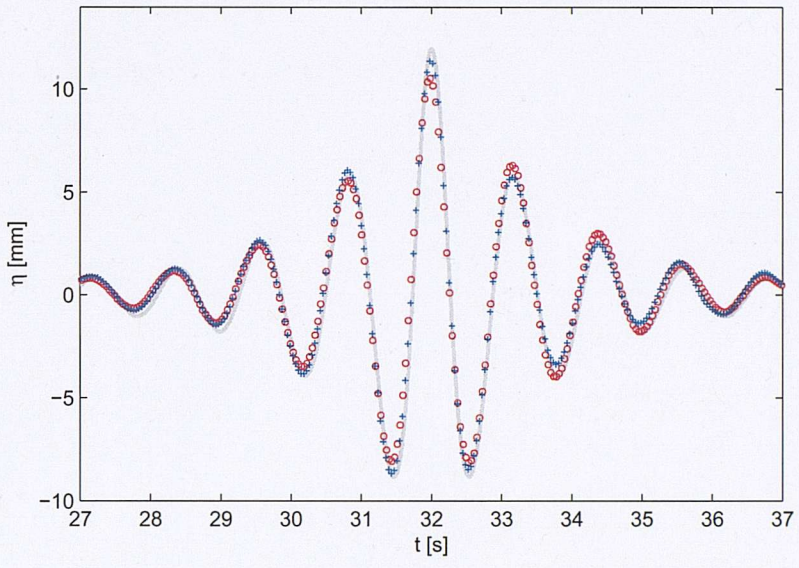


Figure 6.26: Surface profile for multi-directional JONSWAP *NewWave* spectrum with $f_p = 53/64Hz$, $\gamma = 2.5$, $A = 12mm$ and $\sigma_\alpha = 30\,°$; measured and focused at $x = 4.0m$ and $y = +1.2m$; —— Theoretical (linear) solution; Experimental data based on ○ the theoretical force transfer function and + the empirical transfer function of MS

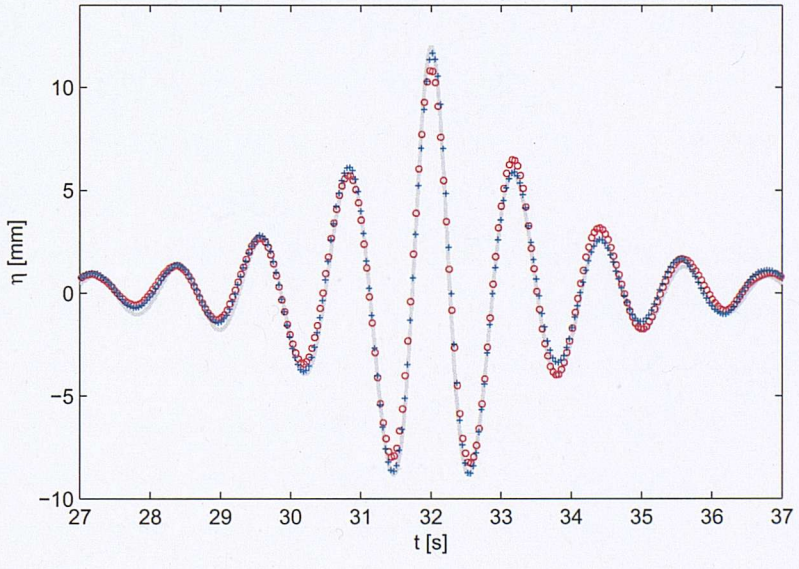


Figure 6.27: Surface profile for multi-directional JONSWAP *NewWave* spectrum with $f_p = 53/64Hz$, $\gamma = 2.5$, $A = 12mm$ and $\sigma_\alpha = 30\,°$; measured and focused at $x = 4.0m$ and $y = -1.2m$; —— Theoretical (linear) solution; Experimental data based on ○ the theoretical force transfer function and + the empirical transfer function of MS

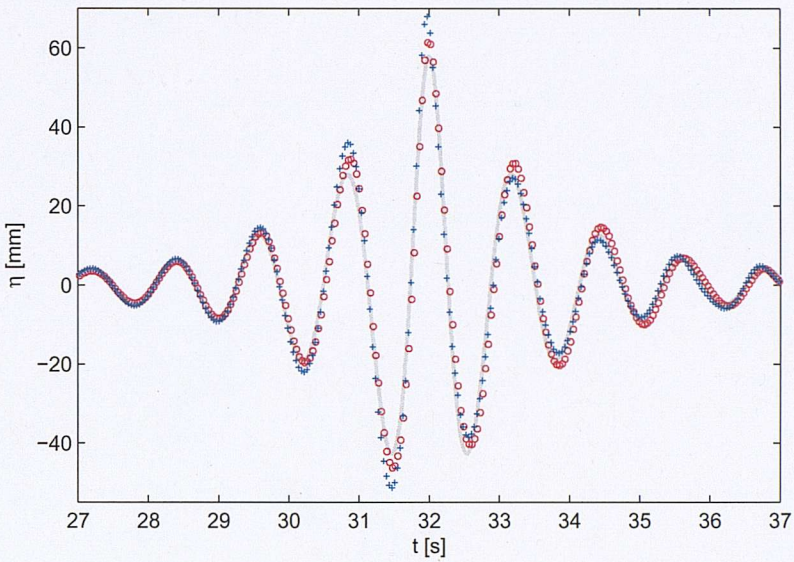


Figure 6.28: Surface profile for a multi-directional JONSWAP *NewWave* spectrum with $f_p = 53/64Hz$, $\gamma = 2.5$, $A = 58mm$ and $\sigma_\alpha = 30\,°$; measured and focused at $x = 4.0m$ and $y = 0m$; —— Theoretical (linear) solution; Experimental data based on ○ the theoretical force transfer function and + the empirical transfer function of MS

is important to note that, due to nonlinear wave-wave interaction effects, the linear solution fails to accurately model the water surface elevation. Nevertheless, the general agreement between the experimental data and the expected surface profile suggests that the two transfer functions are indeed appropriate to the generation of large focused events; a detailed analysis of the higher order wave content being outside the scope of the present study. Comparing the two transfer functions qualitatively, the theoretical transfer function seems to yield a superior agreement in terms of the phase information; evidence of which being provided by the symmetry of focused event. However, in light of the results originally published by MS (not shown herein), it might be concluded that an empirical approach ought to perform better than the data presented in figure 6.28 suggests.

Uni-directional JONSWAP Spectrum

The *NewWave* spectrum discussed thus far is considerably more narrow banded than the underlying JONSWAP spectrum; the former being based on the square of the latter. Consequently, the difference in wave celerity between the largest components in the spectrum is relatively small and, as a result, the generation of a focused wave event is somewhat less sensitive to small phase or positioning errors. The difficulties arising with the generation of a focused event for a more broad banded spectrum are illustrated in figure 6.29. In this case, an amplitude content proportional to the square root of a uni-directional JONSWAP energy spectrum ($f_p = 53/64Hz$, $\gamma = 2.5$, $A = 12mm$ and $\alpha = 0\,°$) has been adopted. Even though the agreement remains satisfactory, the symmetry of the focused event is reduced when compared to comparable data relating to the *NewWave* event; this being particularly pronounced for the case concerning the theoretical force transfer function. In fact, neither approach seems to work well for $t > 32.5s$. The exact reason for this remains unclear, but the most likely explanation lies in a small mismatch in the spatial positioning.

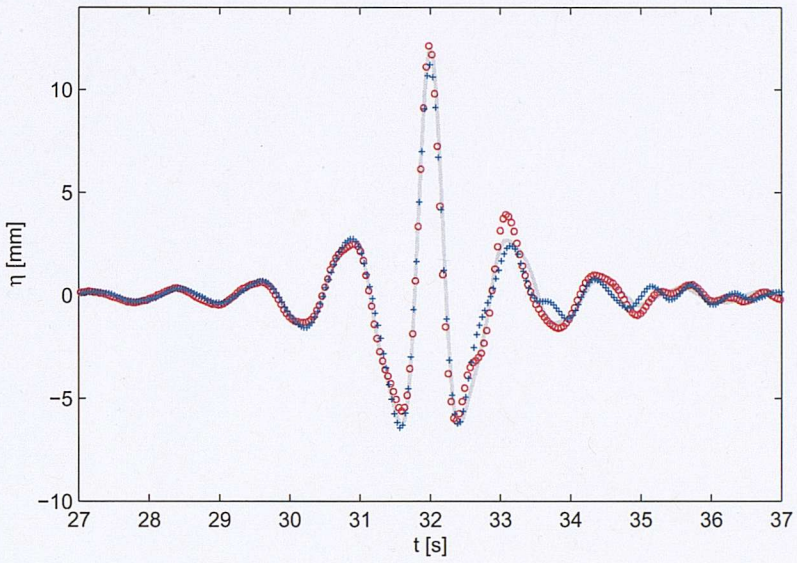


Figure 6.29: Surface profile for a uni-directional JONSWAP spectrum with $f_p = 53/64Hz$, $\gamma = 2.5$, $A = 12mm$ and $\alpha = 0\,°$; measured and focused at $x = 4.0m$ and $y = 0m$; —— Theoretical (linear) solution; Experimental data based on ○ the theoretical force transfer function and + the empirical transfer function of MS

Amplitude Content for the Empirical Transfer Function of MS

Within this section (6.6.2) all the previous figures concerned small amplitude focused wave events; the empirical transfer function of MS leading to a very good agreement with the expected water surface elevations. However, despite this agreement, it is also interesting to consider the amplitude spectra for a uni-directional JONSWAP spectrum with random phase as discussed in Section 6.6.1. Figure 6.30 concerns exactly this case ($f_p = 51/64Hz$, $\gamma = 3.3$ and $H_s \approx 0.02m$) and contrast the experimental data for both the theoretical force transfer function and the empirical calibration of MS. Although the departures apparent for the latter transfer function are small (having little observable effect on the water surface elevation) they cannot as yet be explained. This will be subject of further investigation.

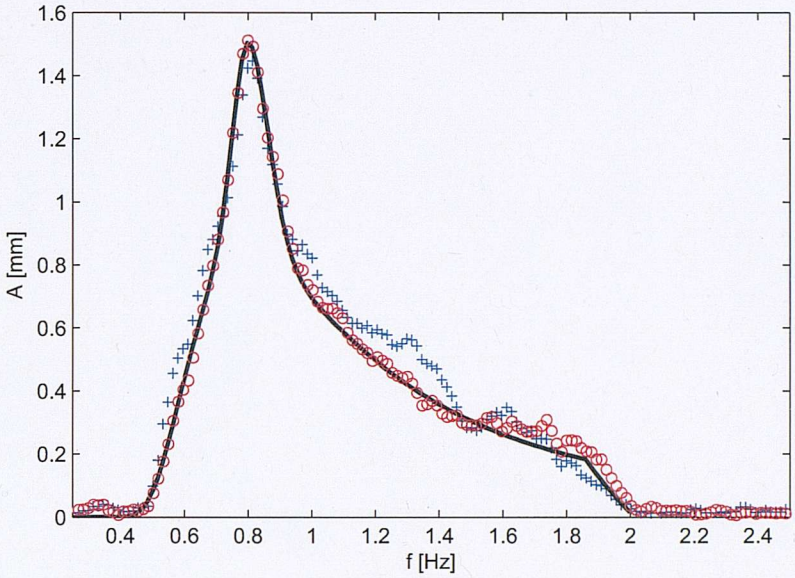


Figure 6.30: Amplitude content for a random phase uni-directional JONSWAP spectrum with $f_p = 51/64Hz$, $\gamma = 3.3$, $H_s \approx 0.02m$ and $\alpha = 0\,^\circ$ —— Theoretical (linear) solution; Experimental data based on ○ the theoretical force transfer function and + the empirical transfer function of MS

6.6.3 Energy Spectrum

In a final set of test cases, the energy content in the wave basin is further observed. The two transfer functions under consideration are the theoretical force transfer function and a recent empirical calibration for the wave basin at Imperial College. A uni-directional random phase JONSWAP spectrum with $f_p = 46/64Hz$, $\gamma = 2.3$ and $H_s \approx 0.02m$ is generated at the wave propagation directions $\alpha = 0\,^\circ$, $\alpha = 20\,^\circ$ and $\alpha = 40\,^\circ$. In accordance with the discussion relating to the amplitude content (§6.6.1) the experimental results illustrated in figures 6.31, 6.32 and 6.33 have been obtained by means of a reflection analysis on data recorded at eight spatial locations ($3.2m \leq x \leq 4.6m$, $y = 0m$).

Observing the figures in detail, one could easily conclude that both approaches give a good representation of the target spectrum. Nevertheless, some interesting differences between the two transfer functions still arise, not least because they are based on an entirely different approach. At first sight, the match between

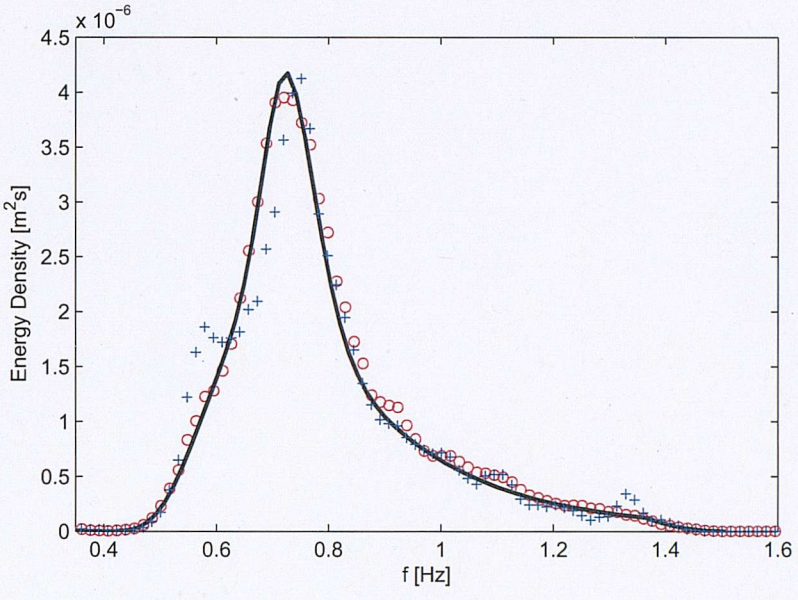


Figure 6.31: Energy content for a uni-directional JONSWAP spectrum with $f_p = 46/64Hz$, $\gamma = 2.3$ and $H_s \approx 0.02m$ generated at $\alpha = 0\,^\circ$ and based on ○ the theoretical force transfer function $c_f(\omega, \alpha)$ and + a recent empirical transfer function for the wave basin at IC

the experimental data and the expected energy content seems superior when the generation is based on the theoretical force transfer function. However, this is a likely outcome since only the incident energy is considered. In contrast, the empirical calibration approach incorporates the beach reflections and seeks to achieve a desired energy content at a particular location in the wave basin.

With any model placed in the wave basin being subjected to both incident and reflected energy, it is questionable which transfer function would model a desired sea state in a more realistic manner. Fortunately, it is outside the scope of the present study to advocate either approach. However, it must be borne in mind that, at least for any broad banded wave spectrum, beach reflections will inevitably be important for part of the frequency range. With an empirical calibration approach, it is possible to partly incorporate these reflections within the transfer function. However, in this approach the wave energy will not necessarily be travelling in the desired directions. Difficulties of this type emphasising the need to reduce unwanted reflections to an absolute minimum.

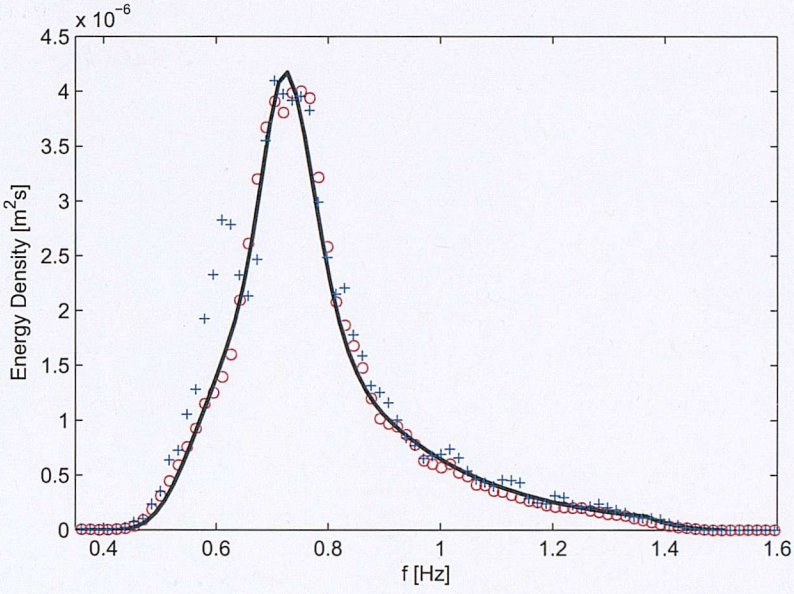


Figure 6.32: Energy content for a uni-directional JONSWAP spectrum with $f_p = 46/64Hz$, $\gamma = 2.3$ and $H_s \approx 0.02m$ generated at $\alpha = 20\,^\circ$ and based on $\circ$ the theoretical force transfer function $c_f(\omega, \alpha)$ and $+$ a recent empirical transfer function for the wave basin at IC

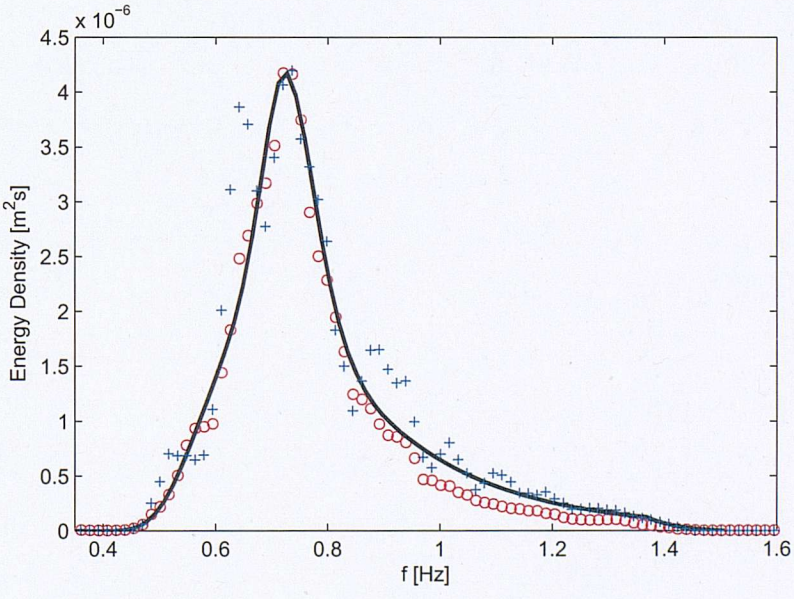


Figure 6.33: Energy content for a uni-directional JONSWAP spectrum with $f_p = 46/64Hz$, $\gamma = 2.3$ and $H_s \approx 0.02m$ generated at $\alpha = 40\,^\circ$ and based on $\circ$ the theoretical force transfer function $c_f(\omega, \alpha)$ and $+$ a recent empirical transfer function for the wave basin at IC

6.7 Conclusions

A theoretical first-order force transfer function appropriate to the generation of multi-directional waves in wave basins has been derived. Based on this transfer function an extensive laboratory study has been undertaken. First, a number of uni-directional JONSWAP spectra propagating at different angles were generated. Whereas the agreement with the expected spectral content was found to be excellent for the longer wave components, some significant departures arose for the shorter wave components, particularly when propagating at large angles. This is believed to be caused by the finite wave maker segment width. In an attempt to overcome this apparent shortcoming, an *ad-hoc* procedure, incorporating the finite segment width, was introduced. Overall, the experimental data based on this *ad-hoc* approach gave very consistent agreement with the expected spectral content. As a result, the development of a theory that properly formulates the influence of the finite wave board width must be recommended for future work.

In a second step, the generation of various focused wave events has shown that the correct application of the phase information did indeed lead to the focusing of the individual wave components at the desired time and location. This investigation includes both uni-directional and multi-directional, or directionally spread, focused wave groups. The data has been directly compared to a previously published empirical calibration approach optimised for the generation of focused wave events. Overall, very good agreement between the two approaches and a linear prediction was achieved.

In a final step, the energy content in the wave basin has been further investigated. For this purpose, the experimental data concerning the theoretical force transfer function has been directly compared to a recent empirical calibration of the wave basin at Imperial College. This latter comparison illustrated some interesting differences between the two approaches. In particular, the effect of beach reflections which, in most wave basins, inevitably contaminate the testing area after a short period of time, has been noted and differences between the two transfer functions have been explained.

7

Conclusions and Recommendations for further Work

This thesis has investigated the problem of absorbing force-controlled wave makers. A new theory, correct up to second order, has been developed and has been shown to be appropriate to both flap- and piston-type wave machines. At first order, the novel theory relates the force demand signal and the amplitude of the progressive wave. This theoretical transfer function has the potential to replace or, at the very least, provide an initial estimate for an empirical calibration. At second order the theory seeks to eliminate the unwanted, or spurious, freely propagating wave components. In this context, the inherent difference between position control and force control has been explained for the first time.

In developing the theoretical framework, the absorption mechanism was investigated in detail. Based on the correct understanding of generation and absorption at first-order, a second-order theory, incorporating the nonlinear hydrodynamic feedback path, was derived. This novel second-order theory is limited to two dimensional wave flumes at present. However, the first-order theory has been extended to include the operation of multi-directional wave basins. A detailed account of each aspect of the work is given below.

7.1 Absorption Characteristic

It has been shown that wave absorption is inherent to the operation of any force-controlled wave machine and, as a result, the correct understanding of the absorption strategy is part and parcel of modelling the machine's behaviour. An absorption strategy based on the optimisation of infinite impulse response (IIR) function filters has been introduced. This strategy overcomes the non-causal control problem that arises when seeking an ideal controller that maintains optimum power absorption for a wide range of frequencies. The IIR method was directly compared to alternative techniques and superior performance shown. Experimental data for both piston-type and flap-type wave machines confirms the theoretical findings. Most importantly, very good absorption could be achieved in both cases.

As yet, the IIR filter technique has never been applied to a numerical wave tank scheme. A complex numerical IIR filter could provide an excellent match to the hydrodynamic coefficients and very effective absorption may therefore be possible. Building on the success of the present results, it is intended to incorporate this absorption strategy into the numerical wave tank developed at Imperial College London. This numerical wave tank employs a boundary element scheme and operates in the time domain. As a result, the absorption filters developed for the physical wave tank facilities are directly relevant to the numerical approach.

The present work is limited to flap- and piston-type wave makers. Investigating the potential benefits of IIR filters for the operation of absorbing plunger-type wave machines is also envisaged for future work. This proposed work could be based on a collaboration with Osaka University where an absorbing circular tank composed of plunger-type wave makers has been installed.

7.2 First-order Behaviour

The first-order transfer function for force-controlled wave makers has been derived. This novel transfer function may be regarded as being of equivalent importance to the first-order Biésel coefficients for position-controlled machines; the latter linking the position of the wave board and the amplitude of the progressive wave mode.

An important difference between position-controlled and force-controlled wave machines was also identified. Whereas the phase shift between the demand signal and the generated progressive wave in position control is 90 degree for all frequencies, a frequency dependent phase shift is introduced in force control. The phase shift in force control arises due to the complex nature of the wave field, represented by the added mass and the hydrodynamic damping, as well as the frequency dependent characteristic of the absorption filter. The added mass term highlights the importance of the evanescent modes.

Furthermore, it was shown that the force transfer function is also influenced by the inertia and spring rate of the wave board itself, a dependency that does not occur in position control. Indeed, it should be noted that the force-control transfer function is considerably more complicated when compared to the position-control equivalent. However, with the absorption mechanism being incorporated in the former, a consistent theory for both generation and absorption can be (indeed has been) derived.

An empirical calibration approach that has been adopted in the past is, for the first time, linked into a theoretical framework. Prior to this thesis, the wider research community was unable to relate the numerical calibration data to a physical process quantity and, as a result, it was impossible to interpret the calibration results and identify errors in the calibration procedure. With the publication of the present work, this apparent shortcoming has been overcome.

7.3 Second-order Behaviour

Based on the success of the first-order results, a second-order theory for force-controlled wave machines, incorporating the nonlinear hydrodynamic feedback, has been derived. Whereas the first-order transfer function for such devices may be obtained using an empirical calibration, such an approach becomes impractical at second order. This is due to the highly complex nature of the interaction between the primary wave components giving rise to higher harmonic bound and spurious free waves in a laboratory environment.

The second-order theory has been evaluated for both flap and piston-type wave board geometries. In particular, the generation of steep regular waves using flap-type boards under force control has shown that very little freely travelling spurious wave content is introduced when based on a first-order demand signal. Under such circumstances, second-order correction may not be required. The present thesis is the first study that concerns the wave quality that can be achieved using force-controlled wave machines. However, prior to this work observation suggested that force-driven flap-type machines indeed introduce less spurious content when compared to equivalent position-controlled devices. This long standing question has now been explained formally. In contrast, a significant amount of freely travelling spurious wave content was identified for force-controlled piston-type machines. In some cases, this spurious content even exceeds the spurious content introduced in first-order position control. In this case a second-order force-control signal must be recommended; this this providing the theoretical framework required to evaluate this signal for any particular wave machine.

An extensive laboratory program accompanies the theoretical work and, overall, very good agreement between the theory and the experimental data has been achieved. Applying a second-order control signal showed that, based on simultaneous generation and absorption, a wave field in very close agreement with the theoretical second-order prediction can be maintained for long periods of time.

7.4 Multi-directional Waves

A theoretical first-order transfer function for the generation of oblique waves in wave basins has been derived. At present, this transfer function is based on the assumption of an infinitely long wave maker consisting of indefinitely small segments. Based on this transfer function an extensive experimental program has been undertaken.

In a first step, concerning the generation of random phase uni-directional JONSWAP spectra, experimental data has shown that this theory is applicable for a wide range of wave conditions. Indeed, it is only for large wave propagation angles and small wave lengths that the theory is less appropriate; this evaluation being based on the correct incident wave amplitude within the wave basin. In seeking an explanation for these effects, the theory has been extended in an *ad-hoc* manner to incorporate the effect of the finite segment width. Laboratory data based on this *ad-hoc* approach suggests a significant enhancement of the range of applicability. As a result, a consistent formulation of a force-based theory incorporating the effect of the finite segment width must be recommended for future work.

In a second step the correct application of the phase information has been investigated. For this purpose, a number of small amplitude focused wave events has been generated. A direct comparison between the theoretical force transfer function and a previously published empirical calibration approach, where the calibration routine is optimised for the generation of focused wave events, has shown that the theoretical phase information enables the generation of highly symmetric, or nearly exactly focused, wave events. In considering the generation of such events, both uni-directional and multi-directional, or directionally spread, cased have been included.

In a final step the energy content within the wave basin has been further investigated. A direct comparison to a recent empirical calibration has been presented. This comparison highlights some interesting differences between the two approaches, particularly concerning the correct reproduction of an incident wave

spectrum with superimposed beach reflections. With any model placed in the wave basin inevitably being subjected to both incident and reflected energy, a calibration approach that incorporates beach reflections may be adopted. The detailed investigation of such an approach is recommended for future work.

A second interesting effect arises from the generation of a directionally spread random-phase spectrum where the generation is based on a pseudo-random technique. Although this does not impact on the data indicated on figures 6.31 - 6.33, since they are uni-directional (albeit at an angle to the paddle face), it is an important point that will be subject of future work. In the case of a directionally spread spectrum, a single bin in the frequency domain may (or almost certainly will) contain information for wave components propagating in different directions. A first approach is to simply add any two wave components in the frequency domain. However, another commonly adopted approach is to generate only one wave component per frequency with an amplitude as the root mean square of the two (or more) desired components. The angle and phase of this single wave is chosen randomly from one of the initial components where the random number generator may be weighted according to the relative energy of the waves. As already noted above, this effect is limited to pseudo-random wave generation techniques. In the light of this, very limited literature discussing this important effect is available and it is envisaged for future work to survey common practice.

7.5 Closing Remarks

The present thesis was the first attempt at providing both a theoretical framework and supporting experimental evidence for the operation of force-controlled wave machines. With advances in laboratory wave generation technology this work has been timely, if not overdue. The author wishes to encourage more researches to contribute to this fascinating and challenging area.

Appendix A - Position-control: Further Development of the Wave Field Coefficients

Two-dimensional wave making environment

With reference to equations (2.28) and (2.31), describing the second-order wave field, the expressions for $H^{\pm}_{jnlm}$, $D^{\pm}_{jnlm}$ and $c_p^{(22)\pm}$ need to be introduced. These follow directly from Schäffer (1996) and are given by

$$H^{\pm}_{jnlm} = (\omega_n \pm \omega_m)\left(\pm\omega_n\omega_m - \frac{g^2 k_{jn}\bar{k}^{*}_{lm}}{\omega_n\omega_m}\right) + \frac{\omega_n^3 \pm \omega_m^3}{2} - \frac{g^2}{2}\left(\frac{k_{jn}^2}{\omega_n} \pm \frac{k_{lm}^2}{\omega_m}\right) \quad \text{(A-1)}$$

and

$$D^{\pm}_{jnlm} = g(k_{jn} \pm \bar{k}^{*}_{lm})\tanh(k_{jn} \pm \bar{k}^{*}_{lm})h - (\omega_n \pm \omega_m)^2. \quad \text{(A-2)}$$

Furthermore, the coefficient $c_p^{(22)\pm}$ is given by

$$\begin{aligned} c_p^{(22)\pm} = \delta_{nm}&\frac{h(\omega_n \pm \omega_m)\cosh^2 K_p^{\pm}h}{g^2 c_{0n}c_{0m}\Lambda_2(K_p^{\pm})} \\ &\left\{\pm\frac{g}{2\omega_n}\sum_{j=0}^{\infty}\frac{c_{jn}k_{jn}^2}{k_{jn}^2 - (K_p^{\pm})^2}\left(\omega_n^2 - (\omega_n \pm \omega_m)^2 + M_2(k_{jn}, K_p^{\pm})\right)\right. \\ &\pm\frac{g}{2\omega_m}\sum_{l=0}^{\infty}\frac{\bar{c}^{*}_{lm}k_{lm}^2}{k_{lm}^2 - (K_p^{\pm})^2}\left(\omega_m^2 - (\omega_n \pm \omega_m)^2 + M_2(\bar{k}^{*}_{lm}, K_p^{\pm})\right) \\ &\left.-\sum_{j=0}^{\infty}\sum_{l=0}^{\infty}c_{jn}\bar{c}^{*}_{lm}\frac{k_{jn} \pm \bar{k}^{*}_{lm}}{(k_{jn} \pm \bar{k}^{*}_{lm})^2 - (K_p^{\pm})^2}H^{\pm}_{jnlm}\right\} \end{aligned} \quad \text{(A-3)}$$

where $M_2(k_{jn}, K_p^{\pm})$ is defined as

$$\begin{aligned} M_2(k_{jn}, K_p^{\pm}) = -\frac{g}{h+l}&\frac{K_p^{\pm}/k_{jn}}{k_{jn}^2 - (K_p^{\pm})^2}\left\{2k_{jn}K_p^{\pm}\left(1 - \frac{\cosh k_{jn}d}{\cosh k_{jn}h}\frac{\cosh K_p^{\pm}d}{\cosh K_p^{\pm}h}\right)\right. \\ &\left.-(k_{jn}^2 + (K_p^{\pm})^2)\left(\frac{\omega_n^2(\omega_n \pm \omega_m)^2}{g^2 k_{jn}K_p^{\pm}} - \frac{\sinh k_{jn}d}{\cosh k_{jn}h}\frac{\sinh K_p^{\pm}d}{\cosh K_p^{\pm}h}\right)\right\}. \end{aligned} \quad \text{(A-4)}$$

With reference to equation (2.34), the wave-wave interaction surface elevation, the term $G^{\pm}_{jnlm}$ needs to be introduced.

$$G^{\pm}_{jnlm} = \frac{\delta_{nm}}{g}\left\{(\omega_n \pm \omega_m)\frac{H^{\pm}_{jnlm}}{D^{\pm}_{jnlm}} - L^{\pm}_{jnlm}\right\}, \tag{A-5}$$

where $L^{\pm}_{jnlm}$ is defined as

$$L^{\pm}_{jnlm} = \frac{1}{2}\left\{\frac{g^2 k_{jn} k^{-*}_{lm}}{\omega_n \omega_m} \mp \omega_n \omega_m - (\omega_n^2 \pm \omega_m^2)\right\}. \tag{A-6}$$

With reference to equations (4.13) and (4.15), the transfer function F^{+} found by Schäffer (1996) is introduced as

$$F^{\pm} = -\frac{c_0^{(22)\pm}}{c_0^{(23)\pm}} \tag{A-7}$$

where $c_0^{(23)\pm}$ is the progressive mode ($p = 0$) of

$$c_p^{(23)\pm} = \sinh K_p^{\pm} h \frac{\Lambda_1(K_p^{\pm})}{\Lambda_2(K_p^{\pm})}. \tag{A-8}$$

Three-dimensional wave making environment

With reference to equation (6.10), further detail concerning the derivation of this result is provided here. The first-order velocity potential appropriate to the generation of uni-directional waves was given by equation (2.19) and may be restated as

$$\Phi^{(1)}(x,z,t) = \frac{1}{2}\left\{\frac{igX_a}{\omega}\sum_{j=0}^{\infty} c_j \frac{\cosh k_j(z+h)}{\cosh k_j h} e^{i(\omega t - k_j x)} + c.c.\right\}. \tag{A-9}$$

In contrast, the velocity potential appropriate to the generation of oblique waves (equation 6.8) is given by

$$\Phi^{(1)}(x,y,z,t) = \frac{1}{2}\left\{\frac{igX_a}{\omega}\sum_{j=0}^{\infty} e_j \frac{\cosh k_j(z+h)}{\cosh k_j h} e^{i(\omega t - \vec{k}_j \vec{x})} + c.c.\right\}. \tag{A-10}$$

The first-order boundary condition on the wave maker may be expressed as

$$\frac{\partial \Phi^{(1)}}{\partial x} = f(z)\frac{\partial X_0^{(1)}}{\partial t} \tag{A-11}$$

in both cases. Substituting (A-9) and (A-10) into (A-11) and comparing the results yields the relation between the first-order wave field coefficients as

$$e_j = \frac{k_j}{k_{xj}} c_j \tag{A-12}$$

which may be rewritten as

$$e_j = \frac{1}{\cos \alpha_j} c_j. \tag{A-13}$$

Appendix B - The Second-order Torques

With reference to equation (4.3), the torques up to second order need to be evaluated. The first-order unsteady wave acceleration $\partial\Phi^{(1)}/\partial t$ integrated up to the first-order free surface induces a torque given by

$$T^{(2)}_{\Phi^{(1)}} = -\int_0^{\eta^{(1)}} \rho\frac{\partial\Phi^{(1)}}{\partial t}(h-d+z)dz = \frac{1}{2}\left\{\rho g X_a \sum_{j=0}^{\infty} c_j[(h-d)\eta_1 + \eta_1^2]e^{i\omega t} + c.c.\right\} \tag{B-1}$$

which can be simplified by retaining only mean- and second-order terms

$$T^{(2)}_{\Phi^{(1)}} = \frac{1}{2}\left\{\frac{\rho g(h-d)X_a^2}{2}\sum_{j=0}^{\infty}\sum_{l=0}^{\infty} c_j c_l e^{i2\omega t} + \frac{\rho g(h-d)X_a X_a^*}{2}\sum_{j=0}^{\infty}\sum_{l=0}^{\infty} c_j c_l^* + c.c.\right\}. \tag{B-2}$$

Following Lighthill (1979), there is also a torque component caused by the changing effective wetted surface of the body which may be expressed as

$$T^{(2)}_{hydro} = -\int_0^{\eta^{(1)}} \rho g z(h-d+z)dz = -\frac{1}{2}\rho g\eta_1^2(h-d) - \frac{1}{3}\rho g\eta_1^3 \tag{B-3}$$

and simplified by retaining only mean- and second-order terms

$$T^{(2)}_{hydro} = \frac{1}{2}\left\{-\frac{\rho g(h-d)X_a^2}{4}\sum_{j=0}^{\infty}\sum_{l=0}^{\infty} c_j c_l e^{i2\omega t} - \frac{\rho g(h-d)X_a X_a^*}{4}\sum_{j=0}^{\infty}\sum_{l=0}^{\infty} c_j c_l^* + c.c.\right\}. \tag{B-4}$$

Examining (B-2) and (B-4) one can note that the hydrostatic second-order torque is of half the magnitude and opposite sign when compared to the torque induced by the first-order unsteady wave potential, $\partial\Phi^{(1)}/\partial t$. This is consistent with the findings presented by Lighthill (1979). The last set of second-order torques induced by the linear potential, $\Phi^{(1)}$, are the components associated with the horizontal and vertical velocity squared terms, u^2 and w^2 respectively. With the horizontal velocity being defined as $u = \partial\Phi^{(1)}/\partial x$, the former of these two contributions may be expressed as

$$T^{(2)}_{u^2} = -\int_{-h+d}^{0} \frac{\rho}{2}\left(\frac{\partial\Phi^{(1)}}{\partial x}\right)^2 (h-d+z)dz \tag{B-5}$$

which evaluates to

$$T_{u^2}^{(2)} = \frac{1}{2}\left\{\frac{\rho g^2 X_a^2}{4\omega^2}\sum_{j=0}^{\infty}\sum_{l=0}^{\infty}\frac{c_j k_j c_l k_l}{\cosh k_j h \cosh k_l h}\Gamma_{u^2}e^{i2\omega t} + \frac{\rho g^2 X_a X_a^*}{4\omega^2}\sum_{j=0}^{\infty}\sum_{l=0}^{\infty}\frac{c_j k_j c_l^* k_l^*}{\cosh k_j h \cosh k_l^* h}\Gamma_{u^2} + c.c.\right\} \quad \text{(B-6)}$$

where Γ_{u^2} is given by

$$\Gamma_{u^2} = \begin{cases} \frac{1}{8k_j^2}\left\{2k_j(d-h)\sinh 2k_j h + \cosh 2k_j h - \cosh 2k_j d - 2k_j^2(d-h)^2\right\} & \text{for } j = l \\ \frac{1}{2(k_j^2 - k_l^2)}\left\{2(d-h)\left[k_j \sinh k_j h \cosh k_l h - k_l \sinh k_l h \cosh k_j h\right]\right. & \\ \quad + \frac{k_j - k_l}{k_j + k_l}\left[\cosh(k_j + k_l)h - \cosh(k_j + k_l)d\right] & \text{for } j \neq l \\ \quad \left. + \frac{k_j + k_l}{k_j - k_l}\left[\cosh(k_j - k_l)h - \cosh(k_j - k_l)d\right]\right\} & \end{cases} \quad \text{(B-7)}$$

Similarly, the torque induced by the vertical velocity term, $w = \partial\Phi^{(1)}/\partial z$ is given by

$$T_{w^2}^{(2)} = -\int_{-h+d}^{0}\frac{\rho}{2}\left(\frac{\partial\Phi^{(1)}}{\partial z}\right)^2(h - d + z)dz \quad \text{(B-8)}$$

and evaluates to

$$T_{w^2}^{(2)} = \frac{1}{2}\left\{-\frac{\rho g^2 X_a^2}{4\omega^2}\sum_{j=0}^{\infty}\sum_{l=0}^{\infty}\frac{c_j k_j c_l k_l}{\cosh k_j h \cosh k_l h}\Gamma_{w^2}e^{i2\omega t} + \frac{\rho g^2 X_a X_a^*}{4\omega^2}\sum_{j=0}^{\infty}\sum_{l=0}^{\infty}\frac{c_j k_j c_l^* k_l^*}{\cosh k_j h \cosh k_l^* h}\Gamma_{w^2} + c.c.\right\} \quad \text{(B-9)}$$

where Γ_{w^2} is given by

$$\Gamma_{w^2} = \begin{cases} \frac{1}{8k_j^2}\left\{2k_j(d-h)\sinh 2k_j h + \cosh 2k_j h - \cosh 2k_j d + 2k_j^2(d-h)^2\right\} & \text{for } j = l \\ \frac{d-h}{2}\left[\frac{1}{k_j+k_l}\sinh(k_j+k_l)h - \frac{1}{k_j-k_l}\sinh(k_j-k_l)h\right] & \\ + \frac{1}{2(k_j+k_l)^2}\left[\cosh(k_j+k_l)h - \cosh(k_j+k_l)d\right] & \text{for } j \neq l \\ - \frac{1}{2(k_j-k_l)^2}\left[\cosh(k_j-k_l)h - \cosh(k_j-k_l)d\right] & \end{cases} \tag{B-10}$$

The torque induced by the second-order Stokes wave potential, $\Phi^{(21)}$, follows from the integration of the respective pressure field and is given by

$$T^{(2)}_{\Phi^{(21)}} = -\int_{-h+d}^{0} \rho \frac{\partial \Phi^{(21)}}{\partial t}(h-d+z)dz \tag{B-11}$$

which evaluates to

$$T^{(2)}_{\Phi^{(21)}} = \frac{1}{2}\left\{\rho\omega X_a^2 \sum_{j=0}^{\infty}\sum_{l=0}^{\infty} \frac{H^+_{jl}}{D^+_{jl}} \frac{c_j c_l}{(k_j+k_l)^2}\Gamma_1(k_j+k_l)e^{i2\omega t} + c.c.\right\}. \tag{B-12}$$

Similarly, the torque induced by the spurious free wave potential, $\Phi^{(22)}$, is given by

$$T^{(2)}_{\Phi^{(22)}} = -\int_{-h+d}^{0} \rho \frac{\partial \Phi^{(22)}}{\partial t}(h-d+z)dz \tag{B-13}$$

and evaluates to

$$T^{(2)}_{\Phi^{(22)}} = \frac{1}{2}\left\{\frac{\rho g c_0^2 X_a^2}{h} \sum_{p=0}^{\infty} \frac{c_p^{(22)+}}{(K_p^+)^2}\Gamma_1(K_p^+)e^{i2\omega t} + c.c.\right\}. \tag{B-14}$$

Appendix C - The Second-order Forces

With reference to equation (5.2), the forces up to second order need to be evaluated. The total second-order force is given by

$$F^{(2)} = \sum_{n=1}^{N}\sum_{m=n}^{N}\Big[F^{(2)+}_{\Phi^{(1)}} + F^{(2)-}_{\Phi^{(1)}} + F^{(2)+}_{h} + F^{(2)-}_{h} + F^{(2)+}_{u^2} + F^{(2)-}_{u^2} + F^{(2)+}_{w^2} + F^{(2)-}_{w^2} + F^{(2)+}_{\Phi^{(21)}} + F^{(2)-}_{\Phi^{(21)}} + F^{(2)+}_{\Phi^{(22)}} + F^{(2)-}_{\Phi^{(22)}}\Big] \quad \text{(C-1)}$$

where all force contributions are evaluated for a pair (n, m) drawn from the series with N components. The first-order unsteady wave acceleration $\partial\Phi^{(1)}/\partial t$ integrated up to the first-order free surface induces a force given by

$$F^{(2)\pm}_{\Phi^{(1)}} = -\int_0^{\eta^{(1)}} \rho\frac{\partial\Phi^{(1)}}{\partial t}dz = \frac{1}{2}\left\{\rho g X_a \sum_{j=0}^{\infty}\frac{c_j}{k_j}\frac{\sinh k_j(\eta^{(1)}+h) - \sinh k_j h}{\cosh k_j h}e^{i\omega t} + c.c.\right\} \quad \text{(C-2)}$$

which can be simplified by retaining only mean- and second-order terms

$$F^{(2)\pm}_{\Phi^{(1)}} = \frac{1}{2}\left\{\delta_{nm}\rho g X_n X_m^{-*}\sum_{j=0}^{\infty}\sum_{l=0}^{\infty}c_{jn}c_{lm}^{-*}e^{i(\omega_n\pm\omega_m)t} + c.c.\right\} \quad \text{(C-3)}$$

Following Lighthill (1979), there is also a force component caused by the changing effective wetted surface of the body which may be expressed as

$$F^{(2)\pm}_{h} = -\int_0^{\eta^{(1)}}\rho g z dz = -\frac{1}{2}\rho g(\eta^{(1)})^2 \quad \text{(C-4)}$$

and simplified by retaining only mean- and second-order terms

$$F^{(2)\pm}_{h} = \frac{1}{2}\left\{-\frac{1}{2}\delta_{nm}\rho g X_n X_m^{-*}\sum_{j=0}^{\infty}\sum_{l=0}^{\infty}c_{jn}c_{lm}^{-*}e^{i(\omega_n\pm\omega_m)t} + c.c.\right\} \quad \text{(C-5)}$$

Examining (C-3) and (C-5) one can note that the hydrostatic second-order force is of half the magnitude and opposite sign when compared to the force induced by the first-order unsteady wave potential, $\partial\Phi^{(1)}/\partial t$. This is consistent with the findings presented by Lighthill (1979). The last set of second-order forces induced

by the linear potential, $\Phi^{(1)}$, are the components associated with the horizontal and vertical velocity squared terms, u^2 and w^2 respectively. With the horizontal velocity being defined as $u = \partial\Phi^{(1)}/\partial x$, the former of these two contributions may be expressed as

$$F_{u^2}^{(2)\pm} = -\int_{-h+d}^{0} \frac{\rho}{2}\left(\frac{\partial\Phi^{(1)}}{\partial x}\right)^2 dz \tag{C-6}$$

which evaluates to

$$F_{u^2}^{(2)\pm} = \frac{1}{2}\left\{-\frac{1}{2}\delta_{nm}\frac{\rho g^2 X_n X_m^{-*}}{\omega_n\omega_m}\sum_{j=0}^{\infty}\sum_{l=0}^{\infty}\frac{c_{jn}c_{lm}^{-*}k_{jn}k_{lm}^{-*}}{\cosh k_{jn}h\cosh k_{lm}^{-*}h}\Gamma_{u^2}^{\pm}e^{i(\omega_n\pm\omega_m)t} + c.c.\right\} \tag{C-7}$$

where $\Gamma_{u^2}^{\pm}$ is given by

$$\Gamma_{u^2}^{\pm} = \begin{cases} \frac{1}{2k_{jn}}\left[\sinh k_{jn}h\cosh k_{jn}h - \sinh k_{jn}d\cosh k_{jn}d + k_{jn}(h-d)\right] \\ \qquad\qquad \text{for } n = m \text{ and } j = l \\ \dfrac{1}{k_{jn}^2 - (k_{lm}^{-*})^2}\left[k_{jn}\sinh k_{jn}h\cosh k_{lm}^{-*}h - k_{lm}^{-*}\sinh k_{lm}^{-*}h\cosh k_{jn}h\right. \\ \qquad\qquad \text{otherwise} \\ \qquad \left. -k_{jn}\sinh k_{jn}d\cosh k_{lm}^{-*}d + k_{lm}^{-*}\sinh k_{lm}^{-*}d\cosh k_{jn}d\right] \end{cases} \tag{C-8}$$

Similarly, the force induced by the vertical velocity term, $w = \partial\Phi^{(1)}/\partial z$, is given by

$$F_{w^2}^{(2)\pm} = -\int_{-h+d}^{0} \frac{\rho}{2}\left(\frac{\partial\Phi^{(1)}}{\partial z}\right)^2 dz \tag{C-9}$$

and evaluates to

$$F_{w^2}^{(2)\pm} = \frac{1}{2}\left\{\frac{1}{2}\delta_{nm}\frac{\rho g^2 X_n X_m^{-*}}{\omega_n\omega_m}\sum_{j=0}^{\infty}\sum_{l=0}^{\infty}\frac{c_{jn}c_{lm}^{-*}k_{jn}k_{lm}^{-*}}{\cosh k_{jn}h\cosh k_{lm}^{-*}h}\Gamma_{w^2}^{\pm}e^{i(\omega_n\pm\omega_m)t} + c.c.\right\} \tag{C-10}$$

where Γ_{w^2} is given by

$$\Gamma_{w^2} = \begin{cases} \frac{\sigma_{jn}}{2k_{jn}} \left[\sinh k_{jn}h \cosh k_{jn}h - \sinh k_{jn}d \cosh k_{jn}d - k_{jn}(h-d)\right] \\ \qquad\qquad\qquad\qquad\qquad\qquad\qquad\qquad \text{for } n = m \text{ and } j = l \\ \frac{1}{k_{jn}^2 - (k_{lm}^{-*})^2} \left[k_{jn} \sinh k_{lm}^{-*}h \cosh k_{jn}h - k_{lm}^{-*} \sinh k_{jn}h \cosh k_{lm}^{-*}h \right. \\ \qquad\qquad\qquad\qquad\qquad\qquad\qquad\qquad \text{otherwise} \\ \qquad\qquad \left. -k_{jn} \sinh k_{lm}^{-*}d \cosh k_{jn}d + k_{lm}^{-*} \sinh k_{jn}d \cosh k_{lm}^{-*}d\right] \end{cases} \tag{C-11}$$

with σ_{jn} being defined as

$$\sigma_{jn} = \begin{cases} -1 & \text{for } j = l \neq 0 \text{ and subharmonics} \\ +1 & \text{otherwise.} \end{cases} \tag{C-12}$$

The force induced by the second-order Stokes wave potential, $\Phi^{(21)\pm}$, follows from the integration of the respective pressure field and is given by

$$F^{(2)\pm}_{\Phi^{(21)}} = -\int_{-h+d}^{0} \rho \frac{\partial \Phi^{(21)\pm}}{\partial t} dz \tag{C-13}$$

which evaluates to

$$F^{(2)\pm}_{\Phi^{(21)}} = \frac{1}{2} \left\{ \delta_{nm} \rho X_n X_m^{-*} \sum_{j=0}^{\infty} \sum_{l=0}^{\infty} \frac{c_{jn} c_{lm}^{-*} (\omega_n \pm \omega_m)}{k_{jn} \pm k_{lm}^{-*}} \frac{H^{\pm}_{jnlm}}{D^{\pm}_{jnlm}} \right. \\ \left. \frac{\sinh(k_{jn} \pm k_{lm}^{-*})h - \sinh(k_{jn} \pm k_{lm}^{-*})d}{\cosh(k_{jn} \pm k_{lm}^{-*})h} e^{i(\omega_n \pm \omega_m)t} + c.c. \right\} \tag{C-14}$$

Similarly, the force induced by the spurious free wave potential, $\Phi^{(22)\pm}$, is given by

$$F^{(2)\pm}_{\Phi^{(22)}} = -\int_{-h+d}^{0} \rho \frac{\partial \Phi^{(22)\pm}}{\partial t} dz \tag{C-15}$$

and evaluates to

$$F^{(2)\pm}_{\Phi^{(22)}} = \frac{1}{2} \left\{ \frac{\rho g A_n A_m^{-*}}{h} \sum_{p=0}^{\infty} \frac{c_p^{(22)\pm}}{K_p^{\pm}} \frac{\sinh K_p^{\pm}h - \sinh K_p^{\pm}d}{\cosh K_p^{\pm}h} e^{i(\omega_n \pm \omega_m)t} + c.c. \right\} \tag{C-16}$$

Appendix D - A Note on Closed Loop Control Systems

Given that many researchers in the field of hydrodynamics may not be familiar with control systems, a brief note on closed-loop control is included here as this is relevant throughout the thesis. Consider the generic closed-loop control system shown in figure D-1. Herein, the transfer functions in the frequency domain are: $H_c(\omega)$ - the system's controller; $H_s(\omega)$ - the system to be controlled, in our specific case the wave machine; $H_a(\omega)$ - a generic feedback path (a); and $H_b(\omega)$ - a generic feedback path (b). Furthermore, the letters $A - C$ identify the quantities present at the respective signal line. In particular, the signal A represents the input and the signal C represents the output of the system. The output signal C is expressed in terms of input signal A by

$$C = H_c(\omega)H_s(\omega)B = [A - H_a(\omega)C - H_b(\omega)C]\, H_c(\omega)H_s(\omega), \qquad \text{(D-1)}$$

which may be rewritten as

$$C = A\frac{H_c(\omega)H_s(\omega)}{1 + H_c(\omega)H_s(\omega)\,[H_a(\omega) + H_b(\omega)]}. \qquad \text{(D-2)}$$

The transfer function of the entire closed-loop system, $H(\omega)$, is generally defined as the ratio of the output signal to the input signal. In addition, the product term in the denominator, $H_c(\omega)H_s(\omega)$, is usually much greater than one and the

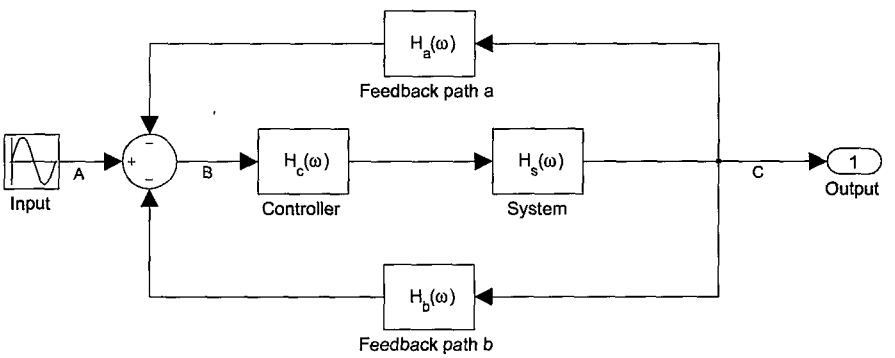


Figure D-1: Generic controller model

transfer function $H(\omega)$ may be simplified to

$$H(\omega) = \frac{C}{A} = \frac{H_c(\omega)H_s(\omega)}{1 + H_c(\omega)H_s(\omega)\left[H_a(\omega) + H_b(\omega)\right]} \approx \frac{1}{H_a(\omega) + H_b(\omega)}. \qquad \text{(D-3)}$$

In this latter simplified version it is clear that the transfer function from input signal to output signal is only affected by the feedback signals; with an ideal controller, the exact behaviour of the system, $H_s(\omega)$, is irrelevant. This is strictly only true for a controller function H_c with an infinite loop gain. In practice, large values of loop gain can be realised and this approximation is often valid.

Appendix E - Directional Wave Maker of Finite Width

The information presented in this appendix is provided as an addition to the discussion in §6.3.1. Within §6.3.1 the final solution, relating to a wave maker of finite width, is given in equation 6.1. Further details concerning the derivation of this result are given below. Following Dalrymple (1985), the velocity potential may be expressed as

$$\Phi(x, y, z, t) = \Phi(x, y, z)e^{-i\omega t}. \tag{E-1}$$

Furthermore, introducing the Fourier transform pair

$$\hat{f}(x, k_y, z) = \int_{-\infty}^{\infty} f(x, y, z)e^{-ik_y y}dy \tag{E-2}$$

and inversely

$$f(x, y, z) = \frac{1}{2\pi}\int_{-\infty}^{\infty} \hat{f}(x, k_y, z)e^{ik_y y}dk_y, \tag{E-3}$$

is helpful in order to obtain a solution for $\Phi(x, y, z)$; k_y being the wave number in the y-direction.

The focus of the present section is to demonstrate the mathematical limitation when considering segmented-type wave makers. To illustrate this, it is sufficient to evaluate the progressive part of the wave potential. Applying the Fourier transform to the boundary conditions stated in Chapter 2 and solving by separation of variables, the solution to the progressive part of the velocity potential in the (x, k_y, z) domain is obtained as

$$\hat{\Phi}_p(x, k_y, z) = -iA_p(k_y)\cosh\left(k(h + z)\right)e^{i\sqrt{k^2-k_y^2}x}, \tag{E-4}$$

where p denotes progressive and $A_p(k_y)$ is an unknown coefficient. Analogous to the discussion relating to the wave field coefficient c_0 in the two dimensional case, $A_p(k_y)$ may be expressed as

$$A_p(k_y) = \frac{\int_{-h}^{0} \hat{U}(k_y, z)\cosh k(h + z)dz}{\sqrt{k^2 - k_y^2}\int_{-h}^{0}\cosh^2 k(h + z)dz}, \tag{E-5}$$

where the orthogonality relation has been applied to the set of orthogonal functions. The final solution of the progressive velocity potential in the time domain is obtained by applying the inverse Fourier transform to equation (E-4)

$$\mathbf{\Phi_p}(x,y,z,t) = -\frac{i}{2\pi}\cosh\left(k(h+z)\right)e^{-i\omega t}\int_{-\infty}^{\infty} A_p(k_y)e^{i\sqrt{k^2-k_y^2}x}e^{ik_y y}dk_y. \quad \text{(E-6)}$$

Assuming a finite-length snake-type wave maker, the velocity imposed along the y-axis at $x = 0$ is given by

$$U(y,z) = \begin{cases} U(z)e^{ik_0 y}, & \text{for } |y| < b \\ 0 & \text{for } |y| > b \end{cases} \quad \text{(E-7)}$$

which is continuous in the interval $|y| < b$. Transforming this representation into the k_y domain gives

$$\hat{U}(k_y,z) = \frac{2\sin(k_{0y}-k_y)b}{k_{0y}-k_y}. \quad \text{(E-8)}$$

Substituting equation (E-8) into (E-5) and the result into equation (E-6) yields

$$\mathbf{\Phi_p}(x,y,z,t) = -\frac{iR}{2\pi}\cosh\left(k(h+z)\right)e^{-i\omega t}\int_{-\infty}^{\infty}\frac{2\sin(k_{0y}-k_y)b}{k_{0y}-k_y}\frac{e^{i\sqrt{k^2-k_y^2}x}}{\sqrt{k^2-k_y^2}}e^{ik_y y}dk_y, \quad \text{(E-9)}$$

where R is a coefficient that solely depends on the geometry of the wave board. Observing this equation it is important to note that for each spatial location (x,y) the infinite integral needs to be evaluated; this clearly being impractical. Dalrymple (1985) showed that, based on reformulating the integral and applying the convolution theorem, the velocity potential may be rewritten as

$$\mathbf{\Phi_p}(x,y,z,t) = -\frac{iR}{2}\cosh k(h+z)e^{-i\omega t}\int_{-b}^{b} e^{ik_{0y}\zeta}H_0^{(1)}\left[k\sqrt{x^2+(y-\zeta)^2}\right]d\zeta, \quad \text{(E-10)}$$

where $H_0^{(1)}$ is the Hankel function of the first kind. Based on this expression of the velocity potential, the surface elevation in the wave basin may be computed.

Appendix F - Comparison of Force-control Theory and An Empirical Calibration Approach

The theoretical force transfer function derived in the present thesis, $c_f(\omega, \alpha)$, relates the input demand signal to the amplitude of the progressive wave and is expressed in the physical dimensions of $[m/Nm]$ if a flap-type machine is considered. In contrast, the empirical transfer function given by Masterton & Swan (2008) (hereafter referred to as MS) is used to compute the required demand signal based on a given wave amplitude. As a result, this empirical transfer function is proportional to the inverse of $c_f(\omega, \alpha)$. A factor of proportionality must be introduced since the empirical transfer function incorporates a gain factor that relates the required demand signal (in $[Nm]$) to an output voltage (in $[V]$) used to control the machine.

For the wave making facility described in MS, the maximum output control voltage is $V_{max} = 5V$ which is scaled to a maximum output torque of $T_{max} = 133Nm$. The factor of proportionality between the empirical and the theoretical transfer function is hence expressed as the ratio of these two values; $c_{max} = V_{max}/T_{max} = 5V/133Nm$. The maximum output torque is determined as the torque required to generate the biggest wave in the tank. For requests exceeding this demand, the output voltage is clipped and limited at $V_{max} = 5V$.

The theoretical transfer function expressed in the same units as the empirical calibration data is given by $c'_f = c_{max}/c_f$. Figure F-1 shows both the empirical calibration curve from MS and the theoretical transfer function, c'_f. The overall agreement between the curves is satisfactory. However, especially at the lowest and the highest frequencies, some distinctive departures arise that need to be examined in detail.

Frequency Domain Analysis

The calibration curves evaluated by MS are based on the generation of a focused wave event and the application of the FFT technique to the time domain data. In this context, the origins of the large departures at low frequencies as well as the

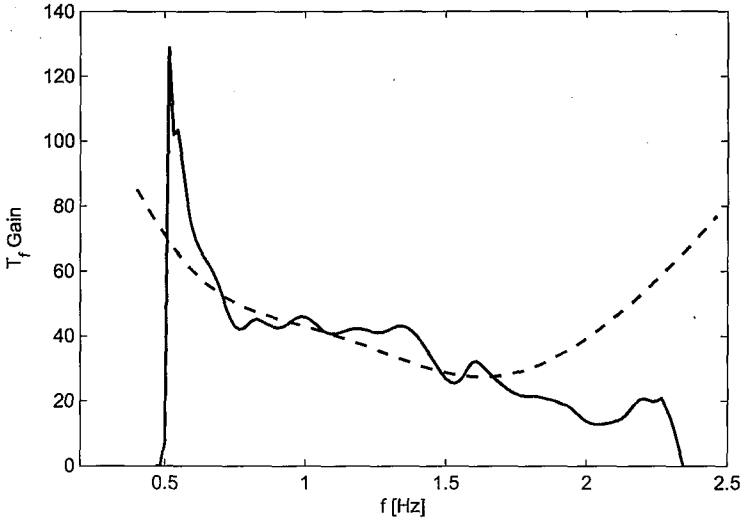


Figure F-1: Frequency dependent gain for a 3D wave basin and $\alpha = 0\,°$; —— Empirical transfer function after Masterton & Swan (2008), – – Theoretical force transfer function $c'_f(\omega, 0)$

ripples in the intermediate frequency range are best understood by considering the Fourier transforms shown figure F-2. The curves are based on the application of the FFT technique to a time domain record representing a focused wave event occuring at $t = 32s$; the latter based upon a tophat spectrum with $f_{min} = 32/64Hz$, $f_{max} = 128/64Hz$ and $\Delta f = 1/64Hz$.

Two cases are considered: (i) the data in the time domain represents the spectrum between $0 \leq t \leq 64s$ and (ii) a rectangular window of width $\pm 5s$ and centred at $t = 32s$, has been applied to the data trace and all data outside this window ($0 \leq t \leq 27s$ and $37s \leq t \leq 64s$) has been set to zero; case (ii) being equivalent to the data processing described by MS. Considering case (ii) ($A(10s)$ within figure F-2), some important deviations that directly affect the calibration results are identified.

1. The frequency domain content in the region $0.6Hz \lesssim f \lesssim 1.9Hz$ is not as smooth as expected; the ripples being most pronounced towards either end of this region.

2. The frequency domain content for $0.5Hz \leq f \lesssim 0.6Hz$ and $1.9Hz \lesssim f \leq 2.0Hz$ is too small. As a result, the values estimated by the calibration

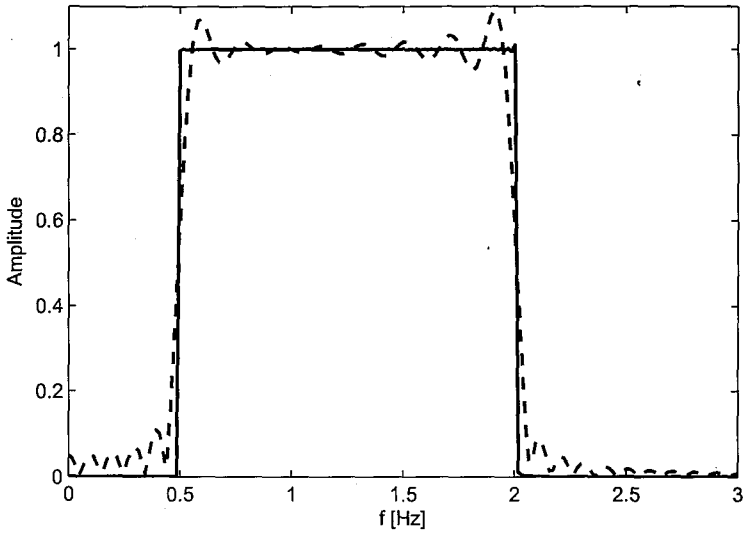


Figure F-2: Effect of a finite window length on the FFT results, tophat spectrum; —— Ideal spectral content $A(64s)$, – – Windowed spectral content $A(10s)$

procedure will be too large in those regions (the calibration attempts to correct for the FFT related errors).

3. The frequency domain content for $f < 0.5Hz$ and $f > 2.0Hz$ is too large; it should be zero in theory.

A tophat spectrum was initially adopted to illustrate these effects. However, to directly compare with the results presented in MS, the procedure of windowing a focused wave event is applied to a time domain record based on a JONSWAP spectrum. Figure F-3 (a) shows both the ideal spectrum, $A(64s)$, and the windowed frequency content, $A(10s)$. The ratio of $A(64s)/A(10s)$ provided in figure F-3 (b) further emphasises the differences between the two cases. This latter representation may explain the distinctive singularity apparent in the low frequency region ($f \approx 0.55Hz$) of the calibration data shown previously (figure F-1). As a result, the data in this region must be excluded from the discussion. Furthermore, some of the ripples observed in figure F-1 may have been introduced by the data post processing. The maximum errors in this intermediate frequency range are in the order of 5%.

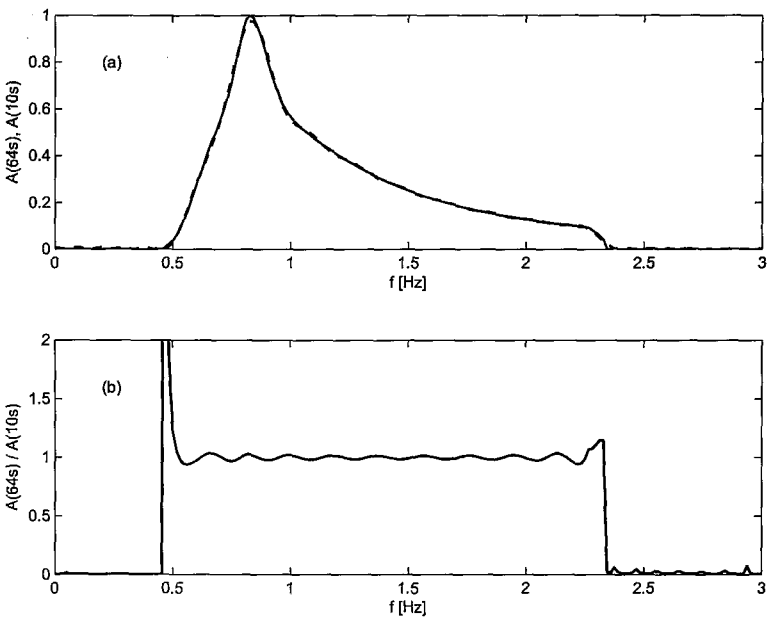


Figure F-3: Effect of a finite window length on the FFT results, JONSWAP spectrum; (a) —— Ideal spectral content $A(64s)$, – – Windowed spectral content $A(10s)$; (b) $A(64s)/A(10s)$

Nonlinear wave effects

Considering figure F-1 once more, the large deviations for the highest frequencies cannot be explained with the data post processing. In seeking an explanation for the the large departures, the second-order spectrum for the focused wave event described by MS is computed; figure F-4 (a) shows both the first-order spectrum, $A^{(1)}$, and the ideal second-order spectrum, $A^{(1)} + A^{(21)}$. In computing the second-order spectrum, all spurious wave modes have been neglected. The ratio of first-order computation and second-order computation is given in sub-plot (b) of figure F-4.

In observing this latter ratio, two interesting effects are identified. First, neglecting the second-order contributions at low frequencies (sub-harmonics) results in an additional singularity in the calibration. In combination with the singularity due to the application of the rectangular window, this is likely to account for the deviations between the theoretical results and the calibration data presented by MS. Moreover, a considerable departure between first- and second-order computation is observed at the highest frequencies; the amplitude content in the second-

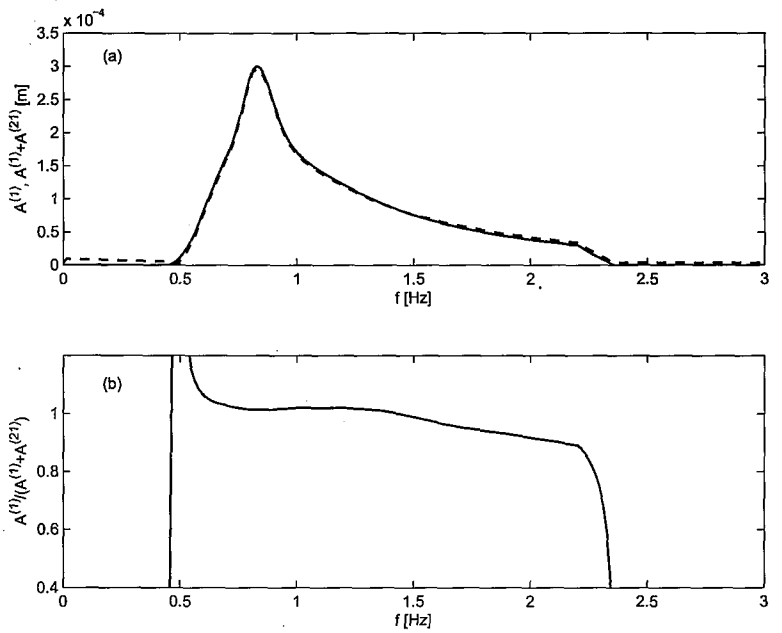


Figure F-4: JONSWAP spectrum (a) —— First-order computation, $A^{(1)}$, – – Second-order computation, $A^{(1)} + A^{(21)}$, (b) ratio $A^{(1)}/(A^{(1)} + A^{(21)})$

order computation being larger than predicted by linear theory for $f > 1.45Hz$. Again, this is likely to account for some of the departures apparent in figure F-1.

It must be noted that the calibration data presented by MS is subject to some data analysis and interpretation errors related to the FFT technique and higher-order wave effects. In particular, the singularity at the lowest frequencies is unrealistic. The discussion illustrated some of the drawbacks related to an empirical calibration approach. In applying such a technique, some significant errors may arise if the physics of the process are not fully incorporated. This becomes even more pronounced for the generation of oblique waves where the spurious modes due to a finite wave maker segment width must be considered (Chapter 6, figures 6.6 and 6.7).

Appendix G - The Experimental Environment

The thesis relies on a large amount of experimental data and this Appendix is included to provide an overview of both the experimental facility and the instrumentation employed. Even though some of this information has already been given in the main text, it is regarded as beneficial to the reader to present a more detailed coverage herein.

Wave Flumes and Wave Basin

Double Ended Wave Flume

Figure G-1 illustrates the wave flume used for the experimental study presented in Chapter 4. The flume is $27m$ long, $0.3m$ wide and the nominal water depth is $h = 0.7m$. Identical bottom hinged flap-type wave makers are installed at either end and the facility is referred to as the *Double Ended Flume* herein. The wave board is approximately $0.28m$ wide and the side-wall gap is approximately $10mm$. The gusset ensures that water is also displaced along the side-wall gaps to avoid discontinuities in the wave generation. Moreover, additional geometric design features (not further discussed) compensate for the fact that, on average, the fluid adjacent to the gusset is displaced with only half the velocity of the wave board. Both wave makers are capable of generating and absorbing simultaneously; their absorption performance being discussed in §4.14.

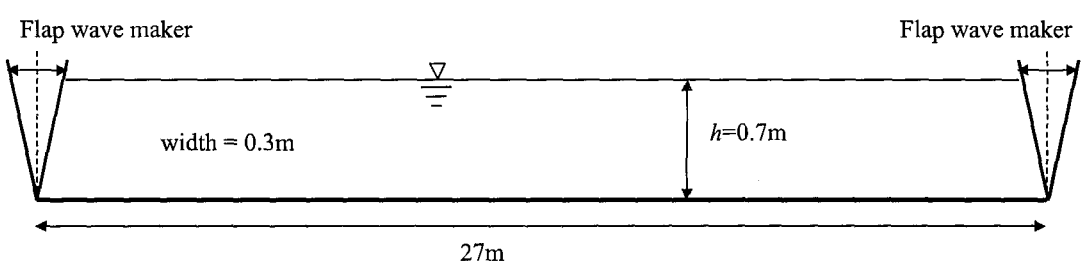


Figure G-1: *Double Ended Wave Flume* definition sketch

Coastal Wave Flume

Figure G-2 illustrates the shallow water wave flume used for the experimental study presented in Chapter 5. The flume is $23m$ long, $0.6m$ wide and, for the purpose of the present study, the water depth was kept constant at $h = 0.6m$. Owing to its shallow water application, this facility is referred to as the *Coastal Flume*. The actual geometry of the piston is more complex than illustrated in figure G-2; a photograph being provided in figure 5.16. A more detailed discussion of the geometry and the various gaps around the wave board is presented in §5.8.2.

A linearly sloping beach is installed on the flume's far side. In observing the surface profiles and energy content within the *Coastal Flume* (Chapter 5), it is important to note that this beach is not a perfect absorber; the frequency dependent reflection coefficient being given in figure G-3. Herein, the reflection coefficient γ is defined as the ratio of reflected wave amplitude over incident wave amplitude. In obtaining this coefficient, the technique presented by Lin & Huang (2004) was applied to the data recorded at eight spatial locations equally spaced at $\Delta x = 200mm$. The first gauge was located at $x = 2.15m$ and an initial wave generation period of $64s$ allowed for the build up of reflections from the far side beach. The data in figure G-3 is presented for two values of wave steepness; $Hk/2 = 0.05$ and $Hk/2 = 0.15$. Overall, the reflection coefficient is below 5% for the wave frequencies of interest. It is only for very low frequencies, or very long wave components, that the coefficient exceeds 5%.

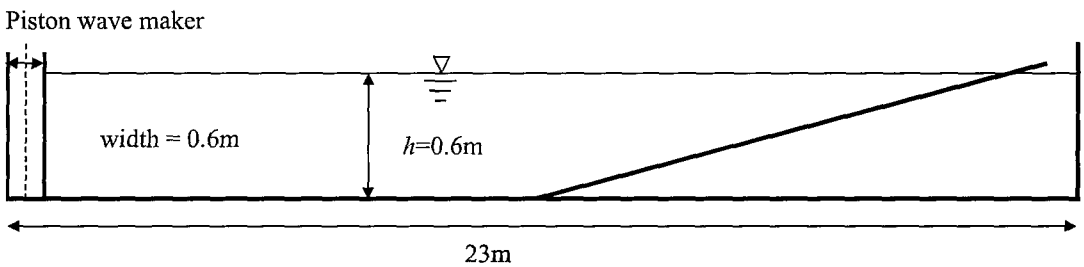


Figure G-2: *Coastal Wave Flume* definition sketch

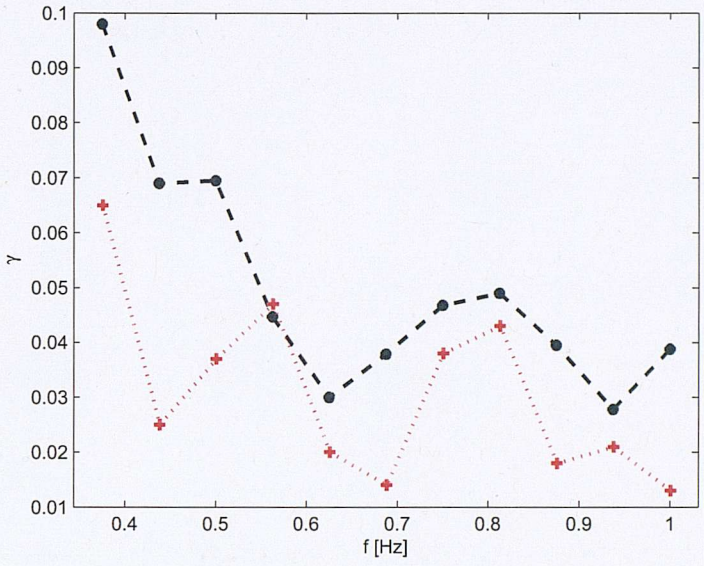


Figure G-3: Beach reflection coefficient, γ, of *Coastal Wave Flume*; Experimental data relating to: — — $Hk/2 = 0.05$ and · · · · $Hk/2 = 0.15$.

Directional Wave Basin

Figure G-4 illustrates the cross section of the directional wave basin used for the experimental study presented in Chapter 6. The basin is $10m$ long, $20m$ wide and the nominal water depth is $h = 1.5m$. Due to ongoing work, this nominal water depth was reduced to $h = 1.25m$ at the time of conducting the experiments presented within this thesis. The wave makers are located along the wide side of the basin ($20m$), enabling the generation of highly directional waves. A total of 56 paddles are installed, each approximately $0.36m$ wide. The paddle segments are operated independently, each combining a motor, a power amplifier and a controller; the latter incorporating the absorption filter. However, even though the demand signal to each segment may vary, the control program (absorption filter, signal summation, loop gain) is identical across all wave paddles.

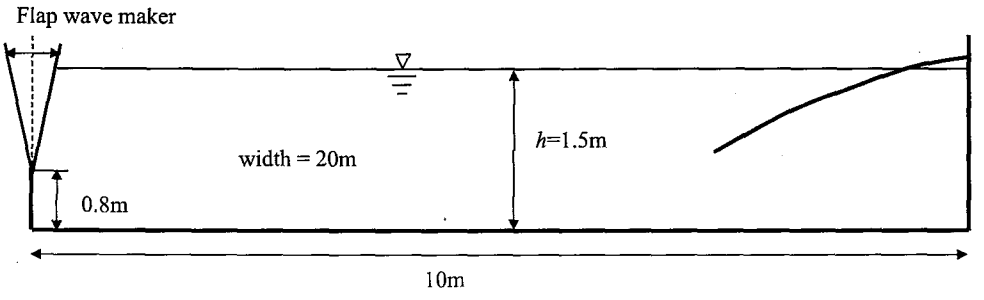


Figure G-4: Cross sectional area of directional wave basin

Wave Gauge Instrumentation

Wave Probes

In the initial stages of the work, conductive rod gauges with a diameter of $1.5mm$ to $3.0mm$ were used. It was observed that the larger diameter rods ($3.0mm$) have a significant impact on the measured surface elevation; both wave scattering and meniscus reversal effects becoming problematic. Using rods of smaller diameter reduces the impact of both effects considerably. However, particularly in steep waves, rods of diameter $1.5mm$ are not sufficiently stiff and oscillate due to the applied fluid loads. To overcome this problem, tensioned wire gauges were used. With a diameter of $0.5mm$, wave scattering and meniscus reversal are believed to be negligible. To give an indication of the surface elevation measurement accuracy, some typical performance data is discussed below.

Noise

The wave gauge instrumentation hardware has been designed and commissioned by the author of the present thesis and is now a commercial product; full design details being given by Spinneken (2006). In the context of the present work it is important to mention that an extremely low level of noise is achieved. The key advantage of the wave gauge hardware described by Spinneken (2006) is the immediate analogue to digital conversion. The leads to the wave probes are kept short ($< 2m$) and the signal is transferred digitally (16-bit) to the PC unit where a software interface governs both the calibration and the data capturing. Using short leads has a further advantage in that such an approach eliminates (or reduces) the

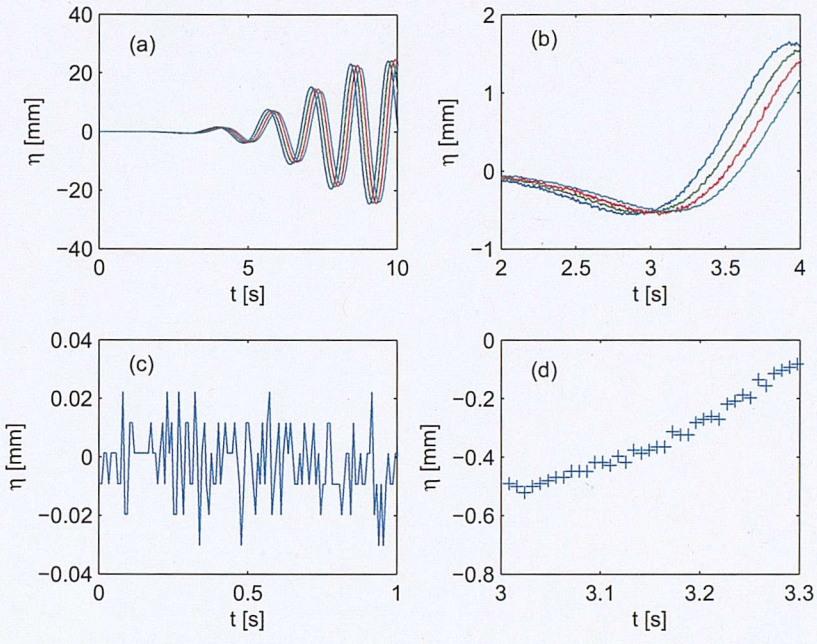


Figure G-5: Wave gauge noise characteristic. Note: All sub-plots relate to the same recording, but the scales on both axes vary considerably. Refer to the main text for further details.

spurious lead wire resistance which may otherwise introduce linearity errors.

An example of the low-noise characteristic is provided in figure G-5. Note that the four sub-plots relate to a single set of recordings, but the scales on both axes vary considerably. Within figure G-5, sub-plots (a) and (b) illustrate data recorded at four closely spaced locations whereas a single trace is shown in sub-plots (c) and (d). The surface elevation is sampled at $f = 128Hz$ with individual data points being shown in sub-plot (d).

In obtaining the data illustrated in figure G-5, the wave probes were calibrated in the range $\pm 100mm$. The noise observed at still water level (figure G-5 c) is in the order of $\pm 30\mu m$ giving a signal to noise ratio of approximately 3333 or 70dB. For traditional systems with long leads and analogue hardware this ratio would have been approximately ten times lower.

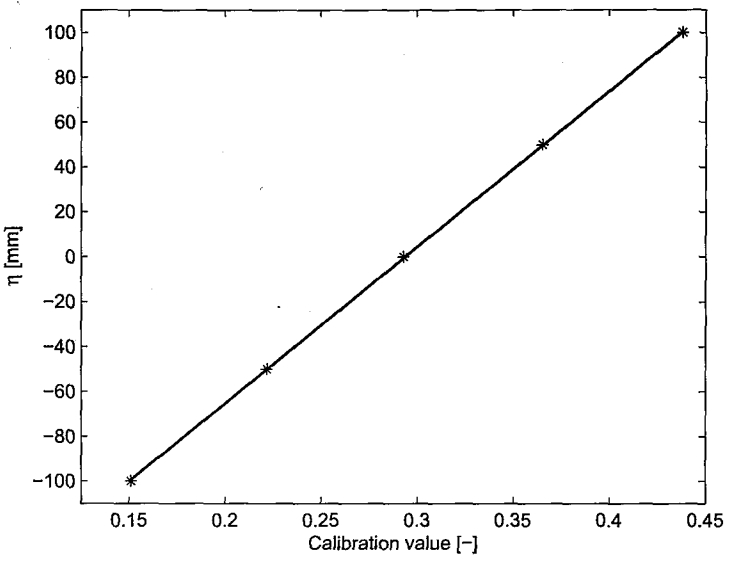


Figure G-6: Typical conductive wave probe calibration curve. Note: The calibration range is $\pm 100mm$ and the maximum departure from the linear best fit is $0.46mm$, $*$ Calibration points; —— Linear best fit.

Calibration and Linearity

A linear dependence between the immersed length of the wave probe and the output signal is assumed throughout. In calibrating the wave probes, the gauges are displaced to known locations (typically five locations) and the output signal is recorded for a certain time interval (typically $30s$). The average values of the output signal at each location are used to obtain a linear best fit; a typical calibration curve being shown in figure G-6. Within this figure the calibration range adopted is $\pm 100mm$ and the maximum departure from the linear fit is $0.46mm$. Further investigation of wave gauge calibration data has shown that maximum departures from the linear best fit line are commonly in the order of $0.5mm$.

The calibration procedure outlined above is often referred to as a static calibration. In contrast, if water waves are incident, a dynamic situation arises and meniscus reversal may cause spurious readings. However, in the case of conductive wave probes, it is the bulk of water between the two rods that determines the conductivity of the arrangement (Spinneken 2006). This is in marked contrast to capacitive wave probes where the local change in water surface elevation becomes

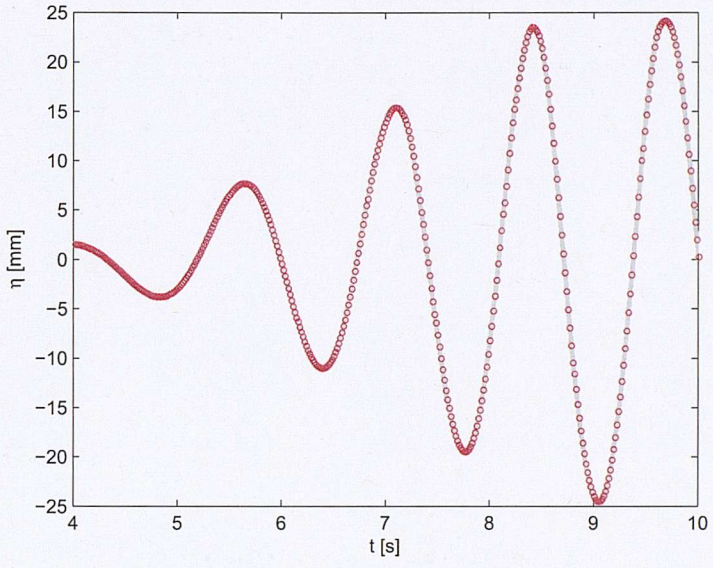


Figure G-7: Repeatability of surface elevation measurement. The two time traces were obtained using an identical wave probe calibration and are recorded 6 hours apart.

important.

Repeatability and Stability

The two data traces shown in figure G-7 were obtained using a single conductive wave probe placed in the *Coastal Wave Flume* and calibrated in the range $\pm 100mm$. An identical wave case was run twice, the time interval between the two experimental runs being six hours. The largest deviation between the two recorded surface elevations is approximately $0.3mm$. To achieve such a level of agreement both the wave gauging system and the wave making system must show excellent stability. Several tests of this kind were performed in all three facilities and the agreement between the recorded data was always found to be excellent. However, to maintain such a high level of certainty it is recommended to calibrate the wave probes once daily at the very least.

Sensors in the Wave Making System

The wave making system employs a number of transducers, most importantly: (i) a force transducer and (ii) a motor shaft encoder. Both transducers are calibration free precision devices. The signals are read continuously and the control program (absorption filter, signal summation, loop gain) is executed at $2048Hz$. The wave maker receives an updated demand signal at $32Hz$ which is considered sufficiently fast given that the highest signal frequency is in the order of $2Hz$. Apart from the absorption filter, no further filtering is applied within the closed-loop. However, to avoid potential glitches in the output signal, the run-time software demand signal is low pass filtered at $4Hz$.

All signal frequencies are periodic in a known interval referred to as the repeat time. At present, the repeat time must be a power of two; the shortest repeat time being $T_r = 16s$. Unless stated otherwise, a repeat time of $T_r = 64s$ was chosen throughout the experimental investigation. A detailed description of the wave synthesis procedure is presented in Rogers & King (1997). At the time of writing, the wave synthesis software is in the process of being revised. The outcome of this work will be published in Rogers et al. (2010).

Bibliography

Baldock, T. E., Swan, C. & Taylor, P. H. (1996), 'A laboratory study of nonlinear surface waves on water.', *Philosophical Transactions of the Royal Society of London A* **354**, 649–676.

Barthel, V., Mansard, E., Sand, S. & Vis, F. (1983), 'Group bounded long waves in physical models.', *Ocean Engineering* **10**(4), 261 – 294.

Benjamin, T. (1967), 'Instability of periodic wavetrains in nonlinear dispersive systems', *Royal Society - Proceedings Series A* **299**(1456), 59 – 75.

Benjamin, T. & Feir, J. (1967), 'Disintegration of wave trains on deep water – part 1. theory', *Journal of Fluid Mechanics* **27**(Part 3), 417 – 430.

Biésel, F. & Suquet, F. (1954), 'Laboratory wave generating apparatus', *St. Anthony Falls Hydraulic Laboratory, University of Minnesota, Minneapolis* **Project Report No. 39**.

Bode, H. (1945), *Network analysis and feedback amplifier design*, New York, NY, United States.

Chatry, G., Clement, A. H. & Gouraud, T. (1998), Self-adaptive control of a piston wave absorber, *in* 'Proceedings of the Eighth International Offshore and Polar Engineering Conference', Vol. 1, pp. 127–133.

Cummins, W. (1962), 'The impulse response function and ship motions', *Schiffstechnik* **47**, 101–109.

Dalrymple, R. A. (1985), *Physical Modelling in Coastal Engineering*, Balkema.

Dean, R. & Dalrymple, R. (1991), *Water Wave Mechanics for Engineers and Scientists*, World Scientific.

Evans, D. V. (1976), 'A theory for wave-power absorption by oscillating bodies', *Journal of Fluid Mechanics* **77**, 1–25.

Falnes, J. (1980), 'Radiation impedances matrix and optimum power absorption for interacting oscillators in surface waves', *Applied Ocean Research* **2**(2), 75–80.

Falnes, J. (1993), Optimum control of oscillation of wave-energy converters, Wave energy converters: Generic technical evaluation study, DG XII Joule Wave Energy Initiative.

Falnes, J. (1995), 'On non-causal impulse response functions related to propagating water waves', *Applied Ocean Research* **17**, 379–389.

Falnes, J. (2002), *Ocean Waves and Oscillating Systems*, Cambridge University Press.

Flick, R. E. & Guza, R. T. (1980), 'Paddle generated waves in laboratory channels', *Journal of Waterway, Port, Coastal and Ocean Engineering* **106**(WW1), 79–97.

Frigaard, P. & Christensen, M. (1994), An absorbing wave-maker based on digital filters, *in* '24th International Conference on Coastal Engineering', Vol. 1, pp. 169–180.

Hald, T. & Frigaard, P. (1997), Alternative method for active absorption in multi-directional waves, *in* 'Multi-directional Waves and their Interaction with Structures, 27th IAHR Congress, San Francisco', pp. 183–194.

Havelock, T. H. (1929), 'Forced surface-wave on water', *Philosophical Magazine* **viii**, 569–576.

Hodge, S. & Cherchas, D. (1988), 'Closed-loop discrete-time control of a hinged wavemakerm', *Automatica* **24**(3), 397–404.

Hughes, S. A. (1993), *Physical Models and Laboratory Techniques in Coastal Engineering*, World Scientific.

Isaacson, M. (1991), 'Measurement of regular wave reflection', *Journal of Waterway, Port, Coastal and Ocean Engineering* **117**(6), 553 – 569.

Jefferys, E. R. (1984), 'Simulation of wave power devices.', *Applied Ocean Research* **6**(1), 31 – 39.

Johannessen, T. B. & Swan, C. (2001), 'A laboratory study of the focusing of transient and directionally spread surface water waves.', *Proc. Roy. Soc. Lond. A* **457**, 1–36.

Johannessen, T. B. & Swan, C. (2003), 'On the nonlinear dynamics of focused wave groups in two and three dimensions.', *Proc. Roy. Soc. Lond. A* **459**, 1021–1052.

Lichten, W. (1985), 'Precise wavelength measurements and optical phase shifts. i. general theory', *Journal of the Optical Society of America A (Optics and Image Science)* **2**(11), 1869 – 76.

Lighthill, J. (1979), 'Waves and hydrodynamic loading.', *Acta Informatica* **1**, 1 – 40.

Lin, C.-Y. & Huang, C.-J. (2004), 'Decomposition of incident and reflected higher harmonic waves using four wave gauges', *Coastal Engineering* **51**(5-6), 395 – 406.

Madsen, O. (1971), 'On the generation of long waves', *Journal of Geophysical Research* **76**(36), 8672 – 83.

Mansard, E., Manoha, B. & Funke, E. (1997), A survey of multi-directional wave facilities, *in* 'Multi-directional Waves and their Interaction with Structures, 27th IAHR Congress, San Francisco', pp. 195–229.

Mansard, E. P. D. & Funke, E. R. (1980), 'Measurement of incident and reflected spectra using a least squares method.', *National Conference Publication - Institution of Engineers, Australia* pp. 95 – 96.

Masterton, S. & Swan, C. (2008), 'On the accurate and efficient calibration of a 3d wave basin', *Ocean Engineering* **35**(8-9), 763 – 773.

McCormick, M. (1983), 'Analysis of optimal ocean wave energy conversion', *Journal of Waterway, Port, Coastal and Ocean Engineering* **109**, 180–198.

McCormick, M., Johnson, D., Hebron, R. & Hoyt, J. (1981), Wave energy conversion in restricted waters by a heaving cylinder/linear-inductance system, *in* 'Proceedings OCEANS 81 (IEEE/MTS), Boston, Massachusetts'.

Milgram, J. H. (1970), 'Active water-wave absorbers', *Journal of Fluid Mechanics* **43**, 845–859.

Naito, S. (2006), 'Wave generation and absorption in wave basins: Theory and applications', *International Journal of Offshore and Polar Engineering* **16**(2), 81–89.

Naito, S. & Nakamura, S. (1985), Wave energy absorption in irregular waves by feedforward control system., *in* 'IUTAM Symposium Lisbon', Berlin, West Ger, pp. 269 – 280.

Nebel, P. (1992), 'Maximizing the efficiency of wave-energy plant using complex-conjugate control', *Proceedings of the Institution of Mechanical Engineers, Part I (Journal of Systems and Control Engineering)* **206**(I4), 225 – 36.

Newman, J. (2008), Analysis of wave generators and absorbers in basins. Unpublished study available online at www.wamit.com.

Ottesen-Hansen, N. E., Sand, S. E., Lundgren, H., Sorensen, T. & Gravesen, H. (1980), Correct reproduction of long group induced waves, *in* 'Proceedings of the 17th Coastal Engineering Conference, Sydney, Australia', pp. 784–800.

Payne, G. S., Richon, J., Ingram, D. & Spinneken, J. (2009), Development and preliminary assessment of an optical wave gauge, *in* 'Proceedings of the 8th European Wave and Tidal Energy Conference', Uppsala, Sweden.

Rogers, D. & King, G. B. (1997), *Wave generation using ocean and wave*, Edinburgh Designs Ltd.

Rogers, D., Spinneken, J. & Jason, I. (2010), A new look at wave synthesis using multiple wave fronts, *in* 'Proceedings of the 29th Americal Towing Tank Conference, In preparation'.

Salter, S. (1982), Absorbing wave-makers and wide tanks, *in* 'Directional Wave Spectra Applications', pp. 185–200.

Salter, S. H., Jeffery, D. C. & Taylor, J. R. M. (1976), 'The architecture of nodding duck wave power generators', *The Naval Architect* **Jan 1976**, 21–24.

Sand, S. (1979), Three-dimensional deterministic structure of ocean waves, Series paper 24, Technical University of Denmark.

Sand, S. E. (1982), 'Long wave problems in laboratory models', *Journal of Waterways, Port, Coastal and Ocean Engineering* **108**(WW4), 492–503.

Sand, S. E. & Donslund, B. (1985), 'Influence of the wave board type on bounded long waves', *Journal of Hydraulic Research* **23**, 147–163.

Sand, S. E. & Mynett, A. E. (1987), Directional wave generation and analysis, *in* 'IAHR Seminar Lausanne'.

Schäffer, H. A. (1996), 'Second-order wavemaker theory for irregular waves', *Ocean Engineering* **23**, 47–88.

Schäffer, H. A. & Jakobsen, K. (2003), Non-linear wave generation and active absorption in wave flumes, *in* 'Long Waves Symposium', pp. 69–77.

Schäffer, H. A. & Klopman, G. (1997), Review of multidirectional active wave absorption methods, *in* 'Multi-directional Waves and their Interaction with Structures'.

Schäffer, H. A. & Klopman, G. (2000), 'Review of multidirectional active wave absorption methods', *Journal of Waterway, Port, Coastal and Ocean Engineering* **126**(2), 88 – 97.

Schäffer, H. A. & Steenberg, C. (2003), 'Second-order wavemaker theory for multidirectional waves', *Ocean Engineering* **30**(10), 1203 – 1231.

Sheikh, R. & Swan, C. (2005), 'The interaction between steep waves and a vertical, surface-piercing column', *Transactions of the ASME. Journal of Offshore Mechanics and Arctic Engineering* **127**(1), 31 – 8.

Smith, S. (1998), *The Scientist and Engineer's Guide to Digital Signal Processing*, California Technical Pub.

Spinneken, J. (2006), Development of a complete stand-alone wave gauge system, Diplomarbeit, Otto-von-Guericke Universität Magdeburg, Germany and Edinburgh Designs Ltd., UK.

Spinneken, J. & Swan, C. (2009*a*), 'Second-order wave maker theory using force-feedback control. part i: A new theory for regular wave generation', *Ocean Engineering* **36**(8), 539 – 548.

Spinneken, J. & Swan, C. (2009*b*), 'Second-order wave maker theory using force-feedback control. part ii: An experimental verification of regular wave generation', *Ocean Engineering* **36**(8), 549 – 555.

Spinneken, J. & Swan, C. (2009c), Wave generation and absorption using force-controlled wave machines, *in* 'Proceedings of the Nineteenth International Offshore and Polar Engineering Conference', Osaka, Japan, pp. 397–404.

Sulisz, W. & Hudspeth, R. T. (1993), 'Complete second-order solution for water waves generated in wave flumes', *Journal of Fluids and Structures* **7**, 253–268.

Swan, C., Taylor, P. & van Langen, H. (1997), 'Observations of wave-structure interaction for a multi-legged concrete platform', *Applied Ocean Research* **19**(5-6), 309 - 327.

Toll, J. S. (1956), 'Causality and the dispersion relation: Logical foundations', *Physical Review* **104**, 1760–1770.

Tromans, P., Anaturk, A. & Hagemeijer, P. (1991), A new model for the kinematics of large ocean wavesapplication as a design wave, *in* '1st Offshore and Polar Engineering Conference (ISOPE)', Vol. 3, pp. 64–71.

van Leeuwen, P. J. & Klopman, G. (1996), 'New method for the generation of second-order random waves', *Ocean Engineering (Pergamon)* **23**(2), 167 - 192.

Wu, Y.-C. (1991), 'Waves generated by a plunger-type wavemaker', *Journal of Hydraulic Research* **29**(6), 851 - 860.

Zaman, M. & Mak, L. (2007), Second order wave generation technique in the laboratory, *in* 'Proceedings of the 26th International Conference on Offshore Mechanics and Arctic Engineering'.

Zhang, H. (2005), A Deterministic Combination of Numerical and Physical Models for Coastal Waves, PhD thesis, Technical University of Denmark.

Zhang, H. & Schäffer, H. A. (2007), 'Approximate stream function wavemaker theory for highly non-linear waves in wave flumes', *Ocean Engineering* **34**(8-9), 1290 - 1302.